35. Particle Detectors at Accelerators

Revised 2023. See the various sections for authors.

35.1 Introduction

This review summarizes the detector technologies employed at accelerator particle physics experiments. Several of these detectors are also used in a non-accelerator context and examples of such applications will be provided. The detector techniques which are specific to non-accelerator particle physics experiments are the subject of Chap. 36. More detailed discussions of detectors and their underlying physics can be found in books by Kolanoski & Wermes [1], Ferbel [2], Kleinknecht [3], Knoll [4], Green [5], Leroy & Rancoita [6], and Grupen [7].

Table 35.1: Typical resolutions and deadtimes of common charged particle detectors. Revised September 2023.

Detector Type	Intrinsinc Spatial Resolution (rms)	Time Resolution	Dead Time
Resistive plate chamber	50 μm	50–1000 ps*	10 ns†
Liquid argon TPC	0.5–1 mm‡	0.01-1 μs§	—¶
Scintillation tracker	$\sim$100 μm	100 ps/n‖	10 ns
Bubble chamber	10–150 μm	1 ms	50 ms**
Wire chambers (proportional and drift chambers)	50–100 μm	5–10 ns††	20–200 ns‡‡
Micro-pattern gas detector	30–40 μm	5–10 ns††	20–200 ns‡‡
Silicon strips/pixels	$\lesssim$ 10 μm§§	few ns¶¶ ‡‡	$\lesssim$ 50 ns‡‡

*LHC: $\sim$2 mm gap, $\sim$1 ns. HL-LHC: $\sim$1 mm gap, $\sim$350 ps. Timing RPC: $\sim$50 ps
†Limited by amplifier and discriminator bandwidth, usually around 100 MHz
‡Detector geometry dependent
§Using the scintillation signal
¶No deadtime for medium
‖n = index of refraction.
**Multiple pulsing time.
††For fast particles
‡‡Depending/limited by the amplifying electronics [8]
§§Depending on electrode pitch, best values around 2–4 μm have been achieved
¶¶Resolutions $<$ 100 ps are reached in dedicated pixel developments

In Table 35.1 are given typical resolutions and deadtimes of common charged particle detectors.

The quoted numbers are usually based on typical devices, and should be regarded only as rough approximations for new designs. The spatial resolution refers to the intrinsic detector resolution, i.e. without multiple scattering. We note that analog detector readout can provide better spatial resolution than digital readout by measuring and averaging the deposited charge in neighboring channels. Quoted ranges attempt to be representative of both possibilities. The time resolution is defined by how accurately the time at which a particle crossed the detector can be determined. The deadtime is the minimum separation in time between two resolved hits on the same channel. Typical performance of calorimetry and particle identification are provided in the relevant sections below.

35.2 Photon detectors

Revised August 2021 by P. Križan (Ljubljana U; Jozef Stefan Inst.).

Most detectors in high-energy, nuclear, and astrophysics rely on the detection of photons in or near the visible range, $100\,\text{nm} \lesssim \lambda \lesssim 1000\,\text{nm}$, or $1\,\text{eV} \lesssim E \lesssim 10\,\text{eV}$. This range covers scintillation and Cherenkov radiation as well as the light detected in many astronomical observations.

Generally, photodetection involves generating a detectable electrical signal proportional to the (usually very small) number of incident photons. The process involves three distinct steps:

1. generation of a primary photoelectron or electron-hole (e-h) pair by an incident photon by the photoelectric or photoconductive effect,
2. multiplication of the photoelectron or electron-hole pair signal to detectable levels, usually by one or more multiplicative bombardment steps and/or an avalanche process, and,
3. detection of charges induced by secondary electrons.

The important characteristics of a photodetector include the following:

1. quantum efficiency (QE or ϵ_Q): the average number of primary photoelectrons generated per incident photon ($0 \leq \epsilon_Q \leq 1$; in silicon more than one e-h pair per incident photon can be generated for $\lambda \lesssim 165$ nm),
2. collection efficiency (CE or ϵ_C): the overall acceptance factor other than the generation of photoelectrons ($0 \leq \epsilon_C \leq 1$),
3. gain (G): the number of electrons collected for each photoelectron generated,
4. dark current or dark noise: the electrical signal when there is no incident photon,
5. precision of measuring the intensity I of the incoming light: electronic noise (ENC or N_e) and statistical fluctuations in the amplification process compound the Poisson distribution of n_γ photons from a given source:

$$\frac{\sigma(I)}{\langle I \rangle} = \sqrt{\frac{f_N}{n_\gamma \epsilon_Q \epsilon_C} + \left(\frac{N_e}{G n_\gamma \epsilon_Q \epsilon_C}\right)^2}, \tag{35.1}$$

   where f_N, or the excess noise factor (ENF), is the contribution to the intensity distribution variance due to multiplication statistics [9],
6. dynamic range, linearity and saturation: relation between the number of incident photons and the sensor output in the pulsed mode,
7. time dependence of the response: this includes the transit time, which is the time between the arrival of the photon and the electrical pulse, and the transit time spread, and
8. rate capability: maximal rate of light pulses at which detection is still possible.

Table 35.2: Representative characteristics of some photodetectors commonly used in particle physics.

Type	λ (nm)	$\epsilon_Q\,\epsilon_C$	Gain	Risetime (ns)	Single photon time resol. (ps)	Area (mm^2)	1-p.e noise * (Hz/mm^2)	HV (V)
PMT †	115–1700	0.15–0.25	10^5–10^7	0.7–10	∼200	10–10^5	10^{-2}–10^2	500–3000
MCP-PMT†	115–650	0.01–0.10	10^3–10^7	0.15–0.3	∼20	1–10^4	1–10	500–3500
HPD†	115–850	0.1–0.3	10^3–10^4	$O(1)$	∼1000	10–10^5	10–100	$\sim 2\times10^4$
HAPD†	115–850	0.1–0.3	10^4–10^5	$O(1)$	∼30	10–10^5	∼1	$\sim 1\times10^4$
GPD†	115–500	0.15–0.3	10^3–10^6	$O(0.1)$	∼100	$O(10)$	∼1	300–2000
APD	300–1700	∼0.7	10–10^8	$O(1)$	- ‡	1–10^3	$O(10^7)$ §	400–1400
SiPM	125–1000	0.15–0.4	10^5–10^6	∼ 1	∼50	1–36	10^4–10^5	30–60

*Normalized to photocathode/sensor area; room temperature operation assumed.

†These devices often come in multi-anode configurations. In such cases, the area is to be considered on a “per readout-channel" basis.

‡No single photon detection possible.

§Since in an APD no single photon detection is possible, dark current is usually quoted instead of the dark count rate; here we assumed a gain of 50 to convert from the dark current to the dark count rate.

The QE is a strong function of the photon wavelength (λ), and is usually quoted at maximum, together with a range of λ where the QE is comparable to its maximum. Spatial uniformity and linearity with respect to the number of photons are highly desirable in a photodetector response.

Optimization of these factors involves many trade-offs and varies widely between applications. For example, while a large gain is desirable, attempts to increase the gain for a given device also increases the ENF and after-pulsing ("echos" of the main pulse). In solid-state devices, a higher QE often requires a compromise in the timing properties. In other types, coverage of large areas by focusing photoelectrons increases the transit time spread.

Other important considerations also are highly application-specific. These include the photon flux and wavelength range, the total area to be covered, and the efficiency required, the volume available to accommodate the detectors, characteristics of the environment such as chemical composition, temperature, magnetic field, ambient background, as well as ambient radiation of different types, mode of operation (continuous or triggered), bias (high-voltage) requirements, power consumption, calibration needs, aging, cost, and so on. Several technologies employing different phenomena for the three steps described above, and many variants within each, offer a wide range of solutions to choose from. The salient features of the main technologies and the common variants are described below. Some key characteristics are summarized in Table 35.2.

35.2.1 *Vacuum photodetectors*

Vacuum photodetectors can be broadly subdivided into three types: photomultiplier tubes, microchannel plate photomultiplier tubes, and hybrid photodetectors.

35.2.1.1 *Photomultiplier tubes*

A versatile class of photon detectors, vacuum photomultiplier tube (PMT) has been employed by a vast majority of all particle physics experiments to date [9]. Both “transmission-" and “reflection-type" PMTs are widely used. In the former, the photocathode material is deposited on the inside of a transparent window through which the photons enter, while in the latter, the photocathode material rests on a separate surface that the incident photons strike. The cathode material has a low work function, chosen for the wavelength band of interest. When a photon hits the cathode and liberates an electron (the photoelectric effect), the latter is accelerated and guided by electric fields

to impinge on a secondary-emission electrode, or dynode, which then emits several(~ 5) secondary electrons. The multiplication process is repeated typically about 10 times in series to generate a sufficient number of electrons, which are collected at the anode for delivery to the external circuit. The total gain of a PMT depends on the applied high voltage V as $G = AV^{kn}$, where $k \approx 0.7$–0.8 (depending on the dynode material), n is the number of dynodes in the chain, and A a constant (which also depends on n). Typically, G is in the range of 10^5–10^7; time resolution is $O(1ns)$ but can be as good as ≈ 100 ps for certain PMT types.

A large variety of PMTs covers a wide span of wavelength ranges from infrared (IR) to extreme ultraviolet (XUV) [10]. They are categorized by the window materials, photocathode materials, dynode structures, and anode configurations. Common window materials are borosilicate glass for IR to near-UV, fused quartz and sapphire (Al_2O_3) for UV, and MgF_2 or LiF for XUV. The choice of photocathode materials include a variety of mostly Cs- and/or Sb-based compounds such as CsI, CsTe, bi-alkali (SbRbCs, SbKCs), multi-alkali (SbNaKCs), GaAs(Cs), GaAsP(Cs), *etc.* Sensitive wavelengths and peak quantum efficiencies for these materials are summarized in Table-35.3. Typical dynode structures used in PMTs are circular cage, line focusing, box-and-grid, venetian blind, and fine mesh.

Multianode PMTs (MaPMTs) of up to 5×5 cm^2 in size are based on the parallel (side-by-side) arrangement of several dynode channels and anodes in the same tube, requiring advanced micro-machining and processing techniques. Fast PMTs with very large windows—measuring up to 508 mm across—have been developed for detection of Cherenkov radiation in neutrino experiments such as Super-Kamiokande and KamLAND among many others. Specially prepared low-radioactivity glass is used to make these PMTs, and they are also able to withstand the high pressure of the surrounding liquid.

PMTs are vulnerable to magnetic fields—sometimes even the geomagnetic field causes large orientation-dependent gain changes. A high-permeability metal shield is often necessary. However, proximity-focused PMTs, *e.g.* the fine-mesh types, can be used even in a high magnetic field ($\geq$ 1 T) if the direction of electric field of the tube is close to the direction of the external magnetic field. CMS uses custom-made vacuum phototriodes (VPT) mounted on the back face of projective lead tungstate crystals to detect scintillation light in the endcap sections of its electromagnetic calorimeters, which are inside a 3.8 T superconducting solenoid. A VPT employs a single dynode (thus, $G \approx 10$) placed close to the photocathode, and a mesh anode plane between the two, to help it cope with the strong magnetic field, which is not too unfavorably oriented with respect to the photodetector axis in the endcaps (within 25°), but where the radiation level is too high for Avalanche Photodiodes (APDs) like those used in the barrel section.

35.2.1.2 *Microchannel plate photomultiplier tubes*

A typical microchannel plate photomultiplier tube (MCP-PMT) consists of two or more $\sim$1 mm thick glass plates with densely packed $O(10\ \mu$m)-diameter cylindrical holes, or "microchannels", sitting between the transmission-type photocathode and anode planes, separated by $O(1$ mm) gaps. Instead of discrete dynodes, the inner surface of each cylindrical hole with a length-to-diameter ratio of 40-100 serves as a continuous dynode for the entire cascade of multiplicative bombardments initiated by a photoelectron. Gain fluctuations are reduced by operating each of the MCPs in the saturation mode. MCPs are stacked in a "chevron" configuration that alternates their bias angle; this reduces ion and photon feed-back effects and optimizes the overall amplification gain.

MCP-PMTs are thin, offer good spatial resolution, have excellent time resolution ($\sim$20 ps), and can tolerate magnetic fields up to 0.1 T and axial fields up to $1 - 2$ T. The technology has significantly evolved over the past 10 years [11]. A main breakthrough was the introduction of the atomic layer deposition (ALD) coatings on the MCP surfaces to increase the lifetime (>20 C/cm^2 of

charge accumulated on the anode) and gain. The Large Area Picosecond Photo-Detector (LAPPD) project [12] is an important attempt to produce at a reasonable cost large (20 by 20 cm^2) sensors with a transit time spread of 50-70 ps.

35.2.1.3 *Hybrid photon detectors*

Hybrid photon detectors (HPD) combine the sensitivity of a vacuum PMT with the excellent spatial and energy resolutions of a silicon sensor [13]. A single photoelectron ejected from the photocathode is accelerated through a large potential difference of ∼20 kV before it impinges on the silicon sensor/anode. The gain nearly equals the maximum number of *e*-*h* pairs that could be created from the entire kinetic energy of the accelerated electron: $G \approx \mathrm{eV}/w$, where e is the electronic charge, V is the applied potential difference, and $w \approx 3.7$ eV is the mean energy required to create an *e*-*h* pair in Si at room temperature. Since the gain is achieved in a single step, one can expect to have the excellent resolution of a simple Poisson statistic with large mean, but in fact it is even better, thanks to the Fano effect discussed in Sec. 35.8.

Low-noise electronics must be used to read out HPDs if one intends to take advantage of the low fluctuations in gain, *e.g.* when counting small numbers of photons. HPDs can have the same $\epsilon_Q\,\epsilon_C$ and window geometries as PMTs and can be segmented down to ∼50 μm. However, they require rather high biases and will not function in a magnetic field. The exception is proximity-focused devices (⇒ no (de)magnification) in an axial field. With time resolutions of ∼10 ps and superior rate capability, proximity-focused HPDs can be an alternative to MCP-PMTs. Applications of HPDs include the CMS hadronic calorimeter and the RICH detector in LHCb. Large-size HPDs with sophisticated focusing may be suitable for future water Cherenkov experiments.

Hybrid APDs (HAPDs) add an avalanche multiplication step following the electron bombardment to boost the gain by a factor of ∼50. This affords a higher gain and/or a lower bias voltage, but also increases the detector capacitance and fluctuations in multiplication. The forward RICH detector of Belle II uses a 144-channel device of this type [14].

Table 35.3: Properties of photocathode and window materials commonly used in vacuum photodetectors. [10]

Photocathode material	λ (nm)	Window material	Peak ϵ_Q (λ/nm)
CsI	115–200	MgF_2	0.13 (130)
CsTe	115–320	MgF_2	0.17 (200)
Bi-alkali	300–650	Borosilicate	0.27 (390)
	160-650	Synthetic Silica	0.27 (390)
"Ultra Bi-alkali"	300–650	Borosilicate	0.43 (350)
	160-650	Synthetic Silica	0.43 (350)
Multi-alkali	300–850	Borosilicate	0.20 (375)
	160-850	Synthetic Silica	0.25 (380)
GaAsP(Cs)	280-720	Borosilicate	0.40 (480-530)

35.2.2 *Gaseous photon detectors*

In a gaseous photon detector (GPD) a photoelectron in a suitable gas mixture initiates an avalanche in a high-field region, producing a large number of secondary impact-ionization electrons. In principle the charge multiplication and collection processes are identical to those employed in gaseous tracking detectors such as multiwire proportional chambers (MWPC), micromesh gaseous detectors (Micromegas), or gas electron multipliers (GEM). These are discussed in Sec. 35.6.4.

The devices can be divided into two types depending on the photosensitive material. One type uses solid photocathode materials much in the same way as PMTs. Since it is resistant to gas mixtures typically used in tracking chambers, CsI is a common choice. In the other type, photoionization occurs on suitable molecules vaporized and mixed in the drift volume. Most gases have photoionization work functions in excess of 10 eV, which would limit their sensitivity to wavelengths far too short. However, vapors of tetrakis dimethyl-amine ethylene (TMAE) or tri-ethyl-amine (TEA), which have smaller work functions (5.3 eV for TMAE and 7.5 eV for TEA), are suited for XUV photon detection [15]. Since devices like GEMs offer sub-mm spatial resolution, GPDs are often used as position-sensitive photon detectors. They can be made into flat panels to cover large areas ($O(1\ \mathrm{m}^2)$), can operate in high magnetic fields, and are relatively inexpensive. Many of the ring imaging Cherenkov (RICH) detectors have used GPDs for the detection of Cherenkov light [16–19]. Special care must be taken to suppress the ion-feedback and photon-feedback processes in GPDs. It is also important to maintain high purity of the gas as minute traces of O_2 or H_2O can significantly degrade the detection efficiency.

35.2.3 *Solid-state photon detectors*

In a phase of rapid development, solid-state photodetectors are competing with vacuum- or gas-based devices for many existing applications and making way for a multitude of new ones. Compared to traditional vacuum- and gaseous photodetectors, solid-state devices are more compact, lightweight, rugged, tolerant to magnetic fields, and often cheaper. They also allow fine pixelization, are easy to integrate into large systems, and can operate at low electric potentials, while matching or exceeding most performance criteria.

Silicon photodiodes (PD) are widely used in high-energy physics as particle detectors and in a large number of applications as photon detectors. The structure is discussed in some detail in Sec. 35.8. In its simplest form, the PD is a reverse-biased p-n junction. Photons with energies above the indirect bandgap energy (wavelengths shorter than about 1050 nm, depending on the temperature) can create e-h pairs (the photoconductive effect), which are collected on the p and n sides, respectively. Often, as in the PDs used for crystal scintillator readout in CLEO, L3, Belle, BaBar, and GLAST, intrinsic silicon is doped to create a p-i-n structure. The reverse bias increases the thickness of the depleted region; in the case of these particular detectors, to full depletion at a depth of about 100 μm. Increasing the depletion depth decreases the capacitance (and hence electronic noise) and extends the red response. Quantum efficiency can exceed 90%, but falls toward the red because of the decrease of the light absorption probability in silicon; the absorption length reaches 100 μm at 985 nm. However, since $G = 1$, electronic signal amplification is necessary. Optimal low-noise amplifiers are slow, but, even so, noise limits the minimum detectable signal in room-temperature devices to several hundred photons.

In APDs, an exponential cascade of impact ionizations initiated by the original photogenerated e-h pair under a large reverse-bias voltage leads to an avalanche multiplication [20–23], and eventually to breakdown in Geiger-mode APDs. As a result, detectable electrical response can be obtained from low-intensity optical signals down to single photons. Excellent junction uniformity is critical, and a guard ring is generally used as a protection against edge breakdown. Well-designed APDs, such as those used in CMS crystal-based electromagnetic calorimeter, have achieved $\epsilon_Q\,\epsilon_C \approx 0.7$ with sub-ns response time. The sensitive wavelength window and gain depend on the semiconductor used. The gain is typically 10–200 in linear and up to 10^8 in Geiger mode of operation. Stability and close monitoring of the operating temperature are important for linear-mode operation, and substantial cooling is often necessary.

One of the most promising recent developments in the field is SiPMs ("Silicon Photomultiplier"), a device consisting of large arrays ($O(10^3)$) of tiny APDs packed over a small area ($O(1\ \mathrm{mm}^2)$) and

operated in a limited Geiger mode [24–26]. Although each cell only offers a binary output, linearity with respect to the number of photons is achieved by summing the cell outputs. The sum of all cells is proportional to the number of photons received so long as the probability of an individual cell receiving multiple photons during a single time gate is negligible. SiPMs are being adopted as the preferred solution for various purposes including medical imaging, *e.g.* positron emission tomography (PET). These compact, rugged, and economical devices allow auto-calibration through decent separation of photoelectron peaks and offer gains of $O(10^6)$ at a moderate bias voltage (∼30 V). However, the single-photoelectron noise of a SiPM, being the logical "or" of $O(10^3)$ Geiger APDs, is rather large: O(10-100 kHz/mm^2) at room temperature. Intensive R&D in recent years [27] led to a substantial reduction in dark count rates and in correlated noise levels, resulting in coverage of larger areas and in a wider range of applications. One way to further improve the signal-to-noise ratio in SiPMs is by using dedicated light collectors, either as quartz Winston cone like arrays [28] or suitably designed meta-materials [29]. In this way, photons propagate from a larger entry window to a considerably smaller semiconductor sensor, resulting in an improved signal photon to dark-count ratio. Intense R&D is expected to improve radiation hardness of these sensors. The fabrication of the sensors and the front-end electronics combined in the same process with the goal of making SiPMs extremely easy to use has already been successful (digital SiPMs) [30], and remains a topic of intense R&D.

More solid-state light sensors have either been developed or are potentially interesting for use in HEP experiments. The Run 2 DØ detector used 86000 Visible-light photon counters (VLPC) to read the optical signal from its scintillating-fiber tracker and scintillator-strip preshower detectors. These light sensors utilize the formation of an impurity band only 50 meV below the conduction band in As-doped Si to generate strong ($G \approx 5 \times 10^4$) yet sharp response to single photons with $\epsilon_Q \approx 0.9$ [31–33]. Only a very small bias (∼7 V) is needed, but high sensitivity to infrared photons requires cooling below 10 K. Another interesting light sensor that has not yet found its use in HEP instrumentation are quantum dots, realized by nanometer-sized semiconductor 'particles' embedded in a semiconductor bulk.

35.2.4 *Superconducting photon detectors*

In this rapidly developing technology field, three most established technologies are the superconducting nano-wire single photon detector (SNSPD), the transition edge sensor (TES), and the microwave kinetic inductance detector (MKID). An SNSPD consists of a thin (4 nm) and narrow (100-250 nm) superconducting nanostrip that is current-biased just below its critical current. Absorption of a photon generates a resistive domain in the superconducting nanostrip, which leads to a transient voltage signal that can be detected. SNSPDs offer a unique combination of speed, both in terms of count rate (∼GHz) and low timing jitter (< 3 ps [34]), large range of wavelength sensitivity from VUV (120 nm) to mid-IR (10 μm), high detection efficiencies (approaching 100% for UV to near-IR), and low dark count rates (∼5-10 Hz), making them appealing for a wide variety of demanding applications.

Examples of present use in particle physics are small nanowire detectors for dark matter and dark photons. Work is in progress that could make these sensors relevant to HEP applications by increasing the area (using 300 mm wafers and larger) and pixel size, coupling via windows to cryogenic stages, and readout of arrays (superconducting electronics for data processing). While the performance of these sensors is impressive, an application in large accelerator-based detectors would require an extensive R&D program because of the severe cryogenic requirements.

35.3 Organic scintillators

Written August 2023 by S. C. Eno (U. Maryland) and Matthieu Hamel (Paris-Saclay U. CEA, LIST).

Organic scintillators produce light when transversed by a charged particle. They can be broadly categorized into four types: single crystal, liquid, plastic, and a recently emerged glass [35]. The most useful scintillators produce photons with wavelengths between 370-750 nm (ultraviolet to red), typically peaking at 425 nm [36] via a series of processes that are initialized when charged particles interact with the material via both excitation and ionization/recombination (see Sec. 34.2 of this *Review*). Typical photon yields are about 1 photon per 100 eV of energy deposit [37], although the collected and transduced signal can be much lower. Methods to guide the light towards the photon-electron converter, such as diffusive paint, reflectors, photonic crystals, or light guides, may be required to optimize light yield.

Organic scintillators have found use in a wide variety of detectors [38]. Plastics are mostly used in collider detectors, and liquids in neutrino experiments. Ease of fabrication into desired shapes and low cost has made plastic scintillator ideal for large detectors. In the form of scintillating fiber, it has found widespread use in tracking and calorimetry. Demand for large volume detectors (e.g. neutrino detectors: MiniBooNE, NOvA) has led to increased use of liquid scintillator, which can be very low cost.

35.3.1 *Scintillation mechanism*

Plastic and liquid scintillators are based on an aromatic "matrix" such as benzene. The p electrons form both "pi" and "sigma" bonds between the atoms; the pi bonds are responsible for scintillation. Scintillation is produced via standard photophysical interactions, shown schematically in Fig. 35.1. While there have been claims of delayed light production on long time scales (labeled "phosphorescence" in the figure), this is still a subject of active debate in the community. As aromatic molecules scintillate in the ultraviolet (UV), useful scintillators have one or several fluorophores dissolved into the matrix as dopants. Common fluorophores include 2,5-diphenyloxazole, *p*-terphenyl, 9,10-diphenylanthracene (9,10-DPA), 1,4-bis(2-methylstyryl)benzene (bis-MSB) and 1,4-bis(5-phenyl-2-oxazolyl)benzene (POPOP). Each molecule has its own role: the matrix (whether liquid or plastic) is where most of the radiation/matter interaction occurs. After radiation interaction, ions may recombine giving birth to excited molecules (excitons). Excitons in the matrix are transferred to a "primary fluorophore", whose concentration is typically 1-3 weight % in commercial plastic and liquid scintillators. This concentration is large enough to ensure exciton transfer – primarily via the Förster mechanism, a resonant dipole-dipole interaction which decreases at sixth the power of the distance between molecules. The concentration, however, can be up to the solubility limit. Transfer via the Förster mechanism increases both speed and light output of the organic scintillator. To reduce reabsorption of the emitted light by the matrix or the primary fluorophore, and the resulting shortened attenuation length, a "secondary fluorophore" is also used to shift the light to longer wavelengths. Transfer from the primary to the secondary is generally radiative. Typical secondary concentrations in plastic and liquids are 0.01-0.2 weight %. The chain of emission and absorption from the matrix to the subsequent fluorophores is shown in Fig. 35.2. Scintillators with two fluorophores typically have absorption lengths of several meters. The longest attenuation lengths require a third fluorophore: when the matrix is transparent up to 1 cm, adding a primary fluorophore increases the light transmission up to $\approx$ 10 cm, whereas the ternary cocktail is transparent up to 2 m and longer [39].

For most scintillators, decay times are in the ns range; rise times are much faster. Sub-ns timing resolutions have been achieved [40].

Organic scintillators do not respond linearly to the ionization density. Very dense ionization

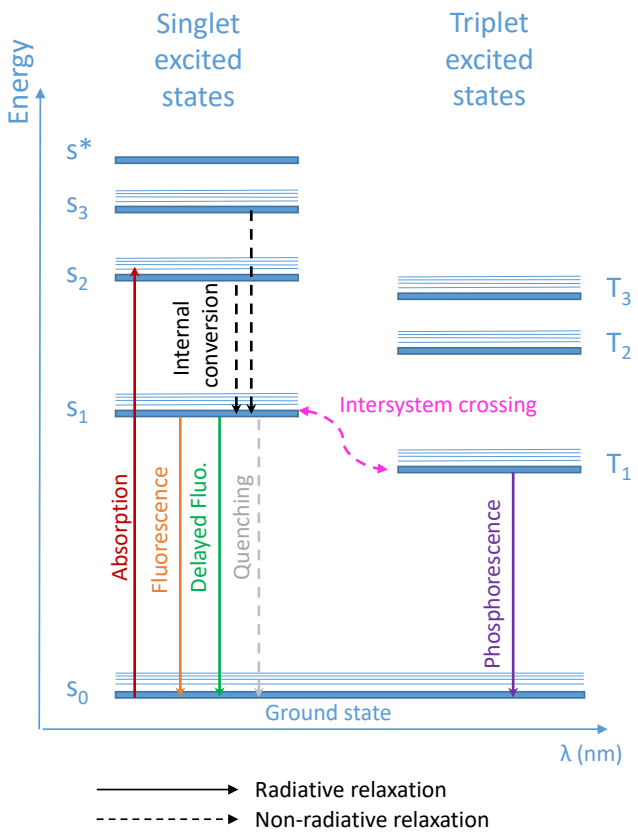

Figure 35.1: Schematic of scintillation mechanism. Schematic of typical excitation and de-excitation of matrix modules.

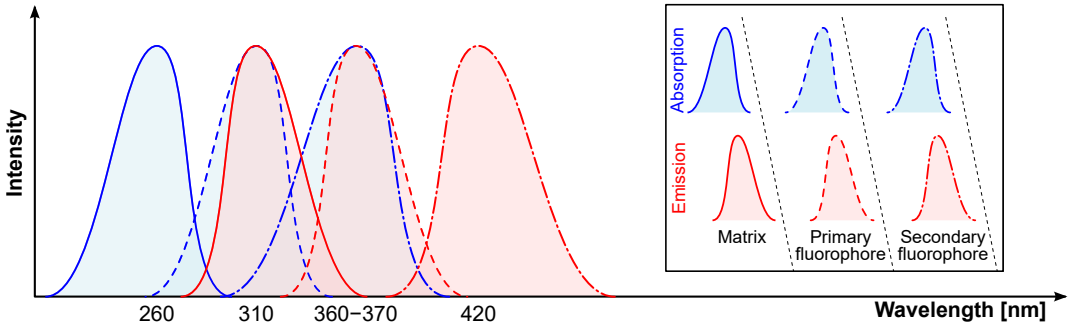

Figure 35.2: Schematic of scintillation mechanism. Typical emission and absorption spectra for the matrix, the primary, and the secondary fluorophore.

tracks, with large dE/dx, emit less light than expected compared to minimum-ionizing particles. A widely used semi-empirical model by Birks posits that recombination and quenching effects between the excited molecules reduce the light yield [41]. These effects are more pronounced the greater the density of the excited molecules. Birks' formula is

$$\frac{d\mathcal{L}}{dx} = \mathcal{L}_0 \frac{dE/dx}{1 + kB\, dE/dx}, \tag{35.2}$$

where $\mathcal{L}$ is the luminescence, $\mathcal{L}_0$ is the luminescence at low specific ionization density, and the product kB is known as Birks' constant, which must be determined for each scintillator by mea-

surement. The value of kB for polystyrene is 0.126 mm/MeV, which is large enough to play an important role in compensation in scintillator-based calorimetry. The high hydrogen content of plastic, which enhances the neutron interaction cross section, as well as the its large mass stopping power, also contributes to calorimetry compensation. In the case of large dE/dx values (e.g. with alpha particles), ion recombination may lead to the creation of triplet excited states instead of singlet excited states. If two triplet states are close enough (typically in the order of 10Å), then triplet-triplet annihilation may occur following the Dexter process [42], leading to delayed fluorescence. This phenomenon is useful for α/β or neutron/γ discrimination and is more efficient in liquid scintillators than in plastics due to the molecular motion.

Extensive research searching for new efficient molecules that can act as matrix, primary, or secondary fluorophores, is ongoing [43]. Other chemical modifications can affect the scintillator emission wavelength and decay time, or be used *e.g.* as stabilizers or to enhance thermal neutron sensitivity. Other parameters that can be modified are the density and the effective atomic number.

35.3.2 *Plastic scintillator practicalities*

Most commercial plastic scintillators use either polystyrene (PS) or poly(vinyltoluene) (PVT) as matrix. A variety of manufacturing techniques [43] are used in the production of plastic scintillator. Cast plastic has the highest light yield, while extruded scintillator is less expensive and allows creation of the scintillator and coating with a diffusive reflector in a single process. In the last couple of years, 3D printing of plastic scintillator has emerged as a reliable production method. The technique has been applied towards plastics for pulse-shape discrimination (PSD) [44]. However, large-scale production (10+ liters) has not yet been achieved. Plastic scintillator is also used to produce scintillating, wavelength-shifting, and clear fibers. These fibers can be useful to guide light to photodetectors, and as the active element in the type of calorimeter pioneered by the RD52/DREAM collaboration [45]. They have even been used in the construction of trackers [46,47].

Plastic scintillators are reliable, robust, and convenient. However, exposure to solvent vapors, high temperatures, mechanical flexing, irradiation, or rough handling will cause degradation. The surface is a particularly fragile region and can "craze" – develop microcracks which degrade transmission of light by total internal reflection. Crazing is particularly likely where oils, solvents, or fingerprints have contacted the surface or when mechanical stresses are present. The light yield is influenced by several environmental factors: it decreases with the partial pressure of oxygen [48] and increases with increasing magnetic field. In particular, the combination of elevated temperature with relative humidity accelerates aging. This apparent fogging is typically observed in radiation portal monitors, which are exposed to harsh environmental conditions. The aging can become irreversible after multiple cycles. Recently the T2K collaboration reported a 10-year light-yield measurement showing damage due to aging [49].

Plastics are susceptible to radiation damage [50]. At high enough dose, the visible color of the plastic can change to yellow or (at high enough dose) even brown. During irradiation, broken atomic bonds ("radicals") absorb light, generally strongly in the UV, with tails to longer wavelengths. Because of this, shifting the light to longer wavelengths reduces the decrease in light output and in attenuation length due to radiation effects. Radicals produce mostly temporary damage that "anneals" when the irradiation ends, as the bonds can reform. Radicals can also polymerize via cross linking, and this leads to a permanent reduction in light yield [51]. In an inert atmosphere at room temperature, the bond reformation timescale is on the order of a month. Oxygen, which diffuses into the plastic during radiation to a depth that scales as the inverse square root of dose rate, can quickly bind to the radicals, reducing but not eliminating temporary damage at the price of a small increased permanent damage [52–54]. After irradiation, oxygen, if present, will diffuse through the entire sample, leading to oxide formation and speeding the annealing process. The

decrease in light output due to permanent damage depends on the dose rate. Lower dose rates show large light losses for the same dose. The ratio of the light output to the unirradiated light output can roughly be parameterized as an exponential. For dose rates typical of current collider detectors at the Large Hadron Collider (from a few 10^{-3} to 10 Gy/hr), an exponential dose constant of tens of kGy is observed.

35.3.3 *Organic glass scintillators*

Starting in 2016, extensive research by Sandia National Laboratories lead to a new organic scintillator family: organic glasses (OGSs) [55]. Whereas polymers are long-chain molecules built from a standard unit called a monomer, OGSs consist of small organic molecules. In addition, polymers such as PS or PVT require dopants, when OGSs are intrinsically good scintillators. This new material has the useful properties present in inorganic single crystals (light yield, PSD properties, along with fast-timing properties), without the poor mechanical characteristics seen in single crystals. The maintenance of the amorphous state of these bulk optical materials was achieved mainly either by using molecules with high configurational disorder or by introducing compositional disorder. OGSs can be prepared in medium to large scales when they are blended with polymers, or pixelated for neutron detection systems, and they can eventually be loaded with heavy elements.

35.3.4 *Liquid scintillator practicalities*

Liquid scintillators have been used in large scale neutrino experiments 36.3.1.1 due to their low cost. They can hermetically fill any vessel shape. Liquid scintillators are also, due to the mobility of the molecules, much less susceptible to radiation damage.

Care must be taken to avoid dissolved water, solvents such as isopropyl alcohol, and oxygen, which reduce light yield. As they can dissolve many materials (e.g. plastics, adhesives, paints..) care must be taken in their handling. Flammability concerns limit their use in practical experiments in intense radiation fields.

35.4 Inorganic scintillators

Revised August 2023 by C.L. Woody (BNL) and R.-Y. Zhu (HEP California Inst. of Technology).

Inorganic crystals form a class of scintillating materials with much higher densities than organic plastic scintillators (typically $\sim$ 4–8 g/cm^3) with a variety of different properties for use as scintillation detectors. Due to their high density and high effective atomic number, they can be used in applications where high stopping power or a high conversion efficiency for electrons or photons is required. These include total absorption electromagnetic calorimeters (see Sec. 35.10.2), which consist of a totally active absorber (as opposed to a sampling calorimeter), as well as serving as gamma ray detectors over a wide range of energies. Many of these crystals also have very high light output, and can therefore provide excellent energy resolution down to very low energies ($\sim$ few hundred keV).

Some crystals are intrinsic scintillators in which the luminescence is produced by a part of the crystal lattice itself. However, other crystals require the addition of a dopant, typically fluorescent ions such as thallium (Tl) or cerium (Ce) which is responsible for producing the scintillation light. However, in both cases, the scintillation mechanism is the same. Energy is deposited in the crystal by ionization, either directly by charged particles, or by the conversion of photons into electrons or positrons which subsequently produce ionization. This energy is transferred to the luminescent centers which then radiate scintillation photons. The light yield LY in terms of the number of scintillation photons produced per MeV of energy deposit in the crystal can be expressed as [56]

$$LY = 10^6 \; S \cdot Q/(\beta \cdot E_g), \tag{35.3}$$

Table 35.4: Properties of several inorganic crystals. Most of the notation is defined in Sec. 6 of this *Review*.

Parameter:	ρ	MP	X_0*	R_M*	dE/dx*	λ_I*	$\tau_{\rm decay}$	$\lambda_{\rm max}$	$n^\dagger$	Relative yield‡	Hygro-scopic?	d(LY)/dT
Units:	g/cm^3	°C	cm	cm	MeV/cm	cm	ns	nm				%/°C§
NaI(Tl)	3.67	651	2.59	4.13	4.8	42.9	245	410	1.85	100	yes	−0.2
BGO	7.13	1050	1.12	2.23	9.0	22.8	300	480	2.15	21	no	−0.9
BaF_2	4.89	1280	2.03	3.10	6.5	30.7	650^s	300^s	1.50	36^s	no	-1.9^s
							$<0.6^f$	220^f		4.1^f		0.1^f
CsI(Tl)	4.51	621	1.86	3.57	5.6	39.3	1220	550	1.79	165	slight	0.4
CsI(Na)	4.51	621	1.86	3.57	5.6	39.3	690	420	1.84	88	yes	0.4
CsI(pure)	4.51	621	1.86	3.57	5.6	39.3	30^s	310	1.95	3.6^s	slight	−1.4
							6^f			1.1^f		
$PbWO_4$	8.30	1123	0.89	2.00	10.1	20.7	30^s	425^s	2.20	0.3^s	no	−2.5
							10^f	420^f		0.077^f		
LSO(Ce)	7.40	2050	1.14	2.07	9.6	20.9	40	402	1.82	85	no	−0.2
PbF_2	7.77	824	0.93	2.21	9.4	21.0	-	-	-	Cherenkov	no	-
CeF_3	6.16	1460	1.70	2.41	8.42	23.2	30	340	1.62	7.3	no	0
$LaBr_3$(Ce)	5.29	783	1.88	2.85	6.90	30.4	20	356	1.9	180	yes	0.2
$CeBr_3$	5.23	722	1.96	2.97	6.65	31.5	17	371	1.9	165	yes	−0.1

*Numerical values calculated using formulae in this review.

†Refractive index at the wavelength of the emission maximum.

‡Relative light yield measured for samples of 1.5 X_0 cube with a Tyvek paper wrapping and a full end face coupled to a photodetector. The quantum efficiencies of the photodetector are taken out.

§Variation of light yield with temperature evaluated at the room temperature.

f = fast component, s = slow component

where $\beta \cdot E_g$ is the energy required to create an e-h pair expressed as a multiple of the band gap energy Eg (eV), S is the efficiency of energy transfer to the luminescent center and Q is the quantum efficiency of the luminescent center. The values of β, S and Q are crystal dependent and are the main factors in determining the intrinsic light yield of the scintillator. The decay time of the scintillator is mainly dominated by the decay time of the luminescent center.

Table-35.4 lists the basic properties of some commonly used inorganic crystals. NaI(Tl) is one of the most common and widely used scintillators, with an emission that is well matched to a bialkali photomultiplier tube, but it is highly hygroscopic and difficult to work with, and has a rather low density. CsI(Tl) and CsI(Na) have high light yield, low cost, and are mechanically robust (high plasticity and resistance to cracking). However, they need careful surface treatment and are slightly and highly hygroscopic respectively. Pure CsI has identical mechanical properties as CsI(Tl), but a faster emission at shorter wavelength and a much lower light yield.

Undoped BaF_2 has a fast component with a less than 0.6 ns decay time, and is the fastest known scintillator. However, it also has a slow component with a much longer decay time ($\sim$ 630 ns). Bismuth gemanate ($Bi_4Ge_3O_{12}$ or BGO) has a high density, and consequently a short radiation length X_0 and Molière radius R_M. Similar to CsI(Tl), BGO's emission is well-matched to the spectral sensitivity of silicon photodiodes, and it is easy to handle and not hygroscopic. Lead tungstate ($PbWO_4$ or PWO) has a very high density, with a very short X_0 and R_M, but its intrinsic light yield is rather low.

Cerium doped lutetium oxyorthosilicate (Lu_2SiO_5:Ce, or LSO:Ce) [57] and cerium doped lutetium-yttrium oxyorthosilicate ($Lu_{2(1-x)}Y_{2x}SiO_5$, LYSO:Ce) [58] are dense crystal scintillators which have a high light yield and a fast decay time. Only the properties of LSO:Ce are listed in Table-35.4 since the properties of LYSO:Ce are similar to that of LSO:Ce except a slightly lower density than LSO:Ce depending on the yttrium fraction (typically 5 to 10%) in LYSO:Ce. This material is also featured with excellent radiation hardness [59, 60], so is expected to be used where extraordinary radiation hardness is required.

Also listed in Table-35.4 are other fluoride crystals such as PbF_2 as a Cherenkov material and CeF_3, which have been shown to provide excellent energy resolution in calorimeter applications. Table-35.4 also includes cerium doped lanthanum tri-halides, such as $LaBr_3$ [61] and $CeBr_3$ [62], which are brighter and faster than LSO:Ce, but they are highly hygroscopic and have a lower density. The FWHM energy resolution measured for these materials coupled to a PMT with bi-alkali photocathode for 0.662 MeV γ-rays from a ^{137}Cs source is about 3%, and has recently been improved to 2% by co-doping with cerium and strontium [63], which is the best among all inorganic crystal scintillators. For this reason, $LaBr_3$ and $CeBr_3$ are expected to be used in applications where a good energy resolution for low energy photons are required, such as homeland security.

Beside the crystals listed in Table-35.4, a number of new crystals are being developed that may have potential applications in high energy or nuclear physics. Of particular interest is the family of yttrium and lutetium perovskites and garnet, which include YAP ($YAlO_3$:Ce), LuAP ($LuAlO_3$:Ce), YAG ($Y_3Al_5O_{12}$:Ce) and LuAG ($Lu_3Al_5O_{12}$:Ce) and their mixed compositions. These have been shown to be linear over a large energy range [64], and have the potential for providing good intrinsic energy resolution.

Aiming at the best jet-mass resolution inorganic scintillators are being investigated for HEP calorimeters with dual readout for both Cherenkov and scintillation light to be used at future lepton colliders. These materials may be used for an electromagnetic calorimeter [65] or a homogeneous hadronic calorimetry (HHCAL) detector concept, including both electromagnetic and hadronic parts [66, 67]. Because of the unprecedented volume (70 to 100 m^3) foreseen for the HHCAL detector concept the materials must be (1) dense (to minimize the leakage) and (2) cost-effective. It should also be UV transparent (for effective collection of the Cherenkov light) and allow for a clear discrimination between the Cherenkov and scintillation light. The preferred scintillation light is thus at a longer wavelength, and not necessarily bright or fast. Dense crystals, scintillating glasses and ceramics offer a very attractive implementation for this detector concept [68].

The fast scintillation light provides timing information about electromagnetic interactions and showers, which may be used to mitigate pile-up effects and/or for particle identification since the time development of electromagnetic and hadronic showers, as well as minimum ionizing particles, are different. The timing information is primarily determined by the scintillator rise time and decay time, and the number of photons produced. For fast timing, it is important to have a large number of photons emitted in the initial part of the scintillation pulse, e.g. in the first ns, since one is often measuring the arrival time of the particle in the crystal using the leading edge of the light pulse. A good example of this is BaF_2, which has $\sim 10\%$ of its light in its fast component with a decay time of less than 0.6 ns. Recent investigation shows that doping with yttrium in BaF_2 reduces its slow component significantly, while keeping its ultrafast scintillation component unchanged [69,70]. The light propagation can spread out the arrival time of the scintillation photons at the photodetector due to time dispersion [71]. The time response of the photodetector also plays a major role in achieving good time resolution with fast scintillating crystals.

Table-35.4 gives the light yield of other crystals relative to NaI(Tl) and their dependence to the temperature variations. The light output was measured for 1.5 X_0 cube crystal samples with a Tyvek paper wrapping and a full end face coupled to a photodetector [72]. The quantum efficiency

of the photodetector is taken out to facilitate a direct comparison of crystal's light yield. However, the measured light output produced by a scintillator is usually quoted in terms of the number of photoelectrons per MeV produced by a given photodetector. The relationship between the light yield (LY) in number of photons/MeV produced (N_{photons}/MeV) and the light output (LO) in number of photoelectrons/MeV detected involves the factors for the light collection efficiency (LCE) and the quantum efficiency (QE) of the photodetector:

$$LO = LY \cdot LCE \cdot QE. \tag{35.4}$$

LCE depends on the size and shape of the crystal sample, and includes effects such as the transmission of scintillation light within the crystal (i.e., the bulk attenuation length of the material), scattering from within the crystal, reflections and scattering from the crystal surfaces, and re-bouncing back into the crystal by wrapping materials. These factors can vary considerably depending on the sample, but can be in the range of ∼10–60%. The internal light transmission depends on the intrinsic properties of the material, e.g. the density and type of the scattering centers and defects that can produce internal absorption within the crystal, and can be highly affected by factors such as radiation damage, as discussed below.

The quantum efficiency depends on the type of photodetector used to detect the scintillation light, which is typically ∼15–30% for photomultiplier tubes and higher for silicon photodetectors for visible wavelengths. The response of the detector is usually highly wavelength dependent and should be matched to the particular crystal of interest to give the highest quantum yield at the wavelength corresponding to the peak of the scintillation emission. Fig. 35.3 shows the quantum efficiency for a Hamamatsu R2059 PMT with bi-alkali cathode and quartz window, and the particle detection efficiency (PDE) for a Hamamatsu S14160-3015ps multi-pixel photon counter (MPPC), which is also called silicon photomultiplier (SiPM), as a function of wavelength. Also shown in the figure are emission spectra of three crystal scintillators, BGO, LSO:Ce/LYSO:Ce and CsI(Tl), and the numerical values of the emission weighted quantum efficiency. The area under each emission spectrum is proportional to crystal's light yield, as shown in Table-35.4, where the quantum efficiencies of the photodetector has been taken out. Results with different photodetectors can be significantly different. For example, the response of CsI(Tl) relative to NaI(Tl) with a standard photomultiplier tube with a bi-alkali photo-cathode, e.g. Hamamatsu R2059, would be 45 rather than 165 because of the photomultiplier's low quantum efficiency at longer wavelengths. For scintillators which emit in the UV, a detector with a quartz window should be used.

For very low energy applications (typically below 1 MeV), non-proportionality of the scintillation light yield may be important. It has been known for a long time that the conversion factor between the energy deposited in a crystal scintillator and the number of photons produced is not constant. It is also known that the energy resolution measured by all crystal scintillators for low energy γ-rays is significantly worse than the contribution from photo-electron statistics alone, indicating an intrinsic contribution from the scintillator itself. Precision measurement using low energy electron beam shows that this non-proportionality is crystal dependent [73]. Recent study on this issue also shows that this effect is also sample dependent even for the same crystal [74]. Further work is therefore needed to fully understand this subject.

One important issue related to the application of a crystal scintillator is its radiation hardness. Stability of its light output, or the ability to track and monitor the variation of its light output in a radiation environment, is required for high resolution and precision calibration [75]. All known crystal scintillators suffer from ionization dose induced radiation damage [76], where a common damage phenomenon is the appearance of radiation induced absorption caused by the formation of color centers originated from the impurities or point defects in the crystal. This radiation

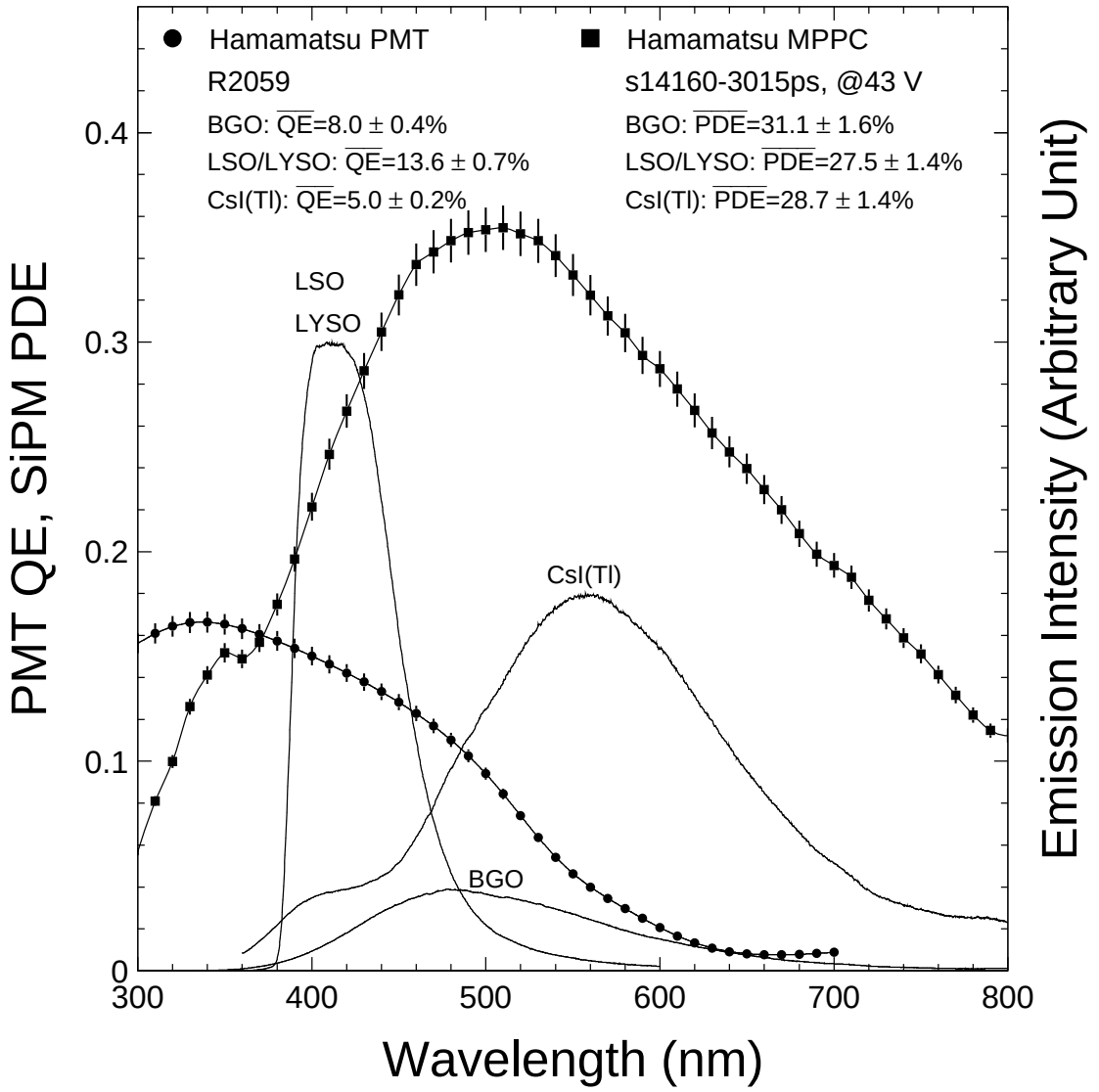

Figure 35.3: The quantum efficiency for a Hamamatsu R2059 PMT with bi-alkali cathode and quartz window and the particle detection efficiency (PDE) for a Hamamatsu S14160-3015ps multi-pixel photon counter (MPPC), which is also called silicon photomultiplier (SiPM), are shown as a function of wavelength. Also shown in the figure are emission spectra of three crystal scintillators, BGO, LSO and CsI(Tl), and the numerical values of the emission weighted quantum efficiencies. The area under each emission spectrum is proportional to crystal's light yield.

induced absorption reduces the light attenuation length in the crystal, and hence its light output. For crystals with high defect density, a severe reduction of light attenuation length may cause a distortion of the light response uniformity, leading to a degradation of the energy resolution. Additional radiation damage effects may include a reduced intrinsic scintillation light yield (damage to the luminescent centers) and an increased phosphorescence (afterglow). For crystals to be used in a high precision calorimeter in a radiation environment, its scintillation mechanism must not be damaged and its light attenuation length in the expected radiation environment must be long enough so that its light response uniformity, and thus its energy resolution, does not change.

While radiation damage induced by ionization dose is well understood [77], investigation is ongoing to understand radiation damage caused by hadrons, including both charged hadrons [78] and neutrons [79]. Two additional fundamental processes may cause defects by hadrons: displacement damage and nuclear breakup. While charged hadrons can produce all three types of damage (and it's often difficult to separate them), neutrons can produce only the last two, and electrons and photons only produce ionization damage. Studies on hadron induced radiation damage to lead tungstate [80] show a proton-specific damage component caused by fragments from fission induced in lead and tungsten by particles in the hadronic shower. The fragments cause a severe, local damage to the crystalline lattice due to their extremely high energy loss over a short distance [80]. Recent investigation also sees evidence of neutron-specfic damage in various crystals [79].

Most of the crystals listed in Table-35.4 have been used in high energy or nuclear physics experiments when the ultimate energy resolution for electrons and photons is desired. Examples are the Crystal Ball NaI(Tl) calorimeter at SPEAR, the L3 BGO calorimeter at LEP, the CLEO CsI(Tl) calorimeter at CESR, the KTeV CsI calorimeter at the Tevatron, and the BaBar, BELLE and BES III CsI(Tl) calorimeters at PEP-II, KEK and BEPC II, respectively. Because of their high density and relative low cost, PWO calorimeters are used by CMS and ALICE at LHC, by CLAS and PrimEx at CEBAF and by PANDA at GSI, and is planned to be used for the Backward Endcap Calorimeter for the ePIC experiment at the EIC. Similarly, PbF_2 calorimeters are used by the A4 experiment at MAINZ and by the g-2 experiment at Fermilab. A CsI calorimeter is being built for the Mu2e experiment at Fermilab. An LYSO:Ce calorimeter is being built for the COMET experiment at J-PARC, and an LYSO:Ce crystal-based precision timing layer is being built for the CMS experiment for the HL-LHC.

35.5 Cherenkov detectors

Revised August 2023 by J. Schwiening (GSI Darmstadt).

Although devices using Cherenkov radiation are often thought of as only particle identification (PID) detectors, in practice they are used over a much broader range of applications including; (1) fast particle counters; (2) hadronic PID; (3) electromagnetic calorimeters (EMC); and (4) tracking detectors performing complete event reconstruction. Examples of applications from each category include; (1) the BaBar luminosity detector [81] and the Quartic fast timing counter for the ATLAS Forward Proton Detector, designed to measure small angle scatters at the LHC [82]; (2) the hadronic PID detectors at the B factory detectors—DIRC in BaBar [83], and the modern Imaging Aerogel and TOP counters at Belle II [84]; (3) the CMS Hadron Forward calorimeter based on Cherenkov light emitted in quartz fibers embedded in a steel absorber [85]; and (4) large water Cherenkov counters such as Super-Kamiokande [86].

Cherenkov counters contain two main elements; (1) a radiator through which the charged particle passes, and (2) a photodetector. As Cherenkov radiation is a weak source of photons, light collection and detection must be as efficient as possible. The refractive index n and the particle's path length through the radiator L appear in the Cherenkov relations allowing the tuning of these quantities for particular applications. One or more of the properties of Cherenkov radiation discussed in the Passages of Particles through Matter section (Sec. 34 of this *Review*) are utilized in Cherenkov detectors: the prompt emission of a light pulse; the existence of a velocity threshold for radiation; and the dependence of the Cherenkov cone half-angle θ_c and the number of emitted photons on the velocity of the particle v_p and the refractive index n of the medium. The Cherenkov angle can be calculated as

$$\cos\theta_c = \frac{1}{n(E)\beta}, \tag{35.5}$$

where $\beta = v_p/c$ with c being the speed of light, and E the photon energy. The number of photoelectrons ($N_{\rm p.e.}$) detected in a given device with radiator of length L is

$$N_{\rm p.e.} = L\frac{\alpha^2 z^2}{r_e\, m_e c^2}\int \epsilon(E)\, \sin^2\theta_c(E) dE, \tag{35.6}$$

where $\epsilon(E)$ is the efficiency for collecting the Cherenkov light and transducing it into photoelectrons, and $\alpha^2/(r_e\, m_e c^2) = 370\ {\rm cm}^{-1}{\rm eV}^{-1}$. The quantities ϵ and θ_c are functions of the photon energy. As the typical energy dependent variation of the index of refraction is modest, a quantity called the *Cherenkov detector quality factor* N_0 can be defined as

$$N_0 = \frac{\alpha^2 z^2}{r_e\, m_e c^2}\ \int \epsilon\, dE, \tag{35.7}$$

so that, taking the charge number $z = 1$ (the usual case in high-energy physics),

$$N_{\rm p.e.} \approx L N_0 \langle \sin^2\theta_c \rangle. \tag{35.8}$$

This definition of the quality factor N_0 is not universal, nor, indeed, very useful for those common situations where ϵ factorizes as $\epsilon = \epsilon_{\rm coll}\epsilon_{\rm det}$ with the geometrical photon collection efficiency ($\epsilon_{\rm coll}$) varying substantially for different tracks while the photon detector efficiency ($\epsilon_{\rm det}$) remains nearly track independent. In this case, it can be useful to explicitly remove ($\epsilon_{\rm coll}$) from the definition of N_0. A typical value of N_0 for a photomultiplier (PMT) detection system working in the visible and near UV, and collecting most of the Cherenkov light, is about 100 ${\rm cm}^{-1}$. Practical counters, utilizing a variety of different photodetectors, have values ranging between about 30 and 180 ${\rm cm}^{-1}$. Radiators can be chosen from a variety of transparent materials (Sec. 34 of this *Review* and Table 6). In addition to refractive index, the choice requires consideration of factors such as material density, radiation length and radiation hardness, transmission bandwidth, absorption length, chromatic dispersion, optical workability (for solids), availability, environmental impact, and cost. When the momenta of particles to be identified is high, the refractive index must be set close to one, so that the photon yield per unit length is low and a long particle path in the radiator is required. In recent years, the gap in refractive index that has traditionally existed between gases and liquid or solid materials has been partially closed with transparent *silica aerogels* with indices that range between about 1.003 and 1.26. Due to the potential ability to tune the refractive index to the exact requirements of an experiment, metamaterials, including photonic crystals, are being investigated as radiators for future Cherenkov counters [87].

Cherenkov counters may be classified as either *imaging* or *threshold* types, depending on whether they do or do not make use of Cherenkov angle (θ_c) information. Imaging counters may be used to track particles as well as identify them. The recent development of very fast photodetectors such as micro-channel plate PMTs (MCP-PMT) (see 35.2 of this *Review*) also potentially allows very fast Cherenkov based time of flight (TOF) detectors of either class [87]. The track timing resolution of imaging detectors can be extremely good as it scales approximately as $\frac{1}{\sqrt{N_{\rm p.e.}}}$.

Threshold Cherenkov detectors [88], in their simplest form, make a yes/no decision based on whether the particle is above or below the Cherenkov threshold velocity $\beta_t = 1/n$. A straightforward enhancement of such detectors uses the number of observed photoelectrons (or a calibrated pulse height) to discriminate between species or to set probabilities for each particle species [89]. This strategy can increase the momentum range of particle separation by a modest amount (to a momentum some 20% above the threshold momentum of the heavier particle in a typical case).

Careful designs give $\langle\epsilon_{\rm coll}\rangle \gtrsim 90\%$. For a photomultiplier with a typical bialkali cathode, $\int \epsilon_{\rm det} dE \approx 0.27$ eV, so that

$$N_{\rm p.e.}/L \approx 90 \text{ cm}^{-1} \langle \sin^2\theta_c \rangle \quad (\textit{i.e.}, N_0 = 90 \text{ cm}^{-1}). \tag{35.9}$$

Suppose, for example, that n is chosen so that the threshold for species a is p_t; that is, at this momentum species a has velocity $\beta_a = 1/n$. A second, lighter, species b with the same momentum has velocity β_b, so $\cos\theta_c = \beta_a/\beta_b$, and

$$N_{\rm p.e.}/L \approx 90 \text{ cm}^{-1} \frac{m_a^2 - m_b^2}{p_t^2 + m_a^2}. \tag{35.10}$$

For K/π separation at $p = p_t = 1(5)$ GeV/c, $N_{\rm p.e.}/L \approx 16(0.8)$ cm^{-1} for π's and (by design) 0 for K's.

For limited path lengths $N_{\rm p.e.}$ will usually be small. The overall efficiency of the device is controlled by Poisson fluctuations, which can be especially critical for separation of species where one particle type is dominant. Moreover, the effective number of photoelectrons is often less than the average number calculated above due to additional equivalent noise from the photodetector (see the discussion of the excess noise factor in 35.2 of this *Review*). It is common to design for at least 10 photoelectrons for the high velocity particle in order to obtain a robust counter. As rejection of the particle that is below threshold depends on *not* seeing a signal, electronic and other background noise, especially overlapping tracks, can be important. Physics sources of light production for the below threshold particle, such as decay to an above threshold particle, scintillation light, or the production of delta rays in the radiator, often limit the separation attainable, and need to be carefully considered. Well designed, modern multi-channel counters, such as the ACC at Belle [90], can attain adequate particle separation performance over a substantial momentum range.

Imaging counters make the most powerful use of the information available by measuring the ring-correlated angles of emission of the individual Cherenkov photons. They typically provide positive ID information both for the "wanted" and the "unwanted" particles, thus reducing misidentification substantially. Since low-energy photon detectors can measure only the position (and, perhaps, a precise detection time) of the individual Cherenkov photons (not the angles directly), the photons must be "imaged" onto a detector so that their angles can be derived [91]. Typically the optics map the Cherenkov cone onto (a portion of) a distorted "circle" at the photodetector. Though the imaging process is directly analogous to familiar imaging techniques used in telescopes and other optical instruments, there is a somewhat bewildering variety of methods used in a wide variety of counter types with different names. Some of the imaging methods used include (1) focusing by a lens or mirror; (2) proximity focusing (i.e., focusing by limiting the emission region of the radiation); and (3) focusing through an aperture (a pinhole). In addition, the prompt Cherenkov emission coupled with the speed of some modern photon detectors allows the use of (4) time imaging, a method which is little used in conventional imaging technology, and may allow some separation with particle TOF. Finally, (5) correlated tracking (and event reconstruction) can be performed in large water counters by combining the individual space position and time of each photon together with the constraint that Cherenkov photons are emitted from each track at the same polar angle (Sec. 36.3.1of this *Review*).

In a simple model of an imaging PID counter, the fractional error on the particle velocity (δ_β) is given by

$$\delta_\beta = \frac{\sigma_\beta}{\beta} = \tan\theta_c \sigma(\theta_c) \ , \tag{35.11}$$

where

$$\sigma(\theta_c) = \frac{\langle\sigma(\theta_i)\rangle}{\sqrt{N_{\rm p.e.}}} \oplus C, \tag{35.12}$$

and $\langle\sigma(\theta_i)\rangle$ is the average single photoelectron resolution, as defined by the optics, detector resolution and the intrinsic chromaticity spread of the radiator index of refraction averaged over the photon detection bandwidth. C combines a number of other contributions to resolution including, (1) correlated terms such as tracking, alignment, and multiple scattering, (2) hit ambiguities, (3) background hits from random sources, and (4) hits coming from other tracks. The actual separation performance is also limited by physics effects such as decays in flight and particle interactions in the material of the detector. In many practical cases, the performance is limited by these effects.

For a $\beta \approx 1$ particle of momentum (p) well above threshold entering a radiator with index of refraction (n), the number of σ separation (N_σ) between particles of mass m_1 and m_2 is approximately

$$N_\sigma \approx \frac{|m_1^2 - m_2^2|}{2p^2\sigma(\theta_c)\sqrt{n^2-1}}. \tag{35.13}$$

In practical counters, the angular resolution term $\sigma(\theta_c)$ varies between about 0.1 and 5 mrad depending on the size, radiator, and photodetector type of the particular counter. The range of momenta over which a particular counter can separate particle species extends from the point at which the number of photons emitted becomes sufficient for the counter to operate efficiently as a threshold device (∼20% above the threshold for the lighter species) to the value in the imaging region given by the equation above. For example, for $\sigma(\theta_c)$ =2 mrad, a fused silica radiator ($n = 1.474$), or a fluorocarbon gas radiator (C_5F_{12}, $n = 1.0017$), would separate π/K's from the threshold region starting around 0.15(3) GeV/c through the imaging region up to about 4.2(18) GeV/c at better than 3σ.

Many different imaging counters have been built during the last several decades [87]. Among the earliest examples of this class of counters are the very limited acceptance *Differential Cherenkov detectors*, designed for particle selection in high momentum beam lines. These devices use optical focusing and/or geometrical masking to select particles having velocities in a specified region. With careful design, a velocity resolution of $\sigma_\beta/\beta \approx 10^{-4}$–$10^{-5}$ can be obtained [88].

Practical multi-track *Ring-Imaging Cherenkov detectors* (generically called RICH counters) are a more recent development. RICH counters are sometimes further classified by 'generations' that differ based on historical timing, performance, design, and photodetection techniques. Prototypical examples of first generation RICH counters are those used in the DELPHI and SLD detectors at the LEP and SLC Z factory e^+e^- colliders [87]. They have both liquid (C_6F_{14}, $n = 1.276$) and gas (C_5F_{12}, $n = 1.0017$) radiators, the former being proximity imaged with the latter using mirrors. The phototransducers are a TPC/wire-chamber combination. They are made sensitive to photons by doping the TPC gas (usually, ethane/methane) with ∼ 0.05% TMAE (tetrakis(dimethylamino)ethylene). Great attention to detail is required, (1) to avoid absorbing the UV photons to which TMAE is sensitive, (2) to avoid absorbing the single photoelectrons as they drift in the long TPC, and (3) to keep the chemically active TMAE vapor from interacting with materials in the system. In spite of their unforgiving operational characteristics, these counters attained good $e/\pi/K/p$ separation over wide momentum ranges (from about 0.25 to 20 GeV/c) during several years of operation at LEP and SLC. Related but smaller acceptance devices include the OMEGA RICH at the CERN SPS, and the RICH in the balloon-borne CAPRICE detector [87]. Despite their excellent match to the radiator requirement for gaseous RICHes, saturated fluorocarbons may soon need to be replaced due to their high global warming impact. Possible alternatives for a similar refractive index include hydrofluoroolefins or Argon, pressurized at a few bar [87].

Later generation counters [87] generally operate at much higher rates, with more detection channels, than the first generation detectors just described. They also utilize faster, more forgiving photon detectors, covering different photon detection bandwidths. Radiator choices have broadened

to include materials such as lithium fluoride, fused silica, and aerogel.

Vacuum-based photodetection systems (*e.g.*, single or multi anode PMTs, MCP-PMTs, or hybrid photodiodes (HPD)) have become increasingly common (see 35.2 of this *Review*). They handle high rates, and can be used with a wide choice of radiators. Examples include (1) the SELEX RICH at Fermilab, which mirror focuses the Cherenkov photons from a neon radiator onto a camera array made of ~ 2000 PMTs to separate hadrons over a wide momentum range (to well above 200 GeV/c for heavy hadrons);(2) the NA62 RICH at CERN, which uses a 17 m long tank filled with neon gas as radiator and spherical mirrors to focus the photons on two arrays of 2 000 PMTs to separate pions from muons for momenta between 15 and 35 GeV/c; (3) the CBM RICH under construction at FAIR where the Cherenkov photons, produced in about 30 m^3 of CO_2 radiator gas, are mirror-focused on arrays of multi-anode PMTs (MaPMTs) with a total of about 55,000 pixels, to identify electrons with momenta up to 10 GeV/c; and (4) the LHCb detector now running at the LHC. It uses two separate counters. One volume contains C_4F_{10} (originally in combination with aerogel, which was removed in 2015) while the second volume contains CF_4. Photons are mirror-focused onto arrays of photon detectors to cover a π/K separation momentum range between 1 and 150 GeV/c. Additional upgrades, including the replacement of the HPDs by MaPMTs and improved readout electronics, were performed to deal with increases in luminosity.

Other fast detection systems that use solid cesium iodide (CsI) photocathodes or triethylamine (TEA) doping in proportional chambers are useful with certain radiator types and geometries. Examples include (1) the CLEO-III RICH at CESR that uses a LiF radiator with TEA doped proportional chambers; (2) the ALICE detector at the LHC that uses proximity focused liquid (C_6F_{14} radiators and solid CsI photocathodes (similar photodectors have been used for several years by the HADES and COMPASS detectors), and the hadron blind detector (HBD) in the PHENIX detector at RHIC that couples a low index CF_4 radiator to a photodetector based on electron multiplier (GEM) chambers with reflective CsI photocathodes [87].

Recent technological advances in the production of aerogel with improved transparency in the UV range and finely tuned refractive indices enable several new RICH designs. The innovative hybrid geometry of the CLAS12 RICH, with complex photon paths that feature multiple passes through the aerogel tiles, is only possible due to the improved scattering length of the aerogel. It minimizes the material inside of the detector acceptance as well as the size and cost of the photon sensor array. Beam tests have demonstrated that the counter will be able to provide clean π/K separation up to 8 GeV/c. The forward endcap Aerogel RICH (ARICH) for the Belle II upgrade at KEKB, designed to provide clean π/K separation for momenta up to 3.5 GeV/c, is an example of the so-called focusing aerogel approach [92]. The radiator is a dual-layer aerogel, with a thickness of 20 mm for each layer and increasing refractive indices of $n = 1.045$ and $n = 1.055$ along the particle path. The Cherenkov ring images from the two layers overlap on the array of Hybrid Avalanche Photo Detectors (HAPDs), which provide efficient single photon detection in the 1.5 T magnetic field.

A DIRC (Detection [of] Internally Reflected Cherenkov [light]) is a distinctive, compact RICH subtype first used in the BaBar detector [83]. A DIRC "inverts" the usual RICH principle for use of light from the radiator by collecting and imaging the total internally reflected light rather than the transmitted light. It utilizes the optical material of the radiator in two ways, simultaneously: as a Cherenkov radiator and as a light pipe. The magnitudes of the photon angles are preserved during transport by the flat, rectangular cross section radiators, allowing the photons to be efficiently transported to a detector outside the path of the particle where they may be imaged in up to three independent dimensions (the usual two in space and, due to the long photon paths lengths, one in time). Because the index of refraction in the radiator is large ($n \sim 1.47$ for fused silica), the momentum range with good π/K separation goes up to 4–5 GeV/c. It is plausible, but difficult, to

extend it up to about 10 GeV/c with an improved design.

The BaBar experiment at the asymmetric PEP-II e^+e^- collider studied CP violation in $\Upsilon(4S)$ decays. Excellent pion/kaon separation for particle momenta up to 4 GeV/c was required. The BaBar DIRC used 4.9 m long, rectangular bars made from synthetic fused silica as radiator and light guide. The photons were imaged via a "pin-hole" through an expansion region filled with 6 000 liters of purified water onto an array of 10 752 densely packed photomultiplier tubes placed at a distance of about 1.2 m from the bar end. During more than 8 years of operation, the BaBar DIRC achieved π/K separation of 2.5 standard deviations or more up to 4 GeV/c momentum. For a pion identification rate around 85% the DIRC provided a kaon misidentification rate well below 1% up to 3 GeV/c.

The next generation of DIRC detectors [93] takes advantage of the new, very fast, pixelated photodetectors becoming available, such as MaPMTs and MCP-PMTs. They typically utilize either time imaging or lens/mirror-focused optics, or both, leading not only to a precision measurement of the Cherenkov angle, but in some cases, to a precise measurement of the particle time of flight, and/or to correction of the chromatic dispersion in the radiator. Examples [87] include (1) the Belle II Time of Propagation (TOP) counter that emphasizes precision timing for both Cherenkov imaging and TOF to perform π/K separation of at least 3 standard deviations up to 4 GeV/c; (2) the DIRC upgrade of the GlueX experiment at Jefferson Lab that places four decommissioned BaBar DIRC modules, coupled to upgraded optics and readout, perpendicular to the beamline, the first application of a DIRC in a detector endcap; (3) the high-performance DIRC for the ePIC detector at the EIC, to be installed in 2030, that will combine lens focusing with fast photon time imaging and is expected to provide more than 3 standard deviations π/K separation up to 6 GeV/c; and (4) the TORCH counter being developed for an LHCb upgrade in 2033 which uses DIRC imaging for individual photons with fast photon detectors to provide π/K separation up to 10 GeV/c via particle TOF with a precision of 10-15 ps per track over a flight path length of 9.5 m.

35.6 Gaseous detectors

35.6.1 *Energy loss and charge transport in gases*

Revised November 2021 by F. Sauli (CERN) and M. Titov (IRFU, CEA, Université Paris-Saclay).

Gas-filled detectors use the localized ionization produced by charged particles, generally after charge multiplication. The statistics of ionization processes, having asymmetries in the ionization trails, affect the coordinate determination deduced from the measurement of drift time, or of the center of gravity of the collected charge. For thin gas layers, the width of the energy loss distribution can be larger than its average, requiring multi-sampling devices or truncated mean analysis to achieve good particle identification. In the truncated mean method for calculating $\langle dE/dx \rangle$, the ionization measurements along the track length are broken into many samples and then a fixed fraction of high-side (and sometimes also low-side) values are rejected [94].

The energy loss of charged particles and photons in matter is discussed in Sec. 34. Every ionization process is a quantum mechanical transition initiated by the Coulomb field of the particle and the field created by neighbouring polarizable atoms; the average energy losses are described by the Bethe-Bloch formula with Sternheimer's density effect corrections. The fluctuations caused by Rutherford scattering on quasi-free electrons follow a Landau distribution and the influence of atomic shells is described by the photoabsorption ionization (PAI) model, which allows simulation of each energy transfer [95], with relaxation cascades and simulation of delta-electrons [96]. Table 35.5 provides values of relevant parameters in some commonly used gases at NTP for unit-charge minimum-ionizing particles (MIPs) [97] [98]. When an ionizing particle passes through the gas it creates electron-ion pairs; often the ejected electrons have sufficient energy to further ionize

Table 35.5: Properties of noble and molecular gases at normal temperature and pressure (NTP: 20° C, one atm). E_X, E_I: first excitation, ionization energy; W_I: average energy for creation of ion pair; $dE/dx|_{\rm min}$, N_P, N_T: differential energy loss, primary and total number of electron-ion pairs per cm, for unit charge minimum ionizing particles. Values often differ, depending on the source, and those in the table should be taken only as approximate.

Gas	Density, $\mathrm{mg\,cm^{-3}}$	E_x eV	E_I eV	W_I eV	$dE/dx\|_{\rm min}$ $\mathrm{keV\,cm^{-1}}$	N_P $\mathrm{cm^{-1}}$	N_T $\mathrm{cm^{-1}}$
H_2	0.084	10.8	13.6	37	0.34	5.2	9.2
He	0.179	19.8	24.6	41.3	0.32	3.5	8
Ne	0.839	16.7	21.6	37	1.45	13	40
Ar	1.66	11.6	15.7	26	2.53	25	97
Xe	5.495	8.4	12.1	22	6.87	41	312
CH_4	0.667	8.8	12.6	30	1.61	28	54
C_2H_6	1.26	8.2	11.5	26	2.91	48	112
iC_4H_{10}	2.49	6.5	10.6	26	5.67	90	220
CO_2	1.84	7.0	13.8	34	3.35	35	100
CF_4	3.78	10.0	16.0	35-52	6.38	52-63	120

the medium. The number of pairs is known as cluster-size distribution, because the secondary electrons are created in the immediate vicinity of the primary encounter and, together with the primary electrons, form clusters of one, several, or sometimes many, electron-ion pairs. As shown in Table 35.5, the total number of pairs (N_T) is a few times larger than the number of primaries (N_P). For different conditions and for mixtures, and neglecting energy transfer processes (*e.g.* Penning effect), one can scale the density, N_P, and N_T with temperature and pressure assuming a perfect gas law.

The probability for a released electron to have an energy E or larger follows an approximate $1/E^2$ dependence (Rutherford law), shown in Fig. 35.4 for Ar at NTP (dotted line, left scale). More detailed estimates taking into account the electronic structure of the medium are shown in the figure, for three values of the particle velocity factor $\beta\gamma$ [99]. The dot-dashed line provides, on the right scale, the practical range of electrons (including scattering) of energy E. As an example, about 0.6% of released electrons have 1 keV or more energy, substantially increasing the total ionization loss. The practical range of 1 keV electrons in argon (dot-dashed line, right scale) is 70 μm and this can contribute to the error in the coordinate determination.

Garfield^{++} [100], together with HEED [96], Degrad [101], Magboltz [102, 103], SRIM, ANSYS, COMSOL, and neBEM [104] software packages represent the core simulation tools for microscopic modelling of gaseous detector response. The number of electron-ion pairs per primary ionization, or cluster size depends little on the medium; it can be computed with the programs mentioned above or experimentally measured. For example, there is about 1% probability for primary clusters to contain ten or more electron-ion pairs in argon [105].

Once released in the gas, and under the influence of an applied electric field, electrons and ions drift in opposite directions and diffuse towards the electrodes. The electron-molecule collision cross sections are determined by the details of atomic and molecular structure and depends strongly on the electron energy and therefore on the electric field **E** for most gases. High values of the total electron scattering cross section reduce the electron diffusion and increase the drift velocity; a large

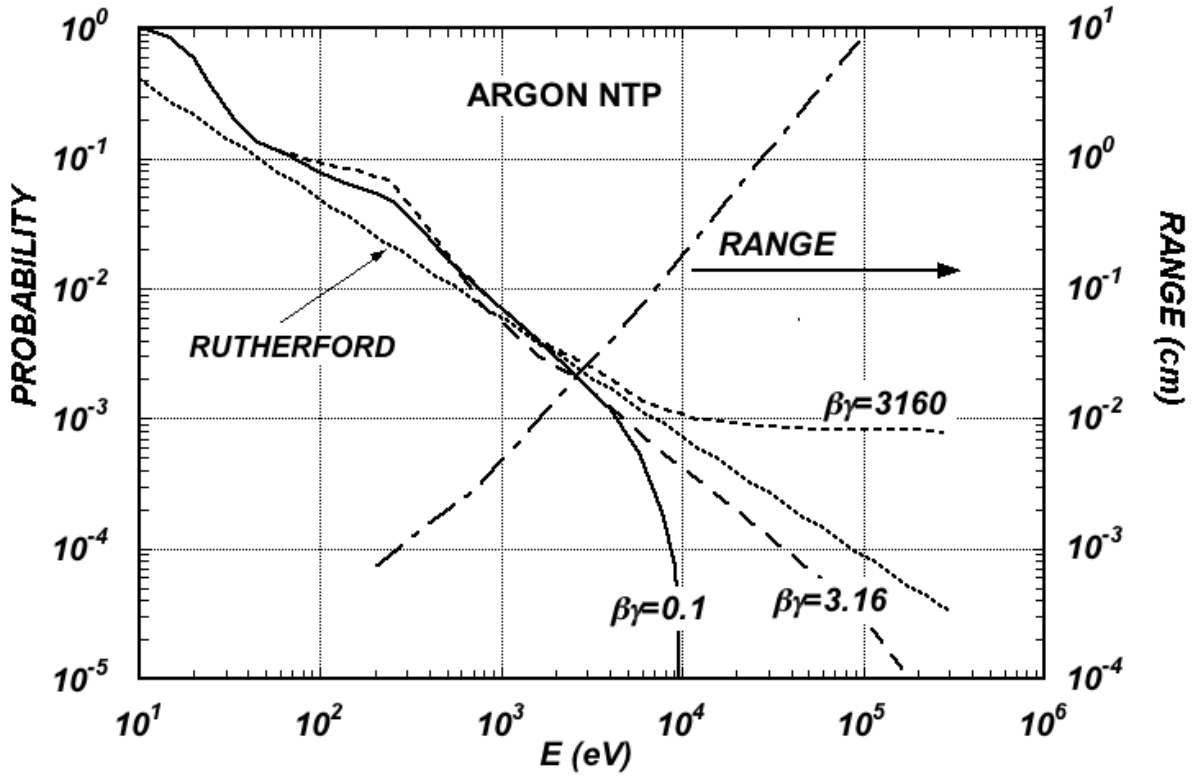

Figure 35.4: Probability of single collisions in which released electrons have an energy E or larger (left scale) and practical range of electrons in Ar at NTP (dot-dashed curve, right scale) [99].

inelasticity implies that high fields are required to raise the electron energy. For noble gases, the inelastic cross section is zero until the electrons reach the first excitation and ionization energies $\mathcal{O}(10\ eV)$; on the contrary, for molecular gases, like CH_4, inelastic channels, involving rotational and vibrational levels, open up at energies above $\sim$ 0.1 eV. Large drift velocities are achieved by adding polyatomic gases (usually hydrocarbons C_xH_y, CO_2, CF_4) having large inelastic component at moderate energies of a few eV; this results in the electron "cooling" into the energy range of the Ramsauer-Townsend minimum (at $\sim$0.5 eV) of the elastic ("momentum-transfer") cross-section in Ar [98]. Under these circumstances, it is not surprising that the addition of very small quantities of one gas to another can dramatically modify the average electron energy and alter the dependence of the drift velocity (v_d) on **E/P** and temperature; this has a particularly strong effect for noble gases, as illustrated in Fig. 35.5 for Ar. Carbon tetrafluoride (CF_4) has the largest drift velocity and the lowest electron diffusion among known gases due to the sizeable Ramsauer-Townsend dip in the elastic cross-section which coincides with a very large vibrational modes. Another principal role of the polyatomic gas is to absorb the ultraviolet photons emitted by the excited noble gas atoms. Addition of molecular gases (hydrocarbons or CO_2 are widely used in the proportional counters as a quencher) to noble gas allows to dissipate a good fraction of energy through rotational and vibrational radiationless transitions without the creation of photons or ions. On the contrary, CF_4 has a small quenching cross-section of excited Ar states and light emission in CF_4 (from the far UV to the visible light) is a complex process, involving the creation of CF_3^+ excited states [106].

Extensive collections of experimental data [107] and theoretical calculations based on transport theory permit evaluation of drift and diffusion properties in pure gases and their mixtures; modern compilations of the electron-molecule cross sections are available at the open-access website LXCAT

[108]. Fig. 35.5 and Fig. 35.6 show drift velocity and transverse diffusion for some commonly used gases at NTP, computed with the Magboltz program [102, 103]. For different conditions, the horizontal axis must be scaled inversely with the gas density. Standard deviations for longitudinal (σ_L) and transverse diffusion (σ_T) are given for one cm of drift, and scale with the the square root of the drift distance.

In a simple approximation, gas kinetic theory provides the drift velocity v_d as a function of the mean collision time τ and the electric field $\mathbf{E}$: $v_d = eE\tau/m_e$ (Townsend's expression). In the presence of an external magnetic field, the Lorentz force acting on electrons between collisions deflects the drifting electrons and modifies the drift properties. The electron trajectories, velocities and diffusion parameters can be computed with Magboltz. The friction force model provides an approximate expression for the vector drift velocity $\boldsymbol{v}$ as a function of electric and magnetic field vectors $\boldsymbol{E}$ and $\boldsymbol{B}$, of the Larmor frequency $\omega = eB/m_e$, and of the mean collision time τ (more precise calculation is available in Magboltz, which computes drift velocity by tracing electrons at the microscopic level through numerous collisions with gas molecules):

$$\boldsymbol{v} = \frac{e}{m_e}\frac{\tau}{1+\omega^2\tau^2}\left(\boldsymbol{E} + \frac{\omega\tau}{B}(\boldsymbol{E}\times\boldsymbol{B}) + \frac{\omega^2\tau^2}{B^2}(\boldsymbol{E}\cdot\boldsymbol{B})\boldsymbol{B}\right) \tag{35.14}$$

To a good approximation, and for moderate fields, one can assume that the energy of the electrons is not affected by B, and use for τ the values deduced from the drift velocity at $B = 0$ (the Townsend expression). For $\boldsymbol{E}$ perpendicular to $\boldsymbol{B}$, the drift angle relative to the electric field vector is $\tan\theta_B = \omega\tau$ and $v = (E/B)(\omega\tau/\sqrt{1+\omega^2\tau^2})$. For parallel electric and magnetic fields, drift velocity and longitudinal diffusion are not affected, while the transverse diffusion can be strongly reduced: $\sigma_T(B) = \sigma_T(B=0)/\sqrt{1+\omega^2\tau^2}$. As an example, the dotted line in Fig. 35.6 represents σ_T for the classic Ar/CH_4 (90:10) mixture at 4 T. Large values of $\omega\tau \sim 20$ at 5 T are consistent with the measurement of diffusion coefficient in $Ar/CF_4/iC_4H_{10}$ (95:3:2). This reduction is exploited to substantially improve spatial resolution in the Drift (Sec. 35.6.2) and Time Projection Chambers (Sec. 35.6.5).

In some mixtures containing molecules with electronic affinity, electrons can be captured to form negative ions. Capture cross sections vary considerably with an energy and, hence, the electric field; as a consequence, the three-body electron attachment coefficients may differ significantly for the same additive in different mixtures. As an example, at moderate fields (up to 1 kV/cm) the addition of 0.1% of oxygen to an Ar/CO_2 mixture results in an electron capture probability about twenty times larger than in Ar/CH_4. Among common molecules, the largest electron affinities are found for the halogenides, O_2 and H_2O. The attachment probability in O_2 or H_2O is large at low fields and electron energies close to thermal, but decreases at increasing fields. On the contrary, CF_4 is not electronegative at low and moderate fields, but has a large electron capture cross section at fields above $\sim$8 kV/cm, before reaching the avalanche field strengths. Depending on the mixture and detector geometry, some signal reduction and energy resolution loss is expected in this gas.

If the electric field is increased sufficiently, electrons gain enough energy between collisions to excite and ionize molecules. Above a gas-dependent threshold, the mean free path for ionization, λ_i, decreases exponentially with the field; its inverse, $\alpha = 1/\lambda_i$, is named the first Townsend coefficient. In wire chambers, most of the increase of avalanche particle density occurs very close to the anode wires, and a simple electrostatic consideration shows that the largest fraction of the detected signal is due to the motion of positive ions receding from the wires. The electron component, although very fast, contributes very little to the signal. This determines the characteristic shape of the detected signals in the proportional mode: a fast rise followed by a gradual increase. The slow component, the so-called "ion tail" that limits the time resolution of the detector, is usually removed by differentiation of the signal. In uniform fields, N_0 initial electrons multiply over a length

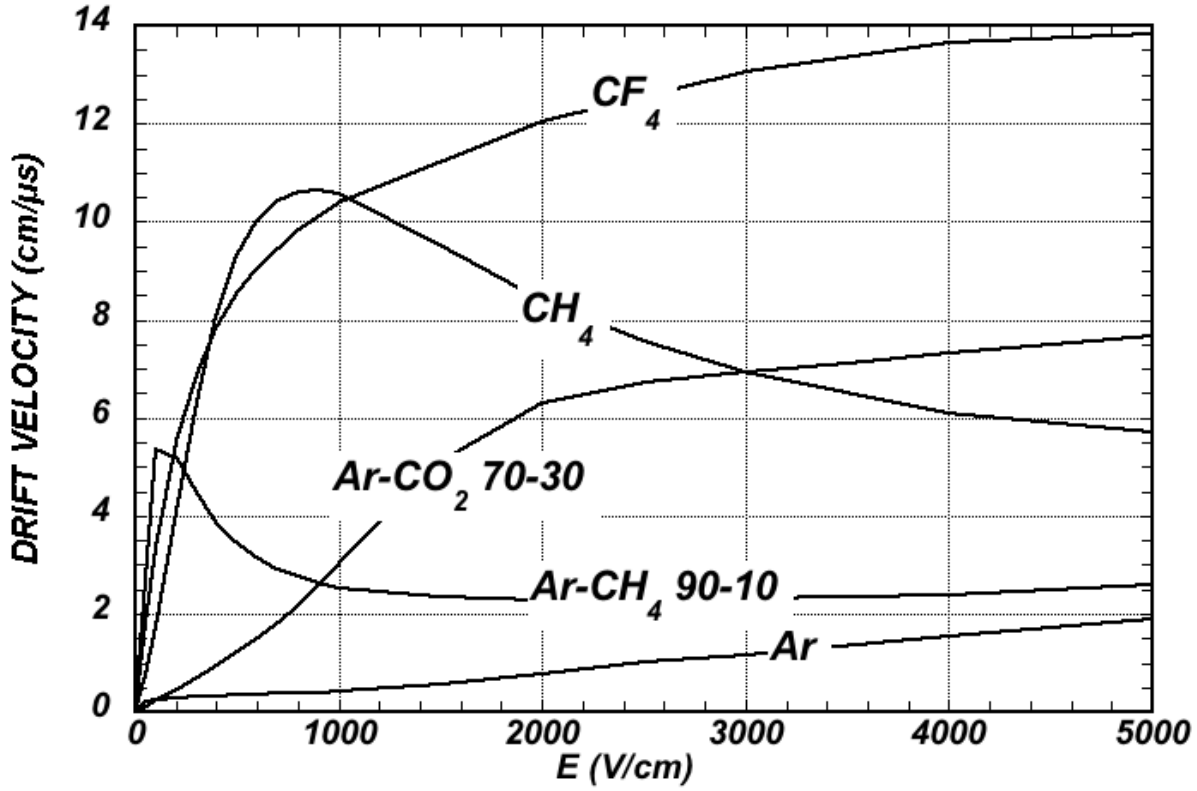

Figure 35.5: Computed electron drift velocity as a function of electric field in several gases at NTP and $B = 0$ [102, 103].

x forming an electron avalanche of size $N = N_0\, e^{\alpha x}$; N/N_0 is the gain of the detector. Fig. 35.7 shows examples of Townsend coefficients for several gas mixtures, computed with Magboltz [102, 103].

Additional ionizing energy transfer mechanisms due to the excited noble gas atoms, called collisional Penning energy transfers, occur when the excitation energy of a noble gas is higher than the ionization potential of an admixture gas. The energy transfer rate, probability that an excited atom ionizes a quenching agent, is a priori not known for a mixture but can be extracted from the fits of the experimental gas gain data [109] using the Magboltz simulations [102, 103]. In the gain calculations, the Penning adjusted Townsend coefficient is defined in terms of the total production frequencies of the noble gas excitations and direct ionizations of the mixture. Systematic gas gain measurements for varying mixing ratios and pressures are critical for determining the efficiency of the different mechanisms involved in the transfers. Collisional energy transfer mostly scales linearly with the gas pressure and the fraction of quenching gas in the mixture, while ionization by photons emitted from excitations is independent of the medium [110]. In addition, collisional Penning transfers of some higher excited states can occur before they decay at atmopheric pressure and are not restricted to metastable states of the excited noble gas. For example, the impact of the Penning effect on gas gain is roughly a factor 10 in Ar-CO_2 mixtures and exceeding a factor of 100 in Ar-C_2H_2 mixtures [110].

Positive ions released by the primary ionization or produced in the avalanches drift and diffuse under the influence of the electric field. Negative ions may also be produced by electron attachment to gas molecules. The drift velocity of ions in the fields encountered in gaseous detectors (up to few kV/cm) is typically about three orders of magnitude smaller than for electrons. The ion mobility

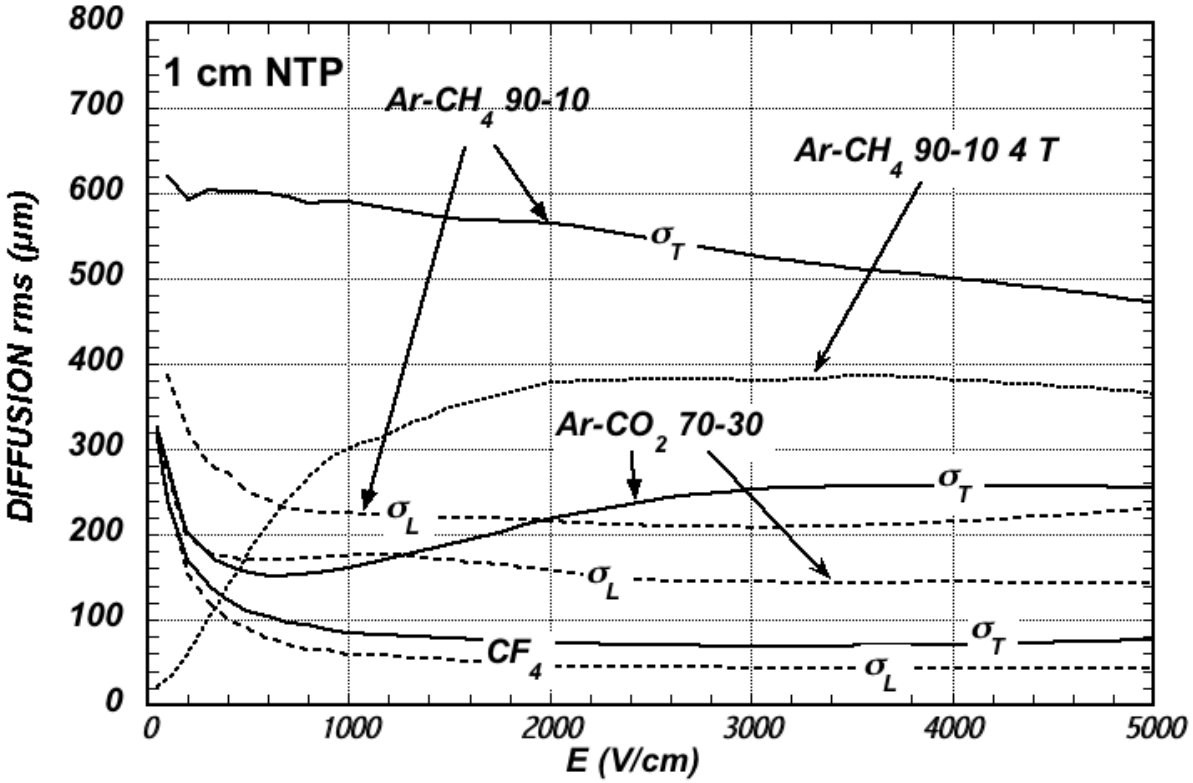

Figure 35.6: Electron longitudinal diffusion (σ_L) (dashed lines) and transverse diffusion (σ_T) (full lines) for 1 cm of drift at NTP and $B = 0$. The dotted line shows σ_T for the P10 mixture at 4 T [102, 103].

μ, the ratio of drift velocity to electric field, is constant for a given ion type up to very high fields. Values of ions mobility at NTP are given in Table 35.6 [111]. For different temperatures and pressures, the mobility can be scaled inversely with the density assuming an ideal gas law. Both the longitudinal and transverse diffusion of ions are proportional to the square root of the drift time, with a coefficient that depends on temperature but not on the ion mass. It has been historically assumed that, due to a very effective charge transfer mechanism, only ions with the lowest ionization potential survive after a short path in the mixture. However, recent experimental data suggests that the signal ions, in e.g. CO_2-quenched mixtures of Ar and Ne are $CO_2^+ \cdot (CO2)_n$ cluster ions, and not CO_2^+ or noble gas ions [112]. Since the cluster ions are slower than the initial ions, the signals induced by ion motion are altered. The effect can be present in constant-field detectors and TPCs (see Sec. 35.6.5), and might affect devices such as Micromegas (see Sec. 35.6.4) and drift tubes. A negative-ion TPC can be used to expand the reach of directional dark matters searches [113].

35.6.2 *Multi-Wire Proportional and Drift Chambers*

Revised November 2021 by F. Sauli (CERN) and M. Titov (IRFU, CEA, Université Paris-Saclay).

Single-wire counters that detect the ionization produced in a gas by a charged particle, followed by charge multiplication and collection around a thin (typically $20 - 50$ μm diameter) wire, have been used for decades. Good energy resolution is obtained in the proportional amplification mode, while very large saturated pulses can be detected in the streamer and Geiger modes [114].

Modern fully electronic devices, multiwire proportional chambers (MWPCs) [115, 116] intro-

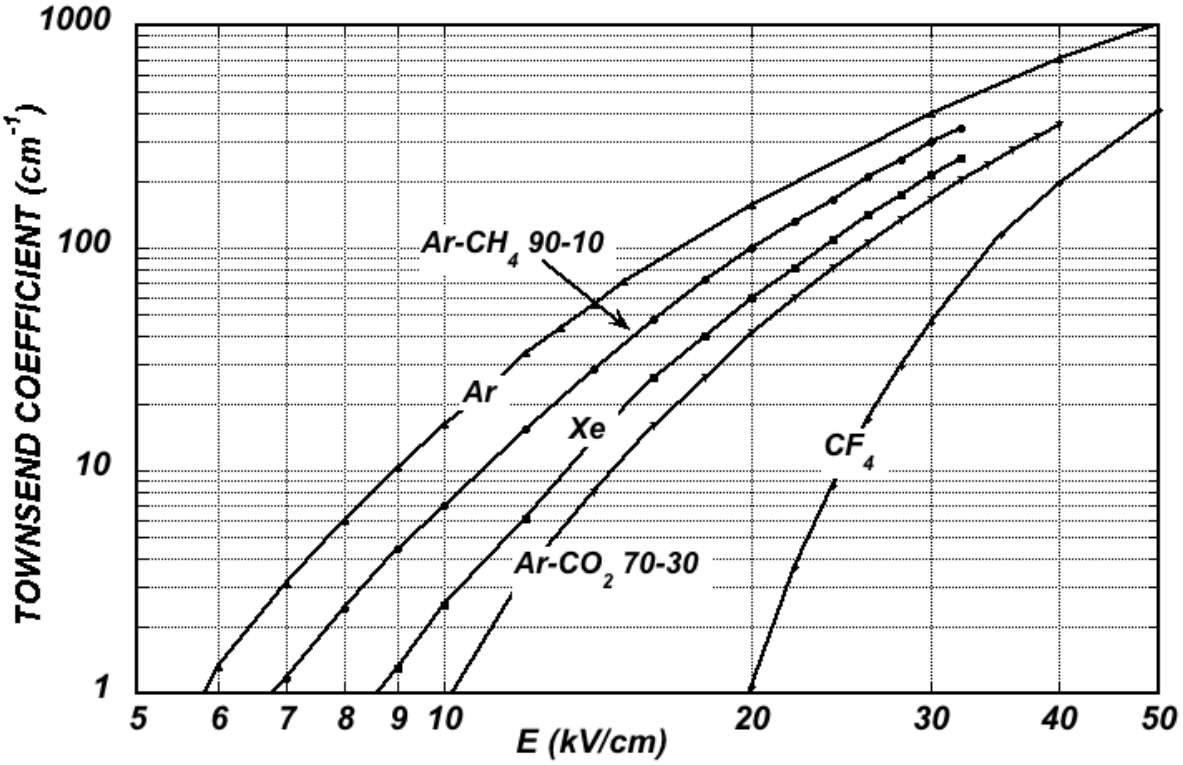

Figure 35.7: Computed first Townsend coefficient α as a function of electric field in several gases at NTP [102, 103].

Table 35.6: Mobility of ions in gases and mixtures at NTP [111].

Gas	Mobility μ ($\mathrm{cm^2\ V^{-1}\ s^{-1}}$)
He	10.4
Ne	4.7
Ar	1.54
$\mathrm{Ar/CH_4}$	1.87
$\mathrm{Ar/CO_2}$	1.72
$\mathrm{CH_4}$	2.26
$\mathrm{CO_2}$	1.09

duced in the late 1960's, detect, localize and measure energy deposit by charged particles over large areas. A mesh of parallel anode wires at a suitable potential, inserted between two cathodes, acts almost as a set of independent proportional counters (see Fig. 35.8a). Electrons released in the gas volume drift towards the anodes and produce avalanches in the increasing field. Analytic expressions for the electric field can be found in many textbooks. The fields close to the wires $E(r)$, in the drift region E_D, and the capacitance C per unit length of anode wire are approximately given by

$$E(r) = \frac{CV_0}{2\pi\epsilon_0}\frac{1}{r} \qquad E_D = \frac{CV_0}{2\epsilon_0 s} \qquad C = \frac{2\pi\epsilon_0}{\pi(\ell/s) - \ln(2\pi a/s)}\ , \tag{35.15}$$

where r is the distance from the center of the anode, s the wire spacing, ℓ and V_0 the distance and

potential difference between anode and cathode, and a the anode wire radius.

Because of electrostatic forces, anode wires are in equilibrium only for a perfect geometry. Small deviations result in forces displacing the wires alternatively below and above the symmetry plane, sometimes with catastrophic results [117]. These displacement forces are countered by the mechanical tension of the wire, up to a maximum unsupported stable length, L_M [118], above which the wire displaces:

$$L_M = \frac{s}{CV_0}\sqrt{4\pi\epsilon_0 T_M} \tag{35.16}$$

The maximum tension T_M depends on the wire diameter and modulus of elasticity. Table 35.7 gives approximate values for tungsten and the corresponding maximum stable wire length under reasonable assumptions for the operating voltage ($V_0 = 5\,\text{kV}$) [119]. Internal supports and spacers can be used in the construction of longer detectors to overcome limits on the wire length imposed by Eq. (35.16).

Table 35.7: Maximum tension T_M and stable unsupported length L_M for tungsten wires with spacing s, operated at $V_0 = 5$ kV. No safety factor is included.

Wire diameter (μm)	T_M (newton)	s (mm)	L_M (cm)
10	0.16	1	25
20	0.65	2	85

Traditionally, several simplifying assumptions are made in such analytical calculations: electrostatic force acting on the wire does not change during wire movements, or varies linearly with the displacement, the wire shape is parabolic; only one wire moves at a time. Therefore, for complicated electrode geometries the approximations listed above are not applicable. The advantage of numerical integrations using Garfield^{++} program is to simulate the collective movement of all wires, which are difficult analytically, and to consider all forces acting on a wire: forces between anode wire and other electrodes (wires, cathode) and a gravitational force [120].

Detection of charge on the wires over a predefined threshold provides the transverse coordinate to the wire with an accuracy comparable to that of the wire spacing. The coordinate along each wire can be obtained by measuring the ratio of collected charge at the two ends of resistive wires. The cathode planes can be fabricated in the form of group of wires or isolated strips, which are often patterned in orthogonal directions. Making use of the charge profile induced by avalanches on segmented cathodes, the so-called electronic center-of-gravity (COG) method allows localization of tracks to sub-mm accuracy. Due to the statistics of energy loss and asymmetric ionization clusters, the position accuracy is $\sim$ 50 μm rms for fast particles perpendicular to the wire plane, but degrades to $\sim$ 250 μm at 30° to the normal [121].

Drift chambers, developed in the early '70's, can be used to estimate the space coordinate perpendicular to the wires by exploiting the arrival time of electrons at the anodes if the time of interaction is known [122]. The distance between anode wires (e.g. Au-plated W) is usually several cm, allowing coverage of large areas at reduced cost. In the original design, a thicker wire (the field wire, often from Cu-Be or Al) at the proper voltage, placed between the anode wires, removes the low-field region at the mid-point between anodes and improves charge collection (Fig. 35.8b). In some drift chamber designs, and with the help of suitable voltages applied to field-shaping electrodes, the electric field structure is adjusted to improve the linearity of space-to-drift-time relation, resulting in better spatial resolution [123].

Drift chambers can reach a longitudinal spatial resolution from timing measurement of order

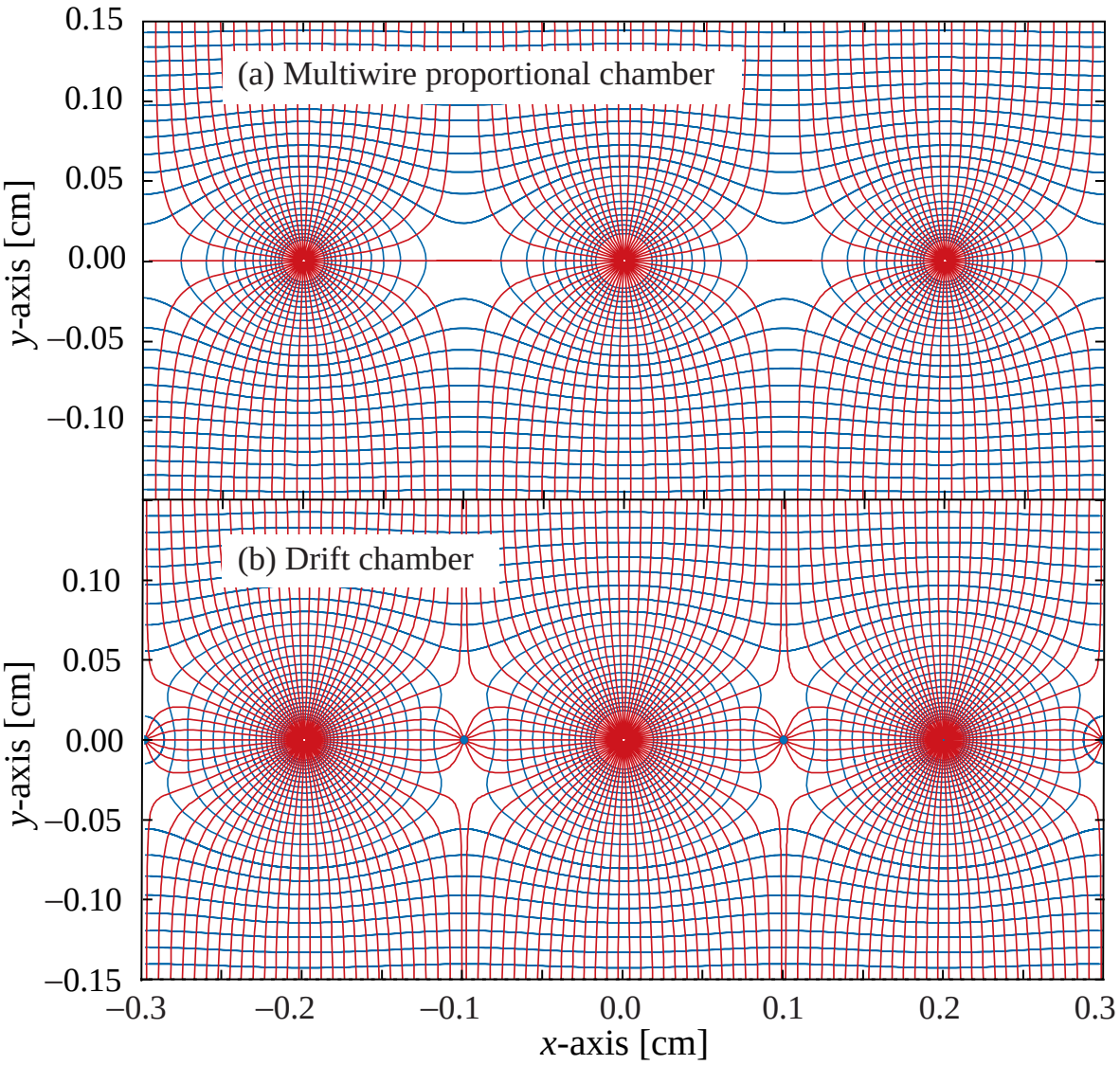

Figure 35.8: Electric field lines and equipotentials in (a) a multiwire proportional chamber and (b) a drift chamber.

100 μm (rms) or better for minimum ionizing particles, depending on the geometry and operating conditions. However, a degradation of resolution is observed [124] due to primary ionization statistics for tracks close to the anode wires, caused by the spread in arrival time of the nearest ionization clusters. The effect can be reduced by operating the detector at higher pressures. Sampling the drift time on rows of anodes led to the concept of multiple arrays such as the multi-drift module [125] and the JET chamber [126]. A measurement of drift time, together with the recording of charge sharing from the two ends of the anode wires provides the coordinates of segments of tracks. An ultimate drift chamber design is the Time Projection Chamber (TPC) concept [127], which provides 3D precision tracking with low material budget and enables particle identification through differential energy loss dE/dx measurement or cluster counting dN_{cl}/dx techniques. In all cases, a good knowledge of electron drift velocity and diffusion properties is required. This has to be combined with the knowledge of the electric fields in the structures [103]. Accumulation of ions

in the gas volume may induce gain reduction and field distortions, especially for long drift distances in TPC (see Sec. 35.6.5). An important major innovation is related to the replacement of MWPC with Micro-Pattern Gaseous Detectors (MPGD) (see Sec. 35.6.4) for the TPC endplate readout, which offers many advantages: reduced track-angle, and negligible $\mathrm{E} \times \mathrm{B}$ track distortion effects, narrower pad response function (PRF), and intrinsic suppression of Ion Back Flow (IBF). For an overview of detectors exploiting the drift time for coordinate measurement see Refs. [118, 128].

Multiwire and drift chambers have been operated with a variety of gas fillings and operating modes, depending on experimental requirements. The so-called "Magic Gas," a mixture of argon, isobutane and Freon [116], permits very high and saturated gains ($\sim 10^6$). This gas mixture was used in early wire chambers, but was found to be susceptible to severe aging processes. DAFNE's KLOE Drift Chamber and the recent version of it developed for the MEG2 experiment [129] are the precursors of the next generation of ultralight central trackers for future colliders. Since the main contribution in terms of radiation length is related to tungsten wires, high transparency can be achieved thanks to the development of new wire materials (e.g. carbon monofilaments) and novel approaches for the wiring and assembly procedures. Drift chambers have been operated with a light helium/hydrocarbon mixtures, which are not reliable for long-term, high-rate operation [130]. Dedicated R&D is necessary to find an alternative hydrocarbon-free mixture adapted to the desired performance at future colliders.

Although very powerful in terms of performance, multi-wire structures have reliability problems when used in harsh or hard-to-access environments, since a single broken wire can disable the entire detector. Introduced in the 1980s, straw and drift tube systems make use of large arrays of proportional counters encased in individual enclosures, each acting as an independent wire counter [131]. Techniques for low-cost mass production of these detectors have been developed for large experiments, such as the Transition Radiation Tracker and the Drift Tubes arrays for CERN's LHC experiments [132]. The state-of-the-art NA62 straw tracker utilizes new construction techniques of ultrasonic welding to close the straw and to keep them straight and withstand the vacuum pressure without breaking [133]. Future efforts for straw detectors, e.g. COMET Phase-II at JPARC or Mu2e-II at Fermilab, will focus on ultra-thin wall development, long and thin wire handling, precise mechanics and innovative designs.

35.6.3 *High Rate Effects*

Revised November 2021 by F. Sauli (CERN) and M. Titov (IRFU, CEA, Université Paris-Saclay).

The production of positive ions in the avalanches and their slow drift before neutralization result in a rate-dependent accumulation of positive charge in the detector. This may result in significant field distortion, gain reduction and degradation of spatial resolution. As shown in Fig. 35.9 [134], the proportional gain drops above a charge production rate around 10^9 electrons per second and mm of wire, independently of the avalanche size. For a proportional gain of 10^4 and 100 electrons per track, this corresponds to a particle flux of $10^3\,\mathrm{s}^{-1}\mathrm{mm}^{-1}$ (1 kHz/mm^2 for 1 mm wire spacing). For the description of rate effects in MPGD, see Sec. 35.6.4.

Although almost any gas can be used to operate wire chambers, CF_4-based mixtures have been preferred due to their properties. Their main advantage for the use in large volume detectors are high drift velocity, low diffusion, non-flammability and low sensitivity to neutrons; also they do not form polymers in avalanches.

However, the problem of greenhouse gases, such as CF_4, could become a fundamental limitation for their future applications in gaseous detectors; due to the EU regulations their prices might go up and future availability is unknown. Performance studies of several eco-friendly mixtures have been initiated, together with a better understanding of their long-term ageing effects [135] (see also Sec. 35.6.4).

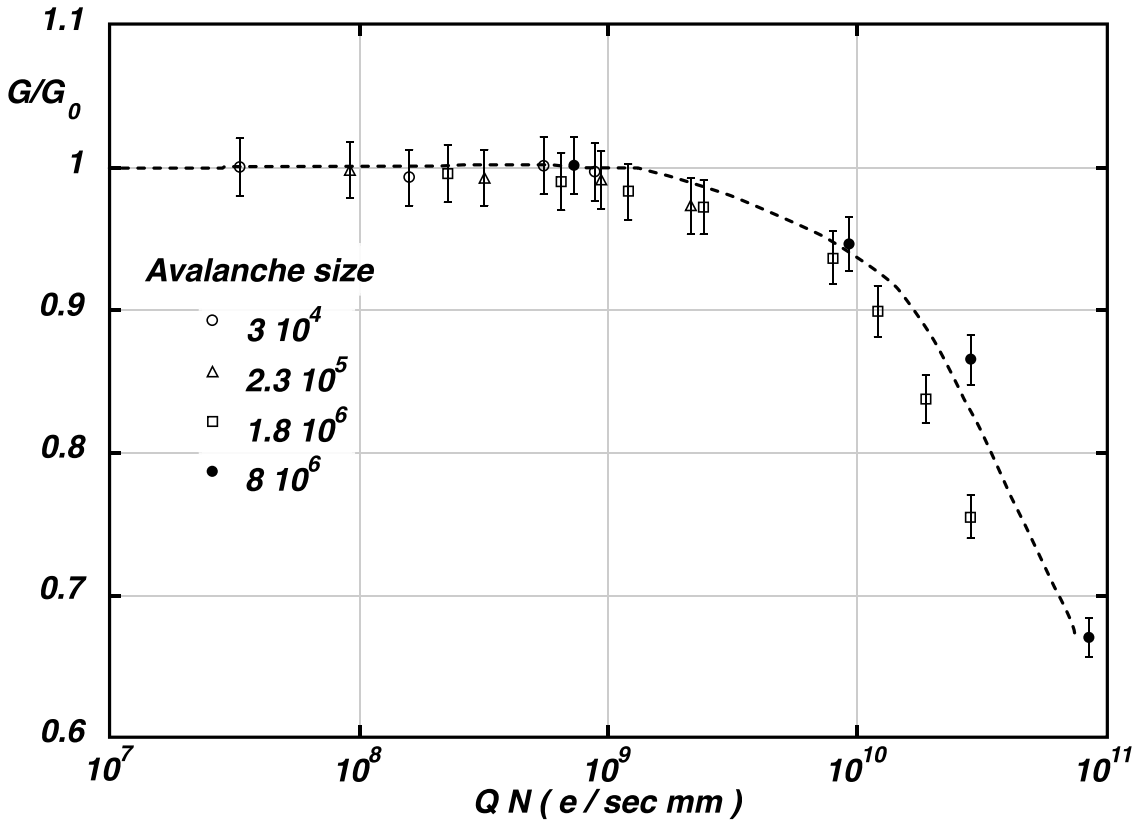

Figure 35.9: Charge rate dependence of normalized gas gain G/G_0 (relative to zero counting rate) in proportional thin-wire detectors [134]. Q is the total charge in single avalanche; N is the particle rate per wire length.

Ageing phenomena (formation of polymer deposits on the electrodes) constitute one of the most complex and serious potential problems which could limit or severely impair the use of gaseous detectors in unprecedented harsh radiation environments and lead to operational instabilities [136] [130]. The process has been extensively investigated, often with conflicting results. Several causes have been identified, including organic pollutants and silicone oils. Addition of small amounts of water in many (but not all) cases has been shown to extend the lifetime of the detectors. Addition of fluorinated gases (*e.g.*, CF_4) or oxygen may result in an etching action that can overcome polymer formation, or even eliminate already existing deposits. However, the issue of long-term survival of gas detectors with these gases is controversial. Under optimum operating conditions, a total collected charge of a few coulombs per cm of wire can usually be reached before noticeable degradation occurs. This corresponds, for one mm spacing and at a gain of 10^4, to a total particle flux of $\sim 10^{14}$ MIPs/cm^2.

35.6.4 *Micro-Pattern Gas Detectors*

Revised November 2021 by F. Sauli (CERN) and M. Titov (IRFU, CEA, Université Paris-Saclay).

Despite various improvements, position-sensitive detectors based on wire structures are limited by basic diffusion processes and space charge effects to localization accuracies of 50–100 μm [137]. Industrial advances in microelectronics and photolithographic technology on flexible and standard PCB substrates has favored the invention, in the last years of the 20th century, of novel Micro-Pattern Gaseous Detectors (MPGD) [138–140]. Since the very beginning, the goal was the develop-

ment of novel devices with high rate capability (up to 10^6 Hz/mm^2) and excellent spatial resolution (down to 30 μm), single photo-electron time resolution in the ns-range, large sensitive area and dynamic range, superior radiation hardness and low-cost for large area coverage. Nowadays, a broad family of MPGD technologies are being developed and optimized for numerous applications, such as [141, 142]: Micro-Strip Gas Chamber (MSGC), Gas Electron Multiplier (GEM), Micro-Mesh Gaseous Structure (Micromegas), THick GEMs (THGEM), also referred to in the literature as Large Electron Multipliers (LEM), Resistive Plate WELL (RPWELL), GEM-derived architecture (μ-RWELL), Micro-Pixel Gas Chamber (μ-PIC), and an integrated readout of gaseous detectors (Gridpix) using solid-state pixel chips (e.g. Medipix or Timepix).

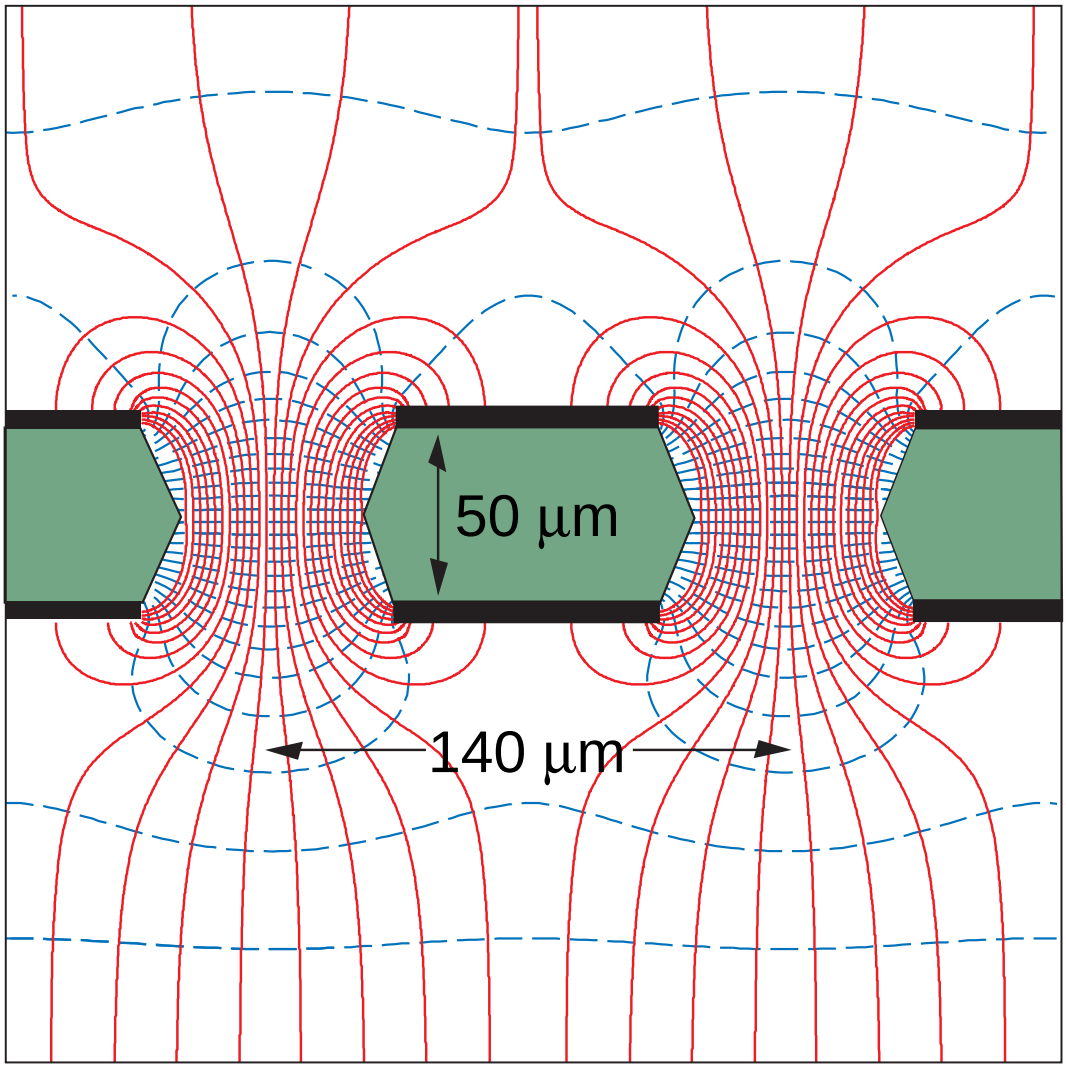

Figure 35.10: Schematic view and typical dimensions of the hole structure in the GEM amplification cell. Electric field lines (solid) and equipotentials (dashed) are shown. Electron trajectories do not strictly follow the field lines as drifting electrons scatter isotropically with gas molecules and diffuse transversally.

The MSGC concept, invented in 1988, was the first of the micro-structure gas chambers [138]. It consists of a set of tiny parallel metal strips laid on a thin resistive support, alternatively connected as anodes and cathodes and resembles a multi-anode proportional counter. Through an accurate

and simple photolithography process, the anode strips can be made very narrow ($\sim 10\ \mu m$) with a typical pitch (distance between strips) of $\sim 100\ \mu m$. When appropriate potentials are applied to the electrodes, electrons released in the drift volume move toward the strips and multiply in the high-field region. Owing to the small anode-to-cathode distance, the fast removal of positive ions by nearby cathode strips reduces space charge build-up, and improves siginicantly the rate capability, compared to wire counter. Despite their promising performance, experience with MSGCs has raised serious concerns about their long-term behavior. There are several major processes, particularly at high rates, leading to the MSGC operational instabilities: substrate charging-up and time-dependent distortions of the electric field, surface deposition of polymers ("aging") during sustained irradiation, and destructive micro-discharges under exposure to heavily ionizing particles [143]. The physical parameters used to manufacture and operate these detectors (substrate material, metal of strips, type and purity of the gas mixture) appeared to play dominant roles in determining the medium- and long-term stability. The problems encountered inspired the development of novel structures, using modern photolithographic processes: GEM, Micromegas and others, having increased reliability and radiation hardness.

A GEM detector consists of a thin-foil copper-insulator-copper sandwich chemically perforated to obtain a high density of holes in which avalanches occur [139,144]. The hole diameter is typically between 25 μm and 150 μm, while the corresponding distance between holes varies between 50 μm and 200 μm. The central insulator is usually (in the original design) a polyimid foil, with a thickness of 50 μm. Application of a potential difference between the two metal sides of the GEM generates the electric fields indicated in Fig. 35.10. Each hole acts as an independent proportional counter. Electrons released by the primary ionization particle in the upper conversion region (above the GEM foil) drift into the holes, where charge multiplication occurs in the high electric field (50–70 kV/cm), and are transferred into the gap below the GEM. Systematic measurements with cascaded multi-GEM structures confirm that the gains and charge transfer processes are predictable from electrostatic considerations and avalanche development models; an overall gas gain well above 10^4 can be reached in the presence of highly ionizing particles, while strongly reducing the risk of discharges [145]. Other important parameters such as attachment, diffusion depend on the gas mixture composition and E/P. The majority of the charges created in the avalanche process follow the field lines and are collected by the metallic electrodes; owing however to diffusion, some may deposit on the dielectric surfaces, modifying the field and affecting gain and transparency of the structures [146]. This effect is known as "charging-up" effect; its time constant and amplitude depend largely on the shape of the holes.

The micro-mesh gaseous structure (Micromegas) is a thin parallel-plate avalanche counter, as shown in Fig. 35.11 [140]. It consists of a drift region and a narrow multiplication gap (25–150 μm) between a thin metal grid (micromesh) and the readout electrode (strips or pads of conductor printed on an insulator board). Electrons from the primary ionization drift through the mesh into the narrow multiplication gap, where they are amplified. The electric field is mostly homogeneous in both the drift (electric field ~ 1 kV/cm) and amplification (50–70 kV/cm) regions and exhibits a funnel-like shape close to the openings of the micromesh: field lines are compressed into a small diameter of the order of a few microns, depending on the electric field ratio between the two gaps. In the narrow multiplication region, small variations of the amplification gap are approximately compensated by an inverse variation of the Townsend coefficient from the electric field, resulting in a more uniform gain. The transverse size of the electron avalanche due to diffusion is of the order of 10–15 μm, depending on the gas mixture, the electric field, and the gap width, giving rise to excellent spatial resolution (12 μm for MIPs) [147]. Most positive ions are quickly removed by the micromesh; this prevents space-charge accumulation and induces very fast signals (~ 100 ns length) due to electrons with a (fast) tail due to ions. Efforts have been also focused on producing

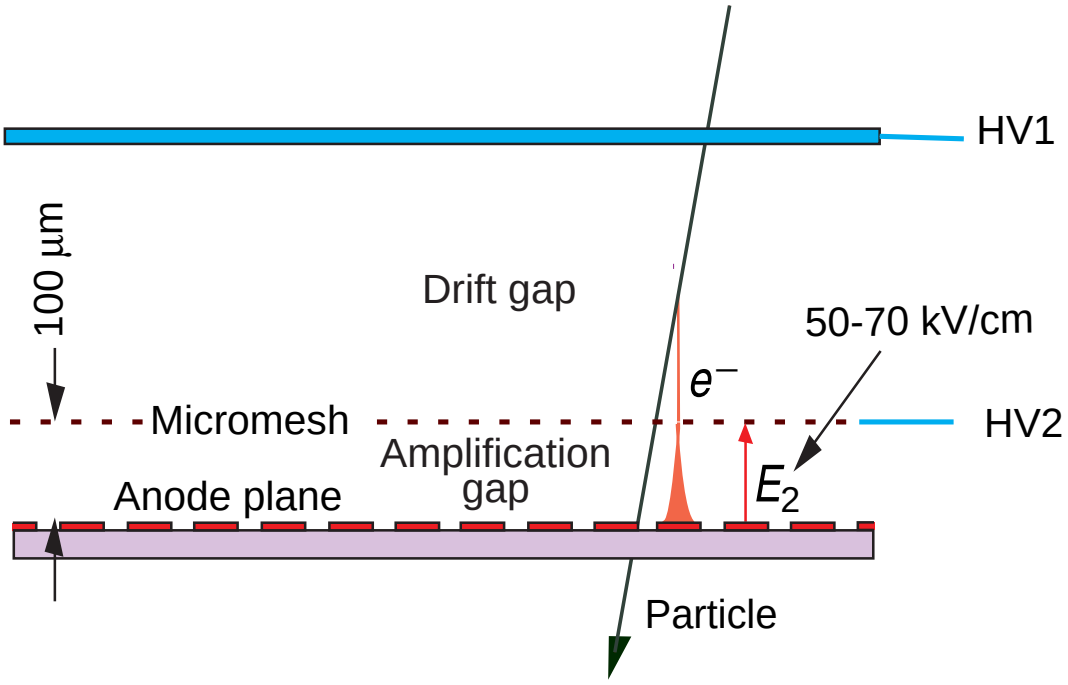

Figure 35.11: Schematic drawing of the Micromegas detector.

Micromegas detector using innovative manufacturing techniques - the "Bulk" and "'MicroBulk" technologies [148].

The absence of space-charge effects in GEMs at the highest rates reached so far, thanks to its fine-pitch structure of a few hundred microns, improves the maximum rate capability by more than two orders of magnitude compared to MWPC (see Fig.35.12) [149] [150]. Even larger rate capability has been reported for Micromegas [151].

The fine granularity and high-rate capability of GEM and Micromegas can be fully exploited by using high-density pixel readout with a size corresponding to the intrinsic width of the detected avalanche charge. An elegant solution is the use of a CMOS pixel ASIC, assembled directly below the GEM or Micromegas amplification structure. Modern wafer post-processing technology allows an integration of a small-scale micromesh grid directly on top of a Timepix chip, thus forming an integrated MPGD readout, called GridPix concept (see Fig.35.13) [152]. With this arrangement, avalanche electrons are collected on the metalized input pads, exposed to the gas and signals are induced at the input gate of a charge-sensitive preamplifier. Every pixel is then directly connected to the amplification and digitization circuits, integrated in the underlying CMOS layers. A thin insulating layer, e.g. a few μm of silicon nitride, is usually deposited on top of CMOS ASIC to protect against destructive discharges across the $\mathcal{O}(50\ \mu m)$ amplification gap. The GridPix concept provides the high granularity needed to resolve individual electron clusters (separated by an average distance of a few hundred microns) and to determine energy loss by the cluster counting technique, rather than by the charge measurement, with a precision of better than 3 %. Despite the enormous challenges, real breakthrough was the development of the TPC readout endplate with a 160 GridPix ASICs, each 2 cm^2, corresponding to 10.5 million pixels, demonstrating for the first time the feasibility of large-area MPGD with CMOS pixel readout [153]. New structures, where a GEM foil is facing the Medipix chip, forming the GEMpix detector, are in use for medical applications [154] as well as for monitoring the radioactive waste [155].

Gaseous detectors represent the most cost-effective solution to cover very large areas with pho-

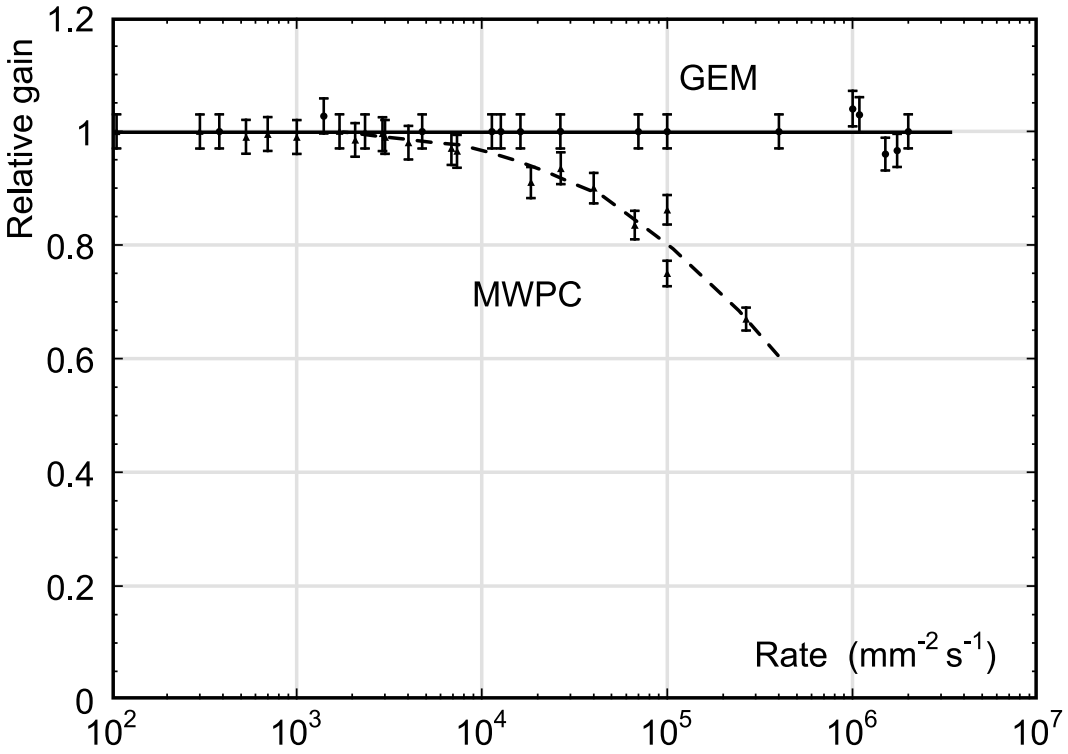

Figure 35.12: Normalized gas gain as a function of particle rate for MWPC [149] and GEM [150].

tosensitive elements. MPGD-based gaseous photomultipliers, conceived with the aim to overcome the limitations of MWPCs, with semi-transparent or reflective photocathodes (PC), allow to minimize PC aging due to the ion and photon feedback and to avoid secondary effects causing electrical instability. For RICH applications requiring large-area coverage and moderate spatial resolution, coarser macro-patterned structures (e.g. THGEM with typical thickness of 0.4–1 mm and hole spacing of 0.7–1.2 mm) offer an interesting cheaper solution [156]. These are derived from the GEM design, scaling up $\sim$ 10-fold geometrical parameters, and can be mass-produced with standard PCB technology and mechanical drilling of large number of holes: some millions per square meter. Systematic studies to find the optimal electrostatic configuration revealed that the presence of a rim, a circular region around the holes where metal is etched away, plays a major role in THGEM performance. A small or zero rim allows to achieve better gain stability in time and under irradiation, while large rims permit to attain larger maximum gain and to reduce discharges, at the cost of significant charging up of the insulating surface, which modify the electric field. Therefore, in spite of the enhanced gain performance, the use of large rim THGEMs must be avoided to guarantee stable detector performance [157]. MPGDs are now in operation for single photon detection in the COMPASS RICH where a hybrid architecture formed by two THGEM layers (one covered by CsI-PC) and a Micromegas, acting as a third amplification stage, has been adopted.

Lately, closed geometry THGEM-based structures (RPWELL) [158], in common with some MPGDs invented at the end of the last century – C.A.T. and WELL, with resistive anodes have been developed, combining THGEM and RPC properties. This concept consists of a single-faced THGEM, copper-clad on its top side only, mounted directly on top of a resistive film deposited on a thin insulating sheet. Compared to THGEM with an induction gap, higher gains could be achieved in RPWELL for lower applied voltage across the THGEM electrode, due to the larger electric field within the closed holes. Another promising GEM-derived architecture is that of the

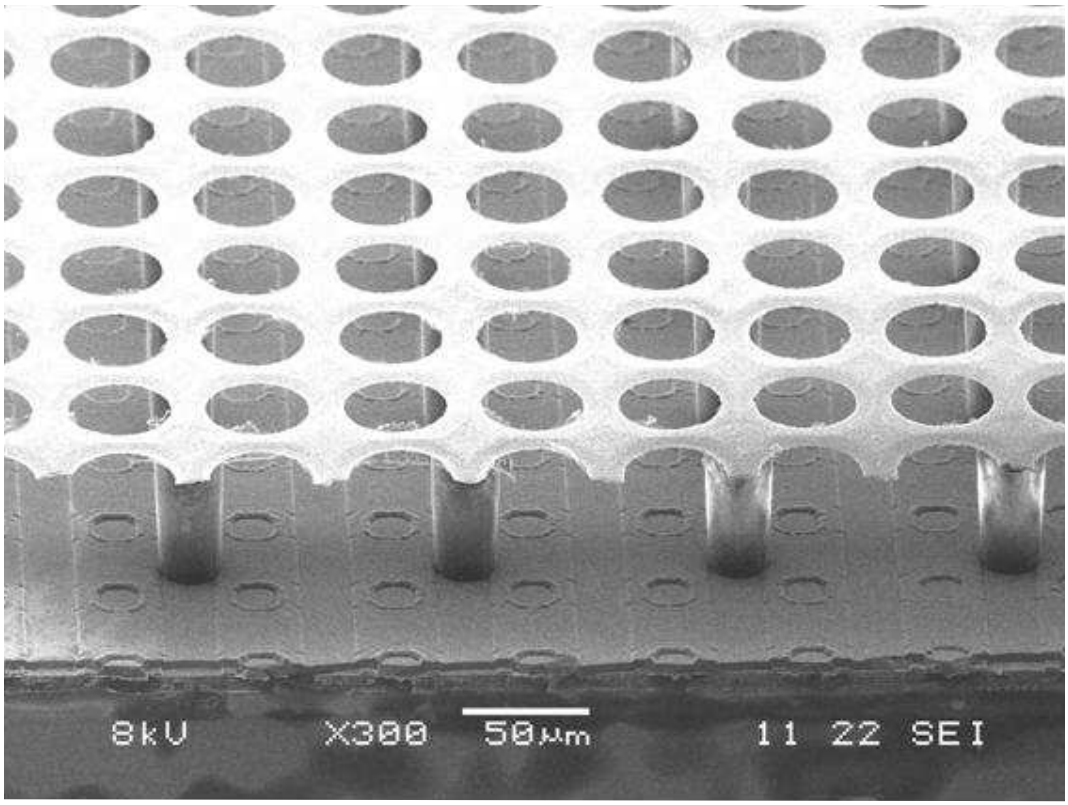

Figure 35.13: Photo of the Micromegas ('GridPix") detector. The grid holes can be accurately aligned with readout pixels of Timepix CMOS chip. The insulating pillars are centered between the grid holes, thus avoiding dead regions.

μ-RWELL [159], with its $\sim$ seven-fold smaller pitch with respect to the RPWELL. Two different layouts for resistive stage have been studied: the simplest one is based on a single-resistive Diamong-Like Carbon (DLC) layer, and grounding by edges (2D charge evacuation for low-rates $\mathcal{O}(\mathrm{kHz/cm^2})$) and a more sophisticated scheme using double-resistive layer with a through-vias between them and the grounding done by means of the readout electrodes (3D charge evacuation for high-rate $\mathcal{O}(\mathrm{MHz/cm^2})$ applications) [160]. The μ-PIC structure is an industrially produced PCB including anode strips on one side and orthogonal cathode strips on the other one. A regular pattern of uncoated regions is present along the cathode strips; an electric conductor buried in the thin PCB substrate transfers the anode voltage to a "dot" at the center of each of the uncoated cathode zones. Electron avalanches occur under the high-electric field around the point-like anodes; the electric field near cathode edges is weaker than in MSGCs, resulting in a lower discharge probability. A resistive coating of the cathode strips (e.g. using DLC layers) ensures tolerance to occasional discharges [161].

A big step in the direction of large-size applications has been obtained both with conceptual consolidation and industrial and cost-effective manufacturing of MPGDs by developing new fabrication techniques: resistive Micromegas (to suppress destructive sparks in hadron environments) [162] and single-mask and self-stretching GEM techniques (to enable production of large-size foils and significantly reduce detector assembly time) [163]. Scaling up of MPGDs to very large single unit detectors of $\mathcal{O}(\mathrm{m^2})$, has facilitated their use in the High Luminosity LHC upgrades: Micromegas will instrument an area of $\mathcal{O}(1000\,\mathrm{m^2})$ in the New Small Wheel of the ATLAS Muon endcaps,

while GEMs be used in the CMS Muon system and for the ALICE TPC readout. Exploiting the Micromegas, GEM, and μ-RWELL ability to measure both position and arrival time of the charge released in the drift gap, a novel μ-TPC concept has been developed; it permits achieving nearly constant spatial resolution over a wide range of particle incident angles and allows 3D track reconstruction with a single MPGD layer [164]. Although normally used as planar detectors, GEM, Micromegas, and μ-RWELL can be bent to form cylindrically curved ultra-light inner tracking systems, without support and cooling structures [165].

The consolidation of the better-established technologies has been accompanied with flourishing of novel ones, often specific to well-defined applications. Modern technologies have been also derived from Micromegas and GEM concepts, hybrid approaches combining different elements in a single device, gaseous with non-gaseous detectors, as is the case for optical read-out. MPGD hybridization, a strategy aiming to strengthen the detector performance, remains a valid asset for addressing future experimental challenges such as high granularity and picosecond-precision timing (e.g. PICOSEC-Micromegas concept [166]). A clear direction for future developments is that of resistive materials and related detector architectures. Their usage improves detector stability, making possible a higher gain in a single multiplication layer. Recent DLC resistive layers studies are the key ingredients for increasing the rate capability of MPGDs [167]. Future developments call for novel materials as well as for new fabrication techniques. Contributions to the detector concepts are required in several domains: resistive materials, solid-state photon and neutron converters, innovative nanotechnology components. Material studies can contribute to requirements related to low out-gassing, radiation hardness, radio-purity, converter robustness, and eco-friendly gases. The development of the next generation of MPGDs can largely profit from emerging technologies as those related to MicroElectroMechanical Systems (MEMS), sputtering, novel photoconverters, 3D printing of amplifying structures and cooling circuits, etc. Nowadays, many intensive MPGD R&D activities and their diversified applications are pursued within the world-wide CERN-RD51 collaboration [168].

35.6.5 *Time-projection chambers*

Revised July 2021 by C. Lippmann (GSI Darmstadt).

The Time Projection Chamber (TPC) concept was invented by David Nygren in the 1970's [169]. It consists of a cylindrical or square field cage that is filled with a gaseous (or liquid) detection medium. Charged particles produce tracks of ionization electrons that drift in a uniform electric field towards a position-sensitive amplification stage which provides a 2D projection of the particle trajectories. The third coordinate can be calculated from the arrival times of the drifted electrons. The start for this drift time measurement is usually derived from an external detector, e.g. a fast interaction trigger detector.

This section focuses on the gas-filled TPCs that are often used in particle or nuclear physics experiments at accelerators on account of their low material budget. For neutrino physics (Sec. 35.11) or for detecting rare events (Sec. 36.4), on the contrary, usually high density and large active mass are required, and a liquid detection medium is favored.

The TPC enables full 3D measurements of charged particle tracks, which gives it a distinct advantage over other tracking detector designs which record information only in two-dimensional detector planes and have less overall segmentation. The track points recorded in a TPC are basically adjacent, which facilitates the track finding enormously. This advantage is often exploited for pattern recognition in events with large numbers of particles, e.g. heavy-ion collisions. Two examples of modern large-volume gaseous TPCs are shown in (Figure 35.14) and (Figure 35.15).

Identification of the charged particles crossing the TPC is possible by simultaneously measuring their momentum and specific energy deposit through ionisation ($\mathrm{d}E/\mathrm{d}x$). The momentum, as well

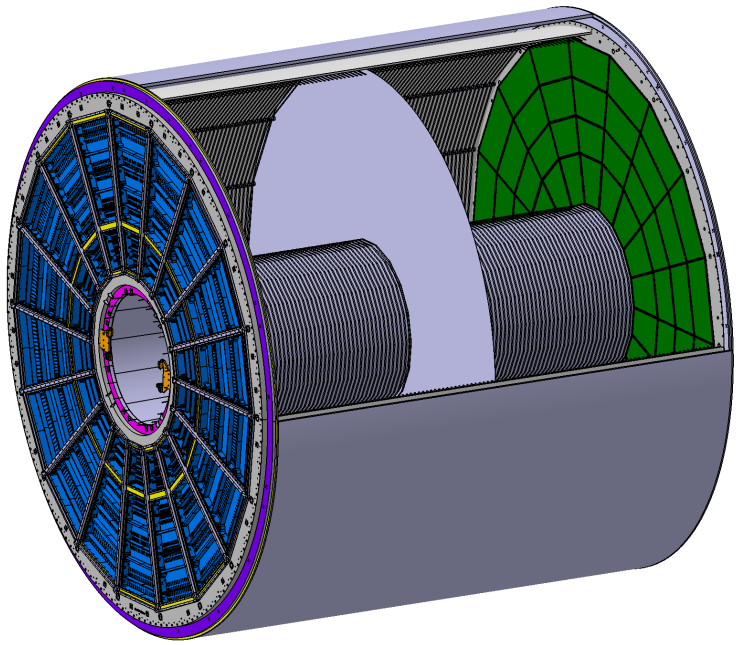

Figure 35.14: Schematic view of the ALICE TPC [170,171]. The drift volume with 5 m diameter is divided into two halves, each providing 2.5 m drift length. The amplification stage has recently been upgraded from wire planes to GEMs.

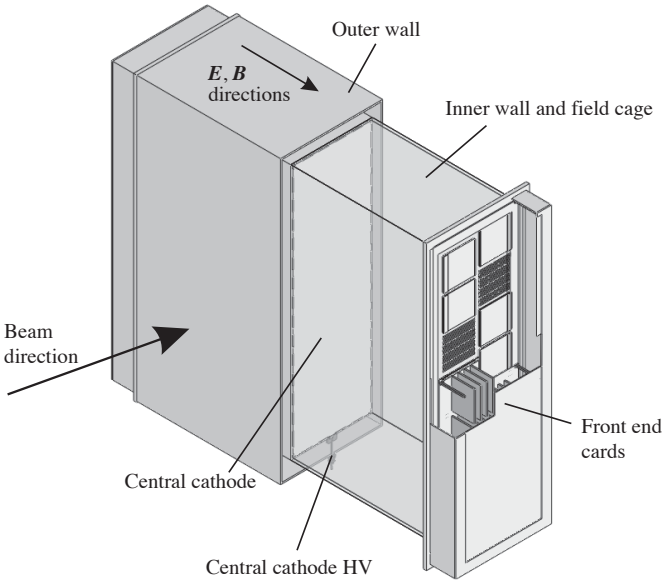

Figure 35.15: One of the 3 TPC modules for the near detector of the T2K experiment [172]. The size is $2 \times 2 \times 0.8\,\mathrm{m}^3$. Micromegas devices are used for gas amplification and readout.

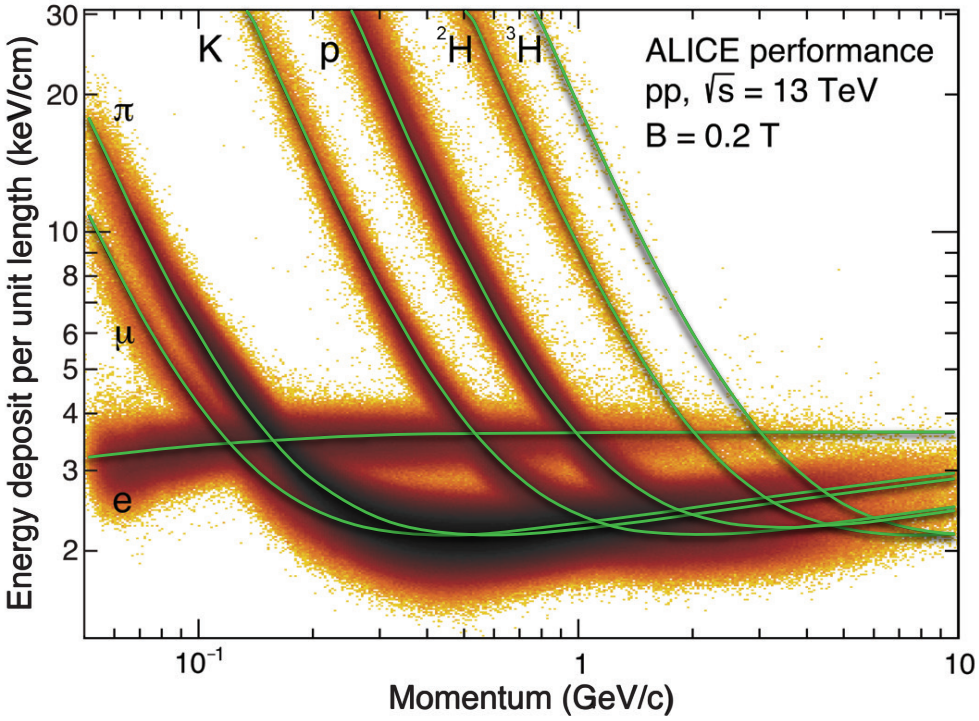

Figure 35.16: Energy deposit versus momentum measured in the ALICE TPC.

as the charge sign, are calculated from a helix fit to the particle trajectory in the presence of a magnetic field (typically parallel to the drift field). For this application, precise spatial measurements in the plane transverse to the magnetic field are most important. The specific energy deposit is estimated from many charge measurements along the particle trajectory (e.g. one measurement per anode wire or per row of readout pads). As the charge collected per readout segment depends on the track angle and on the ambient conditions, the measured values are corrected for the effective length of the track segments and for variations of the gas temperature and pressure. The most probable value of the corrected signal amplitudes for a given track provides the best estimator for the specific energy deposit (see Sec. 34.2.3); it is usually approximated by the truncated mean, i.e. the average of the 50%–70% smallest values. The resulting particle identification performance is illustrated in (Figure 35.16), for the ALICE TPC.

The dependence of the achievable energy resolution on the number of measurements N, on the thickness of the sampling layers t, and on the gas pressure P can be estimated using an empirical formula [173]:

$$\sigma_{dE/dx} = 0.41\ N^{-0.43}(t\,P)^{-0.32}. \tag{35.17}$$

Typical values at nominal pressure are $\sigma_{dE/dx} = 4.5$ to 7.5%, with $t = 0.4$ to 1.5 cm and $N = 40$ up to more than 300. The record, with an unprecedented energy resolution of 3%, is held by the PEP-4/9 TPC [174], due to the high gas pressure of 8.5 bar.

The greatest challenges for a large TPC are due to the length of the drift of up to a few meters. In particular, it can make the device sensitive to small distortions in the electric field. Such distortions can arise from a number of sources, e.g. imperfections in the field cage construction or the presence

of ions in the drift volume. The electron drift in a TPC in the presence of a magnetic field is defined by Eq. (35.14). The $E \times B$ term of Eq. (35.14) vanishes for perfectly aligned electric and magnetic fields, which can however be difficult to achieve in practice. Furthermore, the electron drift depends on the $\omega\tau$ factor, which is defined by the gas mixture and the magnetic field strength. The electrons will tend to follow the magnetic field lines for $\omega\tau > 1$, or the electric field lines for $\omega\tau < 1$. The former mode of operation makes the TPC less sensitive to non-uniformities of the electric field, which is usually desirable.

The drift of the ionization electrons is superposed with a random diffusion motion which degrades their position information. The ultimate resolution of a single position measurement is limited to around

$$\sigma_x = \frac{\sigma_D \sqrt{L}}{\sqrt{n}}\,, \tag{35.18}$$

where σ_D is the transverse diffusion coefficient for 1 cm drift, L is the drift length in cm and n is the effective number of electrons collected. Without a magnetic field, $\sigma_{D,B=0}\sqrt{L}$ is typically a few mm after a drift of $L = 100\,\text{cm}$. However, in a strong magnetic field parallel to the drift field, a large value of $\omega\tau$ can significantly reduce diffusion:

$$\frac{\sigma_{D,B>0}}{\sigma_{D,B=0}} = \frac{1}{\sqrt{1+\omega^2\tau^2}}\,. \tag{35.19}$$

This factor can reach values of up to 10. In practice, the final resolution limit due to diffusion typically lies around $\sigma_x = 100\,\mu\text{m}$.

The drift and diffusion of electrons depend strongly on the gas mixture. The optimal gas mixture varies according to the environment in which the TPC operates. In all cases, the oxygen concentration must be kept very low (few ten parts per million in a large TPC) in order to avoid electron loss through attachment.

Ideally, the drift velocity should depend only weakly on the electric field at the nominal operating condition. The classic Ar/CH_4 (90:10) mixture, known as P10, has a drift velocity maximum of $5\,\text{cm}/\mu\text{s}$ at an electric field of only $125\,\text{V/cm}$ (Figure 35.5). In this regime, the electron arrival time is not affected by small variations in the ambient conditions. Moreover, low electric fields simplify the design and operation of the field cage. The mixture has a large transverse diffusion at $B = 0$, but this can be reduced significantly in a strong magnetic field due to the relatively large value of $\omega\tau$.

For some applications organic gases like CH_4 are not desirable since they may cause aging. An alternative is to replace CH_4 with CO_2. An Ar/CO_2 (90:10) mixture has a low transverse diffusion at all magnetic field strengths, but does not provide a saturated drift velocity for the typical electric fields used in TPCs (up to a few $100\,\text{V/cm}$). As a consequence, it is quite sensitive to the ambient conditions. Freon admixtures like CF_4 can be an attractive option for a TPC as well, since the resulting gas mixtures provide high drift velocities at low electric fields. However, the use of CF_4 always needs to be thoroughly validated for compatibility with all materials of the detector and the gas system.

Historically, the amplification stages used in gaseous TPCs have been planes of anode wires operated in proportional mode. The performance is limited by effects related to the feature size (wire spacing) of a few mm. Since near the wires the electric and magnetic fields are not parallel, the incoming ionisation electrons are displaced in the direction of the wires ("wire $E \times B$ effect"), which degrades the resolution. The smaller feature sizes of Micro-Pattern Gas Detectors (MPGDs) like GEMs and Micromegas lead to many advantages as compared to wire planes (see Sec. 35.6.4). In

particular, $E \times B$ effects in the amplification stage are much smaller. Moreover, the signal induction process in MPGDs leads to a very narrow pad response, allowing for a much finer segmentation, which improves the separation for two very close tracks. Combinations of MPGDs with silicon sensors have resulted in the highest granularity readout systems so far (see Sec. 35.6.4). These devices make it possible to count the number of ionization clusters along the length of a track, which can, in principle, improve the particle identification capability. However, the big challenge for such a system is the huge number of readout channels for a TPC of a typical size.

The accumulation of the positive ions created by the ionization from the particle tracks can lead to time-dependent distortions of the drift field. Due to their low drift velocity, ions from many events may coexist in the drift volume. To reduce the effect of such a build-up of space charge, Argon can be replaced by Neon as the main component of the gas mixture. Neon features a lower number of ionisation electrons per unit of track length (see 35.5) and a higher ion mobility (see 35.6).

Of greater concern are the ions produced in the gas amplification stage. In order to prevent them from entering the drift volume, large TPCs built until now have a gating grid. The gating grid can be switched to transparent mode (usually in the presence of an interaction trigger) to allow the ionization electrons to pass into the amplification region. After all electrons have reached the amplification region, it is usually closed such that it is rendered opaque to electrons and ions. For triggered operation, a combination of a MPGD and a gating structure may be an attractive solution. However, a gating grid implies a principal rate limitation to a few kHz.

A next generation of TPCs (e.g. ALICE [171], sPHENIX [175]) has been developed for applications where a triggered operation would lead to inacceptable data loss. The employed readout schemes are based on MPGDs, as these can be optimised in order to drastically reduce the ion back-flow. Extensive work has been carried out during the 2010's to design such readout structures. In ALICE and sPHENIX ion back-flow values below 1 % are achieved with a thorough adjustment of the various fields in a quadruple GEM system. Similar levels of ion back-flow can be reached with Micromegas detectors [176].

35.6.6 *Transition radiation detectors (TRD's)*

Revised July 2021 by P. Nevski (BNL) and A. Romaniouk (Innsbruck U.; MEPhI Moscow).

Transition radiation (TR) x-rays are produced when a highly relativistic particle ($\gamma \gtrsim 10^3$) crosses a refractive index interface, as discussed in Sec. 34.7. Since the TR yield is about a few % per boundary crossing, radiation from multiple surface crossings (e.g., a stack of foils) is used in practical detectors. The x-rays, ranging from a few keV to a few dozen keV or more, are emitted in a forward direction at small angles (within few mrad) to the particle trajectory. The TR intensity for a single boundary crossing always increases with γ, but, for multiple boundary crossings, interference leads to saturation above a Lorentz factor $\gamma_{\,\mathrm{sat}} = 0.6\ \omega_1\sqrt{\ell_1\ell_2}/c$ [177], where ω_1 is the radiator material plasma frequency, ℓ_1 is its thickness, and ℓ_2 the spacing between material elements. The probability density function of TR is a fairly complex function of γ, radiator parameters, photon energy (ω) and its emission angle (θ). For well defined radiator parameters a measured two-dimensional distribution of photon energy vs its reconstructed emission angle is in very good agreement with the theory predictions [178].

Integration over the angle yields the TR spectrum, which typically features many maxima (see Sec. 34.7). Most of the TR energy is emitted near the last maximum of the spectra determined by radiator material parameters at $\omega_{max} = \ell_1\omega_1^2/2\pi c$. The effective TR photon emission starts at about $\gamma_{thr} = \ell_1\omega_1/c$. By varying radiator parameters one may optimize the particle separation for a given range of the γ-factor. The angular distribution of TR photons has a few maxima and extends up to $\theta_{max} = (1/\gamma^2 + \omega_1^2/\omega^2)^{1/2}$ [179]. For a single foil the largest part of the TR

energy is emitted around the most probable angle $\theta = (1/\gamma^2 + \omega_2^2/\omega^2)^{1/2}$, where ω_2 is the plasma frequency of the gas surrounding the radiator material elements. However, in case of multiple interfaces, interference effects may significantly change this angle and more realistic expression for the angle which corresponds to the last interference maximum of the energy spectra is $\theta \approx \sqrt{1.4\pi^2/\gamma_{\rm sat}^2 - 1/\gamma^2}$ [178]. The higher is the gamma-factor, the larger is the angle of the first interference maximum. It reaches almost its asymptotic limit at $\gamma = \gamma_{sat}$. This effect is illustrated in Fig. 35.17 [178] which shows two-dimensional distribution of the TR photon energy versus the reconstructed production angle obtained in 20 GeV electron beam with the radiator containing a stack of foils of 15.5 μm thickness spaced by 210 μm (the left plot) using a Si-pixel detector. TR produced by 20 GeV electrons is emitted mostly around $\theta \sim 0.9$ mrad. All features of this distribution are well reproduced with MC simulations (the right plot).

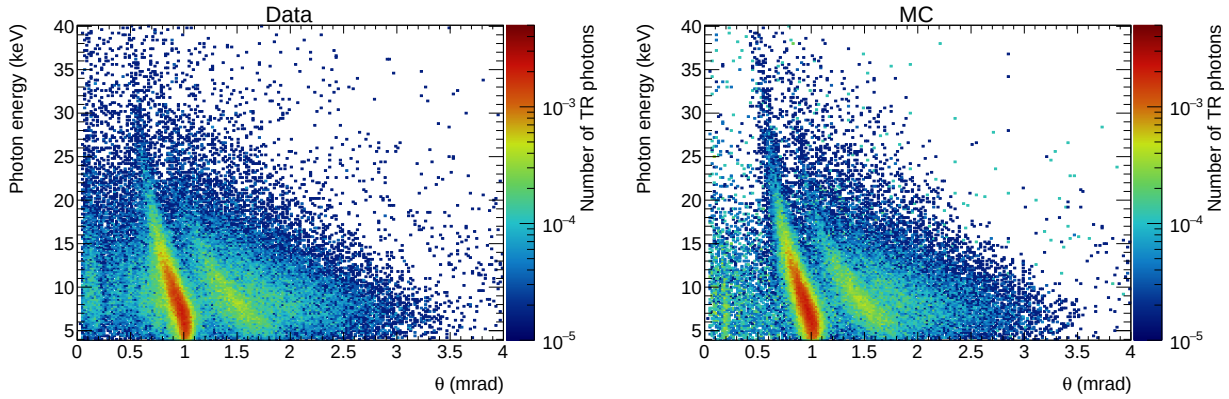

Figure 35.17: Two dimensional distributions of photon energy versus reconstructed production angle obtained with the polypropylene radiator with 20 GeV/c electron beam. Data - the left plot, MC - the right plot. Z-axis is a number of photons per particle [178]

The simplified numerical expressions can be used for practical estimation of the main TR production parameters [178]: $\theta \sim 1.2/\omega_1\sqrt{l_1 l_2}$, $\gamma_{thr} \sim 3 \times 10^3\ \omega_1\ell_1$, $\gamma_{\rm sat} \sim 3 \times 10^3\ \omega_1\sqrt{\ell_1\ell_2}$ and $\omega_{max} = 0.65\ \ell_1\omega_1^2$, where θ in mrad, ω_1 in eV, ω_{max} in keV and l_1 and l_2 in mm.

In the simplest concept, a detector module might consist of a low-Z TR radiator followed by a high-Z active layer made of proportional counters filled with a Xe-rich gas mixture. The atomic number considerations follow from the dominant photoelectric absorption cross section per atom going roughly as Z^n/ω^3, where n varies between 4 and 5 over the region of interest.[1] To minimize self-absorption, materials such as polypropylene, Mylar, carbon, and (rarely) lithium in the form of foils, fibers or foams are used as radiators. The TR signal in the active regions is in most cases superimposed upon the particle ionization losses, which are proportional to Z. In most of the detectors used in particle physics the radiator parameters are chosen to provide $\gamma_{\rm sat} \approx 3000$. Those detectors normally work as threshold devices, ensuring the best electron/pion separation in the momentum range 1 GeV/$c \lesssim p \lesssim$ 150 GeV/c.

One can distinguish two design concepts—"thick" and "thin" detectors. In "thick" detectors the radiator, optimized for a fixed total radiation length at maximum TR yield and maximum TR absorption in the detector, consists of few hundred foils (for instance 300 20 μm thick polypropylene foils). Most of the TR photons are absorbed in the radiator itself. To maximise the number of TR photons reaching the detector, part of the radiator far from the active layers is often made

[1] Photon absorption coefficients for the elements (via a NIST link), and $dE/dx|_{\rm min}$ and plasma energies for many materials are given in https://pdg.lbl.gov/current/AtomicNuclearProperties.

of thicker foils, which shifts the x-ray spectrum to higher energies. The detector thickness, about 2-4 cm for Xe-filled gas chambers, is optimized to absorb most of the incoming x-ray spectrum. A classical detector is composed of several similar modules which respond nearly independently. Such detectors were used in the UA2, NA34 and other experiments [180], are being used in the ALICE experiment [181, 182] and are built for the CBM experiment [183]. In another TRD concept a fine granular radiator/detector structure exploits the soft part of the TR spectrum more efficiently. This can be achieved, for instance, by distributing small-diameter straw-tube detectors uniformly or in thin layers throughout the radiator material. This approach allows to realise a TRD as an integral part of a tracking detector providing many points of measurements on the particle track. Even with a relatively thin radiator stack, radiation below 4 keV is mostly lost in the radiators themselves. However, for photon energies above this value, the absorption is reduced and the radiation can be registered by several consecutive detector layers, thus creating a strong TR build-up effect. Descriptions of detectors using this approach in both accelerator and space experiments can be found in [181, 184–187]. For example, in the ATLAS TR tracker (TRT), charged particles on average cross about 35 straw tube layers embedded in the radiator material [184]. The effective thickness of the Xe gas per straw is about 2.5 mm and the average number of foils per straw is about 40 with an effective foil thickness of about 18 μm. In this approach straw walls also act as radiator and make some contribution to the TR spectrum.

Although the values mentioned above are typical for most of the plastic radiators used with Xe-based detectors, they vary significantly depending on the detector requirements. Careful simulations are usually needed to build a detector optimized for a particular application. For TRD simulations the codes are based on well understood TR emission formulas (see for instance [179] for regular radiators and [188] for irregular radiators). They are realised as the stand-alone simulation programs [178,189,190] or GEANT4 based ones [191] and give both a good agreement of the TR energy spectra and of the angular distributions with data [178, 192, 193].

The discrimination between electrons and pions can be based on the charge deposition measured in each detection module, on the number of clusters – energy depositions observed above an optimal threshold (usually it is 5–7 keV), or on more sophisticated methods such as analyzing the pulse shape as a function of time. The total energy measurement technique is more suitable for thick gas volumes, which absorb most of the TR radiation and where the ionization loss fluctuations are relatively small. The cluster-counting method works better for detectors with thin gas layers, where the fluctuations of the ionization losses are bigger. Cluster-counting replaces the Landau-Vavilov distribution of background ionization energy losses with the Poisson statistics of δ-electrons, responsible for the distribution tails. The latter distribution is narrower than the Landau-Vavilov distribution. In practice, most of the experiments use a likelihood method, which exploits detailed knowledge of the detector response for different particles and gives the best separation. The more parameters are considered, the better achievable separation power. The neural network method is the most powerful tool. When it used by the ALICE TRD (ALICE point in Fig. 35.18) it lead to an increase of the rejection power by another factor of 2–3 with respect to the likelihood method [181].

The major factor in the performance of any TRD is its overall length. This is illustrated in Fig. 35.18, which shows, for a variety of detectors, the pion efficiency at a fixed electron efficiency of 90% as a function of the overall detector length. As TRD performance depends on particle energy, the experimental data in this figure covering a range of particle energies from 1 GeV to 40 GeV, are rescaled to an energy of 10 GeV when possible. Phenomenologically, the rejection power against pions increases as $5 \cdot 10^{L/38}$, where the range of validity is $L \approx 20$–100 cm. Apart from the beam energy variations, the observed scattering of the points in the plot reflects how effectively the detector space is used and how well the exact response to different particles is taken into account in the analysis. For instance, the ATLAS TRT was built as a compromise between

TR and tracking requirements; that is why the test-beam prototype result (lower point) is better than the real End-Cap TRT performance at the LHC shown in Fig. 35.18 for different regions in the detector (in agreement with MC).

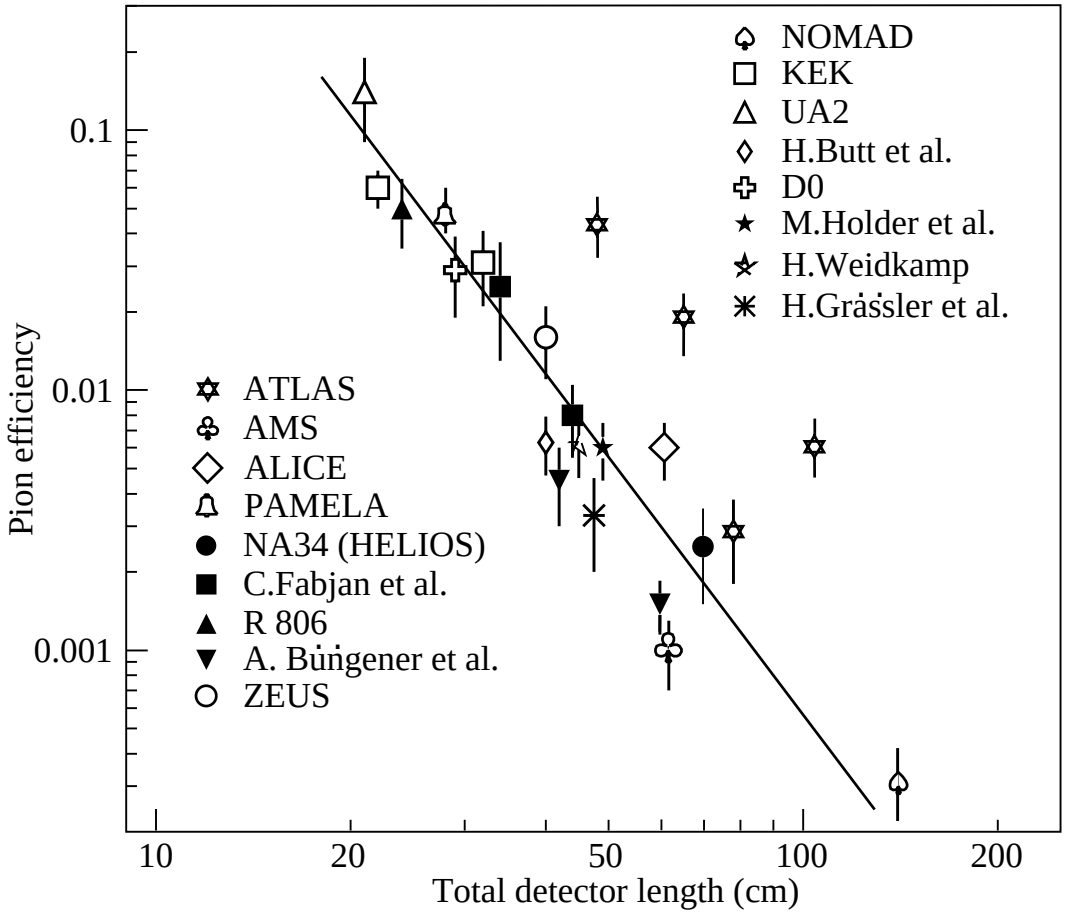

Figure 35.18: Pion efficiency measured (or predicted) for different TRDs as a function of the detector length for a fixed electron efficiency of 90%. The plot is based on the table given in [180]. Results from more recent detectors are added from [181, 185–187, 194].

In most cases, recent TRDs combine particle identification with charged-track measurement in the same detector [181, 183, 186]. This is particularly important for collider experiments, where the available space for the inner detector is very limited. For a modest increase of the radiation length due to the radiator (∼4% X0), a significant enhancement of the electron identification was obtained in the case of the ATLAS TRT. Here, the combination of the two detector functions provides a powerful tool for electron identification even at very high particle densities.

In addition to the enhancement of the electron identification during offline data analysis, TRD signatures are often used in the trigger algorithms at collider experiments. The ALICE experiment [182] is a good example for the use of the TRD in a First Level Trigger. In the ATLAS experiment, the TRT information is used in the High Level Trigger (HLT) algorithms. At increasing luminosities, the electron trigger output rate becomes so high, that a significant increase of the calorimeter energy threshold is required to keep it at an acceptable level. This may affect the trigger efficiency of very important physics channels (e.g. $W \to e\nu$ inclusive decay). Even a very soft TR cut at the HLT level, which preserves high electron efficiency (98%), allows to suppress a significant part of fake

triggers and enhance the purity for physics events with electrons in a final state. The TRT also plays a crucial role in the studies where an electron suppression is required (e.g. hadronic mode of τ–decays). TR information is a completely independent tool for electron identification and allows to study systematic uncertainties of other electron reconstruction methods.

Electron identification is not the only TRD application. Some TRDs for particle astrophysics are designed to directly measure the Lorentz factor of high-energy nuclei by using the quadratic dependence of the TR yield on nuclear charge; see, for instance, in [195]. The radiator configuration (ℓ_1, ℓ_2) is tuned to extend the TR yield rise up to $\gamma \approx 10^5$ using the more energetic part of the TR spectrum (up to 100 keV). High density radiator materials (such as Al) are the best for this purpose. Direct absorption of the TR-photons of these energies with thin detectors becomes problematic and TR detection methods based on Compton scattering have been proposed, see in [196].

The high granularity of the semiconductor pixel or microstrip detectors provides spatial separation of the TR photons and dE/dx losses at relatively modest distances between radiator and detector. These detectors may be the basis for novel devices which combine precise tracking and PID properties [178,190,197]. Use of the TR production angle in addition to its energy can help to improve PID properties of the TRD. The presence of a magnetic field could enhance the separation between TR photons and dE/dx losses [198]. New detector techniques for TRDs are also under consideration. GasPixel detectors allow to reconstruct a track segment with a space point accuracy of < 30 μm and exploit all details of the particle tracks to highlight individual TR clusters in the gas, see in [199]. Thin films of heavy scintillators might be a very attractive option for non-gas based TRD [200].

35.6.7 *Resistive-plate chambers*

Revised August 2023 by G. Aielli (Rome U. Tor Vergata).

The resistive-plate chamber (RPC) is a gaseous detector working at atmospheric pressure developed by R. Santonico and R. Cardarelli in the early 1980's [201]. A precursor of the RPC was the Pestov spark chamber [202] [203], which had a metallic plate cathode and a thick glass plate anode, designed to work at 12 bar to obtain an outstanding 0.1 ns time resolution. Although the original purpose of RPCs was to provide a competitive alternative to large scintillator counters, the RPC's potential for timing tracker systems was quickly recognized given its high detection efficiency (>95%), excellent temporal and spatial resolutions and ease of constructing large-format single frame detectors. The RPC, as sketched in Fig. 35.19, is a large planar capacitor with two parallel high bulk resistivity electrode plates (10^9–10^{13} Ω·cm) separated by a set of insulating spacers. The spacers define a gap in the range from a few millimeters down to 0.1 mm with a precision of a few μm. The gap is filled with a suitable atmospheric-pressure gas mixture which serves as a target for ionizing radiation. The gas gap thickness practically determines the time resolution of the RPC. On the other hand, the limit for reaching full detection efficiency at atmospheric pressure is typically 1 mm (also influenced by the gas molecular weight). Since the primary ionization released in sub-millimeter gas gaps is limited, multiple gaps can be combined to effectively obtain a very high detection efficiency [204]. The electrodes are most commonly made of high pressure phenolic-melaminic laminate (HPL), commonly referred to as "bakelite", or soda-lime glass (glass from now on), having a lower resistivity than borosilicate glass. An uniform electric field of several kV/mm is established on the gas gap, sufficient to promptly start an avalanche multiplication of the primary electrons. The electric field is typically applied through a moderately conductive ($\sim 10^5 to 10^8$ $\Omega/\Box$) graphite varnish, forming an ohmic contact with the external faces of the electrodes. Its conductivity is sufficiently low to be transparent to the fast avalanche signal transients, and high enough to suppress surface voltage gradients arising from the working current flowing in it. Due to the high electrode resistivity in RPCs, the time constant of the equivalent RC circuit

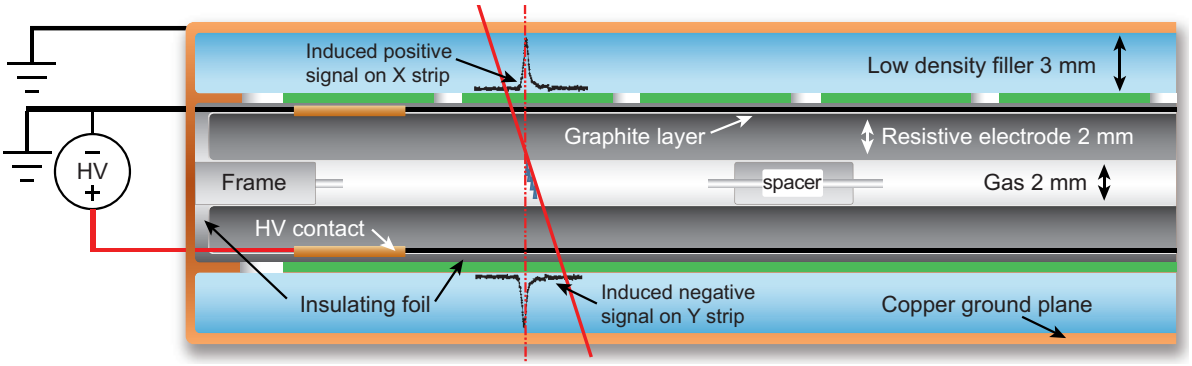

Figure 35.19: Schematic cross section of a generic single gap RPC.

($\tau = \rho\epsilon_r$ being ρ the electrode resistivity and ϵ_r its dielectric constant) is much longer than the discharge processes duration. Therefore only the locally-stored electrostatic energy contributes to the discharge, preventing the formation of sparks and leaving the rest of the detector field unaffected. The gas-facing surface of HPL electrodes are commonly coated with a few μm-thick layer of polymerized linseed oil [205] with the function of smoothing the electrode surface, improving the electric field uniformity. Glass-based RPCs don't require such treatment. It also has the function of protecting the electrode from the being eventually etched by free radicals generated in the discharge e.g. in presence of fluorocarbons. In RPCs the gaseous target and the multiplication region coincide. In the early stage of the avalanche multiplication the uniform electric field exponentially amplifies each primary ionization cluster, as the avalanche progresses away from the location of the primary ionization. Since the ionization clusters generated by the incident MIP are randomly distributed along the ionizing particle track, for low gains the observed RPC charge spectrum is broad and approximately exponentially distributed[2] with the mode close to zero. Because of this, it is difficult to separate noise from signals using a discrimination threshold. This is not the case in gaseous detectors where ionization and amplification occur in separate regions.

For increasingly larger avalanches, the space-charge progressively saturates the avalanche growth from exponential to almost linear, producing a peaked charge spectrum, essential to efficiently separate the signal from the noise [207]. For large gains[3] the avalanche, with increasing probability, onsets a transition to "streamer" [208], a plasma filament connecting the electrodes, depleting all the locally-available energy [209], and generating an almost fixed amplitude signal. This prevents any further evolution of the discharge. This streamer mode was the first ever used by RPCs, until the introduction of very electronegative gases and more sensitive front end electronics made it possible to detect the precursor avalanche independently on the streamer [210, 211] Any of this operating regimes can be used in RPC detectors, depending on the application.

As with other gaseous detectors, the gas mixture is optimized for each specific application. In general it needs to contain a UV photons quencher suppressing the photon-mediated feedback that can lead to self generated after-pulse discharges, and one or more electronegative components, to extend the avalanche growth, free from streamers, to as high as possible electric fields [212]. The addition of small fractions of electronegative molecules with a very high capture cross section for slow electrons, such as SF_6, was proven to inhibit the transition to streamer over a wide electric field range. Even though there is not yet an accepted and robust avalanche-to-streamer-transition model, this effect is commonly explained as a delay in the growth of the electron density of the avalanche front, which perturbates the electric field driving the transition to streamer. As a reference, the mix-

[2] An analytic treatment of the low gain avalanche process shows that the charge distribution is well described by the Γ function [206]

[3] A multiplicity of the order of 10^8 electrons is classically referred as Raether/Meek limit for on-setting a streamer

ture for stable avalanche operation in ATLAS and CMS is $C_2H_2F_4$/i-C_4H_10/SF_6=94.5%/5%/0.3%.

The avalanche induces a fast electron signal on a set of metallic readout electrodes (e.g. pads or strips) commonly placed externally and insulated from the resistive electrodes. The signal is isotropically distributed with respect to the field direction and present with equal but opposite amplitude on both electrodes. Thanks to these features, performances of the readout electrodes on both RPC sides are equivalent. The induced charge density distribution can be ideally calculated for a simplified RPC model [213] [214] as: $\sigma(x) = A/\cosh[(r)/\delta]$ where A is a normalization constant, r is the distance from the center of the avalanche axis and $\delta = (g + 2d)/\pi$ depends on the gap and electrode width (g and d, respectively). Depending on the specific RPC layout and geometry, the interplay between conductive coating and pick-up electrodes typically broadens, by means of a diffusion-like process (see [214] [215]). This effect mostly preserves the information on the avalanche position, which can be obtained using the charge centroid method, with the drawback of increasing the signal space occupancy. Sensitivity to the high-frequency spectrum of electron avalanche signals over large RPC areas requires a correspondingly adequate Faraday cage and readout design. At the same time, to preserve the excellent timing features of the RPC signal, the front end electronics should have a short rise time (ideally $\ll$ than the signal rise time) and low noise, although these requirements could be in competition [216].

35.6.7.1 *RPC types and applications*

RPCs are generally classified in two categories depending on the gas gap structure: single gap RPCs (described above) and multiple gap RPCs [204] (typically referred as MRPCs). While they are both based on the same principle they have different construction techniques, performance and limitations, making them suitable for different applications. Due to its simplicity and robustness, the single gap RPC is ideal for covering very large surfaces. Typical detector systems can have sensitive surface areas up to $\sim 10^4$ m^2, with single module areas of a few m^2, and a space-time resolution down to $\sim$0.4 ns $\times$ 100 μm [217] [218]. Representative examples are the muon systems of ATLAS [219] and CMS [220] or ground and underground based cosmic rays [221] and neutrino arrays [222]. It is interesting to note that CMS implemented a bi-gap structure, i.e. the pickup signal is sandwiched by 2 single gas gaps, both contributing to the signal induction, improving efficiency and time resolution with respect to the single gas gap. Relevant new trends for single gap RPC applications are represented by new Dark Matter search experiments such as CODEX-B [223] and ANUBIS [224], in both cases exploiting RPCs to enclose and instrument large detection volumes with a good space-time tracker. Single gap RPCs have also recently demonstrated good candidates for application in tracking calorimetry [225].

The MRPC [226], as sketched in Fig. 35.20, segments the gaseous target by means of a stack of floating glass electrodes separated by a monofilament (i.e. fishing line) sandwiched between two external electrodes providing the high-voltage bias. Since the current flowing in between the gas gaps must be in average equal, the difference of potential between each couple of adjacent floating electrodes will tend to be the same. An extensive description can be found in [227]. It has been observed that higher time resolution is inversely correlated to the gas gap size, so this configuration allows for smaller gas thicknesses while maintaining a sufficient total gas thickness. This tends to separate primary clusters avalanches in different gas gaps, treating them independently, and determines a shorter avalanche growth time, increasing time resolution by one order of magnitude with respect to the classic RPCs [228]. The mechanical fragility of sub-mm-gap structures makes this technique less suitable for very large detector areas. Moreover the only material nowadays practically suitable for building such structures is soda-lime glass with resistivity above 10^{12} Ω·cm, limiting the rate capability to about 500 Hz/cm^2 [229].

MRPCs have been largely used in Time Of Flight systems such as ALICE [230], HADES [231],

FOPI [232] and BESSIII [233], and in applications such as timing PET [234]. In perspective MRPC will be used for upgraded and new nuclear physics experiments such as CBM@FAIR [235] and SoLID [236].

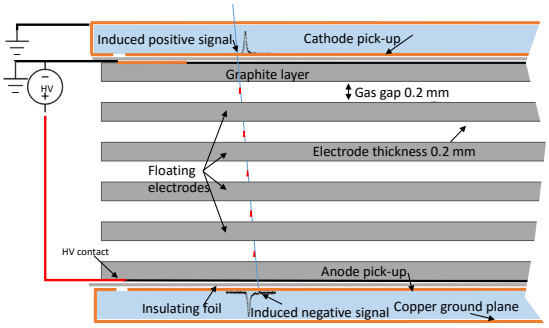

Figure 35.20: Schematic cross section of a generic multi gap RPC.

35.6.7.2 *Time and space resolution*

Space-time uncertainties in RPCs are determined by the statistical fluctuations of the primary and secondary ionization, the avalanche multiplication rate, which is a function of the electric field, and on the Signal/Noise ratio of the front end electronics. The intrinsic signal latency is commonly in a few ns range (avalanche growth time to produce a detectable signal), making the RPC suitable for applications where a low latency is essential.

The gas gap size is a crucial feature for the RPC timing performance: producing the same total charge (for a detectable signal) in a smaller gas gap implies the necessity of increasing the first Townsend coefficient by increasing the electric field, reducing at the same time the total signal duration and the related time fluctuations; moreover the chance of having multiple clusters in the same gas gap decreases with the gap size, suppressing the charge collection fluctuations [237], due to the unknown distance in between the clusters. This chance becomes necessarily higher along with the intrinsic efficiency of the single gas gap. Typical timing performances range from around 1 ns with a 2 mm gas gap, down to 20 ps for a stack of several 0.1 mm gaps [238].

The intrinsic position sensitivity of an RPC is in the range of tens of μm depending on the lateral spread of the avalanche induced charge distribution, influenced also by the gap size. In typical RPC applications the pick up electrodes pitch L ($\sim$1 cm) is much broader than the intrinsic resolution, and being readout via a discriminator, the spatial resolution is geometrically limited in the range of $\mathrm{L}/\sqrt{12}$. A much better result is obtained by using a finer electrodes granularity and measuring the charge in each strip collecting the avalanche charge, so to reconstruct the charge centroid. It has been demonstrated, through charge centroid techniques, that the RPC avalanche space-time localization can be as good as $\sim$50 ps $\times$ 40 μm [239] [240].

35.6.7.3 *Rate capability and ageing*

RPC rate capability is limited by the voltage drop on resistive electrodes, $\Delta V = V_{\mathrm{a}} - V_{\mathrm{gas}} = I \cdot R$ [241]. Here V_{a} is the applied voltage, V_{gas} is the effective voltage on the gas, $R = \rho \cdot d/S$ is the total electrode resistance, ρ being the resistivity and d,S the sample thickness and surface respectively, and I is the working current. Assuming uniform irradiation we can express $I = \phi \cdot S \cdot \langle Q \rangle$ where ϕ is the particle fluence and $\langle Q \rangle$ is average charge per avalanche. So we obtain a state equation for the RPC rate capability:

$$\Delta V/\phi = \rho \cdot d \cdot \langle Q \rangle$$

A large I not only limits the rate capability but also affects the long term performance of the detector since the working current, associated to discharges, depletes the conductive properties of HPL electrodes [242]. In presence of fluorocarbons and water, discharges generate hydrofluoric acid (HF) and other fluorinated compounds, which damage internal detector surfaces, especially if made of glass, known to be not resistant to HF [243]. The practical way to suppress HF formation in glass RPCs is preventing water vapor contamination. Conversely, HPL electrodes, coated with linseed oil, are relatively resistant to HF, but the presence of water can not be avoided since it mediates the HPL conduction. In this case the HF damage is mitigated by removing it with a forced flow of gas through the gas gap.

Operating in the streamer regime places low requirements on the front end electronics sensitivity, but generally limits the counting rate capability to ∼100 Hz/cm^2. Higher-rate operation can be achieved by reducing gas gain in favor of electronic amplification, operating the detector in avalanche mode. Increasing concentrations of electronegative gases, such as $C_2H_2F_4$ and SF_6 [212], shifts the streamer transition to higher gains, thus the avalanche signal can access an higher dynamic range, which puts further stress on the performance request on the front end electronics. By further lowering the avalanche mode gas gain compatibly with the front end performance, efficient and stable performance at high rates (e.g. 10 kHz/cm^2) has been achieved for large area single gap RPCs [216]. Two complementary strategies rely either on the natural redundancy and higher signal yield of multiple micro gap structures [244] or on electrodes made with lower resistivity materials [245]. Lowering the electrode resistivity in presence of high uniform field is increasingly difficult, since high resistivity limits the appearance of larger discharge events and increase of spurious counts, favoured by the effect of local electrode defects on the field gradient. In this case, to safely lower the electrode resistivity, a safety margin would be given by operating with a lower electric field, and a correspondingly lower average charge per count.

35.6.7.4 *Alternative gas mixtures*

The standard gas mixture mentioned above is based on Hydrofluorocarbon (HFC), specifically the R134A, extensively used in the refrigeration industry. R134A features matches very well the RPCs performance requirements. It has high density that results in high primary ionization. It is electronegative, which limits secondary discharge phenomena. It is not flammable, and it has a limited degradation if exposed to UV photons due to the absence of saturated bonds. This last feature permits high rate operation, limiting the ageing effects due to the byproducts of the avalanche discharges. However, this gas has a Global Warming Potential (GWP) of 1450 thus it is not considered anymore a viable option for future industrial applications. Therefore, since a few years the RPC community is researching alternative gases [246, 247] to replace R134A, focusing on the Hydro-Fluoro-Olefins, a category of gases recently proposed for industrial applications. HFOs exhibit important limitations with respect to HFCs, if used in high concentrations. In particular its much higher electronegativity implies an impractically high applied electric field for the existing RPC systems, and a much higher charge per count due to a large fraction of negative ions produced by electron capture, which do not contribute to the prompt signal. A further side effect is a larger production of fluoride ions by UV decomposition of the gas. To contrast the ageing acceleration drive represented by the phenomena stated above, the proposed strategy was to largely dilute HFO whih a neutral gas, such as CO_2, compatibly with keeping an enough dense gaseous target, and whenever possible, operate at a lower gain by using very performing front end electronics. A representative example of the several variants tested [248] is $CO_2/C_3H_2F_4$/i-C_4H_{10}/SF_6=59%/35%/5%/1%. This mixture with a large fraction of CO_2 is suitable for thicker (2mm) gas gap. The presence of CO_2 in 1 mm gas gaps lower the amount of primary electrons thus practically limiting its fraction to no more than 30%. Thus for a safe operation a reduction

of the charge per count by an order of magnitude is necessary to compensate the stronger ageing phenomena. It has to be noted that the research in this field is recent and very intensive [249,250], so relevant updates are expected in future.

35.6.7.5 *A new detector: the **R**esistive **C**ylindrical **C**ounter*

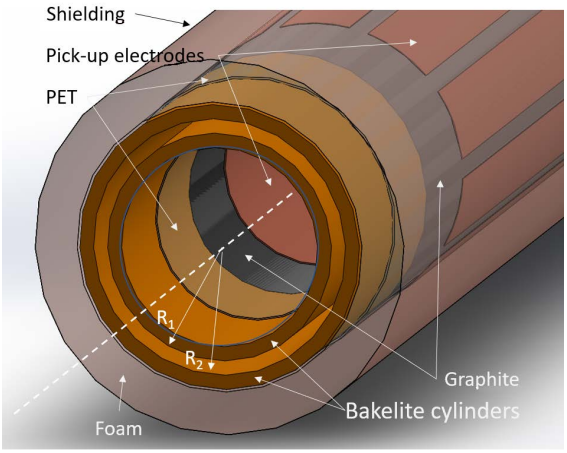

Figure 35.21: Schematic drawing of an RCC.

The RCC, illustrated in fig. 35.20, has been recently proposed as an evolution of the RPC [251] and is essentially an RPC warped to a cylindrical shape. The idea is to combine the advantages of parallel plate geometry and high pressure drift tubes in a single detector. The electric field $E(r)$, which is uniform in RPCs, here depends instead on the distance from the axis r, according to $E(r) = -\frac{V}{r\ln(R_1/R_2)}$. By choosing appropriate values for R_1, R_2, V and its polarization (the innermost cylinder is the cathode), it is possible to virtually segment the cylindrical gap in a innermost sensitive layer, where the field is sufficiently high to start the avalanche multiplication, and an outermost layer where the drift happens, increasing the induced signal with lower or no multiplication at all. This effect is called geometrical quenching and limits the avalanche growth without the necessity of electronegative gases. Moreover a geometrically quenched avalanche would have a much better prompt to total charge ratio, lowering the total operative current, hence increasing the rate capability. The cylindrical structure has a further major advantage with respect to the planar one, it can be easily pressurized overcoming the RPC limitation of working at atmospheric pressure only. Pressurization on one side increases the gaseous target density, thus increasing the efficiency of narrow gaps, on the other, it could largely improve RPC time resolution since the Townsend coefficient $\alpha = A\ p \cdot \exp(-Bp/E)$ (where p is the pressure, E the electric field and A,B are constants), as we learn from the RPC precursor, the Pestov spark chamber [203]. The performance of the RCC concept in terms of time resolution and counting rates are yet to be demonstrated. On the other side, being insensitive to the environmental pressure, potentially extends its range to space and under water applications.

35.7 LAr Time Projection Chamber

Written in October 2021 by F. Pietropaolo (CERN; INFN, Padova) and S. Pordes (FNAL). Revised in August 2023 by A. Fava (FNAL) and F. Pietropaolo (CERN; INFN, Padova).

35.7.1 *Introduction*

Liquid argon is an attractive material for particle detection. Some properties of argon are given in table 35.8; for many more see [252]. Energy deposition in the argon produces scintillation light

Table 35.8: Some physical properties of liquid argon from [253].

Property	Unit	Value
Boiling Point *(BP)* at 1013 hPa	K	87.3
Density (ρ) at 1013 hPa	kg m^{-3}	1395
d*(BP)*/dP	K hPa^{-1}	9×10^{-3}
dρ/dT	kg m^{-3} K^{-1}	-6.2
Latent Heat of Evaporation	kJ kg^{-1}	161
Freezing Point (1013 hPa)	K	83.8

and ionization electrons; in the presence of a moderate electric field, a significant fraction of the electrons escape recombination, making them available for detection as a charge signal. Typical values for a minimum ionizing particle are $\sim$ 40,000 photons/MeV at zero field (lower at finite fields) and $\sim$ 30,000 electrons/MeV at a field of 500 V/cm. That the liquid has a relative density of 1.4, that the free electrons can be drifted many meters with minimal dispersion and that it is abundant in the atmosphere and commercially available as a by-product in the distillation of air to produce nitrogen and oxygen, makes it particularly attractive for use in massive time-projection chambers (TPC) to study rare processes, as realized in [254] and [255]. Since that time, the liquid argon TPC (LAr TPC) has been developed into a detector that combines mm^3 resolution with particle identification, calorimetry, and 100% live time. Detectors with masses up to 600 tons have been built and operated and detectors of 10's of kilotons are being planned.

The operation of a liquid argon time projection chamber requires

1. a cryostat and cryogenic system to maintain ultra-pure liquid argon clean and stable,
2. an electric field that permeates the liquid argon volume and allows ionization electrons to escape recombination, and drifts them to the charge sensors,
3. an array of charge sensors and associated electronics to amplify and digitize the charge signals,
4. sensors to detect the scintillation light and associated electronics,
5. a data-acquisition system to read out and record the data,
6. software to reconstruct and interpret the data.

Surveys of previous, present and proposed detectors are described in the literature [256] [257] and in detailed descriptions of detectors which have operated in experiments [258–264]. This article provides a description of the challenges in achieving items 1 to 4 with some of the solutions presently adopted. Topics 5 and 6, crucial to the successful exploitation of the LAr TPC technology and subject of intense activity, are also introduced [265–267]. References are also given for a number of ancillary devices - cameras that can operate in the liquid argon [264], monitors to provide a rapid measurement of the purity of the argon [268, 269], ionization lasers to measure distortions of the drift field due to space charge or electrical problems [270] - that have been developed to improve performance. A list of experiments with their masses is also given in 35.14.

35.7.2 *A Mass of ultra-pure Liquid Argon*

Argon is commercially available in large quantities as a by-product in the distillation of air to produce liquid nitrogen and oxygen. Critical to any LAr TPC are the cryostat and the cryogenic and purification system to maintain the argon liquid, ultra-clean and stable in temperature and pressure. Evacuable double-walled vacuum cryostats are practical for detectors with a mass of O(100) t. Based on the demonstration that ultra-clean argon can be achieved without initial evacuation [269], current and proposed larger detectors are hosted in foam-insulated non-evacuable

cryostats based on a technology used in liquefied natural gas transport [264]. A convenient feature of these cryostats is that their components (inner walls, insulation, outer structures) are modular and of a size suited to assembly in underground environment. In addition, passive insulation is intrinsically safer than vacuum insulation because the heat input cannot rapidly increase as in the case of vacuum degradation.

The absence of electronegative contaminants, mainly environmental oxygen and water, from the liquid argon is crucial to ensure the ionization electrons drift from their point of production to the charge sensors without being captured (the drift motion of the produced negative ions is too slow to be detectable). The 'electron lifetime', τ, is the parameter describing the purity level of argon. To set a scale, the electron capture time in liquid argon with a concentration of oxygen of 0.1 ppb (part per billion by volume - all concentrations here are by volume) is $\sim$ 3 ms [271, 272], largely independent of electric field in our range of interest. For detectors with electron drift times in the milliseconds, the oxygen level must be well below 0.1 ppb to avoid losing most of the signal. In order to achieve this goal, first the air is removed from the cryostat volume mostly by controlled purging with argon [273], allowing to reach ppm purity levels; a purification system is then required during filling, to purify the commercial argon delivered from its typical ppm oxygen and water levels. Molecular sieve and activated copper on alumina [274] are commonly used to remove water and oxygen, respectively. This purification is performed in the liquid phase and the discovery that purification with standard materials is effective at cryogenic temperatures [275] allowed for an enormous gain in throughput compared to purification in the gas phase. The purification system delivers essentially pure argon - which then mixes with contaminants from outgassing or residual leaks. To avoid the build-up of contaminants, both the boil-off gas and the liquid are continuously recirculated through the purification system. Schematics of experiment cryogenics systems are shown in [259, 261, 264]. While reconstructed tracks eventually determine the argon quality, so-called 'purity monitors', double-gridded ionization chambers, are often installed to give rapid feedback on the purity of the liquid [264].

Another potential contaminant is environmental nitrogen. This does not affect the free electron lifetime at levels up to many ppm but it does affect light production [276] and transmission [277] at the few ppm level.

35.7.3 *Charge and Light Signals*

Figure 35.22 (left) shows how the electron and scintillation yields for a minimum ionizing particle (m.i.p.) change with electric field. The free electron yield from the passage of a charged particle can be calculated from 'W_{el}' = 23.6 eV [278], the energy deposit that generates one ion-electron pair, the dE/dx of the particle, and 'R' the (unfortunately labeled) fraction of electrons that escape recombination - see figure 35.22 (left). Measurements of electron yield have been made at various electric fields and at different ionization densities [279–283] and show good consistency. Of the models proposed to predict recombination [284, 285], none is fully successful; the so-called 'box model' [286] which considers the situation of mobile electrons and stationary ions makes more realistic assumptions than other models and it is commonly used [287]. The data from [282] which are some of the most comprehensive are described by the form $R = \frac{0.8}{(1+0.049(dE/dx)/\mathcal{E})}$ where dE/dx is in MeV/cm and $\mathcal{E}$ in kV/cm. At a drift field of 500 V/cm, The recombination factor R for a minimum ionizing particle is 70%. A comprehensive summary and analysis of charge yield is given in [288].

The movement of the free electron charge towards the charge sensors is characterized by the drift velocity, the charge loss due to impurities, and the diffusion. The drift velocity depends on the strength of the electric field and slightly on the argon temperature (see table 35.9); a measurement of drift velocity vs electric field from [289] with a fit from [290] is shown in 35.22 (right). At an

electric field of 500 V/cm, the drift velocity is 1.55 m/ms at 89 K. The charge loss depends on the purity of the liquid. For a drift of duration, t, the fraction of charge that survives to the sense electrodes is $e^{-t/\tau}$ where τ is the electron lifetime. Values of τ exceeding tens of ms have been achieved [291–293]. Diffusion broadens the charge distribution as it travels to the sensor. The diffusion coefficient, D, defines the contribution to the spatial distribution of the charge at the sensor from diffusion after a drift of time, t, via $\sigma_D^2 = 2Dt$. Several measurements of the longitudinal diffusion component, D_L, have been made with a typical value around 0.4 mm^2/ms [281,294–296]. For a 3 ms drift, this gives a contribution of $(0.4 \cdot 6)^{1/2}$ mm, $\sim$ 1.5 mm, to the spread of the charge.

Table 35.9: Some Detector Relevant Properties of liquid argon.

Property	Unit	Value
Stopping Power (m.i.p.)	MeV g^{-1} cm^2	1.51
Radiation Length	g cm^{-2}	19.6
Nuclear Interaction / Collision Length	g cm^{-2}	120 / 76
W_{el}, Energy to form one electron-ion pair	eV	23.6 ($\pm$0.3) [278,297]
Ion mobility	cm^2 V^{-1} s^{-1}	1.6 $\times 10^{-3}$ [298]
Temperature dependence of drift velocity	% K^{-1}	-1.7 [290]
Longitudinal diffusion coefficient, D_L	mm^2 ms^{-1}	0.4 (see text)
W_{ph}, Energy to produce one scint. photon	eV	25 [299,300]
Scintillation photon wavelength (vacuum)	nm	128 $\pm$8 (FWHM) [301]
Scintillation light inverse velocity	ns m^{-1}	7.46 ($\pm$0.08) [302]
Rayleigh scattering length (predicted)	m	0.9 ($\pm$0.2) [302–304]
Scintillation Decay times fast/slow	ns	6 ($\pm$1)/1500 ($\pm$100) [276,305,306]
Dielectric strength	kV cm^{-1}	>40 [307,308]

The scintillation light comes from the decay of excited argon dimers, Ar_2^*, (excimers) produced through direct excitation and through recombination of ionized argon ions and electrons [309]. The contribution of the latter process is reduced in the presence of an electric field as shown in figure 35.22, (left). The excimer is produced either in a singlet ('allowed' decay) or in a triplet spin state ('forbidden' (spin-flip) decay), with lifetimes of 6 ns and 1.5 μs respectively. The states are almost degenerate and photons are emitted, somewhat inconveniently [310], in the VUV with a spectrum peaked at 128 nm with a $\pm$8 nm (FWHM) spread [301]. The relative populations of the two states depends on the ionization density; typically 1:3 (singlet:triplet) for minimum ionizing and 3:1 for highly ionizing nuclear fragments [305]. The long lifetime of the triplet state makes it sensitive to quenching impurities such as nitrogen or oxygen to which the excitation energy of the dimer can be transferred without the subsequent emission of a visible photon [276,311].

The propagation of the scintillation is affected by two processes: absorption and Rayleigh scattering. While the large Stokes shift [312] makes pure LAr transparent to its own scintillation light, methane at the few ppb level [313] and nitrogen at the few ppm [277] level lead to light absorption. Rayleigh scattering increases the effective travel distance of photons between their production point and their detection and for detectors where the distance between origin and detection covers a range of many meters, the short Rayleigh scattering length for argon scintillation has a serious effect on the uniformity of detection. In this situation, the long lifetime of the triplet state can be exploited by the use of dopants to which the argon dimers can transfer their excitation energy with subsequent photon emission. Xenon, where almost complete transfer of the long-lived state energy is achieved at a concentration of 10's of ppm (mass), is a leading candidate. [314,315].

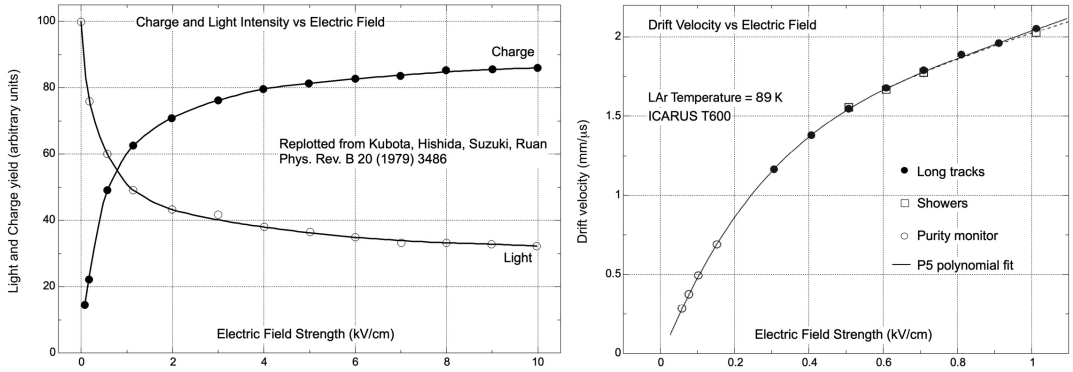

Figure 35.22: (*left*) the form of the light yield and the charge yield vs electric field redrawn from [309]; (*right*) electron drift velocity vs electric field redrawn from [289].

35.7.4 *LAr TPC topologies*

Currently operating LAr-TPC detectors come in a range of sizes but the basic form of a cathode and field cage generating a field which drives the ionization electrons to planes of charge sensors at ground potential is universal. A standard criterion is to make the TPC drift as long as considered possible to maximize the detector mass for a given channel count; this can result in a single drift volume; two drift volumes with a common cathode, or multiple drift volumes with multiple common cathodes. An exception is the DUNE near detector TPC; it is segmented into many small TPCs to help resolve the large interaction rate [316].

The drift field is produced by a planar cathode at -HV, a graded field-cage surrounding the active volume, and the sensing electrodes at a potential near ground which form the anode. The field cage is designed to produce a uniform electric field throughout the drift region although for detectors at surface, the slow-moving positive ions generated by the flux of cosmic rays distort the field, particularly for TPCs with long drift [288, 293, 317–319]. Particular challenges in the drift field system are the feed-through [259, 320] that brings the voltage from the HV supply outside the cryostat to the cathode (the cathode can sit at negative voltages up to 300 kV), avoiding damage to the electronics from a potential cathode discharge [264], and ensuring the integrity of the field-cage resistor chain [321]. Avoiding discharge and current draw in a medium chosen because it allows electron flow is possibly the hardest challenge in the technology.

The schematics in figure 35.23 shows the sensor arrangement using vertical planes of wires as sense electrodes and a horizontal electric field. The sense planes are perpendicular to the drift direction and can be arranged in a stack with the wires in each plane oriented at a different angle. While the schematic shows three planes, in principle only two are needed; however three views are useful in the 3D reconstruction procedures to remove ambiguities in the hit associations and in case of dead or noisy channels. The wire-pitch, p, is a few mm and the plane spacing is similar. As indicated in figure 35.23, the planes are biased such that all field lines from the drift region pass through the intermediate planes and terminate on the final plane as shown in 35.23. (The condition for transparency across one plane is derived in [322].) The drift electrons follow the field lines, inducing bi-polar current pulses on the first two planes, and terminate on the last one, the collection plane, producing a unipolar signal [323].

The raw signal rise and fall times are a few μs as determined by the electron drift velocity and the plane spacing, and any geometric effects from the track angles. The signals from each wire are recorded as wave-forms spanning the maximum drift time at typically 2 or 2.5 MHz sampling rate. The intersection of wires on different planes which record signals at the same time, and the drift

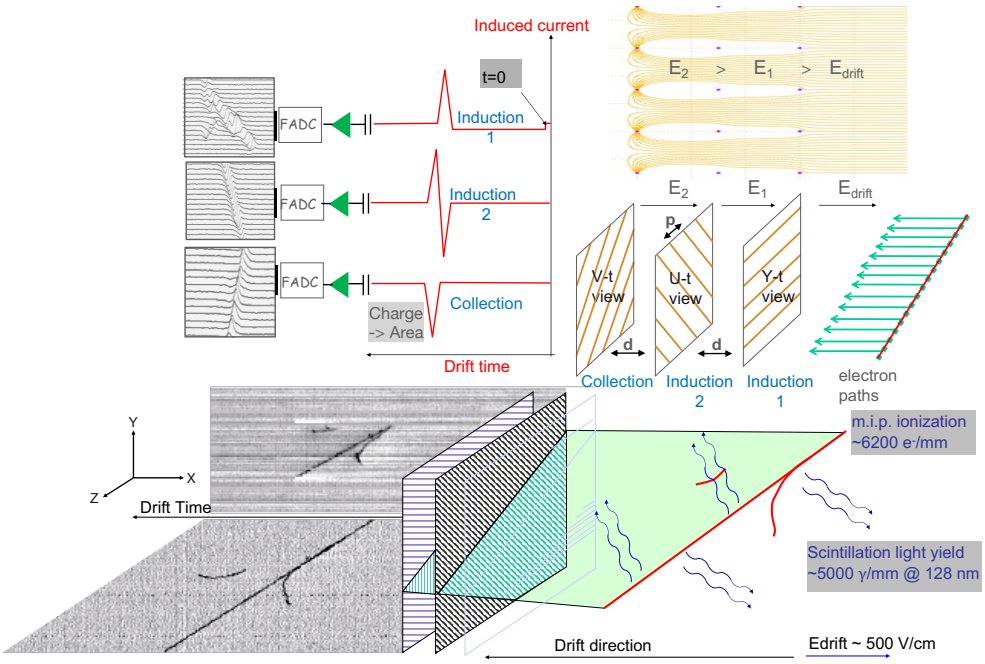

Figure 35.23: Schematic of an event in the ICARUS 3 t LAr TPC; *Top (from right to left)*: field lines from drift region to collection wires, electron flow & arrangement of wire-planes, signal shapes on the wires, and wave-forms from the continuous readout and digitization; *Bottom*: the passage of a muon. The gray scale on the track indicates the ionization density.

time converted to a distance knowing the drift velocity give the position of the charge source.

The design of large (> kiloton) detectors faces an intrinsic electrical challenge in that long (> few m) cables from the sense electrodes to the first-stage amplifier will introduce an unacceptable amount of noise through their capacitance, and attempts to avoid such cables leads to impractical constraints on the charge sensor geometry; both of these are emphasized in [323]. To address this problem, CMOS based ASIC amplifiers that operate in the cold and can be placed next to the charge sensor (wire or strip or pixel) have been developed, their design rules and robustness validated, and successfully deployed [324, 325]. The subsequent problem that individual feed-throughs for each signal in a detector with hundreds of thousands of channels complicate the cryostat structure and raise the specter of leaks has been resolved by the development of flash-ADC and signal multiplexers [326] that also operate in the liquid. These implementations have resulted in equivalent noise charge levels of a few hundred electrons [293, 327] to be compared with a charge yield for a m.i.p of 30000 e/MeV or, equivalently, 60000 e/cm. With such low noise, energy depositions well below 1 MeV on wires/pixels with 0.5 cm pitch or less are quite accessible.

Large LAr detectors usually contain a system to detect the primary scintillation light. These provide an event time for drift time measurement [328], a trigger [329, 330], calorimetry that can be independent of and complementary to the charge [293], and event position information [265]. Given the VUV nature of the scintillation, a wavelength shifter is typically used to move the light into the visible [310]. Photo-multiplier tubes that operate in liquid argon were developed under the ICARUS program [331], while some recent systems are based on Silicon Photo-Multipliers. This latter approach separates the light collection from the light-to-electrical signal transducer, and many designs for the first task are being pursued [264, 332, 333].

35.7.5 *Data Acquisition and event reconstruction*

For the operation of large mass LAr-TPCs, the recording and storage of large volumes of data from the digitised charge waveforms and scintillation light channels is a critical issue. For instance, in the DUNE experiment, the throughput will amount to 1.5 TB/s per detector module (10 kt fiducial mass). To cope with, data reduction strategies are typically applied [334], [335]: (1) channel by channel zero suppression applied to the digitised wave forms, (2) fast signals from photon detectors or from external sources (for instance a neutrino beam), to trigger the readout of the TPC over a limited, predefined time window. The trigger rate is tuned to match the throughput capabilities of the Data AcQuisition (DAQ). Recent advances in communication and computing technologies have reshaped the approach to DAQ for LAr-TPCs. It is now possible to readout the complete digitised data and process them online [336], [337], allowing to identify space-time Regions of Interest (RoI) where charge or light activity is detected. For the DUNE experiment, the data reduction could be in the order of 10^5. With this architecture, charge and photon detectors become truly complementary and their information can be combined online for high efficiency data filtering even for energy depositions at a few MeV scale.

The goals of LArTPC event reconstruction are to provide the building blocks necessary to perform physics analyses: reconstruct the event topology, particle identification and calorimetry. Generally, this proceeds in subsequent stages. (1) Signal Processing: the waveforms providing a measure of the charge deposited in the TPC as a function of time are conditioned to mitigate detector issues, suppress noise, deconvolve the detector/electronic response; this allows to produce hit objects - measurements of the drift time and charge deposited by tracks in the LAr active volume on any readout channel [338] [339] [340]. (2) Wire readout LArTPCs produce 2D images in drift time and coordinate transverse to the wire direction with, generally, 3 planes allowing for stereo imaging for 3D reconstruction. Pattern Recognition (PR) approaches are distinguished between those acting of the 2D images with matching of objects to build the 3D picture and those working in the 3D space directly. The common goal is to find and reconstruct tracks and showers, their common vertices and identify the event topology. An example of 2D to 3D PR is the Pandora package [341]. An example of a pure 3D approach is the WireCell package [342]. Recent efforts in PR aim at employing sophisticated machine learning (ML) techniques. In the 2D-to-3D approach convolution neural networks (CNNs) are applied on 2D images to identify objects which can be matched across planes [343] [344]. In the 3D approach CNNs, graph neural networks (GNNs), etc., are used in several steps to de-ghost the original 3D image and perform full event reconstruction including calorimetry, particle ID, etc. [345]. (3) The reconstructed tracks and showers are then passed to the calorimetry and particle ID modules. These modules utilize the charge deposition per unit length, after calibrations, to compute track and/or shower energy and particle identification [346].

35.7.6 *Developments*

The successful operation [347] of the ICARUS T600 TPC served as clear demonstration of the feasibility of the liquid argon TPC technology on a massive scale. Since this milestone, the liquid argon TPC community has expanded and the technology has continued to evolve. Notable developments include in-liquid electronics, the adoption of Silicon Photo-Multipliers and new light collection technologies, the use of dopants in the argon to improve the light performance, improved techniques for wavelength shifting, the adoption of a cryostat technology which permits detector masses of tens of kilotons and, in a major change to the standard single-phase topology, the implementation of pixelated readout to replace projective geometry in busy environments [348]. Technical R&D is continuing; as examples, the vertical-drift single-phase design for the second DUNE far-detector that uses strips on perforated printed circuit boards as charge sensors [349], a dual-phase TPC readout [350] using fast cameras to read out the scintillation light produced in

the gas region in place of a charge readout; a light detection system powered and readout using optical fiber allowing the readout to operate at any potential and therefore anywhere in the TPC, and efforts to build up the HV directly in the liquid argon with a voltage multiplier (Greinacher design) [351].

An abundance of data from recent experiments is encouraging insights into the liquid argon medium as in [288,352] and revealing new phenomena. For a taste, see [353]. The ground is fertile, busy, and full of opportunity.

35.8 Semiconductor detectors

Revised August 2023 by N. Wermes (Bonn U.).

Semiconductor detectors provide outstanding detection opportunities in terms of position, energy and also time resolution, often in combination. In accelerator experiments, they are most widely used as position-sensing devices, *e.g.* in tracking detectors, or as photodetectors (Sec. 35.2), for example in calorimeters (Sec. 35.10) or in imaging Cherenkov detectors (Sec. 35.5). In recent years also precise time measurement ($\mathcal{O}$(10–30 ps)) with silicon detectors has come into the focus of development. When comparing semiconductor detectors particularly with gaseous detectors, the main features are high density and low ionisation threshold, providing in high resistivity substrates comparatively large signals even without intrinsic amplification. Silicon detectors with active layers only 100–300 µm thick provide adequately large and fast signals on a typical time scale[4] of 10–50 ns. Challenges are the purity of the semiconductor material, characterised by its mobility-lifetime ($\mu\tau$) product, and its radiation resistance. The development of modern semiconductor detectors is strongly interconnected with integrated circuit technology. Micro-processing and micro-electronics technologies enable fabrication of high-density micron-scale electrodes on large wafers (6–8 in $\approx$ 15–20 cm diameter for sensor wafers) and allow for high-density amplification and readout circuits connected to them (chip wafer sizes are up to 12 in $\approx$ 30 cm with typical reticles of 26$\times$33 mm^2).

Some important material properties of common semiconductors used as detectors are summarised in Tab. 35.10. While for particle tracking the excellent position resolution is the main (but not the only) interest, high stopping power and high energy resolution are key parameters in X-ray, gamma-ray, and β spectroscopy, for example in neutrinoless double-beta decay searches. Due to its small bandgap, germanium excels in energy resolution but needs to be operated at very low temperatures (liq. N_2) to reduce thermally generated reverse bias current. Besides Ge, also GaAs, CdTe and CdZnTe (CZT) feature high atomic numbers and hence much higher stopping power and shorter absorption length which is important, especially for X-ray detection. Diamond, fabricated by chemical vapour deposition (CVD) and strictly speaking classified as an insulator with a large bandgap (Tab. 35.10), features low Z and large radiation length X_0. Thanks to its radiation hardness (Sec. 35.8.5) it is used for particle detection in dedicated applications, especially in zones with high particle flux (see *e.g.* [354] and references therein).

Materials R&D for radiation sensors extends to other bulk semiconductors as well, for example, ZnS, SiC, GaN or InP, and also to new material structures and metamaterials. Examples are semiconductor Quantum Dots, realised by nanometer-sized semiconductor "particles" embedded in a semiconductor bulk, or graphene, which – as a zero bandgap 2D material – features extraordinarily high conductivity (electrical and thermal) as well as outstanding photonic properties. A bandgap can be introduced by employing doped bi- or multi-layer graphene structures, thus rendering transistor and sensor realisations possible. The interested reader is referred to references [355] or [356], for example.

Operating usually without intrinsic amplification, semiconductor detectors crucially depend on

[4] Characterised here by the peaking time of the signal pulse.

low-noise electronics (see Sec. 35.9), so the detection sensitivity is determined largely by signal charge and input capacitance. Reviews of semiconductor detectors and electronics can be found for example in Refs. [1, 8, 357–359]

Table 35.10: Properties of some detector-relevant semiconductors; temperature-dependent quantities given at 300 K (from [1] and references therein).

Property	Si	Ge	GaAs	CdTe (CZT*)	Diamond
atomic number (Z)	14	32	31/33	48/(30)/52	6
density ρ (g/cm^3)	2.328	5.327	5.32	5.85	3.51
dielectric constant ϵ	11.9	16.0	13.1	10.2	5.7
semiconductor type	indirect	indirect	direct	direct	indirect
bandgap E_G (eV)	1.12	0.66	1.424	1.44(1.44–2.2)	5.5
intr. carrier density (cm^{-3})	1.09×10^{10}	2.4×10^{13}	2.1×10^{6}	10^7	≈ 0
radiation length X_0 (cm)	9.36	2.30	2.29	1.52	12.15
average energy w_i for (e/h) creation (eV)	3.65	2.96	4.35	4.43	13.1
mobility (cm^2/Vs)					
electrons μ_n	1450	3900	8500	1050	$\approx$1800†
holes μ_h	500	1800	400	90	$\approx$2300†
lifetime					
electrons τ_e	>100 µs	∼ms	1–10 ns	0.1–2 µs	$\approx$100 ns
holes τ_h	>100 µs	∼ms	20 ns	0.1–1 µs	$\approx$ 50 ns

*CZT = CdZnTe with the bandgap depending on the Cd to Zn ratio.
†Approximate averages. Values quoted in the literature for the mobility in diamond vary strongly.

35.8.1 *Signal generation in semiconductors*

35.8.1.1 *Creation of charges*

Semiconductor detectors are solid-state ionisation chambers. Absorbed energy forms electron-hole (e-h) pairs, *i.e.* negative and positive charge carriers which—when moving in an applied electric field—generate a signal current on the electrodes by electrostatic induction (see Sec. 35.8.1.2). For the signal charge carriers to (freely) drift in the electric field and to become detectable, semiconductors must feature small intrinsic charge-carrier densities (as existing for example in diamond and to some extent also in GaAs and CZT) or they must be depleted by reverse-bias junction configurations (as for Si, Ge or CdTe). In addition, they should feature low intrinsic density of defects which can act as trapping or generation/recombination centers (see Sec. 35.8.5).

The minimum energy required to form an e-h pair is the bandgap energy (1.12 eV in Si, 0.66 eV in Ge, 5.5 eV in diamond). However, impinging radiation or particles also release energy to lattice vibrations (phonons) such that the average energy for e-h pair creation is higher. In an "indirect" semiconductor like Si, the valence-band maximum is not at the same position in k-space (crystal-momentum space) as the conduction-band minimum and additional momentum transfer is required for a band transition to occur. Since the "direct" bandgap energy without k-transfer in Si is 3.4 eV, fewer-eV photons must receive momentum from lattice phonons. Because phonons are Bose-Einstein

distributed the needed momentum kick causes a steep rise in photon absorption probability between 1.12 eV and about 3.4 eV. For larger energy deposits the average energy w_i needed to produce an e-h pair assumes a constant value of 3.65 eV at room temperature. For other semiconductors consult Tab. 35.10.

For minimum-ionising particles, the most probable charge deposition in a 300 µm thick silicon detector is about 3.7 fC (∼23 000 electrons). In tracking detectors, a particle's energy loss and scattering in the detector material should be minimal (large X_0), whereas, for energy spectroscopy, *e.g.* of X-ray photons, the stopping power should be maximised by choosing high-Z semiconductors[5]. A smaller bandgap (in fact a smaller w_i) leads to a larger signal per deposited energy and improves the energy resolution, but also (exponentially) increases thermally excited carrier generation. To cope with excessive leakage currents at room temperature, Ge diodes are typically operated at liquid nitrogen temperature (77 K). In pure Si at 300 K, the intrinsic carrier concentration is $n_i \simeq 10^{10}\,\mathrm{cm}^{-3}$ (Tab. 35.10), corresponding to a resistivity in the order of $\rho \simeq (e\mu n)^{-1} \approx 400\,\mathrm{k\Omega\,cm}$. In reality, crystal imperfections and minute impurity concentrations limit Si carrier concentrations to about $10^{11}\,\mathrm{cm}^{-3}$ at 300 K ($\rho \approx 40\,\mathrm{k\Omega\,cm}$). In practice, wafer resistivities up to 20 kΩ cm are available, with mass production ranging from 1 to 10 kΩ cm.

The energy released in a semiconductor is absorbed by electronic excitations (e/h) and lattice excitations (phonons) in an anti-correlated way. Therefore, for a fixed released energy E (for example of an X-ray photon), the variance in the number of charge carriers $N = E/w_i$ follows binomial statistics. Due to the energy constraint, this variance is reduced by the Fano factor F relative to Poisson statistics (F ≈ 0.1 in Si and Ge). Thus, $\sigma_N = \sqrt{FN}$ and the energy resolution is $\sigma_E/E = \sqrt{Fw_i/E}$. However, for semiconductors the measured fluctuations of a detected energy signal are usually dominated by electronic noise rather than by signal fluctuations. The electronic noise contribution depends much on the detector leakage current and the electrode capacitance as well as on pulse shaping (*i.e.* the shaping time) in the signal processing electronics (see Sec. 35.9).

For X-ray detection, a major effort is made to find high-Z materials with a bandgap that is sufficiently large to allow for room-temperature operation while still providing good energy resolution. Compound semiconductors, *e.g.* CZT, can allow this but typically suffer from charge collection problems, which are characterised by the product $\mu\tau$ of mobility and carrier lifetime; this is the depth per field strength that generated carriers can drift before being trapped, *i.e.* in this context the distance over which photon absorption can still be detected.

In Si and Ge $\mu\tau$ is orders of magnitude larger than in compound semiconductors for both electrons and holes (see Tab. 35.10). Since for holes $\mu\tau$ is typically much smaller than for electrons, detector configurations where the electron contribution to the charge signal near the readout electrode dominates—*e.g.* strip or pixel structures with electron collection—usually provide better performance (see also next section).

35.8.1.2 *Signal formation*

The signal and its pulse shape depend on the instantaneous carrier velocity $\vec{v}(\vec{x}) = \mu\vec{E}(\vec{x})$, μ = mobility, and the electrode configuration and its geometry which determine the distribution of induced current according to the Shockley-Ramo theorem

$$i_S(t) = Ne\,\vec{E}_w(\vec{x})\,\vec{v}(\vec{x}(t))\,, \tag{35.20}$$

where Ne represents a drifting charge cloud of N elementary charges, $\vec{E}_w(\vec{x})$ is the "weighting field", which accounts for the coupling of the charge to a specific electrode and depends on the electrode configuration; $\vec{v}$ is the drift velocity. Note the difference between the electric field $\vec{E}$ and the weighting field $\vec{E}_w$ and take account of the fact that the mobility is, in general, field-dependent,

[5] The cross section for photo effect scales as Z^5.

$\mu = \mu(E)$, with $v \approx const$ at high fields (velocity saturation, for electrons in Si approaching 10^7cm/s at $E > 10^4$ V/cm). Both, electron and hole movements contribute to an electrode's signal. Hence, if the carrier mobility is very different for electrons and holes, like *e.g.* in CdTe where $\mu_h \ll \mu_e$ (Tab. 35.10), a photon signal, for example, becomes absorption-point dependent.

Integration of the induced current signal on an electrode yields the "collected charge". The average time to collect the created charge decreases with increasing bias voltage (*i.e.* field strength) until velocity saturation occurs at field strengths of about 10^4 V/cm in Si.

For a simple parallel-plate geometry with two electrodes the weighting field is constant, whereas for structured electrode geometries, like for example strips or pixels, E_w is position dependent which for small electrodes (compared to the sensor dimensions) strongly enhances the contribution of the movement close to the electrode ("small-pixel effect"). More details and practical accounts of the Shockley-Ramo theorem and its usage can be found in [1, 8] and references therein.

Position resolution is ultimately limited by transverse diffusion of the moving charge cloud (typically 3–5 µm for 200–300 µm thickness) and by the emission of δ electrons. The performance then depends on optimal usage of charge sharing between neighbouring electrodes and on noise. In magnetic fields, Lorentz drift deflects the electron and hole trajectories thus increasing the spatial spreading. The total spreading and hence charge sharing between electrodes can be tuned (increased or decreased) by tilting the detector relative to the incoming (average) particle direction. Overall spatial resolutions of 2–4 µm (rms) have been obtained.

35.8.2 *Junction detectors*

Si and Ge detector substrates must be—others like CdTe, GaAs should be and CZT can be—depleted from free charge carriers by operating them as reverse-bias junctions (p-n or Schottky) to be sensitive to the charge created by impinging particles. A typical cross-section of a junction detector is shown in Fig. 35.24, here with structured electrodes at the top. A p-n junction—even without external voltage—forms a sensitive space-charge region across itself depleted of mobile charges, hence also called "depletion region". The space charge establishes an electric field corresponding to a "built-in" voltage V_{bi}. Additional reverse-bias voltage V applied externally increases the space-charge region such that injected charge liberated by radiation is swept to the electrodes by the existing field. Detectors typically use an asymmetric structure, for example, a thin and highly doped p^+ electrode[6] region and a lightly doped n^- substrate region – or vice versa, so that the depletion region extends predominantly into the more lightly doped bulk volume.

In such planar Si (or Ge) devices, the thickness of the depleted region is

$$\begin{aligned} d &= \sqrt{2\epsilon\,(V + V_{bi})/Ne} = \sqrt{2\rho\mu\epsilon\,(V + V_{bi})} \qquad (35.21)\\ &\approx \frac{0.5}{\mu\text{m}} \times \sqrt{\frac{\rho\,V}{\Omega\,\text{cm}\cdot\text{V}}} \qquad \text{for } n\text{-type Si bulk}\\ &\approx \frac{0.3}{\mu\text{m}} \times \sqrt{\frac{\rho\,V}{\Omega\,\text{cm}\cdot\text{V}}} \qquad \text{for } p\text{-type Si bulk} \end{aligned}$$

with (values for Si)

V = external bias voltage
V_{bi} = "built-in" voltage (≈ 0.5 V for typ. used resistivities)
N = doping concentration
e = elementary charge
ϵ = dielectric constant = $11.9\,\epsilon_0 \approx 1$ pF/cm

[6] $n^{+/++}$, $p^{+/++}$ as well as n^-, p^- qualitatively denote relative doping-concentration levels.

ρ = resistivity (typically 1–10 kΩ cm)
μ = charge carrier mobility
($\sim$ 1450 cm^2/Vs (electrons), $\sim$ 500 cm^2/Vs (holes) [360])

The conductive p and n regions together with the depleted volume form a capacitor with capacitance per unit area

$$C' = \frac{\epsilon}{d} \approx \frac{1\,\text{pF/cm}}{d} \qquad \text{in Si.} \tag{35.22}$$

The depletion depth d becomes as large as the sensor's thickness at the "full depletion voltage" $V = V_{fd}$ for which the sensor capacitance reaches a minimum (about 35 pF/cm^2 for $d = 300$ µm). In strip and pixel detectors (see next section) the capacitance is dominated by the fringing capacitance to neighbouring electrodes as the electrode pitch is typically much smaller than the sensor thickness. For example, the strip-to-strip Si fringing capacitance is about 1–1.5 pF per cm of strip length at a strip pitch of 25–50 µm.

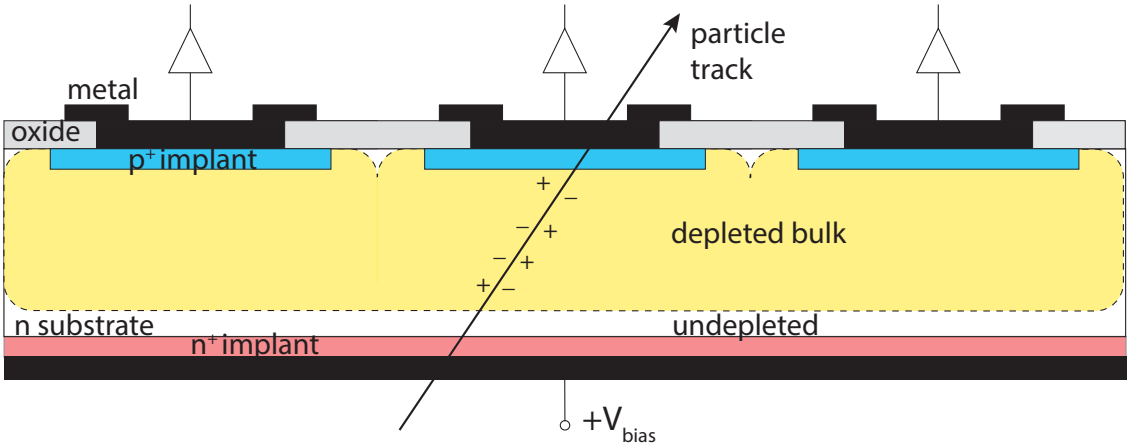

Figure 35.24: Reverse-biased junction detector with planar readout electrodes at the top in a standard sensor configuration (p$^+$-in-n): lightly doped n-type substrate with p^+ implants forming the diode junction at the top side. Electrons move to the bottom electrode and holes to the top. Both movements contribute to the (induced) signal at the top electrodes with amounts as specified by the weighting field (see Sec. 35.8.1.2). The n^+ implant at the bottom side forms an ohmic contact between bulk and metal.

The electric field strength and shape inside the semiconductor bulk are important for efficient signal charge collection. Governed not only by the applied external voltage but also by the space charge inside the semiconductor bulk, leads (for constant space charge) to a linear field-strength decrease from its maximum at the junction's boundary into the depleted semiconductor bulk. Space charge can also occur from ionised lattice defects which either naturally exist for example in GaAs or can be created by irradiation in any semiconductor material. This can lead to low-field regions as well as to changes in the field's shape (deviating from linear), both of which usually deteriorate the charge collection properties of a detector.

In partial depletion (*i.e.* $V < V_{fd}$) the field decreases to zero at the end of the depletion zone. Overbias ($V > V_{fd}$) adds a constant electric field component which avoids a vanishing field region and also provides faster charge collection as long as the carrier drift velocity has not yet saturated. At an average field of $E = 10^4$ V/cm, the onset of velocity saturation, where $\mu_e \approx 7{\times}10^3$ cm^2/Vs, $\mu_h \approx 3.5{\times}10^3$ cm^2/Vs, the collection times for Si are about 15 ps/µm for electrons and 30 ps/µm

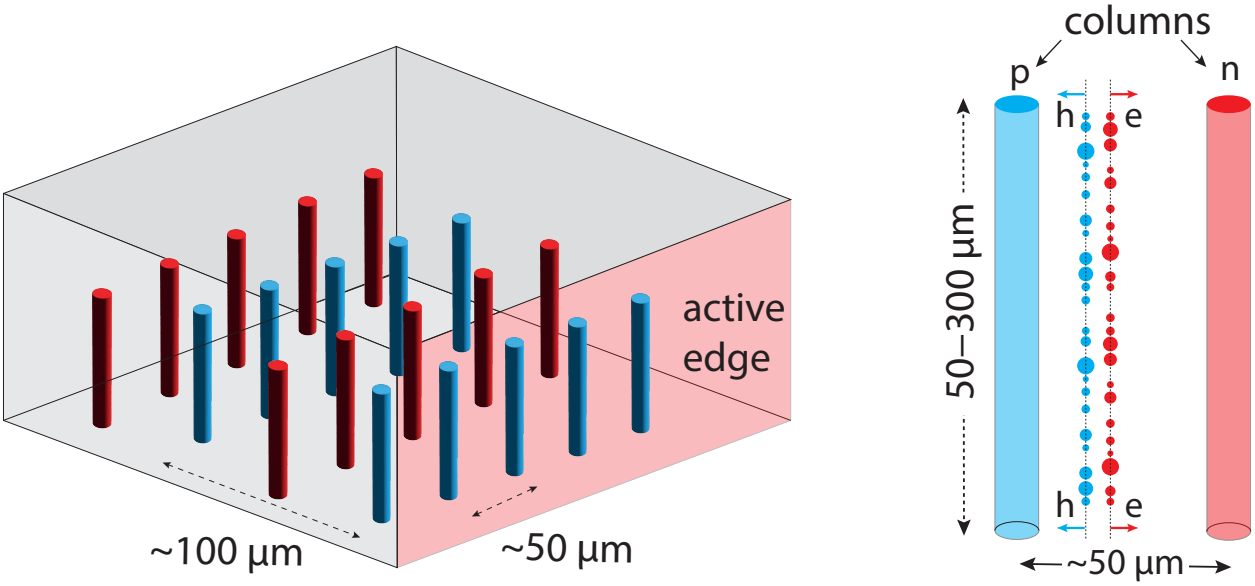

Figure 35.25: Junction detector with vertical electrodes, n (red) and p (blue), and "active" edges called 3D-Si. Dimensions given are typical. This electrode configuration provides short drift paths for moving charges while keeping a large sensing thickness. An active edge minimises dead areas at the sensor boundaries. This geometry has also been employed in CVD diamond substrates.

for holes. In typical fully-depleted detectors, 100–300 µm thick, electrons are collected within less than about 5 ns, and holes within less than about 10 ns.

Large volume ($\sim 10^2 - 10^3\,\mathrm{cm}^3$) germanium detectors, especially for γ-ray detection, are commonly configured in cylindrical or hexagonal rod shapes, for example, a 10 cm long cylindrical n-type crystal with 5–10 cm diameter with an inner 5–10 mm diameter n^+ electrode and an outer p^+ layer forming the diode junction. Germanium can be grown with fairly low impurity levels, 10^9–$10^{10}\,\mathrm{cm}^{-3}$ (HPGe, high-purity germanium), so these large volumes can be depleted with several kilovolts.

Diamond, featuring free charge carrier densities close to zero, needs no further depletion and is operated as a parallel plate capacitor with an insulator dielectric inside. Still, a substantial bias voltage is required to overcome charge trapping.

35.8.3 *Detectors with structured electrodes*

35.8.3.1 *Microstrip-, Si-drift- and hybrid-pixel detectors*

In HEP experiments semiconductor detectors usually aim at good position resolution achieved with electrodes patterned in "strips" or "pixels" with typical dimension scales (electrode pitch) of 50–100 µm, or in "pads" (mm^2–cm^2) if coarser granularity is affordable for the benefit of fewer channels.

Electrodes are usually placed "planar", *i.e.*, at the surface of the sensing Si bulk (Fig. 35.24). In an alternative, but more elaborate way, electrodes can be shaped as columns or trenches running orthogonally to the surface and hence parallel to the average direction of impinging particles (Fig. 35.25) [361]. This geometry (termed "3D-Si", but is also exercised with diamond) enhances the radiation tolerance due to shorter drift distances of charges at the same thickness (see also Sec. 35.8.5).

In strip detectors, the strip ends are connected to dedicated readout ICs where the signals are amplified and processed. Two-dimensonal readout is realised either by angled double-layers of

strip detectors or by "double-sided" strip sensors structured by readout strips on either side (see *e.g.* [1,358] and references therein). For the latter, one electrode surface features n^+n or p^+p strip junctions (rather than pn), respectively, which require dedicated measures, *e.g.* intermediate strips or special doping profiles to break the electron accumulation layer that occurs at an n^+n interface. For p^+p, intermediate n strips or similar are not necessary, thanks to positive oxide charges residing at the Si/SiO_2 interface.

As for gaseous driftchambers, silicon driftchambers provide the position of a hit orthogonal to a strip's coordinate from a measurement of the charge cloud's drift time, drifting over centimeter-long paths inside the silicon bulk. For this to work the bulk is "sidewards depleted" by using junction strip implants of the same polarity on both sides of the sensor (p in n or n in p, respectively), different to standard double-sided strip detectors (see *e.g.* [1]). This way a quadratic potential minimum for electrons is created, confining them amid the sensor bulk, on which a linear electric potential in drift direction is superimposed; holes, instead, drift to the sides. In comparison to strip detectors, much fewer electrodes are necessary for the same active area coverage. Low rate capability is a drawback caused by the long drift path of created charges. Arranged with only one small electrode with low capacitance in the center of a cylindrical disk, so-called silicon-drift diodes (SDD) are low-noise single-channel devices with large area coverage, used for example in X-ray fluorescence analysis and electron microscopy.

Very small pixel structures for particle detection were first realised with CCDs [362]. Most current applications, particularly those for high-rate applications such as at the LHC, employ the "hybrid-pixel" concept in which both, the sensing diode structure as well as the readout IC, have equal electrode structures and patterns (pixels). The connection is made by two-dimensional arrays of solder or indium bumps that mate the two parts by employing flip-chip technology (Fig. 35.26, usually chip-to-chip or chip-to-sensor; more details *e.g.* in [358, 363]). Further advancements in bonding techniques especially address chip-to-wafer or even wafer-to-wafer placements, such as SLID (Solid Liquid Interface Diffusion) employing a very thin liquid metal layer (Sn) in between metals with higher melting points (e.g. Cu). Also, Cu–Cu, Cu–Sn, or oxide–oxide (SiO_2) diffusion bonding without solder is feasible.

The hybrid approach excels in optimally utilising chip and sensor technologies for radiation hardness and rate capability (see *e.g.* [364]). It is, therefore, the technology of choice for pixel trackers in high-rate, high-radiation environments optimised for the purpose by employing very thin modules ($\mathcal{O}(300\,\mu m)$ total). A disadvantage is the complex and cost-intensive module assembly.

35.8.3.2 *Monolithic pixels*

Partially or fully monolithic pixel detectors directly connect the generated signal charge with an embedded active electronics device (*i.e.* one or several transistors). An example of a partially monolithic device is the DEPFET (depleted p-channel FET) pixel sensor (see *e.g.* [365]), employed, for example, in the pixel tracker of the Belle-II detector. A single transistor (pMOSFET) is implemented in every pixel (Fig. 35.27 (a)). The sensor substrate is "sidewards depleted", as similarly done in Si driftchambers (Sec. 35.8.3.1), by means of the backside p-contact and several p regions near the transistor. Depletion is provided by the n^+ *clear* contact (see below) plus a bulk n-implant outside the matrix. In addition, the structure features a deep n-implant located a few micrometers underneath the transistor channel on floating potential. This implant becomes the most positive point of the structure, hence being an electron accumulation point, which acts as an "internal gate" of the transistor. The gate voltage changes by an amount $\alpha q_S/C$, with q_S = signal charge, gate-oxide capacitance $C = C_{ox}\,WL$ with $W \times L$ = gate area, and $\alpha \lesssim 1$ accounting for stray capacitance. The gate voltage changes due to an accumulated signal charge q_S and leads to a detectable change in drain current (in saturation):

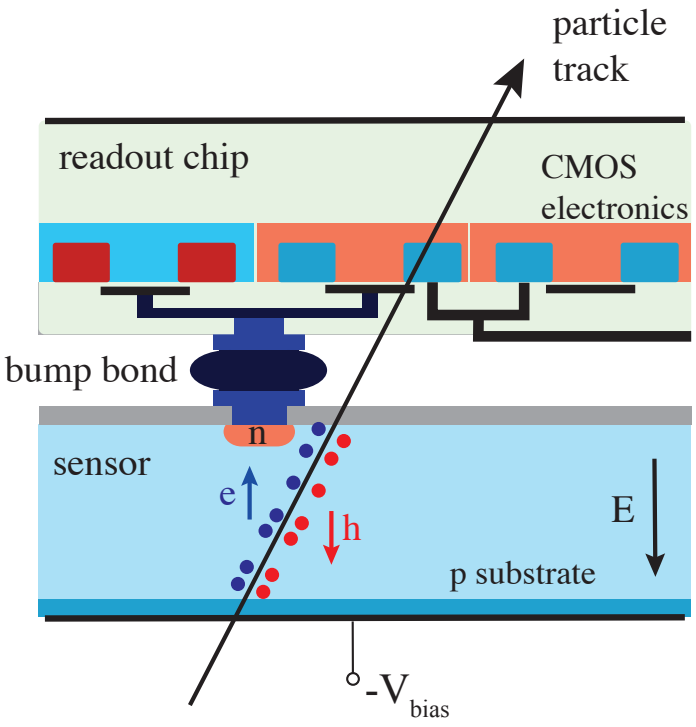

Figure 35.26: Cross-sectional view of a hybrid-pixel detector cell (one pixel) consisting of sensor (bottom) and readout chip (top) with CMOS circuitry illustrated by three transistors (red and blue implant areas plus metal lines). The sensor is a depleted diode structure (here p substrate with n electrode). Both parts are mated by a microbond (bump bond), typically solder or indium.

$$I_D = \frac{W}{2L}\,\mu C_{ox}\left(V_G + \frac{\alpha\, q_S}{C} - V_{th}\right)^2 . \tag{35.23}$$

Other elements in Fig. 35.27 (a) like the external FET gate and the *clear* implant provide control and reset of the structure. The device gain $g_q = dI_D/dq_S \approx \alpha g_m/C$, with transconductance $g_m = \mu C_{ox}\frac{W}{L}(V_G - V_{th})$, is of order 500 pA/e$^-$. The small capacitance of the internal gate (few fF) enables very low noise operation ($\lesssim 2\mathrm{e}^-$) when operating with long shaping times (see Sec. 35.9).

Fully monolithic pixels combine the sensing task and the complete readout circuitry, *i.e.* the two separated parts of hybrid pixels, in one chip. Both functions must be properly shielded against each other, which is achieved by exploiting multi-well IC technology. Realised as MAPS (monolithic active pixel sensors) standard CMOS wafers can be used for pixel detector fabrication. CMOS wafers often feature a Si epitaxial layer where the transistors are implanted. It is possible to use this epi-layer as a sensitive detection volume for particle detection. However, in such detectors, only the immediate regions near the collection nodes (see Fig. 35.27(b)) are depleted. Outside these confined regions there is no or little electric field and charge collection is dominantly governed by slow and non-directional charge diffusion, a problem for high-rate applications. Depleted MAPS (DMAPS) exploit non-standard high resistivity wafers or high-ohmic epi-layers, typically with resistivities $>1\,\mathrm{k\Omega\,cm}$, as well as high bias voltage (up to $\gtrsim 300\,\mathrm{V}$) resulting in charge collection by directed drift motion. Charge collecting electrodes are deep wells (n-wells in Fig. 35.27(b)), either formed as large (typ. $50\times100\,\mu\mathrm{m}^2$) structures to fully contain the CMOS circuitry (Fig. 35.27(b), top) or as small nodes, set aside the electronics (Fig. 35.27(b), bottom), with obvious pros and cons resulting from

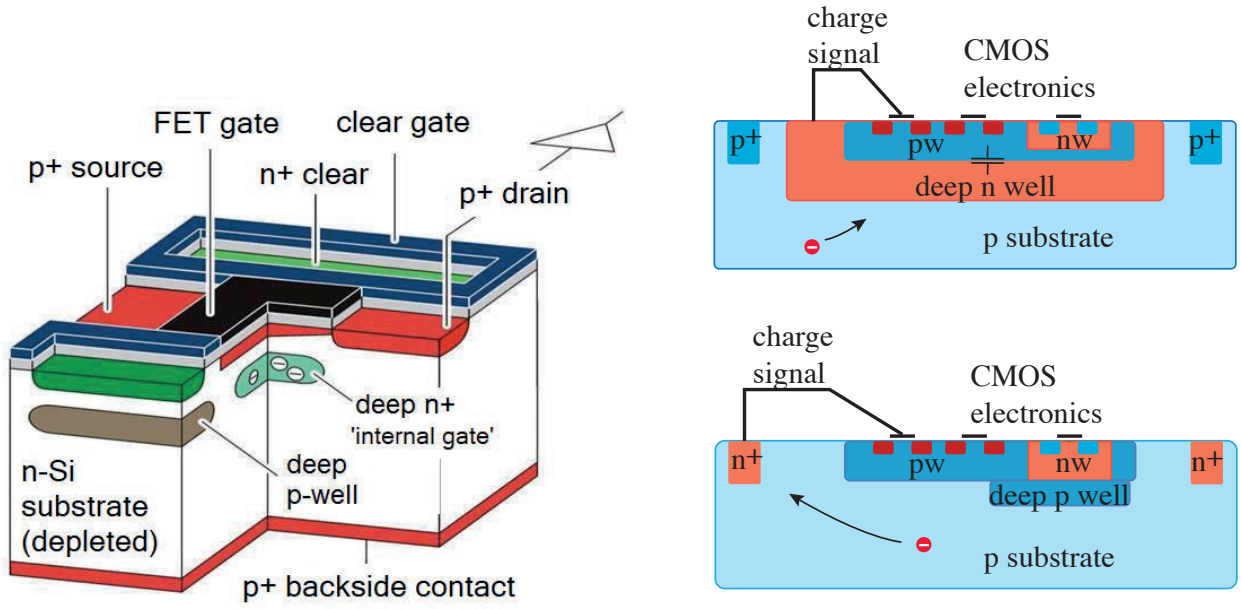

(a) DEPFET pixel structure.

(b) DMAPS pixel structures.

Figure 35.27: Partially (a) and fully (b) monolithic pixels: (a) DEPFET pixel structure with an embedded pMOSFET transistor; source and drain are p implants (red), gate metal (black), oxide (grey), deep-n internal gate (light green), other metal (blue), clear contact (green), and deep p-well (brown). (b) Depleted MAPS with joint sensing and electronics volumes: (top) charge collection by a *large-electrode* which houses the electronics in a deep-n well; (bottom) charge collection by a *small electrode* set aside from the electronics area.

shorter average drift distance (large electrode) versus much smaller capacitance (small electrode). The former benefits radiation tolerance, whereas the latter allows for smaller pixels and benefits from small sensor capacitance in noise and rise time. However, in both approaches radiation tolerance levels of $\gtrsim 10^{15}\,\mathrm{n_{eq}/cm^2}$ (fluence) and 1 MGy (ion. dose) have been demonstrated.

A variant of the monolithic approach are SOI (silicon on insulator) pixels providing high spatial resolution, but less radiation tolerance: A high-resistivity supporting wafer, employed for particle sensing, connects through an embedded insulator (a buried oxide layer, BOX) to the CMOS readout circuitry. The BOX separates the sensing volume from the electronics layer and provides shielding. Because the area between BOX and the transistor layer acts as a "back-gate", transistor operation can be affected requiring dedicated cures (see *e.g.* [366]).

35.8.4 *Precise timing with silicon detectors*

Typical time scales for silicon detector output signals are several tens of nanoseconds (*e.g.* rise times, shaping times, etc.) accompanied by a typical time mark precision in the order of nanoseconds. Essential for achieving precision timing ($< 100\,\mathrm{ps}$) are steep signal rise and low noise according to eq. (35.38) in Sec. 35.9. This, in turn, requires fast charge collection, *e.g.* in thin planar or 3D-Si detectors with high E-fields, as well as fast and strong amplification, both together yielding large slew rates (dS/dt, with S="signal", *e.g.* an induced current or a voltage). Important parameters that influence timing precision are the detector capacitance (including stray contributions) and the amplification gain.

Detectors that have achieved precise time measurement are so-called LGADs (low gain avalanche diodes, Fig. 35.28). They have planar electrode geometry that includes an implanted low-gain ($g = 10$–50) amplification structure on either the top or bottom electrode side to maximise the slew rate. Electrons created from ionising traversing particles are accelerated towards a very high field created by an amplification layer near the (here) top electrode, where impact ionisation creates a multitude of e-h pairs. They induce a very fast and large signal rise, mainly governed by the holes' movement away from the amplification layer. Sufficiently low amplification gain minimises excess noise contributions and avoids the creation of hole-induced avalanches moving in the opposite direction to electron avalanches.

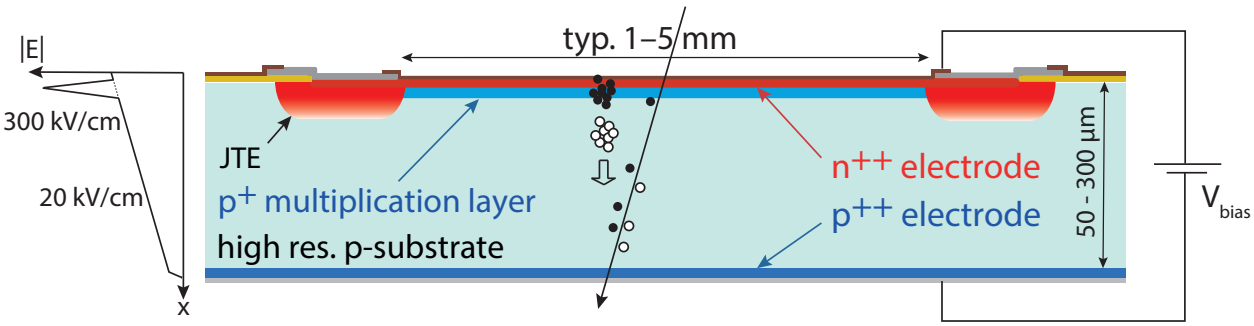

Figure 35.28: LGAD amplification structure for precision timing. Amplification (typ. $\times$ 20–50) occurs at the structure boundary in a highly doped p-n junction near the (here: top) surface (JTE = Junction Termination Extension, deep n-well).

The achievable time resolution has several contributions:

$$\sigma_t^2 \approx \left(\frac{\sigma_S^{thr}}{dS/dt}\right)^2 + \left(\frac{\sigma_n}{dS/dt}\right)^2 + \sigma^2_{\text{arrival}} + \sigma^2_{\text{dist}} + \sigma^2_{\text{TDC}}\,. \tag{35.24}$$

The first term represents "time walk" coming from Landau fluctuations, defined as originating from number and energy-transfer fluctuations in the energy-loss process with σ_S^{thr} being the signal-height variations at discriminator threshold. This term can be kept minimal, *e.g.*, by employing constant fraction discrimination or by applying corrections using amplitude information. The second term is the contribution of noise to the time jitter, which can be approximated by $(t_r/\text{SNR})^2$ with $t_r =$ rise time, SNR = signal-to-noise ratio. Both first terms are kept small by large signal slew rates. An irreducible contribution comes from fluctuations in non-uniform depositions of charge along the particle path (including fluctuations in the amplification process) which causes an intrinsic jitter in the arrival time (third term)[7]. The thinner the detector the less disturbing is this effect. The fourth contribution is signal distortion due to non-uniform weighting field regions and variations in (non-saturated) drift velocities. "Junction Termination Extensions" (JTE, see Fig. 35.28) serve to lower this term. The final term denotes time fluctuations due to uncertainties in digitization, which can, however, be made negligible with GHz TDCs. Timing precision of order 30 ps has been reached. Structural and operational variants to improve charge collection and position resolution are "resistive AC-coupled LGADs", "deep junction LGADs", "trench-isolated LGADs" and others. More details on LGADs are given in [367] and [368].

Columnar electrode geometries such as shown in Fig. 35.25 with small diameter and small pitch are by design a very suitable choice for precision timing due to short collection paths and strong

[7] In LGAD literature these fluctuations are sometimes also referred to as "Landau fluctuations".

fields. Employing an optimised trench-like column shape field- and weighting-field distortions are minimised and time resolutions in the order of 10 ps have been achieved in prototypes [369].

High precision timing can also be approached by exploiting the benefits of SiGe BiCMOS technology: strain mismatch of Si-Ge alloy layers results in a smaller bandgap as well as higher mobility and hence larger transconductance. This benefits the speed in hetero-junction bipolar transistors (HBTs) which also feature less 1/f noise than MOS transistors. Resolutions of order 20 ps have been reached in a monolithic pixel matrix using this technology [370]. More elaborate discussions on timing in silicon detectors can be found *e.g.* in [371].

35.8.5 *Radiation damage in silicon detectors*

High channel density and response times in the nanosecond range render micro-patterned semiconductor detectors particularly suited for high particle rates. This is usually accompanied by high radiation causing damage of sensors and front-end electronics. We restrict ourselves here to damage in Si detectors and their electronics. Radiation damage occurs in semiconductor detectors through two basic mechanisms:

1. *Bulk damage* due to displacement of atoms from their lattice sites resulting in defect energy levels inside the band gap. This leads to increased leakage current, carrier trapping, and build-up of space charge that changes the required operating voltage. Displacement damage results from non-ionizing energy loss (NIEL). The energy imparted to the recoil atoms can initiate a chain of subsequent displacements including "damage clusters". For a description, it is critical to consider both, particle type and energy. Conventionally, for silicon, the received NIEL is normalised to the damage level caused by 1 MeV neutrons and specified in units of neutron-equivalent fluence Φ_{eq} with units n_{eq}/cm^2.
2. *Surface damage* due to charge build-up in surface layers and formation of interface traps at *e.g.* Si–SiO_2 boundaries. These influence transistor currents and thresholds or cause thin charge carrier layers at a silicon surface, leading to increased surface leakage currents in sensors or circuits and affecting electrodes' isolation and/or transistor characteristics. The effects of charge build-up are strongly dependent on the device structure and on fabrication details. The damage is dominantly due to ionising energy loss (IEL) and hence proportional to the absorbed total ionisation dose (TID) measured in Gy (or rad), independent of the particle type.

The increase in reverse bias generation current (leakage current) due to bulk damage is $\Delta I_L = \alpha \Phi_{eq} V$, where V is the volume under an electrode and $\alpha \simeq 4 \times 10^{-17}$ A/cm, a universal constant when normalised to temperature (conventionally 20°C), and measured after annealing for 80 min at 60 °C. Note that for devices with intrinsic amplification, generation current is amplified accordingly. Reverse bias leakage current depends strongly on temperature

$$I_L(T) \propto T^2 \exp\left(-\frac{E_a}{2kT}\right) , \tag{35.25}$$

where $E_a \approx 1.2$ eV (activation energy), so rather modest cooling can reduce the current substantially (∼6-fold reduction in cooling from room temperature to 0 °C).

For bulk damage in silicon, the *NIEL hypothesis* is a good first-order description of the observed damage (especially regarding I_L). It states that all lattice radiation damage in silicon linearly scales with NIEL and can be traced back to the abundance of primary defects (point defects and clusters), irrespective of their initial distribution over energy and space, that is, regardless of the damage's topology and origin. Under the NIEL hypothesis, the observed differences in damage caused by neutrons, protons, pions and electrons are hence usually scaled to each other.

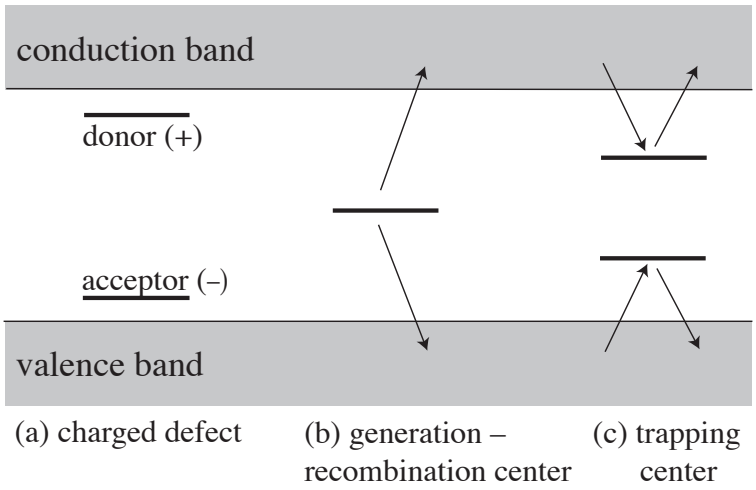

Figure 35.29: Characteristic locations of energy levels caused by bulk radiation damage and their main action effects.

Three main bulk displacement damage effects are sketched in Fig. 35.29: (a) defects acting as charged donors/acceptors, (b) deep defects (near the middle of the bandgap) causing increased leakage current, and (c) carrier trapping centers. Damage effects are not constant with time; for example in n-type bulk, radiation-induced negative space charge anneals at first, reaching a stable damage minimum (beneficial annealing), but later electrically active defects (negative space charge from acceptor-type damage) build up over the time scale of months (reverse annealing).

Acceptor- (usually dominant) or donor-like (deep) defect states, when ionised, build up space charge (dominantly negative), which in turn normally requires an increase in the applied voltage to sweep signal charge through the detector thickness. For n-type bulk starting material, however, donor (*e.g.* phosphorous) removal by forming electrically inactive vacancy-phosphor (V-P) complexes induced by the incipient radiation, leads to a faster decrease in depletion voltage (faster than only by the compensation of donors through generated deep acceptors) until positive and negative space charges effectively balance; only little bias voltage then is required for operation (point of effective space charge inversion, also called "type inversion" (Fig. 35.30)). At larger fluences the negative space charge dominates, and the required operating voltage increases proportional to the increasing effective space charge density N_{eff}, also called effective doping concentration. Also the space-charge distribution can no longer be regarded as constant and homogeneous over the detector volume, thus destroying the linear slope of the electric field from the junction to the backside as was introduced in Sec. 35.8.2; instead "double-junction"-like field distributions typically occur.

Today, p-type silicon with n^+ electrode-implants is the preferred choice for sensors operating in high radiation environments for reasons of cost-effectiveness in production as well as high radiation hardness due to fast (high mobility) electron collection in high electric- and high weighting-field regions at small segmented n^+ electrodes. Space charge inversion is usually not observed since the initial space charge is negative already (Fig. 35.30).

Removal of acceptors (*i.e.* substitution of electrically active boron at its lattice site) in p material is found to be dominantly caused by interstitial silicon replacing boron on its lattice position. The highly active interstitial boron then can cause the formation of other defects such as interstitial oxygen-boron complexes (B_iO_i) which absorb boron atoms into electrically active defects (subscript i for "interstitial").

Various techniques have been explored to neutralise radiation damage effects by defect engineer-

ing. For n-type material, oxygen enrichment with a larger abundance than phosphorus, introduced during the Si growth, successfully reduces the formation of multi-vacancy, acceptor-like complexes which are dominantly produced by charged hadrons, because it enhances instead the formation of electrically neutral V-O complexes. Carbon enrichment, on the other hand, reduces boron removal in p-type Si by building stable C_i-S_i complexes, thus trapping Si interstitials which else would remove boron.

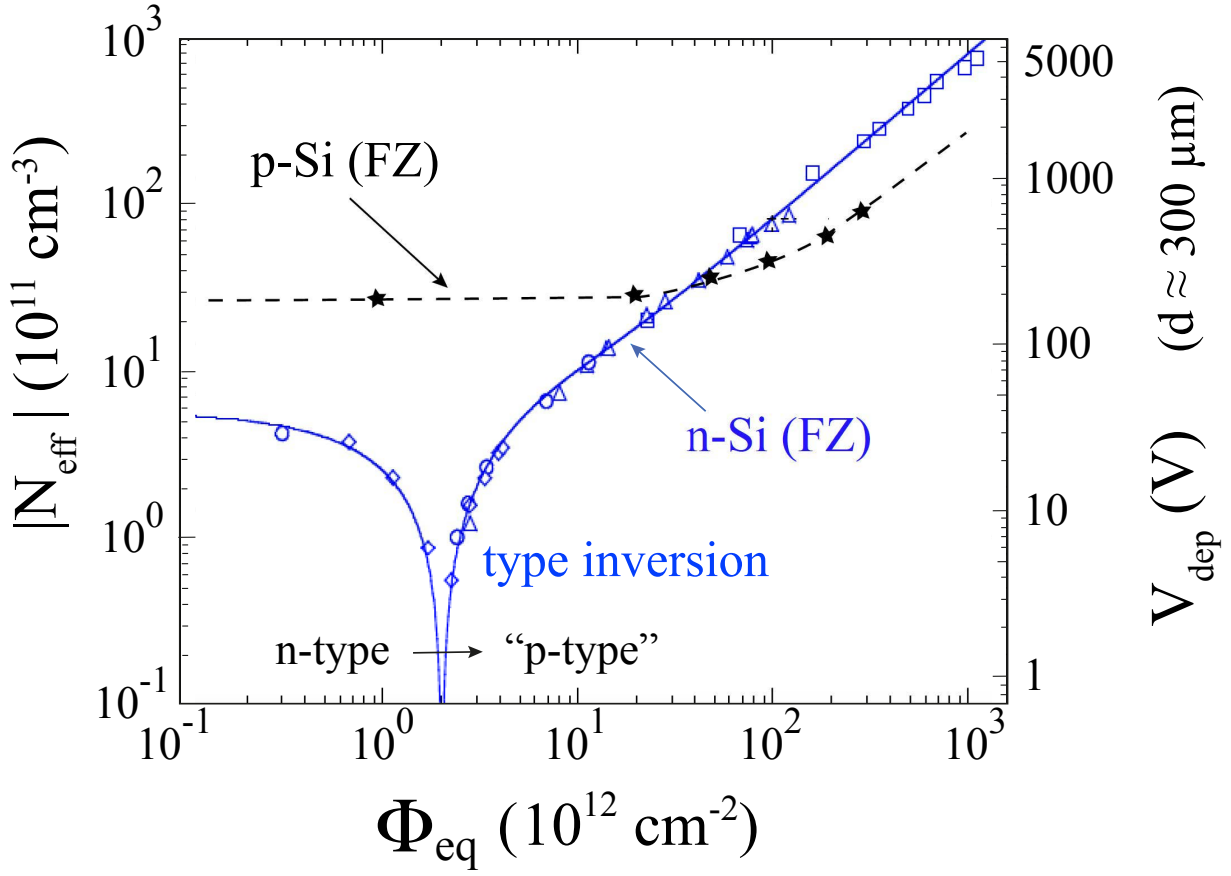

Figure 35.30: Effective space charge concentration N_{eff} (left axis) and required voltage for full depletion V_{dep} (right axis) of approximately 300 µm thick Si sensors as a function of neutron-equivalent radiation fluence for typical n-type (blue) and p-type (black) silicon float zone (FZ) material before annealing. While initial n-type Si inverts to effectively p-type Si, this is not observed for initial p-type silicon. Bias voltage supply for large systems is usually limited to less than 600–1000 V. Figure adapted using [372, 373] and [374].

Dopant removal plays a particularly important role in more complex sensor structures such as, for example, DMAPS or LGADs. In particular, the high p-doping concentration in LGAD's gain layer is vulnerable to acceptor removal causing a drastic gain decrease with increasing fluence.

Deep level defects (Fig. 35.29(b)) typically are the origin of leakage current increase, whereas trapping centers (Fig. 35.29(c)) dominate carrier lifetime and signal loss at high fluences beyond 10^{15} n_{eq}/cm^2. The safe limit on the operating voltage ultimately limits the detector lifetime. Strip and pixel detectors, specifically designed for high voltages, have been extensively operated at bias voltages of 500–600 V. Sensors with columnar electrodes normal to the surface (3D-Si, Fig. 35.25) need significantly lower voltages for full depletion and are prime contenders for radiation-hard

sensors.

Synthetic CVD diamond has proven strong against radiation damage due to its large bandgap (see Tab. 35.10) and strong lattice binding with a roughly twice higher threshold ($\sim 40\,\text{eV}$) for a displacement of lattice atoms than silicon (see *e.g.* [354]). Even for polycrystalline material, charge collection distances (CCD = sum of the mean free paths $\mu\tau E$ of e and h over which charges reach the electrodes) of 300–400 µm have been achieved. Diamond wafer cost, however, is comparatively very high. Smaller scale trackers acting *e.g.* as beam monitors have been built.

GaAs has received interest as a potentially radiation-hard material in the 1990ies. For particle detection it must still be depleted from charge carriers despite comparatively small intrinsic carrier densities (see Tab. 35.10). It suffers from a strong loss in charge collection efficiency when irradiated, dominantly because of electron trapping. Other semiconductor materials such as SiC or GaN feature wider bandgaps (3.26 eV and 3.39 eV, respectively) than Si (but smaller than diamond) and possess other suitable properties relevant to high-fluence operation, such as density, e-h ionisation energy, and displacement energies. They have regained attention after the material quality has improved much due to an industrial push coming from power devices and LEDs. So far, charge collection degrades faster with radiation fluence than for Si and diamond, however.

Strip and pixel detectors have remained functional in large detectors even at particle fluences well beyond $10^{15}\,\text{n}_\text{eq}/\text{cm}^2$ where charge loss due to recombination and trapping becomes significant. Thin planar ($\sim$100 µm) and 3D silicon detectors have been successfully operated at fluences of 2 and $3 \times 10^{16}\,\text{n}_\text{eq}/\text{cm}^2$, respectively, and measurements indicate that operation above $10^{17}\,\text{n}_\text{eq}/\text{cm}^2$ does not seem impossible. The large SNR obtainable with low capacitance pixel structures extends the detector lifetime. The higher mobility of electrons makes them less sensitive to carrier lifetime than holes, so detector configurations that emphasize the electron contribution to the charge signal are advantageous, *i.e.* n^+ strips or pixels on p- or n-substrates. The occupancy of the defect charge states is strongly temperature dependent; competing processes can increase or decrease space charge and the required operating voltage. It is critical to choose the operating temperature judiciously ($-30\,^\circ\text{C}$ to $0\,^\circ\text{C}$ in typical collider detectors) and to limit warm-up periods during maintenance. Detailed discussions of radiation damage and its effects on semiconductor detectors can be found e.g. in [373, 375]; an introduction to the subject can be found in [1].

Tolerance against surface damage, especially in SiO_2 layers as in gates and in oxide trenches of CMOS transistor structures, largely depends on the feature size of a technology and on appropriately designed circuitry. Deep submicron technology nodes of 130 nm and 65 nm sustain total ionisation doses of up to 5 MGy (500 Mrad), corresponding to fluences of up to $5 \times 10^{15}\,\text{cm}^{-2}$ of minimum ionising pions or protons.

35.9 Low-noise detector readout

Revised November 2021 by N. Wermes (Bonn U.), revised November 2013 by H. Spieler (LBNL).

Many detectors rely critically on low-noise readout electronics, for best energy resolution or to allow low thresholds for high detection efficiencies. A typical detector front-end is shown in Fig. 35.31.

In a model relevant to most readout applications, the detector, represented by a capacitance C_d, delivers a delta-function-shaped current signal, represented by a current source in parallel. Bias voltage is applied through resistor R_b and the signal is (often) coupled to the amplifier through a blocking capacitor C_c. The series resistance R_s represents the sum of all resistances present in the input signal path, *e.g.* the electrode resistance, any input protection network, and parasitic resistances in the input transistor. The amplification stage contains the preamplifier providing gain and a pulse shaper (characterized by a shaping time τ), which tailors the overall frequency

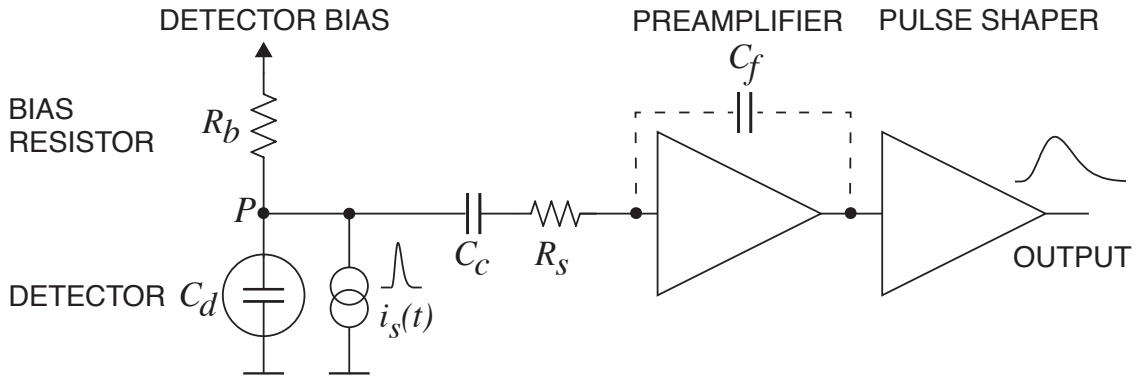

Figure 35.31: Typical detector front-end. The dashed circuit part is a charge-sensitive amplifier (CSA) realization.

response to optimize the signal-to-noise ratio (SNR) while limiting the duration of the signal pulse to accommodate the signal-pulse rate. For a given input signal, purely random noise leads to a gaussianly smeared signal distribution behind the shaper. Even if not explicitly stated, all amplifiers provide some form of pulse shaping due to their limited frequency response.

It is useful to distinguish between noise inherent to a detector's signal amplification and processing circuitry (per channel) on the one hand, depending on the detector specifics and the experimental environment (*e.g.* the data rate), and — on the other hand — external noise sources introduced *e.g.* by systems external to a specific readout circuit often resulting in "common-mode" noise, *i.e.* common to all channels. External noise can be introduced from power supplies, digital signal switching, RF pick-up, or from effects due to "common grounding" allowing noise to couple to the current loop connecting the detector to the preamplifier. These noise sources differ from setup to setup and must be dealt with – and should at best be eliminated – individually. In the following, therefore, only the noise inherent to typical detector signal processing is discussed.

35.9.1 *Principal noise origins*

As principal noise origins in circuit elements we mainly distinguish *thermal noise* resulting from velocity fluctuations of charge carriers (Brownian motion), as well as *shot noise* and $1/f$ *noise*, both resulting from charge carrier number fluctuations. Shot noise is due to emission statistics of electrons crossing a barrier, $1/f$ noise is often — especially in MOSFETs — due to charge trapping–detrapping processes leading to a spectral behaviour as $1/f^{\alpha}$ with $\alpha = 0.5 \ldots 2$. Further noise nomenclature, like for example RTS (random telegraph signal) noise, also called "burst noise' or "popcorn noise", is in its origin usually related to trapping/detrapping processes, like $1/f$ noise. The popping-up nature of individual RTS bursts eventually leads to the $1/f$ noise spectral density when the noise of several traps with (very) different trapping times are superimposed. RTS noise is omitted in the following for simplicity reasons.

35.9.2 *Equivalent noise analysis*

The equivalent circuit for noise analysis (Fig. 35.32) shows contributions of the mentioned noise sources at several circuit points. Originating from fluctuations, noise is expressed as the variance $\langle i^2 \rangle$ or $\langle v^2 \rangle$ of a noise current or voltage distribution. Shot noise, such as that produced in a semiconductor detector by leakage current fluctuations, is represented by a current noise generator in parallel with the detector and the amplifier input. The statistical fluctuations in a charge measurement will scale with the square root of the total number of recorded charges, so this noise contribution increases with the measurement (shaping) time. Thermal noise in resistors produces a

white noise, *i.e.* a noise power density independent of frequency. Hence limiting the bandwidth by a shaper, *i.e.* increasing the shaping time, will decrease the noise at the expense of slowing down the detector response. Usually, resistors shunting the input act as noise current sources and resistors in series with the amplifier input act as noise voltage sources, so that they are often referred to as "parallel" and "series" noise. Thermal fluctuations in the bias resistor result in fluctuations of the voltage at point P in Fig. 35.31 and its noise current source $\langle i_b^2 \rangle$ has the same effect as the shot noise current $\langle i_d^2 \rangle$ from the detector. Conversely, the series resistor R_s acts as a voltage noise generator $\langle v_s^2 \rangle$ for the amplifier input.

Shot noise and thermal noise have a "white" frequency distribution, *i.e.* the (power) spectral densities (f = frequency) $d\langle i^2 \rangle/df$ and $d\langle v^2 \rangle/df$ are constant with magnitudes

$$\begin{aligned} d\langle i_d^2 \rangle &= 2eI_d \, df \,, \\ d\langle i_b^2 \rangle &= \frac{4kT}{R_b} \, df \,, \\ d\langle v_s^2 \rangle &= 4kTR_s \, df \,, \end{aligned} \tag{35.26}$$

where e is the elementary charge, I_d the detector leakage current, and k,T Boltzmann constant and temperature. Hence, in a 1 kΩ resistor at room temperature, for example, one finds a current-independent thermal noise of $\sqrt{d\langle i^2 \rangle/df} = 4\,\mathrm{pA}/\sqrt{\mathrm{Hz}}$ or $\sqrt{d\langle v^2 \rangle/df} = 4\,\mathrm{nV}/\sqrt{\mathrm{Hz}}$, respectively. For $1/f$ noise, by contrast, the spectral power density is proportional to $1/f^\alpha$ ($\alpha = 0.5$–2) with a device specific proportionality constant. In what follows, we will assume $\alpha = 1$ for simplicity reasons, noting though that more complex models exist.

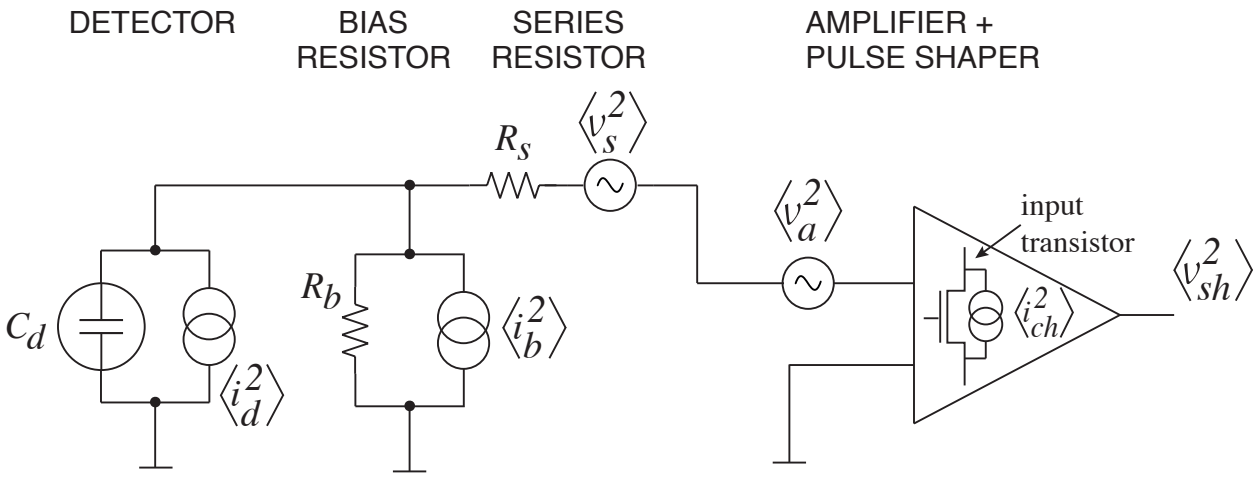

Figure 35.32: Equivalent circuit diagram for noise analysis.

An important noise source is the preamplifier input stage, very often dominated by the first amplification transistor. In what follows we assume a MOSFET at this point, as the large majority of amplification circuits is based on MOS transistors. Noise sources in bipolar amplification is shortly mentioned at the end of this section. A MOS transistor's channel features thermal noise with "resistance" $1/g_m$, where $g_m = \partial I/\partial V$ is the transconductance. Correction factor(s) for parametrization depend on the transistor operation point. Conventionally, a factor γ is applied varying between 0.5 and 1 when temperature dependence is implicit, but is commonly taken as $\gamma \approx 2/3$ for operation in strong inversion and 0.5 in weak inversion.

In addition, especially in MOSFETs, there is $1/f$ noise originating from trapping/detrapping processes of charge carriers at the channel's Si–SiO_2 interface. The channel's current noise is equivalent to a voltage noise at the transistor input (the gate) via

$$\langle i_{ch}^2 \rangle = \langle (g_m v_a)^2 \rangle \tag{35.27}$$

leading to respective noise power spectral densities of

$$\frac{d\langle v_a^2 \rangle}{df} = 4kT\gamma \frac{1}{g_m} + K_f \frac{1}{C'_{ox} W L} \frac{1}{f}\,, \tag{35.28}$$

where the individual (uncorrelated) noise contributions add in quadrature. The "$1/f$ noise constant" K_f has magnitude in the order of 10^{-24} – 10^{-26}J depending on the device type and the technology[8]. C'_{ox} is the oxide capacitance per unit area, and W, L are width and length of the gate.

Particle and radiation detectors typically convert the deposited energy into charge (usually e-ion or e-h pairs) which can be measured by integrating the current induced on an electrode by the drifting charge pairs (see *e.g.* Sec. 35.8) employing a "charge-sensitive (pre)amplifier" (CSA), realized by feeding back the preamp's output to the input through capacitor C_f (dashed circuit part of Fig. 35.31). The feedback capacitance must be discharged for the next pulse to appear, for example by a resistor, a (constant) current source or a switch. Noise contributions from such components can usually be kept small in comparison.

For a CSA the noise output voltage after the preamplifier $\langle v_{pa}^2 \rangle$ relates to the input (current or voltage) noise sources via the transimpedance $1/\omega C_f$ as

$$\left\langle v_{pa}^2 \right\rangle = \left\langle i_{in}^2 \right\rangle \left(\frac{1}{\omega C_f} \right)^2 \quad \text{or} \quad \left\langle v_{pa}^2 \right\rangle = \left\langle v_{in}^2 \right\rangle \left(\frac{\omega C_D}{\omega C_f} \right)^2 \tag{35.29}$$

with $\omega = 2\pi f$. The capacitance C_D includes the detector capacitance C_d plus all capacitances shunting the input. Considering only the (usually) dominant noise sources, being the detector shot noise as well as the transistor channel noise, and neglecting the resistor parallel and serial noise sources of (35.26) by choosing R_b large and keeping R_s small, one obtains

$$\frac{d\left\langle v_{pa}^2 \right\rangle}{d\omega} = \sum_{k=-2}^{0} c_k\, \omega^k \tag{35.30}$$

with

$$c_{-2} = \frac{e}{\pi} I_d \frac{1}{C_f^2}\,, \quad c_{-1} = K_f \frac{1}{C'_{ox} W L} \frac{C_D^2}{C_f^2}\,, \quad c_0 = \frac{2\gamma}{\pi} kT \frac{1}{g_m} \frac{C_D^2}{C_f^2}\,, \tag{35.31}$$

which correspond to the discussed main noise components, c_{-2}: shot noise, c_{-1}: $1/f$ noise, c_0: thermal noise, respectively.

The filtering effect of the shaper limits the bandwidth of the system and is generally described by a transfer function $H(\omega)$ for $\langle v_{pa}^2 \rangle$ integrated over the full bandwidth

$$\left\langle v_{\rm sh}^2 \right\rangle = \int_0^\infty \frac{d\langle v_{\rm pa}^2 \rangle}{d\omega}\, |H(\omega)|^2\, d\omega \tag{35.32}$$

with $\langle v_{sh}^2 \rangle$ being the shaper output voltage noise. $H(\omega)$ depends on the filter circuit, *i.e.* the shape of the pulse formed by the shaper, and is characterized by a characteristic time τ, the shaping time,

[8] Other $1/f$ noise parametrizations also exist with correspondingly different numerical values for K_f.

which can, for example, be the peaking time of a semi-gaussian pulse or the sampling interval in a correlated double-sampler (see *e.g.* [8]). The peaking time is an important quantity for readout systems since for peaking times large compared to the duration of the input signal the amplitude at peaking time corresponds to the total input charge.

For a simple time-invariant CR–RC filter, consisting of a high-pass followed by a low-pass filter with equal time constants, the transfer function is

$$|H(\omega)|^2 = A^2 \left(\frac{\omega\tau}{1+\omega^2\tau^2} \right)^2 \tag{35.33}$$

and (35.30) becomes

$$\left\langle v_{\mathrm{sh}}^2 \right\rangle = \frac{\pi}{4} A^2 \left(c_{-2}\,\tau + \frac{2}{\pi} c_{-1} + c_0 \frac{1}{\tau} \right) \tag{35.34}$$

with A being an overall gain factor.

The system noise for a charge measurement is conveniently expressed as an equivalent noise charge (ENC) referring the noise to the equivalent signal of one electron at the input:

$$\mathrm{ENC}^2 = \frac{\langle v_{\mathrm{sh}}^2 \rangle}{v_{\mathrm{signal}}^2(1e^-)}\,. \tag{35.35}$$

While being dimensionless by definition, ENC is commonly expressed as an equivalent number of electrons (e^-) at the input or alternatively as equivalent Coulombs (C) when multiplying by the elementary charge or as equivalent deposited energy (eV), where $1e^-$ equivalent charge corresponds to 3.65 eV of equivalent deposited energy in Si (see Tab. 35.10 in Sec. 35.8).

A charge of one electron at the input yields a voltage signal (peak) behind the shaper of $v_{\mathrm{signal}} = \dfrac{A}{2.71}\dfrac{e}{C_f}$. Hence with (35.35) and (35.34) one obtains:

$$\begin{aligned} \mathrm{ENC}^2\,(e^{-2}) &= \frac{(2.71)^2}{4e^2} \left(eI_d\tau + 2C_D^2\,K_f \frac{1}{C'_{ox}WL} + \gamma \frac{2kT}{g_m} \frac{C_D^2}{\tau} \right) \\ &= a_{\mathrm{shot}}\,\tau + a_{1/\mathrm{f}}\,C_D^2 + a_{\mathrm{therm}}\,\frac{C_D^2}{\tau}\,, \end{aligned} \tag{35.36}$$

where 2.71 is Euler's number resulting from the amplitude peak value behind the (CR–RC) shaper (for $t = \tau$), while e is the elementary charge and (e^-) explicitly denotes the equivalent number of electrons at the input.

Equation (35.36) accentuates the main noise dependencies of the system. The contribution from parallel current shot noise (*i.e.* detector leakage) increases with shaping time, *i.e.* with pulse duration, whereas thermal noise (here serial voltage noise at the gate, originating from transistor channel noise) decreases with increasing shaping time, *i.e.* with reduced bandwidth. Noise with a $1/f$ spectrum depends only on the ratio of upper to lower cutoff frequencies (low pass to high pass time constants) and is hence independent of τ for a given shaper topology. Furthermore, the contribution of serial noise voltage ($1/f$ and thermal noise) to ENC increases with input (detector) capacitance C_D. Pulse shapers can be designed to optimize the noise performance of a system or to mitigate operation variations with time (*e.g.* due to radiation damage) deteriorating the performance, at the expense of loss of simplicity. For example, a shaper with one high-pass filter followed by four cascaded low-pass filters, increases the pulse symmetry and tends to decrease the current noise, but increases the voltage noise contributions for the circuit of Fig. 35.32, if the same peaking time is assured by adjusting the individual time constants of the filter stages. If instead

the low-pass filters cause the peaking time of the pulse to increase, the opposite can be true. More details about shaping filters can be found *e.g.* in [8, 376–378].

Figure 35.33 shows a typical example of eq. (35.36) displaying ENC as a function of shaping time τ for a system. At short shaping times, thermal noise dominates, whereas for longer shaping times the shot noise contribution takes over. The total noise has a minimum at a shaping time where shot and thermal noise contributions are equal. The minimum is flattened by the presence of $1/f$ noise. Increasing the detector capacitance increases the thermal and $1/f$ contributions and shifts the noise minimum to larger shaping times. One can hence exploit the shaping time dependence of the total noise to determine the individual noise contributions of a system.

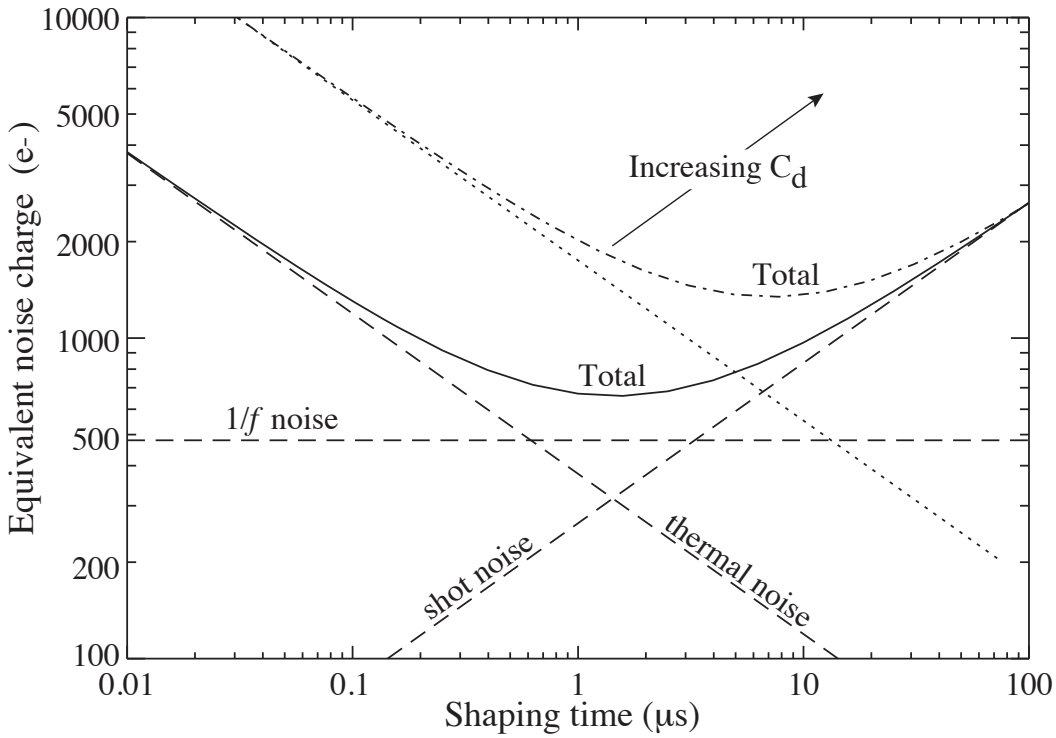

Figure 35.33: Equivalent noise charge *vs* shaping time. Changing the detector capacitance C_D affects thermal and $1/f$ noise contributions and moves the noise minimum as indicated by the dotted and dash-dotted lines. The $1/f$ noise contribution is small for the chosen parameters ($C_D = 20\,\text{pF}$, $I_d = 10\,\text{nA}$, $g_m = 1\,\text{mS}$) in this example.

For quick estimates (35.36) is cast into a useful equation for a typical CSA-shaper system [1]:

$$\text{ENC}^2\,(e^{-2}) = 11\,\frac{I_d}{\text{nA}}\,\frac{\tau}{\text{ns}} + 740\,\frac{1}{WL/(\mu\text{m}^2)}\,\frac{C_D^2}{(100\,\text{fF})^2} + 4000\,\frac{1}{g_m/\text{mS}}\,\frac{C_D^2/(100\,\text{fF})^2}{\tau/\text{ns}}\,, \qquad (35.37)$$

where $\gamma = 2/3$, $K_f = 33 \times 10^{-25}\text{J}$, and $C'_{ox} = 6\ \text{fF}/\mu\text{m}^2$ has been used, the latter being typical for CMOS technologies as employed for example for the detector readout chips of the LHC experiments and their upgrades. Generally, noise performance is improved by reducing the detector capacitance and the leakage current, judiciously selecting all resistances in the input circuit, and by choosing the optimum shaping time constant τ. Another noise contribution to consider is the fact that noise can cross-couple from the neighbouring front-ends in detectors with structured electrodes through the inter-electrode capacitance.

As mentioned, the noise parameters of the amplifier depend primarily on the input device (input transistor(s)). In field-effect transistors, the input noise current contribution of the transistor itself is very small. Hence, if the experiment's time structure permits, reducing the detector leakage current and increasing the bias resistance will allow long shaping times with correspondingly lower noise. For amplifiers employing bipolar transistors, shot noise sources originate from both, base-emitter and collector-base, junctions and from the series resistance at the base which is especially important for small structures optimized for radiation hardness. For the shot-noise contribution, the input base current I_B sets a lower bound on the noise current, such that these devices are best at short shaping times.

35.9.2.0.1 Examples Using (35.37) one finds for a typical pixel detector (before heavy irradiation) with $C_D = 200\,\mathrm{fF}$, $I_d = 1\,\mathrm{nA}$, $\tau = 50\,\mathrm{ns}$, $W = 20\,\mu\mathrm{m}$, $L = 0.5\,\mu\mathrm{m}$, $g_m = 0.5\,\mathrm{mS}$:

$$\mathrm{ENC}^2 \approx (24\,e^-)^2\Big|_{\mathrm{shot}} + (17\,e^-)^2\Big|_{1/\mathrm{f}} + (25\,e^-)^2\Big|_{\mathrm{therm}} \approx (40\,e^-)^2\,.$$

For a typical silicon microstrip detector after radiation damage (fluence $\gtrsim 10^{14}\mathrm{n_{eq}/cm^2}$, assuming no degradation of the front-end electronics due to radiation) one obtains for $C_D = 20\,\mathrm{pF}$, $I_d = 1\,\mu\mathrm{A}$, $\tau = 50\,\mathrm{ns}$, $W = 2000\,\mu\mathrm{m}$, $L = 0.4\,\mu\mathrm{m}$, $g_m = 5\,\mathrm{mS}$:

$$\mathrm{ENC}^2 \approx (750\,e^-)^2\Big|_{\mathrm{shot}} + (200\,e^-)^2\Big|_{1/\mathrm{f}} + (800\,e^-)^2\Big|_{\mathrm{therm}} \approx (1100\,e^-)^2\,.$$

Apart from the larger leakage current, the larger capacitance of strips compared to pixels leads to a much worse noise performance which can only be partially compensated by allowing more power in the amplification transistor, *i.e.* by increasing g_m.

A liquid argon calorimeter cell is a suitable example of a detector with a large electrode capacitance with typical parameters (similar to the ATLAS central electromagnetic calorimeter, see Sec. 35.10). Using $C_D = 1.5\,\mathrm{nF}$, $I_d = < 2\,\mu\mathrm{A}$, $\tau = 50\,\mathrm{ns}$, $W = 3000\,\mu\mathrm{m}$, $L = 0.25\,\mu\mathrm{m}$, $g_m = 100\,\mathrm{mS}$, one obtains:

$$\mathrm{ENC}^2 \approx (1000\,e^-)^2\Big|_{\mathrm{shot}} + (15000\,e^-)^2\Big|_{1/\mathrm{f}} + (13500\,e^-)^2\Big|_{\mathrm{therm}} \approx (20200\,e^-)^2\,.$$

Here only a small (negligible) parallel shot noise (leakage current) contribution is assumed, which is typical for liquid argon calorimeters.

Practical noise levels range from $\sim 1e^-$ for CCD's at long shaping times to $\sim 10^4\,e^-$ in high-capacitance liquid argon calorimeters. Gaseous micropattern detectors like GEMs or MicroMegas (see Sec. 35.6.4) typically feature noise levels between $1000\,e^-$ and $1500\,e^-$, depending on the ability to correct for common-mode noise. Silicon strip detectors typically operate at levels of $\sim 10^3\,e^-$, whereas pixel detectors with fast readout typically have noise levels below about 100 electrons.

35.9.3 *Timing measurements*

In timing measurements, the slope-to-noise ratio must be optimized, rather than the signal-to-noise ratio alone, so the rise time t_r of the pulse is important. The "jitter" σ_t of the timing distribution is

$$\sigma_t = \frac{\sigma_n}{(dS/dt)_{\mathrm{trig}}} \approx \frac{t_r}{SNR}, \tag{35.38}$$

where σ_n is the rms noise, SNR the signal-to-noise ratio and the "slew rate" dS/dt, *i.e.* the derivative of the signal, is evaluated at the trigger level. The rise-time of a CSA again depends on the detector and feedback capacitances and on the amplifier transconductance

$$t_r \propto \frac{C_D}{C_f \cdot g_m}\,. \tag{35.39}$$

To increase dS/dt without incurring excessive noise, the amplifier bandwidth should match the rise time of the detector signal. The 10% to 90% rise time of an amplifier with bandwidth f_U is $0.35/f_U$. For example, an oscilloscope with 350 MHz bandwidth has a 1 ns rise time. For cascaded amplifiers, the individual rise times add in quadrature to first order.

As increasing SNR also improves the time resolution, minimizing the total input capacitance is extremely important for timing measurements (see also Sec. 35.8). At high signal-to-noise ratios, the time jitter can be much smaller than the rise time. The time-mark distribution of pulses may shift with the signal level ("time walk"), but this can be corrected by various means, either in hardware or in software.

For applications aiming at extreme time resolution charge-sensitive (integrating) amplification can be less optimal. Transimpedance or voltage amplifiers converting current/voltage to voltage are usually preferred. Also, when aiming for picosecond timing using voltage amplifiers, *e.g.*, with LGAD detectors having C_D of $\mathcal{O}$(pF) (see Sec. 35.8), not only the preamplifier rise time t_r but also the signal pulse duration t_d at the preamplifier input is important, *i.e.*, the preamplifier must react draining the charge from C_D before the input voltage $v_{in} = Q_S/C_D$ (Q_S = signal charge) reaches its peak. Both times must reasonably match, $t_r \approx t_d$, resulting in a time jitter of [379]

$$\sigma_t^2 \approx \frac{C_D^2}{Q_S^2} \frac{d\langle v_n^2 \rangle}{df}\, t_d\,, \tag{35.40}$$

where $d\langle v_n^2 \rangle/df$ is the voltage noise spectral density.

35.9.4 *Digital signal processing*

The filtering principles apply to both analog and digital signal processing. In digital signal processing the pulse shaper shown in Fig. 35.31 is replaced by an analog to digital converter (ADC) followed by a digital processor that determines the pulse shape. Digital signal processing allows great flexibility in implementing filtering functions. The software can be changed readily to adapt to a wide variety of operating conditions and it is possible to implement filters that are impractical or even impossible using analog circuitry. However, this comes at the expense of increased circuit complexity and increased demands on the ADC compared to analog shaping.

If the sampling rate of the ADC is too low, high frequency components will be transferred to lower frequencies ("aliasing"). The sampling rate of the ADC must be high enough to capture the maximum frequency component of the input signal. Apart from missing information on the fast components of the pulse, undersampling introduces spurious artifacts. If the frequency range of the input signal is much larger than the sampling rate, the noise at the higher frequencies will be transferred to lower frequencies and will increase the noise level in the frequency range of pulses formed in the subsequent digital shaper. The Nyquist criterion states that the sampling frequency must be at least twice the maximum relevant input frequency. This requires that the bandwith of the circuitry preceding the ADC must be limited. The most reliable technique is to insert a low-pass filter.

The digitization process also introduces inherent noise, since the voltage range ΔV corresponding to a minimum bit step introduces quasi-random fluctuations relative to the exact amplitude

$$\sigma_n = \frac{\Delta V}{\sqrt{12}}\,. \tag{35.41}$$

When the Nyquist condition is fulfilled the noise bandwidth Δf_n is spread nearly uniformly and extends to 1/2 the sampling frequency f_S, so the spectral noise density is

$$\frac{\sigma_n}{\sqrt{\Delta f_n}} = \frac{\Delta V}{\sqrt{12}} \cdot \frac{1}{\sqrt{f_S/2}} = \frac{\Delta V}{\sqrt{6 f_S}}\,. \tag{35.42}$$

Sampling at a higher frequency spreads the total noise over a larger frequency range, so oversampling can be used to increase the effective resolution. In practice, this quantization noise is increased by the ADC's differential non-linearity (DNL). Furthermore, the equivalent input noise of ADCs is often rather high, so the overall gain of the stages preceding the ADC must be sufficiently large for the preamplifier to override the ADC input noise.

35.9.5 *What to use when?*

When implemented properly, digital signal processing provides significant advantages in systems where the shape of detector signal pulses changes greatly, for example in large semiconductor detectors for gamma rays or in gaseous detectors (*e.g.* TPCs) where the duration of the current pulse varies with drift time, which can range over orders of magnitude. Analog signal processing is best or most efficient in systems that require fast time response, but the high power requirements of high-speed ADCs are prohibitive. Systems that are not sensitive to pulse shape can use fixed shaping time constants and rather simple filters (like CR–RC), which can be either continuous or sampled. In high-density systems that require small circuit area and low power (*e.g.*, in strip and pixel detectors), analog filtering often yields the required response and tends to be most efficient.

As stressed already in the introduction, it is important to consider that additional noise is often introduced externally. Recognizing additional noise sources and minimizing cross-coupling to the detector current loop is often essential to obtain the best overall noise performance. Understanding basic physics and its practical effects is important in forming a broad view of the detector system and recognizing potential problems (*e.g.* modified data), rather than merely following standard recipes.

More comprehensive treatments of low noise detector readout and signal processing can be found, for example, in [8, 376, 378] and in [1, 363].

35.10 Calorimeters

35.10.1 *Introduction*

Revised August 2023 by F. Sefkow (DESY, Hamburg) and F. Simon (KIT).

A calorimeter measures the energy and direction of particles by absorption in the detector material and registration of the energy deposited in an (ideally) contained electromagnetic (EM) or hadronic shower. Calorimeters are central components of modern high energy physics experiments, due to their ability to measure not only the energy of charged particles (with the exception of muons), but also of photons and neutral hadrons, thus enabling the reconstruction of π^0 and η decays and of exclusive final states involving long-lived neutral kaons, or neutrons. They are indispensable for the measurement of particle jets and for the reconstruction of total event properties, which, via the measurement of missing energy (or missing transverse energy in hadron colliders). enable the detection of the presence of "invisible" particles such as neutrinos and hypothetical particles such as dark-matter candidates. Calorimeters are also important for the identification of particle species, using information on the longitudinal and transverse shape of the energy deposition to separate electrons, photons, hadrons and muons. While the performance of calorimeters is typically assessed by the quality of their energy measurements, position resolution, both for EM and hadronic showers, is also highly relevant, for example for the reconstruction of effective jet masses. The capability to measure high-level observables that serve to classify events, such as particle and jet energies, missing energy and isolated leptons, makes calorimeters central components of the trigger systems in high-energy physics experiments.

In collider experiments, the importance of calorimeters tends to increase with increasing collision energies since the relative energy resolution improves with increasing particle energy while the depth required for full containment of the showers shows only logarithmic growth with energy. This

is in contrast to the precision of track-based measurements, which is decreasing with increasing momentum. With recent advances in timing capabilities calorimeters are also contributing to the rejection of pile-up from multiple interactions within the same bunch crossings at colliders.

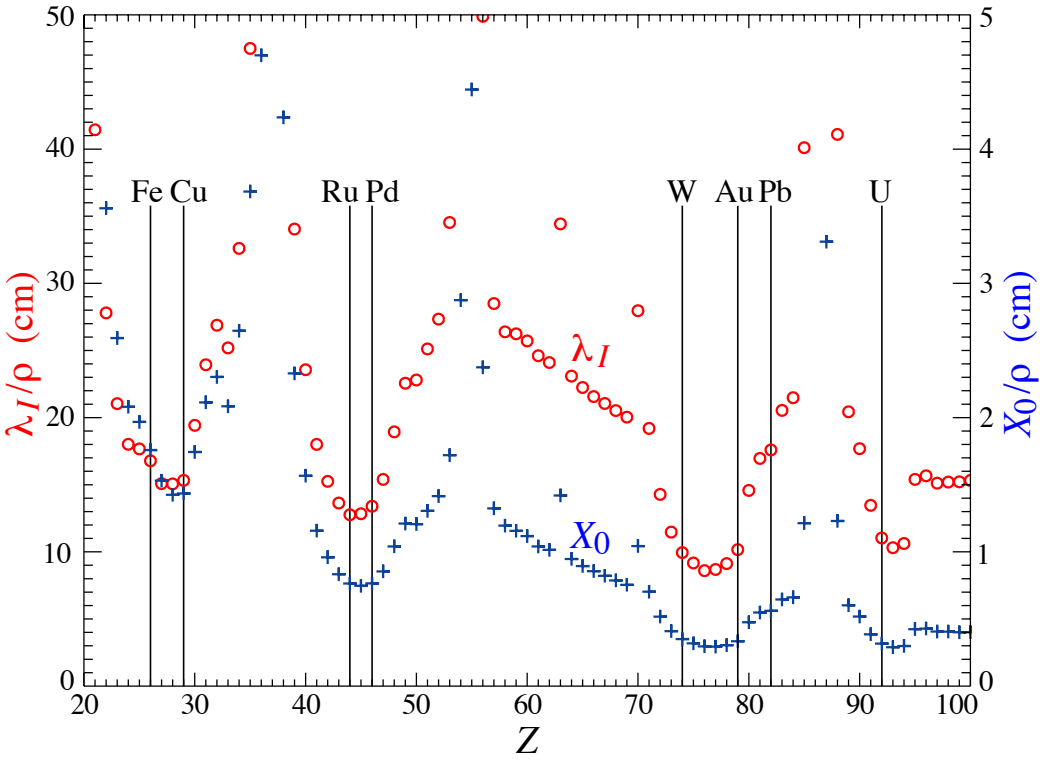

Figure 35.34: Nuclear interaction length λ_I/ρ (circles) and radiation length X_0/ρ (+'s) in cm for the chemical elements with $Z > 20$ and $\lambda_I < 50$ cm.

The characteristic length scale for EM showers is the radiation length X_0, which ranges from 1.8 cm (13.8 g cm^{-2}) in iron to 3.2 mm (6.0 g cm^{-2}) in uranium for materials used to generate showers in calorimeters.[9] Similarly, the characteristic nuclear interaction length λ_I varies from 16.8 cm (132.1 g cm^{-2}) (Fe) to 11.0 cm (209 g cm^{-2}) (U).[10] There is a premium on small λ_I/ρ and X_0/ρ (both with units of length). These quantities are shown for elements with $Z > 20$ in Fig. 35.34. The minima for both X_0 and λ_I correspond to elements between W and Au. Some of these elements are very difficult to work with (e.g. W) or expensive (e.g. Au), so, depending on the application (size of the required calorimeter) other materials, such as Fe, Cu, Pb, and different alloys like brass and CuW are often chosen. For EM calorimeters high Z is preferred; here Pb is a popular choice, while W provides even higher density and is generally affordable due to the limited volume of EM systems.

Most existing calorimeters are subdivided into a front EM section (ECAL) and a hadronic part (HCAL) behind; electrons and photons are measured in the ECAL, while hadrons and jets are measured in the combined ECAL and HCAL system. The detailed design depends on energy range and performance requirements as well as on size and cost constraints for the entire system. EM calorimeters tend to be 15–30 X_0 deep, while hadronic calorimeters are usually optimised for cost and performance at 5–8 λ_I. The depth of the ECAL typically corresponds to approximately

[9] $X_0 = 120\ \mathrm{g\,cm^{-2}}\ Z^{-2/3}$ to better than 5% for $Z > 23$.
[10] $\lambda_I = 37.8\ \mathrm{g\,cm^{-2}}\ A^{0.312}$ to within 0.8% for $Z > 15$.
See https://pdg.lbl.gov/current/AtomicNuclearProperties for actual values.

1 λ_I, with the exact value depending on the material. This means that approximately 70% of all hadronic showers will already begin in the electromagnetic calorimeter, making its response to a hadronic cascade highly relevant for the overall performance of the system. The choice of the calorimeter technology for the ECAL is thus a result of simultaneous optimisation for EM and hadronic performance of the overall system.

Sampling calorimeters consist of a high-density, normally metallic absorber sandwiched (or threaded) with an active material which generates a signal in response to shower particles. The active medium may be a scintillator, a noble liquid, a gas, silicon, or a Cherenkov radiator. These active media all have a relatively low Z, a significantly lower density, and larger X_0 and λ_I values than typical absorber materials. The average radiation and interaction lengths in the full detector are thus larger than those of the absorber alone.

There are also *homogeneous calorimeters*, in which the entire volume contributes to the signal. Homogeneous calorimeters may be built with inorganic heavy scintillating crystals or non-scintillating Cherenkov radiators such as lead glass and lead fluoride. Nuclear interaction lengths in inorganic crystals range from 17.8 cm ($LuAlO_3$) to 42.2 cm (NaI). Materials with low X_0 used in large systems are for example BGO with $\lambda_I = 22.3\,\text{cm}$ and $X_0 = 1.12\,\text{cm}$, and $PbWO_4$ (20.3 cm and 0.89 cm). Properties of these and other commonly used inorganic crystal scintillators can be found in Table 35.4. Cryogenic noble liquids, where scintillation light and/or inonization can be detected, are also suitable materials for homogeneous detectors.

Homogeneous calorimeters at colliders are usually only used for the EM section. For the use of homogeneous calorimeters for hadron energy measurement, the large differences in the response to EM and hadronic parts of the shower are a significant challenge, as is the three-dimensional segmentation. This is still requiring substantial R&D, including the search for affordable materials. In non-accelerator physics experiments or at neutrino beams, homogeneous calorimeters, where the sensitive medium can be water or ice, scintillator, a noble liquid or the atmosphere itself, are used to detect both EM and hadronic showers.

Comprehensive tables of particle-physics calorimeters are given as Appendix C in Ref. [380].

35.10.1.1 *Energy Resolution and System Performance*

The energy resolution of calorimeters is a complex observable, due to the variety of contributing processes with different energy dependencies, and response functions often not perfectly Gaussian. Nevertheless, a simplified picture is useful in practice, and in particular for EM calorimeters also numerically accurate. For hadronic calorimeters additional complications must be taken into account. In such a simplified picture, due to the stochastic nature of shower evolution, the intrinsic calorimeter energy resolution, σ, is proportional to $\sqrt{E}$, as the number of charged particles, or the total ionising track length in a shower are on average proportional to the incident particle energy E. The relative resolution σ/E therefore improves with $A/\sqrt{E}$, where A denotes the so-called *stochastic term*. The readout system of the active medium will contribute noise to the resolution, $\sigma_N = B$, which in general is not energy-dependent. Effects that are proportional to the total deposited energy result in a *constant term*, $\sigma_C = C \cdot E$. Different sources contribute to this term, depending on the type of calorimeter. For both EM and hadronic calorimeters, imperfections of the detector, inhomogeneities such as density variations or those introduced by the detector mechanics, instabilities in time, imperfections of the readout or incorrect calibration of channels contribute. Shower leakage, which depends on particle energy, also contributes to the resolution with approximately linear dependence on energy. In non-compensating hadronic calorimeters, fluctuations of the EM fraction f_{em} from shower to shower, together with the energy dependence of the average f_{em} value, can lead to a significant constant term that often dominates over the instrumental effects. Adding up all contributions in quadrature yields the standard parameterisation of the relative

energy resolution of a calorimeter:

$$\frac{\sigma}{E} = \frac{A}{\sqrt{E}} \oplus \frac{B}{E} \oplus C\,. \tag{35.43}$$

In particular the effects specific to hadronic showers give rise to non-Gaussian distributions of the energy response. Therefore care must be used in performance comparisons, as different parameterisations of the line shape and different definitions of the resolution are in use. In some cases, a linear rather than a quadratic addition of the stochastic and constant term may provide a better description of the energy resolution as a function of energy. It should be noted that the individual terms then lose the simplified interpretation discussed above, and care has to be taken when comparing performance based on fits to the energy dependence of the resolution.

Typically, primarily the stochastic term — which is determined by the calorimeter design in terms of material and geometry — is considered in order to describe the overall properties of a calorimeter. For the calorimeters of the multi-purpose experiments at the LHC, the stochastic terms are $3-10\%$ for electromagnetic and $50-80\%$ for hadronic calorimeters. In practice, the energy resolution of a calorimeter at high energies is limited by the constant term C, which in the EM case mainly reflects the precision and stability of the mechanical construction, electronic readout system and calibration. Typical constant terms are a few per-mil for EM and a few percent for hadronic calorimeters. For concrete examples and references see Tables 35.11 and 35.13.

For sampling calorimeters, the stochastic term depends on the *sampling fraction* f_{samp}, i.e. the ratio of energies deposited in the active and passive material. Also the *sampling frequency* enters, which is determined by the number N of different sampling elements present in the region in which the shower develops. The stochastic term A scales approximately with $1/\sqrt{f_{\text{samp}}}$, and for given f_{samp} and total depth, with $1/\sqrt{N}$.

While the energy resolution for single hadrons (most commonly pions) is often used as the key performance criterion for a hadronic calorimeter, it has to be noted that this value is only of limited relevance in high-energy physics experiments. In most experiments, the calorimetric measurement of hadrons is based on the combined system consisting of ECAL and HCAL. Moreover, for the physics capabilities of a detector at a high-energy particle collider, also the combined calorimetric resolution for single hadrons is not a sufficient criterion to fully characterise hadronic performance, but rather the jet energy resolution, the resolution for missing (transverse) energy, and the capability to cope with high background and pile-up levels. These quantities cannot be measured directly with prototypes in beam tests, and strongly depend on overall system aspects and reconstruction tools. However, the performance in these observables can be reliably inferred from system simulations once the simulated response to single particles and the simulated topology of showers has been validated in detail by beam tests.

Besides energy resolution, response linearity is an important factor in the design of calorimeters. While a non-linear response for single particles can be corrected for if appropriate calibration measurements exist, such corrections deteriorate the energy resolution, in particular in the case of superposition of several showers, as it often occurs in jets. Sources for non-linearities can be intrinsic to the design, for example due to saturation effects in the active medium with increasing energy density, due to leakage, or connected to shower physics as discussed in section 35.10.3.

The energy resolution for hadrons is intrinsically limited by large event-to-event fluctuations of the shower evolution and of "invisible" components not contributing to the detector signal. It remains the limiting factor for single particles and for the high-level performance for jets and total event properties. This has motivated intense research in the past decades. One direction aims at improving the hadronic resolution by extracting additional signals to disentangle the shower composition, e.g.with so-called dual read-out methods, and is explained in the hadron calorimeter section 35.10.3. Another, so-called "particle flow" approach described below optimises the combination of

measurements of individual particles in different detector components. Ideally, both methods can be combined.

35.10.1.2 *Role of Simulations*

Simulations have become indispensable for the design of detectors and the development of reconstruction algorithms. Since event-to-event fluctuations drive calorimeter performance, Monte Carlo techniques that accurately model the evolution of particle cascades in material are required. By far the most common computer code in use today is the *GEANT4* toolkit [381, 382], which provides a step-based simulation of the passage of particles through matter. Thanks to the relative simplicity of EM cascades, simulations of EM showers are typically highly accurate. The modelling of hadronic showers is more complex, and suffers from larger uncertainties. Significant improvement has been achieved in this area, moving from simpler parameterised models to physics-driven interaction models. From early on, detailed codes and data describing nuclear break-up and neutron transport like *CALOR* [383] or *FLUKA* [384,385] contributed crucially to the understanding of hadron calorimetry. The simulations reproduce the general features of the substructure of hadronic showers, characterised by dense shower activity and sparser ionising track segments, and their accuracy is adequate for most purposes of quantitative design optimisations. Details of the implementation of physics models in *GEANT4* are discussed in [386].

35.10.1.3 *Particle flow approach*

In a typical collider experiment, the EM and hadronic calorimeter system surrounds a charged-particle tracking volume devised for momentum measurement in a magnetic field. Matching tracks to calorimetric energy deposits provides corrections for the magnetic deflection of the charged particles, necessary for the reconstruction of invariant masses in multi-jet final states, or of the total momentum imbalance. Furthermore, for charged particles the track-based measurements are far more precise for particles in jets with energies of up to several hundred GeV, so using these instead of calorimeter energies may optimise the jet energy resolution. This so-called "particle flow" approach aims at reconstructing each particle individually, using a combination of the best measurements from the detector.

About 60% of the energy in a typical jet is carried by charged particles, predominantly hadrons, 30% by photons and only 10% by long-lived neutral hadrons (K_L^0 and n), for which hadronic calorimetry is unavoidable. Assuming, as motivated by detector designs proposed for a future Higgs factory, $15\%/\sqrt{E(\mathrm{GeV})}$ for photons and $55\%/\sqrt{E(\mathrm{GeV})}$ for hadrons, then, in the ideal case, where each particle is resolved, a jet energy resolution of $19\%/\sqrt{E(\mathrm{GeV})}$ could be obtained. Here the dominant part ($18\%/\sqrt{E(\mathrm{GeV})}$) is still due to the calorimeter resolution for neutral hadrons.

The particle flow method places high demands on the imaging capabilities of the calorimeters, and on the pattern recognition performance of the reconstruction algorithms. Only energy deposits not associated with charged particles and not identified as photons, will be interpreted as neutral hadrons. In practice, this cannot always be done unambiguously, and mis-assignments give rise to an additional measurement uncertainty, which is called *confusion*. For simulated detectors at proposed future Higgs factories jet energy resolutions of 3-4% have been demonstrated, significantly larger than in the ideal case, but sufficient for the required efficient separation of W and Z hadronic final states.

Particle flow-like techniques were first applied in the ALEPH detector [387], which achieved a jet energy resolution of $60\%/\sqrt{E}$, or 6.2 GeV for hadronic Z decays. More recently, particle flow techniques are successfully used in the CMS experiment [388], for example improving the missing energy resolution by one third over a wide range.

The Pandora particle flow algorithm (PFA) [389] is the most developed and best performing today in the context of future lepton colliders. The algorithms make use of topological information,

including the sub-structure of showers, as well as the compatibility of calorimetric and track-based measurements. In this way the purely calorimetric performance for the jet is either retained or improved. In the framework of studies for CLIC [390], it was shown that the required jet energy resolution of 3.5% can be achieved with the PF technique for jet energies up to 1500 GeV.

For the use of energy-momentum matching in the assignment of energy depositions, and for energy flow treatment of dense jets, particle flow calorimeters with their emphasis on imaging must still feature a good energy resolution. Furthermore, the neutral hadron energy uncertainty is the dominant contribution to the jet resolution for low energy jets, where particles are well separated, while at higher energies the confusion effects take over.

High granularity in all three space dimensions comparable to or smaller than the length scales of particle showers given by X_0 and ρ_M for both ECAL and HCAL brings additional advantages; for example it offers ideal conditions for the application of software compensation methods, which improves the intrinsic resolution and also reduces "confusion" [391]. A particular strength is the possibility to use topological information such as the reconstructed starting point of the shower for the estimation of leakage. Moreover, the combination of fine-grained topological reconstruction and cuts on cluster-wise timing with a precision of few tens of pico-seconds allows for powerful pile-up rejection. This extends the application range of particle flow methods towards collider environments with less benign background conditions, like multi-TeV e^+e^- collisions, and it is an asset on its own for high-intensity hadron colliders, even if particle flow methods are difficult to apply.

The performance of highly granular calorimeters depends, among others, on the particle separation and pattern recognition capabilities and on the single particle energy and timing resolution. They are thus not only optimised for energy measurement, but also for multi-dimensional shower reconstruction and particle separation in space and time. The potential of such calorimeters can be further enhanced by combining a fine spatial segmentation with maximised information on energy, time, and possibly the nature of the energy deposition, for example by using dual-readout methods. This may be achieved, for example, by combining multiple optical materials sensitive to different components in the shower in finely segmented sandwich calorimeters, or by using timing information to extract the position of the energy deposition along a fibre. For future collider experiments, different approaches based on silicon, scintillator, noble liquid, fibre and crystal readout are being pursued [392]. They all foresee, with different level of emphasis, high granularity to enable the application of particle flow methods, and in some cases to further enhance their performance by additional information not exploited in current algorithms. One such example is the proposal [393] to benefit from the superior electromagnetic energy performance of crystals to pair photons from π^0 decays and thereby resolve jet finding ambiguities to improve the jet energy resolution.

35.10.2 *Electromagnetic calorimeters*

Revised August 2023 by C.L. Woody (BNL) and R.-Y. Zhu (HEP California Inst. of Technology).

The development of electromagnetic showers is discussed in the section on "Passage of Particles Through Matter" (Sec. 34 of this *Review*). Formulae are given which approximately describe average showers, but since the physics of electromagnetic showers is well understood, a detailed and reliable Monte Carlo simulation is possible. EGS4 [394] and GEANT [381] have emerged as the standards.

Electromagnetic calorimeters are devices that are designed to measure the total energy of electrons and photons by total absorption. They come in two general categories: homogeneous and sampling. In a homogeneous calorimeter, all of the particle's energy is deposited in the active detector volume and is used to produce a measurable signal (either scintillation light, Cherenkov light or charge). Homogeneous electromagnetic calorimeters are typically constructed using high density,

Table 35.11: Resolution of typical electromagnetic calorimeters. E is in GeV.

Technology (Experiment)	Depth	Energy resolution	Date
NaI(Tl) (Crystal Ball)	$20X_0$	$2.7\%/\mathrm{E}^{1/4}$	1983
$Bi_4Ge_3O_{12}$ (BGO) (L3)	$22X_0$	$2\%/\sqrt{E} \oplus 0.7\%$	1993
CsI (KTeV)	$27X_0$	$2\%/\sqrt{E} \oplus 0.45\%$	1996
CsI(Tl) (BaBar)	16–$18X_0$	$2.3\%/E^{1/4} \oplus 1.4\%$	1999
CsI(Tl) (BELLE)	$16X_0$	1.7% for $E_\gamma > 3.5$ GeV	1998
CsI(Tl) (BES III)	$15X_0$	2.5% for $E_\gamma = 1$ GeV	2010
$PbWO_4$ (PWO) (CMS)	$25X_0$	$3\%/\sqrt{E} \oplus 0.5\% \oplus 0.2/E$	1997
$PbWO_4$ (PWO) (ALICE)	$19X_0$	$3.6\%/\sqrt{E} \oplus 1.2\%$	2008
Lead glass (OPAL)	$20.5X_0$	$5\%/\sqrt{E}$	1990
Liquid Kr (NA48)	$27X_0$	$3.2\%/\sqrt{E} \oplus 0.42\% \oplus 0.09/E$	1998
Scintillator/depleted U (ZEUS)	20–$30X_0$	$18\%/\sqrt{E}$	1988
Scintillator/Pb (CDF)	$18X_0$	$13.5\%/\sqrt{E}$	1988
SciFi/Pb spaghetti (KLOE)	$15X_0$	$5.7\%/\sqrt{E} \oplus 0.6\%$	1995
SciFi/W (sPHENIX)	$20X_0$	$13\%/\sqrt{E}$	2022
Liquid Ar/Pb (NA31)	$27X_0$	$7.5\%/\sqrt{E} \oplus 0.5\% \oplus 0.1/E$	1988
Liquid Ar/Pb (SLD)	$21X_0$	$8\%/\sqrt{E}$	1993
Liquid Ar/Pb (H1)	20–$30X_0$	$12\%/\sqrt{E} \oplus 1\%$	1998
Liquid Ar/depl. U (DØ)	$20.5X_0$	$16\%/\sqrt{E} \oplus 0.3\% \oplus 0.3/E$	1993
Liquid Ar/Pb accordion (ATLAS)	$25X_0$	$10\%/\sqrt{E} \oplus 0.4\% \oplus 0.3/E$	1996

high Z inorganic scintillating crystals such as BaF_2, BGO, CsI, CsI(Tl), LYSO, NaI(Tl) and PWO, non-scintillating Cherenkov radiators such as lead glass and lead fluoride (PbF_2), or ionizing noble liquids such as liquid argon, liquid krypton or liquid xenon. The properties of some commonly used inorganic crystal scintillators can be found in Table 35.4. Total absorption homogeneous calorimeters such as those built with heavy crystal scintillators provide the best energy resolution for measuring electromagnetic showers and are generally used when the best possible performance is required, particularly at lower energies. Attention, however, needs to be paid to radiation damage in inorganic scintillators when exposed to the typical environment of high luminosity proton colliders, as discussed below and in Section 35.4.

A sampling calorimeter consists of an active medium which generates a signal and a passive medium which functions as an absorber. In this case, most of the particle's energy is deposited in the absorber and only a fraction of the energy is detected in the active medium. The ratio of energy in the sampling medium to the total enegy in calorimeter is called the sampling fraction. The active medium may be a scintillator, an ionizing noble liquid, a semiconductor, or a gas ionization detector. The absorber is typically a heavy metal with a high Z such as lead, tungsten, iron, copper, or depleted uranium. The active material is interspersed with the passive absorber in a variety of ways, e.g. by using alternating plates of active material and absorber or embedding the active material, such as scintillating fibers, into the absorber. The main difficulty in this approach is extracting the signal from the active material. One possibility is a simple stack of alternating absorber and active material, which, however, usually leads to gaps for services and hence non-uniformities. This can be improved by using a so-called "spaghetti" design, where scintillating

fibers are brought to the front or back of the detector and read out. This can also be done with either wavelength shifting plates or fibers, such as in a so-called "shashlik" design where wavelength shifting fibers run through the stack of alternating scintillator and absorber plates and are read out at end, or embedding wavelength shifting fibers in the scintillating plates which are then brought out to the edges or back of the detector and read out. For ionization detectors, there is also an "accordion" design which avoids all gaps for services and where the absorber plates are folded into an accordion shape along with interspersed electrodes to collect the ionization charge [395]. While these readout schemes are generally more complicated than those for homogeneous calorimeters, the sampling calorimeter design allows the construction of large calorimeters at much lower cost than homogeneous calorimeters.

The energy resolution σ_E/E of a calorimeter can be parameterized as $a/\sqrt{E} \oplus b \oplus c/E$, where $\oplus$ represents addition in quadrature and E and σ_E are in GeV. The stochastic term a represents statistics-related fluctuations such as intrinsic shower fluctuations, photoelectron statistics, dead material at the front of the calorimeter, and sampling fluctuations for minimum ionizing particles. For a fixed number of radiation lengths, the stochastic term a for a sampling calorimeter is expected to be proportional to $\sqrt{t/f}$, where t is plate thickness and f is sampling fraction [396–398]. The stochastic term a is typically of the order of a few percent for a homogeneous calorimeter, and is generally in the range of 8 to 20% for sampling calorimeters, depending on the sampling fraction.

The main contributions to the systematic, or constant, term b are detector non-uniformity and calibration uncertainties. In the case of hadronic cascades discussed below, non-compensation also contributes deviations from $\sqrt{E}$ scaling. Another important contribution to the energy resolution of calorimeters that are used in high radiation environments such as high lumnosity colliders is radiation damage of the active medium. Radiation damage can induce optical absorption in scintillating materials which reduces the measured light output and produces non-uniformities in light collection. This can be mitigated by developing radiation-hard active media [399], by reducing the signal path length [400] and by frequent *in situ* calibration and monitoring [75, 398]. With effort, the constant term b can be reduced to below one percent. The term c is due mainly to electronic noise summed over the readout channels required to measure the shower energy (typically a few Molière radii).

The position resolution depends on the effective Molière radius and the transverse granularity of the calorimeter. Like the energy resolution, it can be factored as $a/\sqrt{E} \oplus b$, where a is the stochastic term, typically of the order of a few mm to 20 mm, and b can be as small as a fraction of mm for a dense calorimeter with fine granularity. Fine granularity also helps particle flow analysis discussed in the hadron calorimeters section below.

Electromagnetic calorimeters may also provide angular measurements for electrons and photons. This is particularly important for photon-related physics to identify the correct primary vertex, since photons are not detected by the tracking system of the overall experiment. The typical photon angular resolution is about 45 mrad$/\sqrt{E}$, which can be achieved by implementing longitudinal segmentation [395] for a sampling calorimeter or by adding a preshower detector [401] for a homogeneous calorimeter without longitudinal segmentation.

There have been many electromagnetic calorimeters built and used in particle physics experiments for a variety of applications. Table 35.11 provides a short list of the major ones used in some of the larger experiments. Also listed are calorimeter depths in radiation lengths (X_0) and the achieved energy resolution. Whenever possible, the performance of the calorimeters *in situ* is quoted, which is usually in good agreement with prototype test beam results as well as EGS or GEANT simulations, provided that all systematic effects are properly included. Details about detector design and performance can be found in Appendix C of reference [398] and Proceedings of the International Conference series on Calorimetry in High Energy Physics.

35.10.3 *Hadronic calorimeters*

Revised August 2021 by F. Sefkow (DESY, Hamburg) and F. Simon (KIT).

Hadronic calorimetry [380, 402, 403] is considerably more complex than electromagnetic (EM) calorimetry due to the wider range and different nature of physical processes contributing to shower development and energy deposition, which in turn are characterised by different length and time scales. Hadronic showers are initiated by inelastic strong interactions of highly-energetic charged and neutral hadrons with atomic nuclei. These interactions result in the production of secondary particles, which drive the development of the shower. Among these are energetic hadrons, as well as lower-energy nucleons, photons and nuclear fragments. Energy transferred to nuclear break-up, excitation or recoil does not, in general, produce a signal, but remains *invisible*, and event-to-event fluctuations of this invisible energy deposit ultimately limit the resolution of hadronic calorimeters (HCALs).

The length scale of the interaction of relativistic hadrons is given by the nuclear interaction length λ_I. As discussed in Section 35.10.1, λ_I is a factor 10 to 30 larger than X_0 for common materials used in the construction of calorimeters. HCALs thus require a significantly larger geometrical depth for full containment than electromagnetic calorimeters (ECALs), albeit not by the factor suggested by the ratio of λ_I/X_0 due to the different nature of the showers. A key role is played by the production of π^0s and their subsequent decay into two photons. These result in the formation of electromagnetic sub-showers which evolve on the scale given by the radiation length X_0, and thus require sufficiently fine sampling of the shower activity to capture also this electromagnetic component. The two different length scales occurring in hadronic showers, and the large fluctuations of hadronic, electromagnetic and invisible activity, result in significant event-to-event variations of the energy response and of the shower topology. This topology is characterized by a lumpy structure, with compact regions of high local energy density originating from electromagnetic sub-showers, and sparser hadronic activity with minimum-ionizing hadrons.

Figure 35.35 (left) shows the distribution of the longitudinal position of the first inelastic interaction measured for pion-induced hadronic showers with the highly-granular scintillator-steel HCAL of the CALICE collaboration [404]. The figure illustrates the exponential distribution, with a slope consistent with the pion interaction length expected from the geometry and material composition of the calorimeter. This distribution is well reproduced by simulations using GEANT4 [381, 386]. Figure 35.35 (right) shows the mean longitudinal shower profile, given by the mean energy deposition in each calorimeter layer, both relative to the front face of the calorimeter (dots, without corrections for dead cells) and relative to the measured shower starting point given by the first inelastic interaction (filled histogram). The latter is much more compact than the former, which is a convolution of the latter with the distribution of shower starting point shown in the left panel of the figure. This shows that the detector depth required for adequate shower containment is significantly influenced by the fluctuations of the position of the first hadronic interaction. Detection of this position allows for an estimate of leakage from a finite calorimeter volume, and it enables stringent tests of shower evolution models. In the past years, motivated by precision needs at the next generation of e^+e^- colliders, the CALICE collaboration has constructed a number of prototypes with high 3-dimensional spatial granularity and recorded large sets of data at test beams, allowing for studies of shower evolution processes in unprecedented detail. The refined simulations support the trend to proceed from research focused on understanding the global intrinsic properties of showers, e.g. for the purpose of compensation, towards the study of detailed information, in space, time, and energy deposition type, through many and multiple readout channels.

In an inelastic hadronic collision a significant fraction f_{em} of the energy is removed from further hadronic interaction by the production of secondary π^0/η's, whose decay photons generate high-

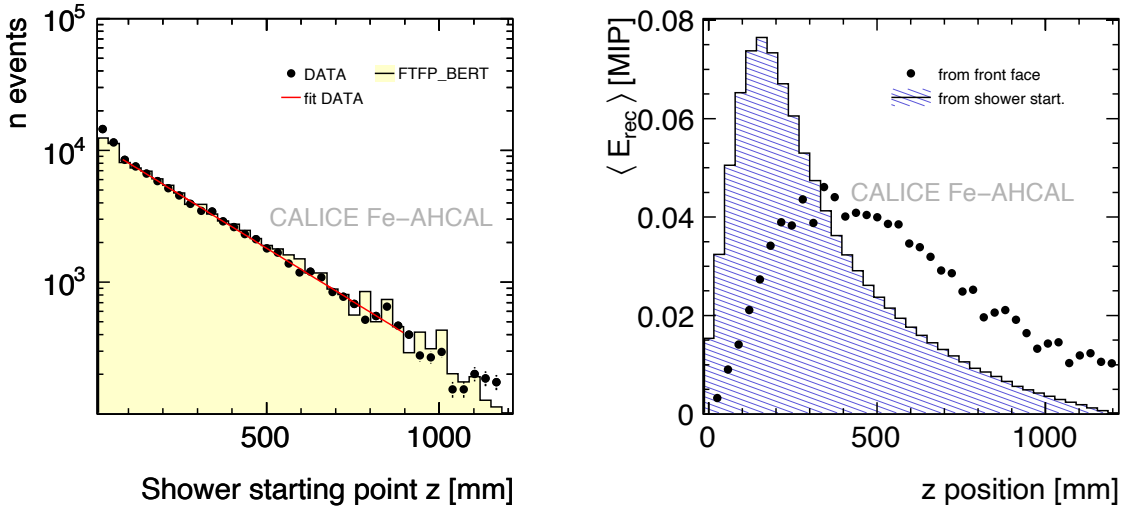

Figure 35.35: Longitudinal profile of hadronic showers induced by 45 GeV negative pions measured in he CALICE highly-granular steel-scintillator sampling calorimeter [404]. Left: Reconstructed position of the first inelastic interaction, compared to simulations (GEANT4 9.4p03, FTFP_BERT), and an exponential fit yielding a slope consistent with the expected pion interaction length. Right: Longitudinal shower profile measured from the front face of the calorimeter (dots, without corrections for dead cells) and relative to the position of the shower start given by the first inelastic interaction (filled histogram). The visible energy is given in units of the most probable energy loss of a minimum-ionizing particle (MIP). The integrals of the distributions are normalized to unity.

energy electromagnetic showers. Charged secondaries ($\pi^{\pm}$, p, ...) deposit energy via ionization and excitation, but also interact with nuclei, producing evaporation neutrons, spallation protons and neutrons, and heavier spallation fragments. The charged collision products produce detectable ionization, as do the showering γ-rays from the prompt de-excitation of highly excited nuclei. The recoiling nuclei generate little or no detectable signal, as mentioned previously. The neutrons lose kinetic energy in elastic collisions which generate ionization signals via recoiling protons, thermalize on a time scale of several μs, and are finally captured, with the production of more γ-rays—usually outside the acceptance gate of the electronics. Between endothermic spallation losses, nuclear recoils, and late neutron capture, a significant fraction of the hadronic energy (20%–40%, depending on the absorber and energy of the incident particle) is used to overcome nuclear binding energies and is therefore lost or "invisible."

In a hadron-nucleus collision a large fraction of the incident energy is carried by a "leading particle" with the same quark content as the incident hadron. If the projectile is a charged pion, the leading particle is usually a pion, which can be neutral and hence contributes to the EM sector. This is not true for incident protons. The result is an increased mean hadronic fraction for incident protons.

The complexity of hadronic showers also has a significant impact on the energy measurement. In contrast to EM showers, hadronic cascade processes are characterised by the production of relatively few high-energy particles. The number multiplicity of these particles produced in hadronic interactions increases only logarithmically with energy. The lost energy and f_{em} are highly variable from event to event, and on average increase with increasing energy [405]. Electromagnetic sub-showers typically result in a higher response than the hadronic parts of the cascade, where undetectable energy loss due to nuclear dissociation, the long time scales and the material dependence

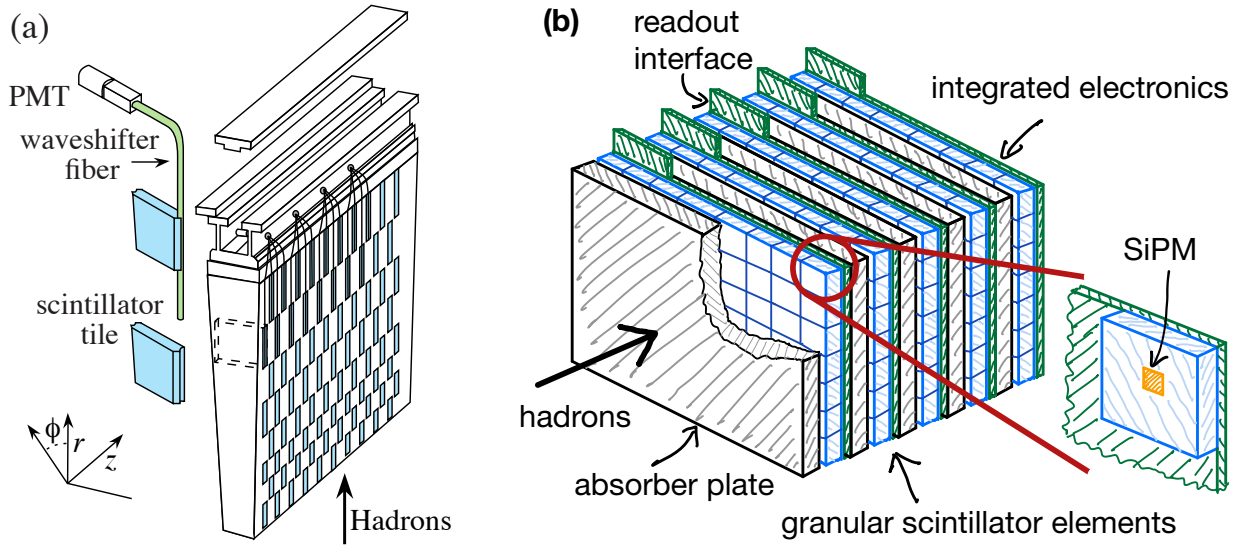

Figure 35.36: Two examples of geometrical structures of scintillator-based HCALs. (a) A wedge of the ATLAS central tile calorimeter consisting of scintillator tiles in iron, read out via wavelength-shifting fibers and PMTs [406]. The coordinate system is that of the ATLAS calorimeter within the experiment, with the z axis along the beam direction, r pointing radially outward, and ϕ being the azimuthal angle. (b) An illustration of the "SiPM-on-tile" structure used in the CALICE analogue HCAL prototype, and in the CMS High-Granularity Calorimeter (HGCAL), highly granular calorimeters with steel absorbers and small scintillator tiles directly read out via SiPMs with embedded electronics [403, 407–409].

of neutron signals, as well as other effects reduce the measured signal. This difference in response is often expressed by the $\langle h/e \rangle$ ratio, a calorimeter-dependent quantity which is smaller than unity for many, but not all, HCALs. The increase of the electromagnetic fraction with energy thus introduces a non-linear contribution to the response. Combined with the significant event-by-event fluctuations between electromagnetic and hadronic fractions of the showers and between different hadronic processes the non-equality of h and e deteriorates the energy resolution of HCALs. Different strategies to address this exist, as discussed further below.

Most large HCALs are parts of complex 4π detectors at colliding beam facilities. To date, all these HCALs are sampling calorimeters. This choice is imposed by the physics of hadronic showers, both by the required depth for containment which favours high-density materials with short λ_I, and by the differences in response to electromagnetic and hadronic parts of the cascade, which are particularly severe for homogeneous calorimeters. Common absorber materials are Fe, Cu, Pb, and U, with W also used occasionally. A large variety of different active materials are used, depending on application and optimisation, from plastic scintillators (plates, tiles, bars, fibers), crystals and Cherenkov media, silicon, liquid argon (LAr), to gaseous detectors. The energy loss of particles in the active medium is either detected directly by collecting charge, or via scintillation or Cherenkov light observed with conventional photomultipliers (PMTs), photodiodes or silicon photomultipliers (SiPMs). The choice of both active and passive materials is driven by different, sometimes conflicting, constraints, including performance requirements, space and other mechanical boundary conditions, radiation tolerance, and cost considerations.

A wide range of different geometries of absorbers and sensors is used, with design choices depending on the chosen priorities of addressing these constraints, also considering the need to bring

the signals to the outside of the detector while achieving a hermetic coverage and other constraints. In this context it is important to note that a classic sandwich structure with absorber plates and active elements approximately perpendicular to the particle incidence is not required, and arbitrary orientations are viable for good calorimetric measurements, as long as channelling, meaning the extended passage of primary particles through low-density active regions, is excluded. Figure 35.36 shows two examples of plastic scintillator-based calorimeters to illustrate differences in design between coarsely-segmented and highly-granular calorimeters. The ATLAS tile calorimeter [406] uses scintillator tiles coupled to wavelength-shifting fibers which collect the light from the tiles and guide them to PMTs outside of the active region of the calorimeter. The calorimeter is segmented in ϕ (azimuthal angle) and η (pseudorapidity, defined as $\eta = -\ln\tan(\theta/2)$, where θ is the angle relative to the beam axis), with coarse longitudinal segmentation. The technological prototype of the CALICE analog HCAL, a highly granular SiPM-on-tile calorimeter is based on scintillator tiles directly coupled to SiPMs, which, together with the front-end electronics, are embedded inside of the the active volume of the calorimeter. The CMS HGCAL [409] uses the same concept in part of the detector, and in addition embeds elements for digital data concentration and power distribution in the active volume. Other detector solutions include scintillating fibres threading an absorber [410], liquid-argon-filled tubes [411] and the "accordion" LAr detector [412]. The latter has zig-zag absorber plates to minimize channeling effects; the calorimeter is hermetic (no cracks), and plates are oriented so that cascades cross the same plate repeatedly.

In particular, but not exclusively, the combination of heavy absorber materials (Pb, U) with plastic scintillators allows the construction of HCALs that have a near-equal response to electromagnetic and hadronic parts of the cascade, so-called compensating calorimeters [413]. In this first study, it was recognized that nuclear fission can amplify the hadronic signal when using uranium absorbers. However, the key drivers of compensation are the reduction of the electromagnetic response with high-Z absorbers and an increased sensitivity to neutrons, which are strongly correlated to otherwise invisible energy loss due to nuclear dissociation, with a hydrogeneous active medium [414–418]. Since the electromagnetic cross section increases, and the critical energy decreases with Z, and since most of the energy of an electromagnetic shower is deposited by low-energy, short-range electrons, a disproportionate fraction of the total electromagnetic energy is deposited in the absorber in the high-Z case. Hydrogenous active media, such as organic scintillators, have a high sensitivity to spallation neutrons via elastic $n-p$ scattering. The number of produced neutrons is highly correlated with the invisible energy of the hadronic cascade. Increasing the sensitivity to these particles can thus boost the visible hadronic signal. Achieving compensation requires carefully-chosen sampling fractions and frequencies, with the response to the hadronic parts of the shower also sensitive to the integration time of the electronics due to the time structure of the neutron component of the signal.

Since Cherenkov light, for example in quartz plates or fibers, or in crystals, is produced only by relativistic particles in the cascade and thus predominantly by the electromagnetic component of the shower, such media are less common in hadronic than in ECALs. Notable exceptions are applications that require high radiation tolerance, and dual-readout calorimeters which specifically exploit this feature, as discussed below.

Silicon offers high compactness, high granularity, high radiation tolerance, long-term stability and fast charge collection, and is thus an interesting active material for sampling calorimeters. A thorough overview of the development and of the features of this technology can be found in a recent review paper [419]. The first silicon-based calorimeter in a collider experiment was a HCAL, the H1 PLUG calorimeter [420] covering the very forward region of the H1 experiment at HERA. The SICAPO collaboration has demonstrated the conceptual possibility of constructing compensating HCALs using silicon sensors [421]. Silicon is currently the technology of choice for several ECALs

for future Higgs factories [422–424]. It is also being used extensively in the CMS HGCAL [409] in both electromagnetic and hadronic sections, complemented by scintillator tiles with on-tile SiPM readout where the radiation levels allow.

More generally, high-granularity calorimeters play an increasingly important role, in particular motivated by the use of particle-flow algorithms for global event reconstruction (see Section 35.10.1). The associated technologies for both electromagnetic and HCALs have been pioneered by the CALICE collaboration, which has built and tested an increasingly sophisticated series of "imaging" calorimeters with a highly granular readout [425]. In the area of HCALs, this includes the scintillator-based analog HCAL [426] with the latest SiPM-on-tile technological prototype with fully-integrated electronics having approximately 22,000 channels [407,408], as well as digital [427] and semidigital [428] calorimeters using gas detectors, such as RPCs (Sec. 35.6.7) and micropattern gas detectors (Sec. 35.6.4), with channel counts of up to 500,000. The large numbers of channels of high-granularity calorimeters presents a significant integration challenge for full detector systems, and requires the full integration of the front-end electronics inside of the active volume of the detector, as well as very compact data concentration and interface units. The first such detector in construction for a collider experiment is the CMS HGCAL [409]. Beam tests with a combined prototype using both silicon and scintillator-SiPM instrumented active layers have confirmed simulation-based expectations [429]. The total silicon area of the full HGCAL amounts to about 600 m^2, and about 240,000 SiPMs are foreseen. The calibration of such calorimeters requires the monitoring of a large number of cells, which is achieved in-situ using reconstructed track segments within hadronic showers [409,430] or externally identified muons. For this method, the capability to detect the most probable energy loss of a minimum-ionizing particle in a single cell is essential. This is required over the full lifetime of the detector, also after the active elements have received significant radiation damage, resulting in increased noise and reduced charge or signal collection efficiency. Due to the large number of cells contributing to the measurement of one shower, the requirements on the precision of the calibration of individual cells is relaxed relative to the global energy calibration of the calorimeter.

The energy resolution of HCALs is severely affected by fluctuations between different components of the cascade, exacerbated by differences in response to purely hadronic and to electromagnetic sub-showers. In many detectors, fluctuations in the electromagnetic energy fraction, $f_{\rm em}$, and the related, consequential variations in nuclear energy dissociation losses, represent the biggest single contribution to the hadron energy resolution. One strategy to address this problem is the construction of intrinsically-compensating calorimeters, which imposes stringent constraints on materials and geometries as discussed above. Compensating calorimeters are not used in current large collider experiments, and are at the moment not considered for future collider detectors. Two different strategies are presently followed to improve the energy resolution in non-compensating calorimeters: Offline weighting or software compensation in longitudinally-segmented or in highly-granular calorimeters; and dual-readout calorimetry.

Software compensation techniques exploit the fact that electromagnetic sub-showers typically have a higher spatial density than the purely hadronic parts of the cascade. Amplitude (or energy-density) dependent weights are applied in the reconstruction to reduce the effects of shower-to-shower fluctuations. These techniques were pioneered by the CDHS collaboration for a longitudinally segmented steel-plastic scintillator calorimeter [431], where an improvement of the energy resolution of 10% (at 10 GeV) to 30% (at 140 GeV) for charged pion showers was achieved. Similar techniques were successfully applied in the H1 [432] liquid argon calorimeter system resulting in a stochastic term of $51\%/\sqrt{E}$, and in the ATLAS [433] endcap calorimeters, also based on liquid argon, with an energy resolution of $84\%/\sqrt{E}$. Inspired by these approaches, a software compensation

technique using the detailed spatial information provided by highly-granular calorimeters of the CALICE collaboration has been developed, achieving up to 25% improvement of the energy resolution compared to the resolution without software compensation, resulting in a stochastic term of $45\%/\sqrt{E}$ [434] in a scintillator tile calorimeter with steel absorbers. This technique has also been successfully transferred to particle-flow reconstruction [435], resulting in an improvement of the jet-energy resolution in simulated events by 8% - 15%, depending on jet energy. Highly-granular calorimeters with software compensation and particle-flow reconstruction are currently studied as the baseline configuration for several Higgs-factory detectors.

The *dual-readout method*, originally proposed by Mockett in 1983 [436], measures $f_{\rm em}$ event by event in parallel to the total deposited energy. It uses the fact that most of the relativistic particles in the shower originate from the electromagnetic part, and that only those produce Cherenkov light, while the signal of the hadronic part is mostly due to non-relativistic protons. In practice either two different active media, e.g. scintillator and quartz, are used to register scintillation and Cherenkov light, respectively, or the optical signals from the two processes occurring in heavy crystals are disentangled, using their different spectral, directional or timing properties.

The Cherenkov and scintillation signals, normalised to the response for electrons, are given by

$$C = [f_{\rm em} + (h/e)_C(1 - f_{\rm em})]E\,, \tag{35.44}$$
$$S = [f_{\rm em} + (h/e)_S(1 - f_{\rm em})]E\,, \tag{35.45}$$

respectively, which can be solved for the fraction $f_{\rm em}$ and the energy

$$E = (\xi S - C)/(\xi - 1)\,, \tag{35.46}$$

where $\xi = [1 - (h/e)_C]/[1 - (h/e)_S]$ and $(h/e)_{C,S}$ denote the average ratios of hadronic to electromagnetic response in the Cherenkov and scintillator parts, respectively. This is illustrated in Figure 35.37, which shows their correlation for a set of simulated negative pion events [437] using FLUKA [385].

It was noted that the method demands a steep slope ξ, which implies that the scintillator read-out should be as compensating as possible, which however reduces the room for improvement by adding Cherenkov information.

The method was tested by the DREAM/RD52 collaboration [438, 439], using a 1 ton copper matrix with embedded quartz and scintillating fibers. The value of ξ was about 3 in this detector. With this detector, a resolution of $70\%/\sqrt{E(\mathrm{GeV})}$ was obtained for single hadrons [440]. Due to the small size of the module, this includes contributions from transverse leakage which prevent the full exploitation of key features of dual readout, and thus underestimates the potential of the method.

The separate Cherenkov read-out evidently provides excellent pion-electron separation for particle identification. In another RD52 prototype, each fiber is read out individually by SiPMs, giving also a superior transverse granularity. A fiber-based calorimeter with full solid-angle coverage requires a pointing geometry due to the limited or missing longitudinal segmentation. The resulting challenges for a mechanical design are studied in the framework of the IDEA detector concept [441].

Table 35.12 shows selected examples of the energy resolution of HCALs for single charged pions achieved in beam tests. The examples are selected to illustrate the performance achieved with different designs ranging from intrinsic compensation to software compensation and dual readout, with a focus on results by R&D projects. It should be noted that the exact values of the different resolution terms depend on the functional form used in the fit, here the addition in quadrature is used for the cases where more than just the stochastic term is quoted. The results shown in the table

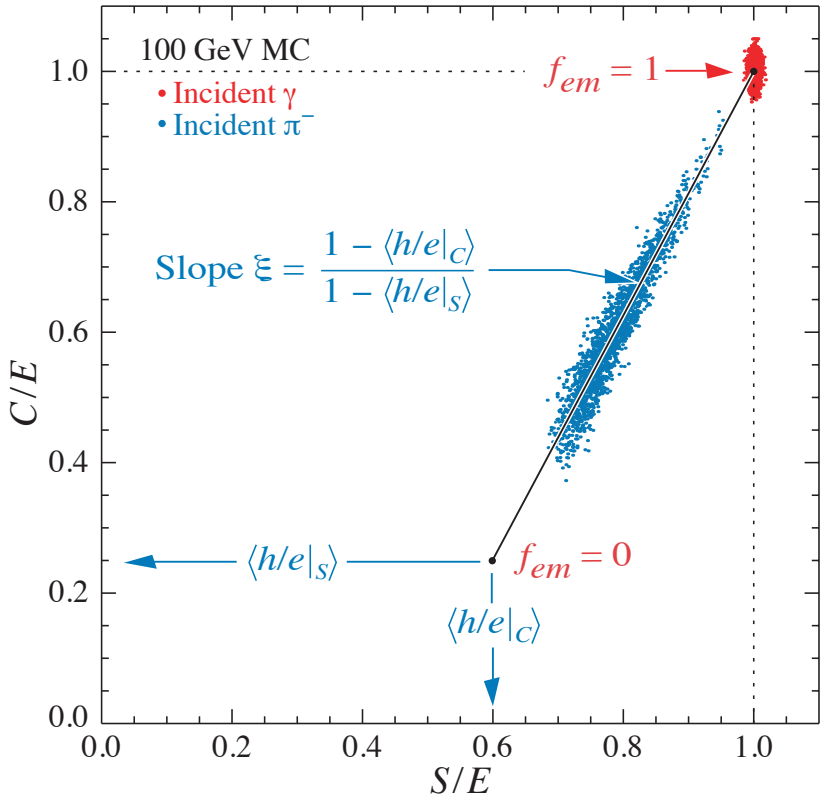

Figure 35.37: Scatter plot of Monte Carlo C/E (Cherenkov) vs S/E (scintillator) signals for individual events in a dual-readout calorimeter for 100 GeV negative pions and photons. Hadronic events are shown in blue, and scatter about the indicated event locus. Electromagnetic events cluster about $(C/E, S/E) = (1,1)$. In this case worse resolution (fewer p.e.'s) was assumed for the Cherenkov events, leading to the "elliptical" distribution.

Table 35.12: Energy resolution of selected hadron calorimeters for single charged hadrons obtained in beam tests.

Calorimeter	Passive	Active	Resolution	Ref.
Bernardi *et al.*	Pb	Scintillator layers	$44.2\%/\sqrt{E}$ §	[442]
CALICE AHCAL	Fe	Scintillator tiles	$44.3\%/\sqrt{E} \oplus 1.8\%$ †	[434]
CALICE W-AHCAL	W	Scintillator tiles	$57.9\%/\sqrt{E} \oplus 4.6\% \oplus 0.065/E$ §	[443]
CDHS	Fe	Scintillator layers	$58\%/\sqrt{E}$ ♯	[431]
DREAM/RD52	Pb	Scint.+ Quartz fibers	$70\%/\sqrt{E}$ *	[440]
HELIOS	U	Scintillator layers	$34\%/\sqrt{E}$ §	[444]
SPACAL	Pb	Scintillating fibers	$33.3\%/\sqrt{E} \oplus 2.2\%$ §	[445]

§ Bernardi *et al.*, CALICE W-AHCAL, HELIOS, SPACAL: (near-)compensating calorimeters.

† CALICE AHCAL: Local software compensation exploiting the high granularity of the calorimeter.

♯ CDHS: Offline weighting using longitudinal information.

* DREAM/RD52: Due to the relatively small transverse size of the detector lateral leakage was significant, deteriorating the energy resolution with respect to the full potential of the dual readout method.

illustrate that (close to) compensating calorimeters with optimized sampling fraction and frequency, such as HELIOS (U-plastic scintillator) and SPACAL (Pb-plastic scintillator), achieve a very good energy resolution. The comparison with Bernardi *et al.*, which has the same Pb/scintillator ratio by volume as SPACAL, but coarser sampling in a sandwich structure, illustrates the importance of the geometrical details. Beyond the examples shown in the table, liquid argon has also been explored as an active medium, for example in the context of the SLD detector with different absorber options [446]. Due to the reduced sensitivity to neutrons in the shower, not the same resolution as for plastic-scintillator-based systems is achieved. This technology has also been used in the D0 experiment, as discussed below. The dual-readout method has the potential to reach or surpass this performance, but would require a prototype sufficiently large for full longitudinal and transverse shower containment for an experimental demonstration. The two CALICE calorimeters shown, which use the same active elements (5 mm thick scintillator tiles) but different absorbers (21.4 mm Fe vs 10 mm W + 4 mm Fe) per layer, illustrate the impact of the absorber choice on energy resolution and reconstruction possibilities. While the tungsten-based W-AHCAL setup is very close to compensating, the steel-based AHCAL achieves a better energy resolution when software compensation is applied, profiting from the finer sampling of the electromagnetic parts of the cascade and the correction for shower-to-shower fluctuations of the electromagnetic fraction in the reconstruction. In the case of tungsten, software compensation does not significantly improve the energy resolution, as expected. The comparison of the CALICE AHCAL performance with the one of CDHS illustrates the benefits of higher granularity for software compensation techniques, but it should be noted that the absorber thickness of the latter is 25 mm, with the same scintillator thickness as in the case of CALICE.

As explained in the introduction, in most high-energy physics experiments, the HCAL follows after an ECAL, making the response of the latter to hadronic cascades highly relevant for the overall performance of the combined ECAL HCAL system. For scenarios where the electromagnetic and the HCAL have very different $\langle h/e \rangle$, as is typically the case for crystal-based ECALs, the fluctuations of the fraction of the hadronic shower contained within the ECAL result in a significant deterioration of the energy resolution for hadrons. A deterioration of the hadronic performance also results from larger amounts of not-instrumented material, e.g. supports and services, between electromagnetic and hadronic sections. In particle-flow calorimeters, a large value of the λ_I/X_0 ratio of the absorber material, like in tungsten, maximises the longitudinal separation of electromagnetic and hadronic showers. This is reflected in the design of particle-flow-based detector concepts for future Higgs Factories.

Table 35.13: Energy resolution of selected combined electromagnetic and hadronic calorimeter systems in past and present high-energy collider experiments for single hadrons. The results are taken from beam tests of prototypes with the electromagnetic calorimeter upstream of the hadronic calorimeter.

Experiment	technology (ECAL, HCAL)	Combined hadronic resolution	Reference
H1	Pb/LAr, Steel / LAr	$46\%/\sqrt{E} \oplus 2.6\% \oplus 0.73/E$	[447]
ZEUS	depleted U / plastic scintillator	$35\%/\sqrt{E}$	[448]
CDF	Pb/plastic scint., Steel/plastic scint.	$68\%/\sqrt{E} \oplus 4.1\%$	[449]
D0	depleted U / LAr	$44.6\%/\sqrt{E} \oplus 3.9\%$	[450]
ATLAS	Pb/LAr, Steel/plastic scintillator	$52\%/\sqrt{E} \oplus 3.0\% \oplus 1.6/E$	[451]
CMS	$PbWO_4$, brass/plastic scintillator	$84.7\%/\sqrt{E} \oplus 7.4\%$	[452]

Table 35.13 summarizes the single hadron energy resolution obtained from test beams of the combined ECAL and HCAL systems of the large multi-purpose experiments at HERA, the Tevatron and at the LHC. These systems are examples of different optimization strategies. D0 and ZEUS are near-compensating systems with the same technology in ECAL and HCAL emphasizing hadronic performance. ATLAS and H1 use sampling ECALs with good electromagnetic resolution and weighting techniques exploiting longitudinal and transverse shower information for hadronic energy reconstruction. CMS, with a crystal ECAL and a scintillator-brass HCAL, prioritizes electromagnetic performance, with very different $\langle h/e \rangle$ in the electromagnetic and hadronic system. Of the detectors shown in the table, CMS has the best electromagnetic resolution by a comfortable margin, but consequently the weakest hadronic resolution. The best hadronic performance is achieved with the compensating calorimeter of ZEUS, which however has a weaker electromagnetic performance than the other calorimeter systems shown here. It should be noted that an excellent single-hadron resolution in general does not fully propagate into the jet-energy performance. Inactive material in front of the calorimeter can significantly worsen the energy resolution for jets, with an impact in particular on lower-energy particles. For example, the core of the invariant mass distribution of hadronically-decaying Z^0 bosons measured in ZEUS, which had a superconducting coil in front of the calorimeter, is well described by a Gaussian with a σ of 6 GeV [453], approximately 40% wider than would be expected for a jet-energy resolution that is identical to the single-hadron performance.

35.10.4 *Free electron drift velocities in liquid ionization chambers*

Revised August 2009 by W. Walkowiak (Siegen U.).

Drift velocities of free electrons in LAr [290] are given as a function of electric field strength for different temperatures of the medium in Fig. 35.38. The drift velocites in LAr have been measured using a double-gridded drift chamber with electrons produced by a laser pulse on a gold-plated cathode. The average temperature gradient of the drift velocity of the free electrons in LAr is described [290] by

$$\frac{\Delta v_d}{\Delta T\, v_d} = (-1.72 \pm 0.08)\ \%/\mathrm{K}. \tag{35.47}$$

Previous measurements [454,455,457,458] range from 13% higher [455] to 18% lower [457] than these measurements. They used different techniques and show drift velocities for free electrons which cannot be explained by the temperature dependence mentioned above.

Drift velocities of free electrons in LXe [454] as a function of electric field strength are also displayed in Fig. 35.38. The drift velocity saturates for $|E| > 3$ kV/cm, and decreases with increasing temperature for LXe as well as measured e.g. by [459].

The addition of small concentrations of other molecules like N_2, H_2 and CH_4 in solution to the liquid typically increases the drift velocities of free electrons above the saturation value [454, 457], see example for CH_4 admixture to LAr in Fig. 35.38. Therefore, actual drift velocities are critically dependent on even small additions or contaminations.

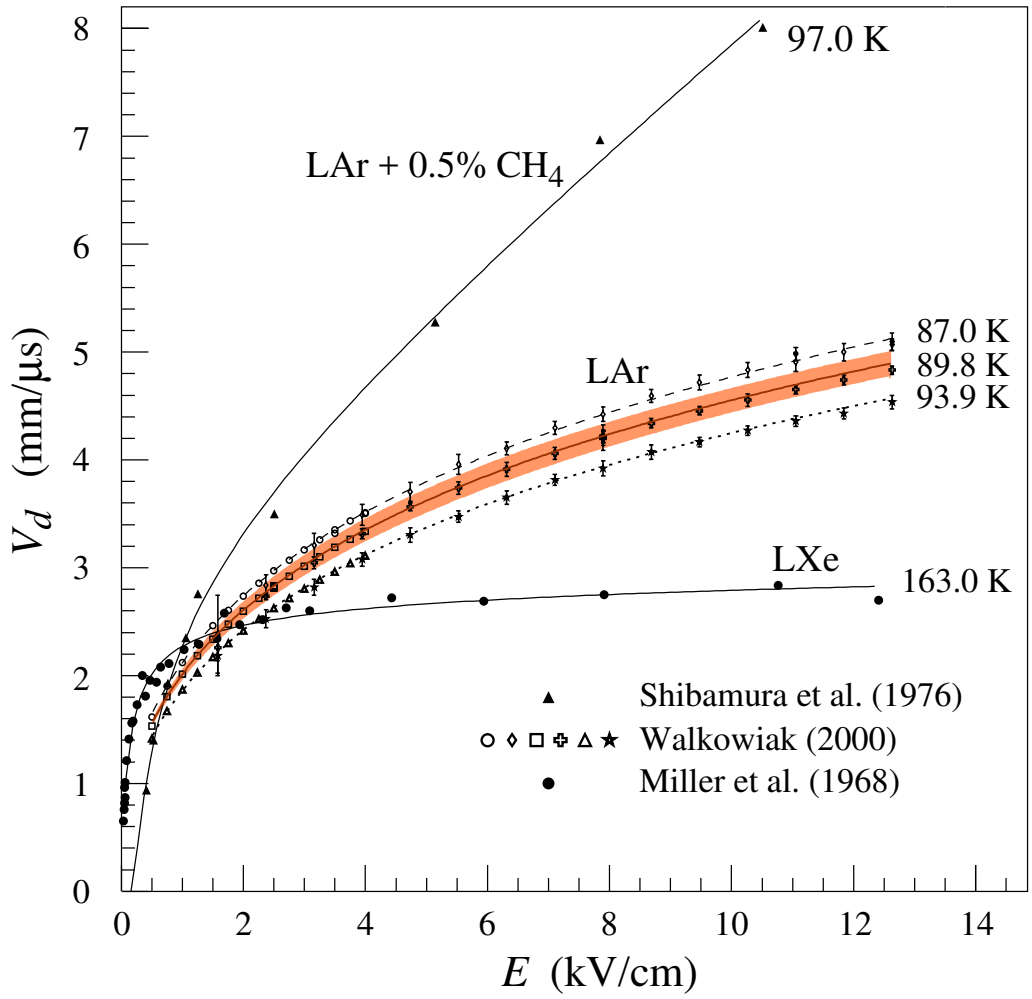

Figure 35.38: Drift velocity of free electrons as a function of electric field strength for LAr [290], LAr + 0.5% CH_4 [454] and LXe [455]. The average temperatures of the liquids are indicated. Results of a fit to an empirical function [456] are superimposed. In case of LAr at 91 K the error band for the global fit [290] including statistical and systematic errors as well as correlations of the data points is given. Only statistical errors are shown for the individual LAr data points.

35.11 Accelerator-based neutrino detectors

Written by M.O. Wascko (Imperial Coll. London). Minor revision in August 2023 by A. Fava (FNAL) and F. Pietropaolo (CERN; INFN, Padova).

35.11.1 *Introduction*

Accelerator-based neutrino experiments span many orders of magnitude in neutrino energy, from a few MeV to hundreds of GeV. This wide range of neutrino energy is driven by the many physics applications of accelerator-based neutrino beams. Foremost among them is neutrino oscillation, which varies as the ratio L/E_ν, where L is the neutrino baseline (distance traveled), and E_ν is the neutrino energy. But accelerator-based neutrino beams have also been used to study the nature of the weak interaction, to probe nucleon form factors and structure functions, and to study nuclear structure.

The first accelerator-based neutrino experiment used neutrinos from the decays of high energy

pions in flight to show that the neutrinos emitted from pion decay are different from the neutrinos emitted by beta decay [460]. The field of accelerator-based neutrino experiments would likely not have expanded beyond this without Simon van der Meer's invention of the magnetic focusing horn [461], which significantly increased the flux of neutrinos aimed toward the detector. In this mini-review, we focus on experiments employing decay-in-flight beams—pions, kaons, charmed mesons, and taus—producing fluxes of neutrinos and antineutrinos from $\sim$ 10 MeV to $\sim$ 100 GeV.

Neutrino interactions with matter proceed only through the weak interaction, making the cross section extremely small and requiring high fluxes of neutrinos and large detector masses in order to achieve satisfactory event rates. Therefore, neutrino detector design is a balancing act taking into account sufficient numbers of nuclear targets (often achieved with inactive detector materials), adequate sampling/segmentation to ensure accurate reconstruction of the tracks and showers produced by neutrino-interaction secondary particles, and practical readout systems to allow timely analysis of data.

35.11.2 *Signals and Backgrounds*

The neutrino interaction processes available increase with increasing neutrino energy as interaction thresholds are crossed; in general neutrino-interaction cross sections grow with energy; for a detailed discussion of neutrino interactions see [462]. The multiplicity of secondary particles from each interaction process grows in complexity with neutrino energy, while the forward-boost due to increasing E_ν compresses the occupied phase space in the lab frame, impacting detector designs. Because decay-in-fight beams produce neutrinos at well-defined times, leading to very small duty factors, the predominant backgrounds usually stem from unwanted beam-induced neutrino interactions, i.e. neutrinos interacting via other processes than the one being studied. A noteworthy exception is time projection chambers, wherein the long drift times can admit substantially more cosmic backgrounds than most other detection methods. Cosmic backgrounds are more rare at higher energies because the secondary particles produced by neutrino interactions yield detector signals that resemble cosmic backgrounds less and less.

Below, we describe a few of the dominant neutrino interaction processes, with a focus on the final state particle content and topologies.

35.11.2.1 *Charged-Current Quasi-Elastic Scattering and Pion Production*

Below $\sim$ 2 GeV neutrino energy, the dominant neutrino-nucleus interaction process is quasi-elastic (QE) scattering. In the charged current (CC) mode, the CCQE base neutrino reaction is $\nu_\ell\, n \to \ell^-\, p$, where $\ell = e, \mu, \tau$, and similarly for antineutrinos, $\overline{\nu}_\ell\, p \to \ell^+\, n$. The final state particles are a charged lepton, and perhaps a recoiling nucleon if it is given enough energy to escape the nucleus. Detectors designed to observe this process should have good single-particle track resolution for muon neutrino interactions, but should have good μ/e separation for electron neutrino interactions. Because the interaction cross section falls sharply with Q^2, the lepton typically carries away more of the neutrino's kinetic energy than the recoiling nucleon. The fraction of backward-scattered leptons is large, however, so detectors with 4π coverage are desirable. The dominant backgrounds in this channel tend to come from single pion production events in which the pion is not detected.

Near 1 GeV, the quasi-elastic cross section is eclipsed by pion production processes. A typical single pion production (CC1π) reaction is $\nu_\ell\, n \to \ell^-\, \pi^+\, n$, but many more final state particle combinations are possible. Single pion production proceeds through the coherent channel and many incoherent processes, dominated by resonance production. With increasing neutrino energy, higher-order resonances can be excited, leading to multiple pions in the final state. Separating these processes from quasi-elastic scattering, and indeed from each other, requires tagging, and ideally reconstructing, the pions. Since these processes can produce neutral pions, electromagnetic (EM)

shower reconstruction is more important here than it is for the quasi-elastic channel. The predominant backgrounds for pion production change with increasing neutrino energy. Detection of pion processes is also complicated because near threshold the quasi-elastic channel creates pion backgrounds through final state interactions of the recoiling nucleon, and at higher energies backgrounds come from migration of multiple pion events in which one or more pions is not detected.

35.11.2.2 *Deep Inelastic Scattering*

Beyond a few GeV, the neutrino has enough energy to probe the nucleon at the parton scale, leading to deep inelastic scattering (DIS). In the charged-current channel, the DIS neutrino reaction is $\nu_\ell\, N \to \ell^-\, X$, where N is a nucleon and X encompasses the entire recoiling hadronic system. The final state particle reconstruction revolves around accurate reconstruction of the lepton momentum and containment and reconstruction of the hadronic shower energy. Because of the high neutrino energies involved, DIS events are very forward boosted, and can have extremely long particle tracks. For this reason, detectors measuring DIS interactions must be large to contain the hadronic showers in the detector volume.

35.11.2.3 *Neutral Currents*

Neutrino interactions proceeding through the neutral current (NC) channel are identified by the lack of a charged lepton in the final state. For example, the NC elastic reaction is $\nu_l\, N \to \nu_l\, N$, and the NC DIS reaction is $\nu_l\, N \to \nu_l\, X$. NC interactions are suppressed relative to CC interactions by a factor involving the weak mixing angle; the primary backgrounds for NC interactions come from CC interactions in which the charged lepton is misidentified.

35.11.3 *Instances of Neutrino Detector Technology*

Below we describe many of the actual detectors that have been built and operated for use in accelerator-based neutrino beams.

35.11.3.1 *Spark Chambers*

In the first accelerator-based neutrino beam experiment, Lederman, Schwartz, and Steinberger [460] used an internally-triggered spark chamber detector, filled with 10 tons of Al planes and surrounded by external scintillator veto planes, to distinguish muon tracks from electron showers, and hence muon neutrinos from electron neutrinos. The inactive Al planes served as the neutrino interaction target and as radiators for EM shower development. The detector successfully showed the presence of muon tracks from neutrino interactions. It was also sensitive to the hadronic showers induced by NC interactions, which were unknown at the time. In 1963, CERN also built and ran a large (20 ton) Al plane spark chamber in a wideband beam based on the PS accelerator [463]. More than a decade later, the Aachen-Padova [464] experiment at CERN employed a 40 ton Al spark chamber in the PS-WBB.

35.11.3.2 *Bubble Chambers*

Several large bubble chamber detectors were employed as accelerator neutrino detectors in the 1970s and 80s, performing many of the first studies of the properties of the weak interaction. Bubble chambers provide exquisite granularity in the reconstruction of secondary particles, allowing very accurate separation of interaction processes. However, the extremely slow and labor-intensive acquisition and analysis of the data from photographic film led to them being phased out in favor of electronically read out detectors.

The Gargamelle [465] detector at CERN used Freon and propane gas targets to make the first observation of neutrino-induced NC interactions and more. The BEBC [466] detector at CERN was a bubble chamber that was alternately filled with liquid hydrogen, deuterium, and a neon-hydrogen mixture; BEBC was also outfitted with a track-sensitive detector to improve event tagging, and sometimes used with a small emulsion chamber. The SKAT [467] Freon bubble chamber was

Table 35.14: Properties of detectors for accelerator-based neutrino beams. Revised in August 2023 by A. Fava (FNAL) and F. Pietropaolo (CERN; INFN, Padova).

Name	Type	Target	Total Mass (fiducial) [t]	$\langle E_\nu \rangle$ [GeV]	Location	Dates
Lederman et al.	Spark	Al	10	[0.2-3]	BNL	1962
CERN-spark.	Spark	Al	20	1.5	CERN	1963
Serpukhov	Spark	Al	20	[3-30]	IHEP	1974-82
Aachen-Padova	Spark	Al	40(20)	1.4	CERN	1976-77
Gargamelle	Bubble	Freon	12	[1-10]	CERN	1970-79
BEBC	Bubble	H,D,Ne-H	2-42	[50-150],20	CERN	1977-84
SKAT	Bubble	Freon	8	7	IHEP	1976-1987
ANL-12ft	Bubble	H,D	1-2	0.5	ANL	1970
BNL-7ft	Bubble	HD	0.4-0.9	1.3,3	BNL	1976-82
Fermilab-15ft	Bubble	D, Ne	1,20	[50-180],[25-100]	FNAL	1973-92
CITF	Iron	Fe	92	[50-180]	FNAL	1974-83
CDHS	Iron	Fe	1250(520)	10-200	CERN	1976-84
MINOS	Iron	Fe	980(23.7), 5.5k (4.2k)	3	FNAL, SUL	2005-2012
MINOS+	Iron	Fe	980, 5.5k	4-10	FNAL, SUL	2013-2016
INGRID	Iron	Fe	160	0.6-3	J-PARC	2010-
SuperKamiokande	Cherenkov	H_2O	50k (22.5k)	0.6	Kamioka	1996-2018
SuperK-Gd	Cherenkov	H_2O doped with Gd	50k (22.5k)	0.6	Kamioka	2020-
HyperK	Cherenkov	H_2O	260k(190k)	0.6	Kamioka	2027-
K2K-1kt	Cherenkov	H_2O	25	0.8	KEK	1998-2004
MiniBooNE	Cherenkov	CH_2	818(440)	0.5	FNAL	2002-19
ANNIE	Cherenkov	H_2O with GD sulfate	26	0.8	FNAL	2021-
HWPF	Scintillation	CH_2, Fe	160	[50-180]	FNAL	1974-78
LSND	Scintillation	CH_2	167	0.003-0.06	LANL	1993-1998
NOvA	Scintillation	CH_2	300, 14k	2	FNAL,Ash River	2014-
SciBar	Scintillation	CH	15(9.5)	0.6	KEK	2003-2004
SciBooNE,	Scintillation	CH	15(9.5)	0.8	FNAL	2007-08
Captain Mills	Scintillation	Ar	10	0.003-0.06	LANL	2022-2024
ICARUS	LArTPC	Ar	760(476)	17	LNGS	2006-12
ICARUS	LArTPC	Ar	760(476)	0.8	FNAL	2020-
Argoneut	LArTPC	Ar	0.025	3	FNAL	2009-10
MicroBooNE	LArTPC	Ar	170(85)	0.8	FNAL	2014-21
SBND	LArTPC	Ar	220(112)	0.8	FNAL	2024-
DUNE	LArTPC	Ar	70(40)	3	FNAL,SURF	2027-
FNAL-E-531	Emulsion	Ag, Br	0.009	22	FNAL	1984
CHORUS	Emulsion	Ag, Br	0.8	27	CERN	1994-97
DONuT	Emulsion	Fe	0.26	53	FNAL	1997
OPERA	Emulsion	Pb	1.25k	17	LNGS	2008-12
NINJA	Emulsion	Fe	0.002(0.001)	0.6	J-PARC	2015-
FASERν	Emulsion	W	1.2	[360-6300]	CERN (LHC)	2022-
CHARM	Hybrid	$CaCO_3$	(27),156(122)	20	CERN	1978-84
CHARM-II	Hybrid	glass	692	20	CERN	1984-91
BNL-E-734	Hybrid	CH_2	172	1.3	BNL	1981-86
BNL-E-776	Hybrid	concrete	240	1.4	BNL	1986
NOMAD	Hybrid	CH	2.9(2.7)	27	CERN	1995-98
CCFR	Hybrid	Fe	690	[30-260]	FNAL	1985-88
NuTeV	Hybrid	Fe	690	[70-180]	FNAL	1996-97
MINERvA	Hybrid	CH,H_2O,Fe,Pb,C,He	8	3.8	FNAL	2010-19
T2K-ND280	Hybrid	CH,H_2O	2	0.6	J-PARC	2010-
COHERENT	Hybrid	several	between 0.01 and 1.3	0.03	ORNL	2015-
SND@LHC	Hybrid	Emulsions & SciFi	0.81	[100-1000]	CERN (LHC)	2022-

exposed to wideband neutrino and antineutrino beams at the Serpukhov laboratory in the former Soviet Union. A series of American bubble chambers in the 1970's and 1980's made measurements on free nucleons that are still crucial inputs for neutrino-nucleus scattering predictions. The 12-foot bubble chamber at ANL [468] in the USA used both deuterium and hydrogen targets, as did the 7-foot bubble chamber at BNL [469]. Fermilab's 15 foot bubble chamber [470] used deuterium and neon targets.

35.11.3.3 *Iron Tracking Calorimeters*

Because of the forward boost of high energy interactions, long detectors made of magnetized iron interspersed with active detector layers have been very successfully employed. The long magnetized detectors allow measurements of the momentum of penetrating muons. The iron planes also act as shower-inducing layers, allowing separation of EM and hadronic showers; the large number of iron planes provide enough mass for high statistics and/or shower containment. Magnetized iron spectrometers have been used for studies of the weak interaction, measurements of structure functions, and searches for neutrino oscillation. Non-magnetized iron detectors have also been successfully employed as neutrino monitors for oscillation experiments and also for neutrino-nucleus interaction studies.

The Caltech-Fermilab counter (CITF) [468] combined a 92 ton iron-scintillator target-calorimeter detector with a downstream toroidal magnet to perform early studies of weak interactions—including observations of neutral currents. The CDHS [471] detector used layers of magnetized iron modules interspersed with wire drift chambers, with a fiducial mass of 1250 t, to detector neutrinos in the range 10–200 GeV. Within each iron module, 5 cm (or 15 cm) iron plates were interspersed with scintillation counters. The MINOS [472] detectors, a near detector of 980 t at FNAL and a far detector of 5500 t in the Soudan Underground Laboratory (SUL), were functionally identical magnetized iron calorimeters, comprised of iron plates interleaved with layers of 4 cm wide plastic scintillator strips in alternating orientations. The T2K [473] on-axis detector, INGRID, consists of 16 non-magnetized iron scintillator sandwich detectors, each with nine 6.5 cm iron plane (7.1 t total) interspersed between layers of 5 cm wide plastic scintillator strips readout out by multi-pixel photon counters (MPPCs) coupled to WLS fibers. Fourteen of the INGRID modules are arranged in a cross-hair configuration centered on the neutrino beam axis.

35.11.3.4 *Cherenkov Detectors*

Open volume water Cherenkov detectors were originally built to search for proton decay. Large volumes of ultra-pure water were lined with photomultipliers to collect Cherenkov light emitted by the passage of relativistic charged particles. See Sec. 36.3.1 for a detailed discussion of deep liquid detectors for rare processes. The Cherenkov light, which has significant production in the visible range, appears on the walls of the detectors in distinctive ring patterns, and topological characteristics of the rings are employed to separate muon-induced rings from electron-induced with very high accuracy. As neutrino detectors, Cherenkov detectors optimize the design balance since the entire neutrino target is also active detector medium.

When used to detect $\sim$ GeV neutrinos, the detector medium acts as a natural filter for final state particles below the Cherenkov threshold; this feature has been exploited successfully by the K2K, MiniBooNE (using mineral oil instead of water), and T2K neutrino oscillation experiments. This makes event reconstruction simple and robust since electrons and muons have very different signatures, but does require making assumptions when inferring neutrino energy since not all final state particles are observed. At higher energies Cherenkov detectors become less accurate because the overlapping rings from many final state particles become increasingly difficult to resolve.

The second-generation Cherenkov detector in Japan, Super-Kamiokande [86] (Super-K), comprises 22.5 kt of water viewed by 50 cm photomultiplier tubes with 40% photocathode coverage;

it is surrounded by an outer detector region viewed by 20 cm photomultipliers. Super-K is the far detector for K2K and T2K, and is described in greater detail elsewhere in this review. The K2K experiment also employed a 1 kt water Cherenkov detector in the suite of near detectors [474], with 40% photocathode coverage. The MiniBooNE detector at FNAL was a 0.8 kt [475] mineral oil Cherenkov detector, with 20 cm photomultipliers giving 10% photocathode coverage, surrounded by a veto detector also with 20 cm photomultipliers. The ANNIE detector also at FNAL consists of a 26-ton water Cherenkov detector loaded with gadolinium sulfate (Gd2O12S3), complemented by a muon range detector and a veto wall. In addition to traditional PMTs, it exploits novel Large Area Picosecond Photodetectors (LAPPDs) for the detection of the Cherenkov light.

35.11.3.5 *Scintillation Detectors*

Liquid and solid scintillator detectors also employ fully (or nearly fully) active detector media. Typically organic scintillators, which emit into the ultraviolet range, are dissolved in mineral oil or plastic and read out by photomultipliers coupled to wavelength shifters (WLS). Open volume scintillation detectors lined with photomultipliers are conceptually similar to Cherenkov detectors, although energy reconstruction is calorimetric in nature as opposed to kinematic (see also Sec. 36.3.1). For higher energies and higher particle multiplicities, it becomes beneficial to use segmented detectors to help distinguish particle tracks and showers from each other.

The HWPF collaboration [476] employed a 2 t liquid scintillator total-absorption hadron calorimeter followed by a magnetic spectrometer to observe neutral current events in the early days of Fermilab. The LSND [477] detector at LANL was a 130 t open volume liquid scintillator detector employed to detect relatively low energy (<300 MeV) neutrinos. The NOvA [478] detectors use segmented volumes of liquid scintillator in which the scintillation light is collected by WLS fibers in the segments that are coupled to avalanche photodiodes (APDs) at the ends of the volumes. The NOvA far detector, located in Ash River, MN, is comprised of 896 layers of 15.6 m long extruded PVC scintillator cells for a total mass of 14 kt; the NOνA near detector is comprised of 214 layers of 4.1 m scintillator volumes for a total mass of of 300 t. Both are placed in the NuMI beamline at 0.8° off-axis. The SciBar (Scintillation Bar) detector was originally built for K2K at KEK in Japan and then re-used for SciBooNE [479] at FNAL. SciBar used plastic scintillator strips with 1.5 cm×2.5 cm rectangular cross section, read out by multianode photomultipliers (MAPMTs) coupled to WLS fibers, arranged in alternating horizontal and vertical layers. Both SciBooNE and K2K employed an EM calorimeter downstream of SciBar and a muon range detector (MRD) downstream of that.

The Coherent Captain Mills (CCM) detector is an upright cylindrical cryostat 2.58 m in diameter and 2.25 m high that holds 10 tons of LAr and is designed to be movable for distances between 20 m to 40 m from the neutrino source. It is instrumented with 120 8-inch PMTs, out of which 96 are coated with Tetraphenyl Butadiene (TPB) wavelength shifter.

35.11.3.6 *Liquid Argon Time Projection Chambers*

Liquid argon time projection chambers (LAr-TPCs) were conceived in the 1970s as a way to achieve a fully active detector with sub-centimeter track reconstruction [480]. A massive volume of purified liquid argon is put under a strong electric field (hundreds of V/cm), so that the liberated electrons from the paths of ionizing particles can be drifted to the edge of the volume and read out, directly by collecting charge from wire planes or non-destructively through charge induction in the wire planes. Dual-phase readout methods have also been developed, in which the charge is drifted vertically and then passed through an amplification region inside a gas volume above the liquid volume; the bottom of the liquid volume is equipped with a PMT array for detecting scintillation photons form the liquid argon. The first large scale LAr-TPC was the ICARUS T-600 module [481], comprising 760 t of liquid argon with a charge drift length of 1.5 m read out by wires

with 3 mm pitch, which operated in LNGS, both standalone and also exposed to the CNGS high energy neutrino beam. The ICARUS detector has been transported to Fermilab and installed and presently operated in an on-axis position in the Booster Neutrino Beamline at 600 m from target, where it is also exposed to off-axis neutrinos from the NuMI beamline. It will be complemented by the SBND detector(100 m from BNB target, 112 t fiducial mass), currently in the final phases of installation to search for possible anomalies in short baseline neutrino oscillation in the context of the SBN Program.

The ArgoNeuT [482] detector at FNAL, with fiducial mass 25 kg of argon read out with 4 mm pitch wires, was exposed to the NuMI neutrino and antineutrino beams. The MicroBooN [483] detector at FNAL comprises 170 t (85t active) of liquid Ar, read out with 3 mm wire pitch, which began collecting data in the Booster Neutrino Beam Oct 2015. A LAr-TPC has also been chosen as the multi-kton detector design for the future DUNE [484] neutrino oscillation experiment, from FNAL to Sanford Underground Research Facility. The design choices for the first two DUNE far detector modules (each with a total LAr mass of 17 kt) are being validated in the NP04 (horizontal drift) and the NP02 (vertical drift) experiments at the CERN Neutrino Platform facility [485,486].

35.11.3.7 *Emulsion Detectors*

Photographic film emulsions have been employed in particle physics experiments since the 1940s [487]. Thanks to advances in scanning technology and automation [488], they have been successfully employed as neutrino detectors. Emulsions are used for experiments observing CC tau neutrino interactions, where the short lifetime of the tau, $\tau_\tau = 2.90 \times 10^{-13}$s, leading to the short mean path length, $c \times \tau = 87\mu$m, requires extremely precise track resolution. They are employed in hybrid detectors in which the emulsion bricks are embedded inside fine-grained tracker detectors. In the data analysis, the tracker data are used to select events with characteristics typical of a tau decay in the final state, such as missing energy and unbalanced transverse momentum. The reconstructed tracks are projected back into an emulsion brick and used as the search seed for a neutrino interaction vertex.

E531 [489] at Fermilab tested many of the emulsion-tracker hybrid techniques employed by later neutrino experiments, in a detector with approximately 9 kg of emulsion target. The CHORUS [488] experiment at CERN used 1,600 kg of emulsion, in a hybrid detector with a fiber tracker, high resolution calorimeter, and muon spectrometer, to search for $\nu_\mu \to \nu_\tau$ oscillation. The DONuT [490] experiment at FNAL used a hybrid detector, with 260 kg of emulsion bricks interspersed with fiber trackers, followed by a magnetic spectrometer, and calorimeter, to make the first direct observation of tau neutrino CC interactions. The OPERA [491] [492] [493] experiment used an automated hybrid emulsion detector, with 1,25x0 t of emulsion, to make the first direct observation of the appearance of ν_τ in a ν_μ beam. Recently, the NINJA collaboration has developed an emulsion cloud chamber detector to observe neutrinos in the J-PARC neutrino beam [494].

FASERν [495] (a sub-detector of the FASER [496] experiment) is designed to detect and study all neutrino flavors produced at the LHC in the far-forward region of the ATLAS interaction point at the TeV energies scale. It consists of emulsion films interleaved with tungsten plates with a total target mass of 1.2 tons, enabling the identification of the leptons in charged current ν interactions. Placed 480m downstream of ATLAS, FASERν will measure neutrino cross sections at energies where they are currently unconstrained and will bound models of forward particle production.

35.11.3.8 *Hybrid Detectors*

In the previous neutrino detector examples, one can point to a specific detection technology or configuration that defines a category of detectors. In this section we look at detectors that combine multiple elements or techniques, without one facet being specifically dominant or crucial; we call these detectors hybrids.

The CHARM detector [497] at CERN was built to study neutral-current interactions and search for muon neutrino oscillation. It was a fine-grained ionization calorimeter tracker with approximately 150 t of marble as neutrino target, surrounded by a magnetized iron muon system for tagging high angle muons, and followed downstream by a muon spectrometer. The CHARM II detector [498] at CERN comprised a target calorimeter followed by a downstream muon spectrometer. Each target calorimeter module consists of a 4.8 cm thick glass plate followed by a layer of plastic streamer tubes, with spacing 1 cm, instrumented with 2 cm wide pickup strips. Every fifth module is followed by a 3 cm thick scintillator layer. The total mass of the target calorimeter was 692 t.

The Brookhaven E-734 [499] detector was a tracking calorimeter made up of 172 t liquid scintillator modules interspersed with proportional drift tubes, followed by a dense EM calorimeter and a muon spectrometer downstream of that. The detector was exposed to a wideband horn-focused beam with peak neutrino energy near 1 GeV. The Brookhaven E-776 [500] experiment comprised a finely segmented EM calorimeter, with 2.54 cm concrete absorbers interspersed with planes of drift tubes and acrylic scintillation counters, with total mass 240 t, followed by a muon spectrometer.

The FNAL Lab-E neutrino detector was used by the CCFR [501] and NuTeV [502] collaborations to perform a series of experiments in the Fermilab high energy neutrino beam (50 GeV$<$ E_ν $<$ 300 GeV). The detector was comprised of six iron target calorimeter modules, with 690 t total target mass, followed by three muon spectrometer modules, followed by two drift chambers. Each iron target calorimeter module comprised 5.2 cm thick steel plates interspersed with liquid scintillation counters and drift chambers.

The NOMAD [503] detector at CERN consisted of central tracker detector inside a 0.4 T dipole magnet (the magnet was originally used by the UA1 experiment at CERN) followed by a hadronic calorimeter and muon detectors downstream of the magnet. The main neutrino target is 3 t of drift chambers followed downstream by transition radiation detectors which are followed by an EM calorimeter. NOMAD was exposed to the same wideband neutrino beam as was CHORUS.

MINERvA [504] is a hybrid detector based around a central plastic scintillator tracker: 8.3 t of plastic scintillator strips with triangular cross section read out by MAPMTs coupled to WLS fibers. The scintillator tracker is surrounded by electromagnetic and hadronic calorimetry, which is achieved by interleaving thin lead (steel) layers between the scintillator layers for the ECAL (HCAL). MINERvA is situated upstream of the MINOS near detector which acts as a muon spectrometer. Upstream of the scintillator tracker is a nuclear target region containing inactive layers of C (graphite), Pb, Fe (steel), and O (water). MINERvA's physics goals span a wide range of neutrino-nucleus interaction studies, from form factors to nuclear effects.

T2K [473] in Japan employs two near detectors at 280 m from the neutrino beam target, one centered on the axis of the horn-focused J-PARC neutrino beam and one placed 2.5° off-axis. The on-axis detector, INGRID, is described above. The 2.5° off-axis detector, ND280, employs the UA1 magnet (at 0.2 T) previously used by NOMAD. Inside the magnet volume are three separate detector systems: the trackers, the Pi0 Detector (P0D), and several ECal modules. The tracker detectors comprise two fine-grained scintillator detectors (FGDs), read out by MPPCs coupled to WLS fibers, interleaved between three gas TPCs read out by micromegas planes. The downstream FGD contains inactive water layers in addition to the scintillators. Upstream of the tracker is the P0D, a sampling tracker calorimeter with active detector materials comprising plastic scintillator read out by MPPCs and WLS fibers, and inactive sheets of brass radiators and refillable water modules. Surrounding the tracker and P0D, but still inside the magnet, are lead-scintillator EM sampling calorimeters.

The COHERENT collaboration aims to measure CEvNS (Coherent Elastic Neutrino-Nucleus Scattering) using the high-quality pion-decay-at-rest neutrino source at the Spallation Neutron

Source in Oak Ridge, Tennessee. For doing so, it is deploying a suite of detector systems in a hallway in the basement of the SNS target hall with a phased approach. This includes CsI[Na] crystal, LAr scintillation detector, NaI[Tl], interwoven EJ200 scintillator and gadolinium-doped Mylar, thorium-232 metal plates and Germanium detectors.

The SND@LHC experiment [505] will perform measurements with high-energy neutrinos (100 GeV–1 TeV) produced at the LHC in the pseudo-rapidity region $7.2 < \eta < 8.6$. It allows the identification of all neutrino flavours with high efficiency. It is located 480 m downstream and off-axis with respect to the ATLAS interaction point and consists of a target region followed by a muon identification system. The target (810 kg) is instrumented with nuclear emulsions and Scintillating Fibre (SciFi) planes. The muon identification system is made of iron slabs interleaved with scintillating bars planes. SND@LHC is complementary to FASERν as it intercepts different components of the neutrino flux from LHC collisions, mainly those produced in heavy flavour decays, mostly charm.

35.11.4 *Outlook*

Detectors for accelerator-based neutrino beams have been in use, and constantly evolving, for six decades now. The rich program of neutrino oscillation physics and attendant need for newer and better neutrino-nucleus scattering measurements means that more neutrino detectors with broader capabilities will be needed in the coming decades.

One of the most intriguing prospects is a large volume, high pressure gas time projection chamber (HPTPC). With the prospect of megawatt power accelerator-based neutrino beams, it is entirely feasible to collect high statistics data sets with a gas target. The low momentum thresholds for particle detection, and excellent momentum resolution and particle identification capabilities, of an HPTPC would open a new window into the physics of neutrino-nucleus scattering. Moreover, the ability to change the gas mixtures in the HPTPC would allow measurements in the same detector on multiple nuclear targets, which would, in turn, allow unprecedentedly accurate constraints and tuning of neutrino-nucleus interaction models.

35.12 Superconducting magnets for collider detectors

Revised August 2023 by Y. Makida (KEK).

35.12.1 *Solenoid Magnets*

In all cases SI unit are assumed, so that the magnetic field, B, is in Tesla, the stored energy, E, is in joules, the dimensions are in meters, and vacuum permeability of $\mu_0 = 4\pi \times 10^{-7}$.

The magnetic field (B) in an simple solenoid with a flux return iron yoke, in which the magnetic field is lower than magnetic saturation of < 2 T, is given by

$$B = \frac{\mu_0 \, n \, I}{L} \tag{35.48}$$

where n is the number of turns, I is the current and L is the coil length.

In an air-core solenoid case, the central field is given by

$$B(0,0) = \mu_0 \, n \, I \frac{1}{\sqrt{L^2 + 4R^2}} \ , \tag{35.49}$$

where R is the coil radius.

In most cases, momentum analysis is made by measuring the circular trajectory of the passing particles according to $p = mv = qrB$, where p is the momentum, m the mass, q the charge, r the bending radius. The sagitta, s, of the trajectory is given by

$$s = q \, B \, \ell^2 / 8p \ , \tag{35.50}$$

where ℓ is the path length in the magnetic field. In a practical momentum measurement in colliding beam detectors, it is more effective to increase the magnetic volume than the field strength, since

$$dp/p \propto p/B\,\ell^2 \ , \tag{35.51}$$

where ℓ corresponds to the solenoid coil radius R. The energy stored in the magnetic field of any magnet is calculated by integrating B^2 over all space:

$$E = \frac{1}{2\mu_0}\int B^2 dV \tag{35.52}$$

If the coil thin and inside an iron return yoke , (which is the case if it is to superconducting coil), then

$$E \approx (B^2/2\mu_0)\pi R^2 L \ . \tag{35.53}$$

For a detector in which the calorimetry is outside the aperture of the solenoid, the coil must be transparent in terms of radiation and absorption lengths. This usually means that the superconducting solenoid and its cryostat is of minimum real thickness and is made of a material with long radiation length. There are two major contributors to the thickness of a thin solenoid:

Table 35.15: Progress of superconducting magnets for particle physics detectors.

Experiment	Laboratory	B [T]	Radius [m]	Length [m]	Energy [MJ]	X/X_0	E/M [kJ/kg]
TOPAZ*	KEK	1.2	1.45	5.4	20	0.70	4.3
CDF*	Tsukuba/Fermi	1.5	1.5	5.07	30	0.84	5.4
VENUS*	KEK	0.75	1.75	5.64	12	0.52	2.8
AMY*	KEK	3	1.29	3	40	†	
CLEO-II*	Cornell	1.5	1.55	3.8	25	2.5	3.7
ALEPH*	Saclay/CERN	1.5	2.75	7.0	130	2.0	5.5
DELPHI*	RAL/CERN	1.2	2.8	7.4	109	1.7	4.2
ZEUS*	INFN/DESY	1.8	1.5	2.85	11	0.9	5.5
H1*	RAL/DESY	1.2	2.8	5.75	120	1.8	4.8
BaBar*	INFN/SLAC	1.5	1.5	3.46	27	†	3.6
D0*	Fermi	2.0	0.6	2.73	5.6	0.9	3.7
BELLE*	KEK	1.5	1.8	4	42	†	5.3
BES-III	IHEP	1.0	1.475	3.5	9.5	†	2.6
ATLAS-CS	ATLAS/CERN	2.0	1.25	5.3	38	0.66	7.0
ATLAS-BT	ATLAS/CERN	1	4.7–9.75	26	1080	(Toroid)†	
ATLAS-ET	ATLAS/CERN	1	0.825–5.35	5	2×250	(Toroid)†	
CMS	CMS/CERN	4	6	12.5	2600	†	12
SiD**	ILC	5	2.9	5.6	1560	†	12
ILD**	ILC	4	3.8	7.5	2300	†	13
SiD**	CLIC	5	2.8	6.2	2300	†	14
ILD**	CLIC	4	3.8	7.9	2300	†	13
FCC**		6	6	23	54000	†	12

* No longer in service
** Conceptual design in future
† EM calorimeter is inside solenoid, so small X/X_0 is not a goal

1. The conductor consisting of the current-carrying superconducting material (usually Nb-Ti/Cu) and the quench protecting stabilizer (usually aluminum) are wound on the inside of a structural support cylinder (usually aluminum alloy). The coil thickness scales as B^2R, so the thickness in radiation lengths (X_0) is

$$t_{\rm coil}/X_0 = (R/\sigma_h X_0)(B^2/2\mu_0) \ , \tag{35.54}$$

where $t_{\rm coil}$ is the physical thickness of the coil, X_0 the average radiation length of the coil/stabilizer material, and σ_h is the hoop stress in the coil [506]. $B^2/2\mu_0$ is the magnetic pressure. In large detector solenoids, the aluminum stabilizer and support cylinders dominate the thickness; the superconductor (Nb-TI/Cu) contributes a smaller fraction. The main coil and support cylinder components typically contribute about 2/3 of the total thickness in radiation lengths.

2. Another contribution to the material comes from the outer cylindrical shell of the vacuum vessel. Since this shell is susceptible to buckling collapse, its thickness is determined by the diameter, length and the modulus of the material of which it is fabricated. The outer vacuum shell represents about 1/3 of the total thickness in radiation length.

35.12.2 *Properties of collider detector magnets*

The physical dimensions, central field stored energy and thickness in radiation lengths normal to the beam line of the superconducting solenoids associated with the major collider are given in Table 35.15 [507]. Fig. 35.39 shows thickness in radiation lengths as a function of B^2R in various collider detector solenoids.

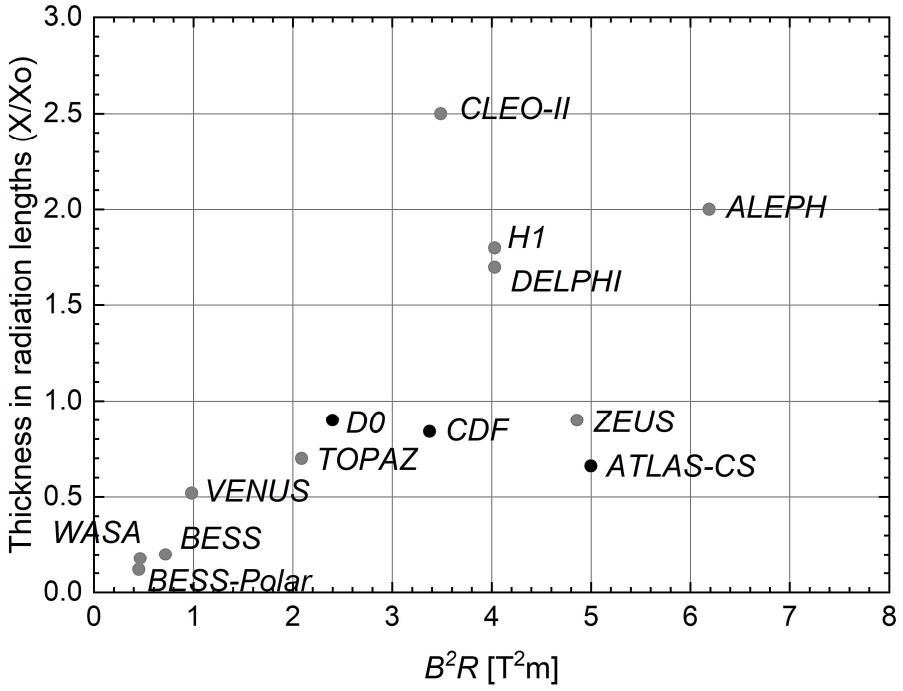

Figure 35.39: Magnet wall thickness in radiation length as a function of B^2R for various detector solenoids. Gray entries are for magnets no longer in use.

The ratio of stored energy to cold mass (E/M) is a useful performance measure. It can also be

expressed as the ratio of the stress, σ_h, to twice the equivalent density, ρ, in the coil [506]:

$$\frac{E}{M} = \frac{E}{\rho\, 2\pi t_{\rm coil} RL} \approx \frac{\sigma_h}{2\rho} \tag{35.55}$$

The E/M ratio in the coil is approximately equivalent to H,[¶¶] the enthalpy of the coil, and it determines the average coil temperature rise after energy absorption in a quench:

$$E/M = H(T_2) - H(T_1) \approx H(T_2) \tag{35.56}$$

where T_2 is the average coil temperature after the full energy absorption in a quench, and T_1 is the initial temperature. E/M ratios of 5, 10, and 20 kJ/kg correspond to ∼65, ∼80, and ∼100 K, respectively. The E/M ratios of various detector magnets are shown in Fig. 35.40 as a function of total stored energy. One would like the cold mass to be as small as possible to minimize the thickness, but temperature rise during a quench must also be minimized. An E/M ratio as large as 12 kJ/kg is designed into the CMS solenoid, with the possibility that about half of the stored energy can go to an external dump resistor. Thus the coil temperature can be kept below 80 K if the energy extraction system works well. The limit is set by the maximum temperature that the coil design can tolerate during a quench. This maximum local temperature should be <130 K (50 K + 80 K), so that thermal expansion effects, which are remarkable beyond 80 K, in the coil are manageable less than 50 K.

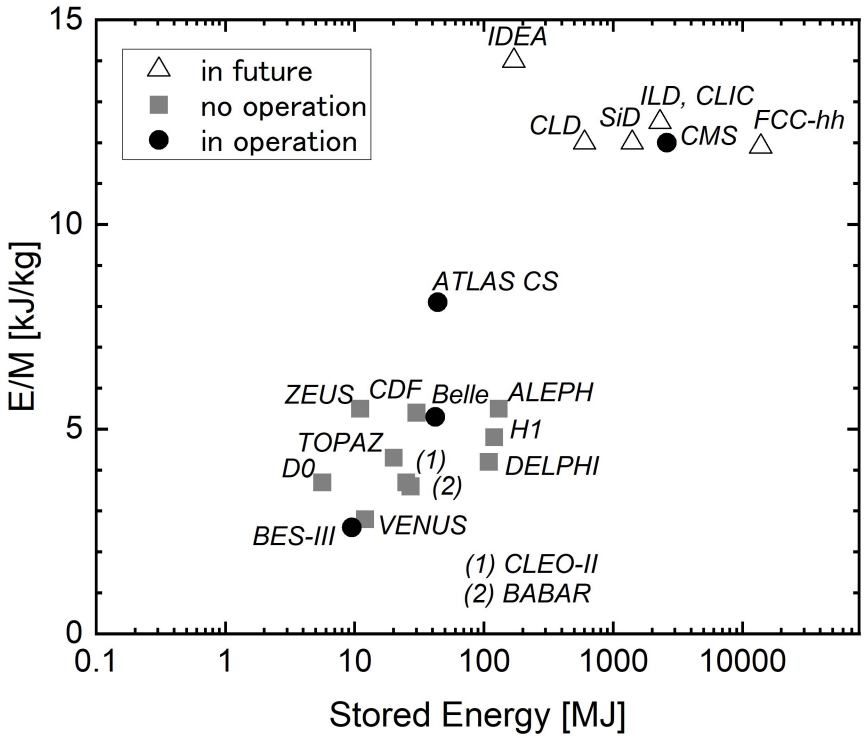

Figure 35.40: Ratio of stored energy to cold mass for major detector solenoids. Gray indicates magnets no longer in operation.

[¶¶]The enthalpy, or heat content, is called H in the thermodynamics literature. It is not to be confused with the magnetic field intensity B/μ.

35.12.3 *Toroidal magnets*

Toroidal coils uniquely provide a closed magnetic field without the necessity of an iron flux-return yoke. Because no field exists at the collision point and along the beam line, there is, in principle, no effect on the beam. On the other hand, the field profile generally has $1/r$ dependence. The particle momentum may be determined by measurements of the deflection angle combined with the sagitta. The deflection (bending) power BL is

$$BL \approx \int_{R_i}^{R_0} \frac{B_i R_i \, dR}{R \sin\theta} = \frac{B_i \, R_i}{\sin\theta} \ln(R_0/R_i) \ , \tag{35.57}$$

where R_i is the inner coil radius, R_0 is the outer coil radius, and θ is the angle between the particle trajectory and the beam line axis . The momentum resolution given by the deflection may be expressed as

$$\frac{\Delta p}{p} \propto \frac{p}{BL} \approx \frac{p \sin\theta}{B_i R_i \ln(R_0/R_i)} \ . \tag{35.58}$$

The momentum resolution is better in the forward/backward (smaller θ) direction. The geometry has been found to be optimal when $R_0/R_i \approx 3$–4. In practical designs, the coil is divided into 6–12 lumped coils in order to have reasonable acceptance and accessibility. This causes the coil design to be much more complex. The mechanical structure needs to sustain the decentering force between adjacent coils, and the peak field in the coil is 3–5 times higher than the useful magnetic field for the momentum analysis [508].

35.13 Measurement of particle momenta in a uniform magnetic field

The trajectory of a particle with momentum p (in GeV/c) and charge ze in a constant magnetic field $\overrightarrow{B}$ is a helix, with radius of curvature R and pitch angle λ. The radius of curvature and momentum component perpendicular to $\overrightarrow{B}$ are related by

$$p \cos\lambda = 0.3 \, z \, B \, R \ , \tag{35.59}$$

where B is in tesla and R is in meters.

The distribution of measurements of the curvature $k \equiv 1/R$ is approximately Gaussian. The curvature error for a large number of uniformly spaced measurements on the trajectory of a charged particle in a uniform magnetic field can be approximated by

$$(\delta k)^2 = (\delta k_{\rm res})^2 + (\delta k_{\rm ms})^2, \tag{35.60}$$

where δk = curvature error
$\delta k_{\rm res}$ = curvature error due to finite measurement resolution
$\delta k_{\rm ms}$ = curvature error due to multiple scattering.

If many ($\geq$ 10) uniformly spaced position measurements are made along a trajectory in a uniform medium,

$$\delta k_{\rm res} = \frac{\epsilon}{L'^2} \sqrt{\frac{720}{N+4}}, \tag{35.61}$$

where N = number of points measured along track
L' = the projected length of the track onto the bending plane
ϵ = measurement error for each point, perpendicular to the trajectory.

If a vertex constraint is applied at the origin of the track, the coefficient under the radical becomes 320.

For arbitrary spacing of coordinates s_i measured along the projected trajectory and with variable measurement errors ϵ_i the curvature error $\delta k_{\rm res}$ is calculated from:

$$(\delta k_{\rm res})^2 = \frac{4}{w}\,\frac{V_{ss}}{V_{ss}V_{s^2s^2} - (V_{ss^2})^2}, \tag{35.62}$$

where V are covariances defined as $V_{s^m s^n} = \langle s^m s^n - \rangle s^m \langle s^n$ with $\rangle s^m = w^{-1}\sum({s_i}^m/{\epsilon_i}^2)$ and $w = \sum {\epsilon_i}^{-2}$.

The contribution due to multiple Coulomb scattering is approximately

$$\delta k_{\rm ms} \approx \frac{(0.016)(\text{GeV}/c)z}{Lp\beta\cos^2\lambda}\sqrt{\frac{L}{X_0}}, \tag{35.63}$$

where p = momentum (GeV/c)
z = charge of incident particle in units of e
L = the total track length
X_0 = radiation length of the scattering medium (in units of length; the X_0 defined elsewhere must be multiplied by density)
β = the kinematic variable v/c.

More accurate approximations for multiple scattering may be found in the section on Passage of Particles Through Matter (Sec. 34 of this *Review*). The contribution to the curvature error is given approximately by $\delta k_{\rm ms} \approx 8 s^{\rm rms}_{\rm plane}/L^2$, where $s^{\rm rms}_{\rm plane}$ is defined there.

References

[1] H. Kolanoski and N. Wermes, *Particle Detectors - Fundamentals and Applications*, Oxford University Press (2020), ISBN 978-0-19-885836-2.

[2] T. Ferbel, *Experimental techniques in high energy physics; 1st ed.*, Frontiers in physics, Addison-Wesley, Menlo Park, CA (1987), URL https://cds.cern.ch/record/110951.

[3] K. Kleinknecht, *Detectors for particle radiation* (1998), ISBN 978-0-521-64854-7.

[4] G. Knoll, *Radiation Detection and Measurement (4th ed.)*, John Wiley, Hoboken, NJ (2010), ISBN 978-0-470-13148-0.

[5] D. Green, *The physics of particle detectors*, Cambridge University Press, Cambridge, UK (2000), ISBN 9780521675680.

[6] C. Leroy and P.-G. Rancoita, *Principles of radiation interaction in matter and detection*, World Scientific, Singapore (2011), ISBN 978-981-238-909-1.

[7] C. Grupen and B. Schwartz, *Particle detectors*, Cambridge University Press, Cambridge, UK (2008), ISBN 9780521187954.

[8] H. Spieler, *Semiconductor Detector Systems*, Oxford University Press, Oxford (2005), ISBN 978-0-19-852784-8.

[9] K. Arisaka, Nucl. Instrum. Meth. **A442**, 80 (2000).

[10] N. Matsunaga (ed.), *Photomultiplier Tubes: Basics and Applications*, 4th edition, Hamamatsu Photonics K.K., Hamamatsu (2017), https://www.hamamatsu.com/resources/pdf/etd/PMT_handbook_v4E.pdf.

[11] M. Böhm *et al.*, JINST **15**, 11, C11015 (2020).

[12] M. J. Minot *et al.*, Nuovo Cim. C **43**, 1, 11 (2020).
[13] A. Braem *et al.*, Nucl. Instrum. Meth. **A518**, 574 (2004).
[14] S. Korpar *et al.*, Nucl. Instrum. Meth. A **766**, 145 (2014).
[15] R. Arnold *et al.*, Nucl. Instrum. Meth. **A314**, 465 (1992).
[16] P. Mangeot *et al.*, Nucl. Instrum. Methods **A216**, 79 (1983).
[17] R. Apsimon *et al.*, IEEE Trans. **NS33**, 112 (1986).
[18] R. Arnold *et al.*, Nucl. Instrum. Meth. **A270**, 255 (1988).
[19] D. Aston *et al.*, Nucl. Instrum. Meth. **A283**, 582 (1989).
[20] R. Haitz *et al.*, J. Appl. Phys. **36**, 3123 (1965).
[21] R. McIntyre, IEEE Trans. Electron Devices **13**, 164 (1966).
[22] H. Dautet *et al.*, Applied Optics, **32**, 3894 (1993).
[23] Perkin-Elmer Optoelectronics, *Avalanche Photodiodes: A User's Guide*, (2003).
[24] P. Buzhan *et al.*, Nucl. Instrum. Meth. **A504**, 48 (2003).
[25] Z. Sadygov *et al.*, Nucl. Instrum. Methods **A504**, 301 (2003).
[26] V. Golovin and V. Savelev, Nucl. Instrum. Meth. **A518**, 560 (2004).
[27] F. Simon, Nuclear Instruments and Methods in Physics Research Section A: Accelerators, Spectrometers, Detectors and Associated Equipment **926**, 85–100 (2019), ISSN 0168-9002, URL http://dx.doi.org/10.1016/j.nima.2018.11.042.
[28] S. Korpar *et al.*, Nucl. Instrum. Meth. **A766**, 107 (2014).
[29] R. H. Pots *et al.*, Nucl. Instrum. Meth. **A940**, 254 (2019).
[30] D. R. Schaart *et al.*, Nuclear Instruments and Methods in Physics Research Section A: Accelerators, Spectrometers, Detectors and Associated Equipment **809**, 31 (2016).
[31] M. Petrov, M. Stapelbroek, and W. Kleinhans, Appl. Phys. Lett. **51**, 406 (1987).
[32] M. Atac and M. Petrov, IEEE Trans. **NS36**, 163 (1989).
[33] M. Atac *et al.*, Nucl. Instrum. Meth. **A314**, 56 (1992).
[34] B. Korzh *et al.*, Nature Photonics **14**, 250 (2020).
[35] J. S. Carlson *et al.*, J. Am. Chem. Soc. **139**, 28, 9621 (2017).
[36] J.B. Birks, *The Theory and Practice of Scintillation Counting*, Pergamon, London (1964).
[37] D. Clark, Nucl. Instru. Meth. **117**, 1, 295 (1974).
[38] Y. Kharzheev, Ann. Rev. Nucl. Part. **4**, 1 (2017).
[39] S. Moser *et al.*, Rad. Phys. and Chem. **41**, 1, 31 (1993), ISSN 0969-806X.
[40] M. Moszyński and B. Bengtson, Nucl. Instrum. Methods **158**, 1 (1979).
[41] J. B. Birks, Proc. Phys. Soc. **A64**, 874 (1951).
[42] D. Dexter, J. Chem. Phys. **21**, 836 (1953).
[43] C. Dujardin and M. Hamel, *Introduction—Overview on Plastic and Inorganic Scintillators*, 3–33, Springer International Publishing, Cham (2021).
[44] C. Chandler and et al., Additive Manufacturing **73**, 103688 (2023).
[45] S. Lee, M. Livan and R. Wigmans, Rev. Mod. Phys. **90**, 025002 (2018).
[46] R. C. Ruchti, Ann. Rev. Nucl. Part. **46**, 281 (1996).
[47] C. Joram, G. Haefeli and B. Leverington, JINST **10**, 08, C08005 (2015).

[48] D. Horstmann and U. Holm, Radiat. Phys. Chem. **41**, 1, 395 (1993), ISSN 0969-806X.

[49] K. Abe and et al. (T2K), JINST **17**, P10028 (2022).

[50] Y. Kharzheev, Phys. Part. Nucl. **50**, 1, 42 (2019).

[51] C. Zorn, in F. Sauli, editor, "Instrumentation in high-energy physics, Advanced Series on Directions in High Energy Physics," volume 9, 218, World Scientific (1992).

[52] CMS Collaboration, J. Instrum. **15**, 06, P06009 (2020).

[53] K. Gillen and R. Clough, Polymer **38**, 1929 (1992).

[54] T. Seguchi *et al.*, Radiat. Phys. Chem. **17**, 195 (1981), ISSN 0146-5724.

[55] P. Feng and et al., *Organic glass scintillators*, 243–283, Springer International Publishing, Cham (2021).

[56] S.E. Derenzo, W.-S. Choong and W.W. Moses, Phys. Med. Biol. **59**, 3261 (2014).

[57] C. Melcher and J. Schweitzer, Nucl. Instrum. Methods **A314**, 212 (1992).

[58] D.W. Cooke *et al.*, J. Appl. Phys. **88**, 7360 (2000).

[59] J.M. Chen *et al.*, IEEE Trans. **NS54**, 718 (2007).

[60] J.M. Chen *et al.*, IEEE Trans. **NS54**, 1319 (2007).

[61] E.V.D. van Loef *et al.*, Nucl. Instrum. Methods **A486**, 254 (2002).

[62] W. Drozdowski *et al.*, IEEE Trans. **NS55**, 1391 (2008).

[63] M.S. Alekhin *et al.*, Appl. Phys. Lett. **102**, 161915 (2013).

[64] C. Kuntner *et al.* (Crystal Clear), Nucl. Instrum. Meth. **A493**, 131 (2002).

[65] N. Akchurin *et al.*, Nucl. Instrum. Meth. **A595**, 359 (2008).

[66] H. Wenzel, Journal of Physics: Conference Series **404**, 012049 (2012).

[67] A. Benaglia *et al.*, IEEE Transactions on Nuclear Science **63**, 2, 574 (2016).

[68] R.H. Mao, L.Y. Zhang and R.Y. Zhu, IEEE Trans. **NS59**, 2229 (2012).

[69] R. Y. Zhu, TIPP 2017, SPPHY 213, 70 (2018).

[70] C. Hu *et al.*, IEEE Transactions on Nuclear Science **66**, 7, 1854 (2019).

[71] W.W. Moses, W.-S. Choong and S.E. Derenzo, Acta Physica Polonica **B7**, 725 (2014).

[72] R.H. Mao, L.Y. Zhang and R.Y. Zhu, IEEE Trans. **NS55**, 2425 (2008).

[73] B.D. Rooney and J.D. Valentine, IEEE Trans. **NS44**, 509 (1997).

[74] W.W. Moses *et al.*, IEEE Trans. **NS55**, 1049 (2008).

[75] G. Gratta, H. Newman and R. Y. Zhu, Ann. Rev. Nucl. Part. Sci. **44**, 453 (1994).

[76] R.-Y. Zhu, in "Handbook of Particle Detection and Imaging," 1–25, Springer International Publishing (2020).

[77] F. Yang *et al.*, IEEE Trans. **NS63**, 612 (2016).

[78] F. Yang *et al.*, IEEE Trans. **NS64**, 665 (2017).

[79] C. Hu *et al.*, IEEE Transactions on Nuclear Science **67**, 6, 1086 (2020).

[80] G. Dissertori *et al.*, Nucl. Instrum. Methods **745**, 1 (2014), and references therein.

[81] S. Ecklund, C. Field and G. Mazaheri, Nucl. Instr. and Meth. Res. Sect. **A463**, 68 (2001).

[82] M. G. Albrow *et al.*, JINST **7**, P10027 (2012), [arXiv:1207.7248].

[83] B. Aubert *et al.* (BaBar), Nucl. Instr. and Meth. Res. Sect. **A479**, 1 (2002), [hep-ex/0105044].

[84] E. Torassa (Belle-II PID Group), Nucl. Instr. and Meth. Res. Sect. **A824**, 152 (2016).

[85] G. Bayatian *et al.* (CMS), Eur. Phys. J. **C53**, 139 (2008).

[86] Y. Fukuda *et al.* (Super-Kamiokande), Nucl. Instrum. Meth. **A501**, 418 (2003).

[87] Proceedings of the International Workshops on Ring Imaging Cherenkov Detectors, Nucl. Instr. and Meth. Res. Sect. **A343**, 1 (1993); Nucl. Instr. and Meth. Res. Sect. **A371**, 1 (1996); Nucl. Instr. and Meth. Res. Sect. **A433**, 1 (1999); Nucl. Instr. and Meth. Res. Sect. **A502**, 1 (2003); Nucl. Instr. and Meth. Res. Sect. **A553**, 1 (2005); Nucl. Instr. and Meth. Res. Sect. **A595**, 1 (2008); Nucl. Instr. and Meth. Res. Sect. **A639**, 1 (2011); Nucl. Instr. and Meth. Res. Sect. **A766**, 1 (2014); Nucl. Instr. and Meth. Res. Sect. **A876**, 1 (2017); Nucl. Instr. and Meth. Res. Sect. **A 952**, 1 (2019).

[88] J. Litt and R. Meunier, Ann. Rev. Nucl. Part. Sci. **23**, 1 (1973).

[89] D. Bartlett *et al.*, Nucl. Instr. and Meth. Res. Sect. **A260**, 55 (1987).

[90] A. Abashian *et al.*, Nucl. Instr. and Meth. Res. Sect. **A479**, 117 (2002).

[91] B. N. Ratcliff, Nucl. Instr. and Meth. Res. Sect. **A502**, 211 (2003).

[92] T. Iijima *et al.*, Nucl. Instr. and Meth. Res. Sect. **A548**, 383 (2005), [arXiv:physics/0504220].

[93] B. Ratcliff and J. Va'vra, Nucl. Instrum. Meth. **A**, 163442 (2020).

[94] W. Blum, W. Riegler, and L. Rolandi, *Particle Detection with Drift Chambers*, Springer-Verlag, Berlin (2008).

[95] R. M. Sternheimer and R. F. Peierls, Phys. Rev. B **3**, 3681 (1971); L. Landau, J. Phys. (USSR) **8**, 201 (1944); W. W. M. Allison and J. H. Cobb, Ann. Rev. Nucl. Part. Sci. **30**, 253 (1980).

[96] I. Smirnov, Nucl. Instrum. Meth. **A554**, 474 (2005); I. Smirnov, HEED - High Energy Electro Dynamics, http://ismirnov.web.cern.ch/ismirnov/heed.

[97] L.G. Christophorou, *Atomic and Molecular Radiation Physics*, John Wiley & Sons, Hoboken (1971); J. Berkowitz, *Atomic and Molecular Photoabsorption*, Academic Press, Cambridge (2015).

[98] F. Sauli, *Gaseous Radiation Detectors: Fundamentals and Applications*, Cambridge University Press (2014).

[99] H. Bichsel, Nucl. Instrum. Meth. **A562**, 154 (2006).

[100] R. Veenhof, Garfield - Simulation of Gaseous Detectors, http://garfield.web.cern.ch/garfield/.

[101] Degrad - cluster size distribution and primary cluster distribution in gas mixtures for minimum ionising particles and X-rays, http://magboltz.web.cern.ch/magboltz/.

[102] S. F. Biagi, Nucl. Instrum. Meth. **A421**, 1-2, 234 (1999).

[103] S. Biagi, R. Veenhof, Magboltz - Boltzmann transport equations for electrons in gas mixtures under the influence of electric and magnetic fields, http://magboltz.web.cern.ch/magboltz/.

[104] S. Mukhopadhyay and N. Majumdar, in "17th DAE-BRNS High Energy Physics Symposium," (2007), [arXiv:physics/0703009].

[105] H. Fischle, J. Heintze and B. Schmidt, Nucl. Instrum. Meth. **A301**, 202 (1991).

[106] M. M. F. R. Fraga *et al.*, Nucl. Instrum. Meth. A **504**, 88 (2003).

[107] A. Peisert and F. Sauli, "Drift and diffusion of electrons in gases: A compilation (with an introduction to the use of computing program)," CERN-84-08, CERN-YELLOW-84-08 (1984).

[108] https://fr.lxcat.net/instructions/categories.php.

[109] O. Şahin, T. Z. Kowalski and R. Veenhof, Nucl. Instrum. Meth. A **768**, 104 (2014).

[110] O. Şahin *et al.*, JINST **5**, 05, P05002 (2010); O. Şahin, JINST **16**, 03, P03026 (2021).

[111] E. McDaniel and E. Mason, *The Mobility and Diffusion of Ions in Gases*, John Wiley & Sons, Hoboken (1973); G. Schultz, G. Charpak and F. Sauli, Rev. Phys. Appl. **12**, 1, 67 (1977).

[112] Y. Kalkan *et al.*, JINST **10**, 07, P07004 (2015).

[113] T. Ikeda *et al.*, JINST **15**, 07, P07015 (2020), [arXiv:2004.09706].

[114] G.F. Knoll, *Radiation Detection and Measurement*, 3nd edition, John Wiley & Sons, New York (1999).

[115] G. Charpak *et al.*, Nucl. Instrum. Methods **A62**, 262 (1968).

[116] G. Charpak and F. Sauli, Ann. Rev. Nucl. Sci. **34**, 285 (1984).

[117] G. Charpak *et al.*, Nucl. Instrum. Methods **A97**, 377 (1971).

[118] W. Blum, W. Riegler, and L. Rolandi, *Particle Detection with Drift Chambers*, Springer-Verlag, Berlin (2008).

[119] T. Ferbel (ed.), *Experimental Techniques in High Energy Physics*, Addison-Wesley, Menlo Park, CA (1987), see "Principles of Operation of Multiwire Proportional and Drift Chambers".

[120] R. Veenhof, Nucl. Instrum. Meth. A **419**, 726 (1998).

[121] G. Charpak *et al.*, Nucl. Instrum. Methods **A167**, 455 (1979).

[122] A.H. Walenta *et al.*, Nucl. Instrum. Methods **A92**, 373 (1971).

[123] A. Breskin *et al.*, Nucl. Instrum. Methods **A124**, 189 (1975).

[124] A. Breskin *et al.*, Nucl. Instrum. Methods **A156**, 147 (1978).

[125] R. Bouclier *et al.*, Nucl. Instrum. Meth. **A265**, 78 (1988), [,556(1987)].

[126] H. Drumm *et al.*, Nucl. Instrum. Methods **A176**, 333 (1980).

[127] D.R. Nygren and J.N. Marx, Phys. Today **31N10**, 46 (1978).

[128] C. Grupen, *Particle Detectors*, Cambridge Monographs on Particle Physics, Nuclear Physics and Cosmology, Cambridge University Press (2008).

[129] G. F. Tassielli *et al.*, JINST **15**, 09, C09051 (2020), [arXiv:2006.02378].

[130] M. Titov, ICFA Instrum. Bull. **26**, 002 (2004), [arXiv:physics/0403055]; M. Titov *et al.*, ICFA Instrum. Bull. **24**, 22 (2002), [hep-ex/0204005].

[131] P. S. Baringer *et al.*, Nucl. Instrum. Meth. **A254**, 542 (1987).

[132] J. Virdee, Phys. Reports **403**, 401 (2004).

[133] A. Sergi, Phys. Procedia **37**, 530 (2012).

[134] A. H. Walenta, Phys. Scripta **23**, 354 (1981).

[135] https://indico.cern.ch/event/1022051/ .

[136] J. A. Kadyk, Nucl. Instrum. Meth. A **300**, 436 (1991); J. Va'vra, ICFA Instrum. Bull. **24**, 1 (2002).

[137] M. Aleksa *et al.*, Nucl. Instrum. Meth. **A446**, 435 (2000).

[138] A. Oed, Nucl. Instrum. Meth. **A263**, 351 (1988).

[139] F. Sauli, Nucl. Instrum. Meth. **A386**, 531 (1997).

[140] Y. Giomataris *et al.*, Nucl. Instrum. Meth. **A376**, 29 (1996).

[141] Input to the European Particle Physics Strategy no. 87 (2019), S. Dalla Torre, E. Oliveri, L. Ropelewski, M. Titov, Development of the Micro-Pattern Gaseous Detector Technologies: an overview of the CERN-RD51 Collaboration, https://indico.cern.ch/event/765096/contributions/3295721.

[142] F. Sauli, *Micro-pattern gaseous detectors principles of operation and applications*, World Scientific, Singapore (2020).

[143] R. Bouclier *et al.*, Nucl. Instrum. Meth. A **381**, 289 (1996); Y. Bagaturia *et al.*, Nucl. Instrum. Meth. A **490**, 223 (2002).

[144] A. Bressan *et al.*, Nucl. Instrum. Meth. **A425**, 262 (1999).

[145] S. Bachmann *et al.*, Nucl. Instrum. Meth. **A479**, 294 (2002); A. Bressan *et al.*, Nucl. Instrum. Meth. **A424**, 321 (1999).

[146] M. Alfonsi *et al.*, Nucl. Instrum. Meth. A **671**, 6 (2012).

[147] J. Derre *et al.*, Nucl. Instrum. Meth. A **459**, 523 (2001).

[148] I. Giomataris *et al.*, Nucl. Instrum. Meth. A **560**, 405 (2006); S. Andriamonje *et al.*, JINST **5**, P02001 (2010).

[149] A. Breskin *et al.*, Nucl. Instrum. Meth. **124**, 189 (1975).

[150] J. Benlloch *et al.*, IEEE Trans. Nucl. Sci. **45**, 234 (1998).

[151] Y. Giomataris, Nucl. Instrum. Meth. **A419**, 239 (1998).

[152] M. Chefdeville *et al.*, Nucl. Instrum. Meth. A **556**, 490 (2006).

[153] M. Lupberger *et al.*, IEEE Trans. Nucl. Sci. **64**, 5, 1159 (2017).

[154] J. Leidner, F. Murtas and M. Silari, Applied Sciences **11**, 1 (2021).

[155] A. Curioni *et al.*, Nucl. Instrum. Meth. A **849**, 60 (2017).

[156] R. Chechik *et al.*, Nucl. Instrum. Meth. A **535**, 303 (2004); M. Alexeev *et al.*, JINST **8**, C12005 (2013).

[157] S. Dalla Torre, Nucl. Instrum. Meth. A **639**, 111 (2011).

[158] L. Moleri *et al.*, JINST **12**, 10, P10017 (2017), [arXiv:1707.00125].

[159] G. Bencivenni *et al.*, JINST **10**, 02, P02008 (2015), [arXiv:1411.2466].

[160] G. Bencivenni *et al.*, JINST **15**, 09, C09034 (2020).

[161] F. Yamane *et al.*, Nucl. Instrum. Meth. A **951**, 162938 (2020), [arXiv:1901.03836].

[162] T. Alexopoulos *et al.*, Nucl. Instrum. Meth. A **640**, 110 (2011).

[163] D. Abbaneo *et al.*, Nucl. Instrum. Meth. A **718**, 383 (2013).

[164] T. Alexopoulos *et al.*, Nucl. Instrum. Meth. A **617**, 161 (2010); L. Lavezzi *et al.*, in "2017 IEEE Nuclear Science Symposium and Medical Imaging Conference," (2017), [arXiv:1803.07266].

[165] A. Balla *et al.*, Nucl. Instrum. Meth. A **732**, 221 (2013).

[166] J. Bortfeldt *et al.*, Nucl. Instrum. Meth. A **903**, 317 (2018), [arXiv:1712.05256].

[167] RD51 DLC Workshop Report, RD51-NOTE-2021-002 (2021) .

[168] RD51 Collaboration: https://rd51-public.web.cern.ch/ ; S. Dalla Torre *et al.* (2018), [arXiv:1806.09955].

[169] D.R. Nygren and J.N. Marx, Phys. Today **31N10**, 46 (1978).

[170] J. Alme *et al.*, Nucl. Instrum. Meth. **A622**, 316 (2010), [arXiv:1001.1950].

[171] J. Adolfsson *et al.*, Journal of Instrumentation **16**, 03, P03022 (2021), URL https://doi.org/10.1088/1748-0221/16/03/p03022.

[172] N. Abgrall *et al.* (T2K ND280 TPC), Nucl. Instrum. Meth. A **637**, 25 (2011), [arXiv:1012.0865].

[173] A. H. Walenta *et al.*, Nucl. Instrum. Meth. **161**, 45 (1979).

[174] H. Aihara *et al.*, IEEE Trans. **NS30**, 63 (1983).

[175] K. Dehmelt (sPHENIX), PoS **MPGD2017**, 044 (2019).

[176] P. Colas, I. Giomataris and V. Lepeltier, Nucl. Instrum. Meth. **A535**, 226 (2004).

[177] X. Artru, G. B. Yodh and G. Mennessier, Phys. Rev. **D12**, 1289 (1975).

[178] J. Alozy *et al.*, Nucl. Instrum. Meth. **A961**, 163681 (2020).

[179] M. L. Cherry *et al.*, Phys. Rev. **D10**, 3594 (1974).

[180] B. Dolgoshein, Nucl. Instrum. Meth. **A326**, 434 (1993).

[181] A. Andronic and J. P. Wessels, Nucl. Instrum. Meth. **A666**, 130 (2012).

[182] S. Acharya *et al.* (ALICE), Nucl. Instrum. Meth. **A881**, 88 (2018), [arXiv:1709.02743].

[183] M. Petris *et al.*, Nucl. Instrum. Meth. **A714**, 17 (2013).

[184] T. Akesson *et al.* (ATLAS TRT), Nucl. Instrum. Meth. **A522**, 131 (2004).

[185] M. Ambriola *et al.*, Nucl. Instrum. Meth. **A522**, 77 (2004).

[186] J. Adelman (ATLAS), Nucl. Instrum. Meth. **A706**, 33 (2013).

[187] T. Kirn (AMS 02 TRD), Nucl. Instrum. Meth. **A706**, 43 (2013).

[188] G. M. Garibian, L. A. Gevorgian and C. Yang, Nucl. Instrum. Meth. **125**, 133 (1975).

[189] P. Nevski, Nucl. Instrum. Meth. **A522**, 116 (2004).

[190] J. Alozy *et al.*, Nucl. Instrum. Meth. **A927**, 1 (2019), [arXiv:1901.11265].

[191] V. M. Grishin and S. S. Sadilov, Nucl. Instrum. Meth. **A522**, 122 (2004).

[192] B. Beischer *et al.*, Nucl. Instrum. Meth. **A583**, 485 (2007).

[193] A. A. Savchenko *et al.*, JINST **15**, 06, C06024 (2020).

[194] T. Akesson *et al.* (ATLAS TRT), Nucl. Instrum. Meth. **A412**, 200 (1998).

[195] M. Ave *et al.*, Nucl. Instrum. Meth. **A654**, 140 (2011).

[196] M. L. Cherry, Nucl. Instrum. Meth. **A706**, 39 (2013).

[197] J. Alozy *et al.*, J. Phys. Conf. Ser. **1690**, 1, 012041 (2020).

[198] M. Brigida *et al.*, Nucl. Instrum. Meth. **A706**, 69 (2013).

[199] F. Hartjes *et al.*, Nucl. Instrum. Meth. **A706**, 59 (2013).

[200] V. V. Berdnikov *et al.*, Nucl. Instrum. Meth. **A706**, 65 (2013).

[201] R. Santonico and R. Cardarelli, Nucl. Instrum. Meth. **187**, 377 (1981).

[202] V. Parkhomchuck, Y. Pestov and N. Petrovykh, Nuclear Instruments and Methods **93**, 2, 269 (1971).

[203] G. V. Fedotovich, Y. N. Pestov and K. N. Putilin, in "International Conference on Instrumentation for Colliding Beam Physics," 127–131 (1982).

[204] E. Cerron Zeballos *et al.*, Nucl. Instrum. Meth. **A374**, 132 (1996).

[205] J. Juita *et al.*, Fire Science Reviews **1** (2012).

[206] P. Fonte, Journal of Instrumentation **8**, 04, P04017 (2013), URL https://dx.doi.org/10.1088/1748-0221/8/04/P04017.

[207] G. Aielli *et al.*, Nucl. Instrum. Meth. **A508**, 6 (2003).

[208] J. M. Meek, Phys. Rev. **57**, 722 (1940), URL https://link.aps.org/doi/10.1103/PhysRev.57.722.

[209] R. Cardarelli, R. Santonico and V. Makeev, Nucl. Instrum. Meth. **A382**, 470 (1996).

[210] R. Cardarelli, A. Di Ciaccio and R. Santonico, Nucl. Instrum. Meth. **A333**, 399 (1993).

[211] R. Cardarelli, Sci Acta **8**, 159 (1993).

[212] P. Camarri *et al.*, Nucl. Instrum. Meth. **A414**, 317 (1998).

[213] L. Pontecorvo, ATLAS Muon Internal note **20** (1993).

[214] W. Riegler, JINST **11**, 11, P11002 (2016).

[215] R. Santonico, Nucl. Instrum. Meth. **A456**, 1 (2000).

[216] R. Cardarelli *et al.*, JINST **8**, P01003 (2013).

[217] G. Aielli *et al.*, JINST **9**, 09, C09030 (2014).

[218] R. Santonico, JINST **9**, 11, C11007 (2014).

[219] G. Aad *et al.* (ATLAS), JINST **3**, S08003 (2008).

[220] S. Chatrchyan *et al.* (CMS), JINST **3**, S08004 (2008).

[221] G. Aielli *et al.*, Nucl. Instrum. Meth. A **562**, 92 (2006).

[222] A. Bertolin *et al.*, Nucl. Instrum. Meth. A **602**, 631 (2009).

[223] Aielli, Giulio *et al.*, Eur. Phys. J. C **80**, 12, 1177 (2020).

[224] M. Bauer *et al.*, "Anubis: Proposal to search for long-lived neutral particles in cern service shafts," (2019), [arXiv:1909.13022].

[225] M. Bedjidian *et al.*, JINST **6**, P02001 (2011), [arXiv:1011.5969].

[226] P. Fonte, A. Smirnitsky and M. C. S. Williams (ALICE), Nucl. Instrum. Meth. **A443**, 201 (2000).

[227] M. Abbrescia, V. Peskov and P. Fonte, *Resistive Gaseous Detectors: Designs, Performance, and Perspectives*, Wiley (2018), ISBN 9783527340767.

[228] W. Riegler and C. Lippmann, Nucl. Instrum. Meth **A508**, 14 (2003).

[229] P. Fonte (AIDA2020), "Validation of new resistive materials for RPCs ," .

[230] A. Akindinov *et al.*, Eur. Phys. J. Plus **128**, 44 (2013).

[231] D. Belver *et al.*, Nucl. Instrum. Meth. A **602**, 687 (2009).

[232] A. Schuttauf (FOPI), Nucl. Instrum. Meth. A **533**, 65 (2004).

[233] M. Ablikim *et al.*, Nucl. Instrum. Meth. A **614**, 3, 345 (2010), ISSN 0168-9002.

[234] e. a. P. Fonte, Nucl.Instrum.Meth.A **1051** (2023).

[235] I. Deppner and N. Herrmann, JINST **15**, 10, C10030 (2020).

[236] J. P. Chen *et al.*, "A white paper on solid (solenoidal large intensity device)," (2014), [arXiv:1409.7741].

[237] M. Benoit *et al.*, Journal of Instrumentation **11** (2015).

[238] S. An *et al.*, Nucl. Instrum. Meth. **A594**, 39 (2008).

[239] A. Blanco *et al.*, JINST **7**, P11012 (2012).

[240] C. Iacobaeus *et al.*, Nucl. Instrum. Meth. **A513**, 244 (2003), [arXiv:physics/0210006].

[241] G. Aielli *et al.*, Nucl. Instrum. Meth. **A456**, 82 (2000).

[242] G. Aielli *et al.*, Nucl. Instrum. Meth. **533**, 1, 86 (2004), ISSN 0168-9002, proceedings of the Seventh International Workshop on Resistive Plate Chambers and Related Detectors.

[243] H. Sakai *et al.*, Nucl. Instrum. Meth. **A484**, 153 (2002).

[244] R. Santonico, JINST **8**, P04023 (2013).

[245] L. Lopes *et al.*, Nucl. Instrum. Meth. **A533**, 69 (2004).

[246] B. Liberti *et al.*, Journal of Instrumentation **11**, 09, C09012 (2016), URL https://dx.doi.org/10.1088/1748-0221/11/09/C09012.

[247] S. Pisano *et al.*, Journal of Instrumentation **14**, 08, C08008 (2019), URL https://dx.doi.org/10.1088/1748-0221/14/08/C08008.

[248] G. Rigoletti, B. Mandelli and R. Guida, Journal of Instrumentation **15**, 11, C11003 (2020), URL https://dx.doi.org/10.1088/1748-0221/15/11/C11003.

[249] R. Guida, B. Mandelli and G. Rigoletti, Nuclear Instruments and Methods in Physics Research Section A: Accelerators, Spectrometers, Detectors and Associated Equipment **1039**, 167045 (2022), ISSN 0168-9002, URL https://www.sciencedirect.com/science/article/pii/S0168900222004685.

[250] G. Proto *et al.*, Journal of Instrumentation **17**, 05, P05005 (2022), URL https://dx.doi.org/10.1088/1748-0221/17/05/P05005.

[251] R. Cardarelli, JINST **16**, 05, C05004 (2021).

[252] "Summary of Liquid Argon Properties," Accessed August 2021, URL https://lar.bnl.gov/properties/.

[253] E. W. Lemmon *et al.*, "NIST Standard Reference Database 23: Reference Fluid Thermodynamic and Transport Properties-REFPROP, Version 10.0, National Institute of Standards and Technology," (2018), URL https://www.nist.gov/srd/refprop.

[254] C. Rubbia, "The liquid-argon time projection chamber: a new concept for neutrino detectors: CERN-EP-INT-77-8," (1977), URL https://cds.cern.ch/record/117852.

[255] H. H. Chen and J. F. Lathrop, Nucl. Instrum. Meth. **150**, 585 (1978).

[256] A. Marchionni, Ann. Rev. Nucl. Part. Sci. **63**, 269 (2013), [arXiv:1307.6918].

[257] K. Majumdar and K. Mavrokoridis, Appl. Sciences **11**, 6, 2455 (2021), [arXiv:2103.06395].

[258] F. Arneodo *et al.* (The ICARUS-Milano Collaboration), Phys. Rev. D **74**, 112001 (2006).

[259] S. Amerio *et al.* (ICARUS), Nucl. Instrum. Meth. A **527**, 329 (2004).

[260] C. Anderson *et al.* (ArgoNeuT), JINST **7**, P10019 (2012), [arXiv:1205.6747].

[261] R. Acciarri *et al.* (MicroBooNE), JINST **12**, 02, P02017 (2017), [arXiv:1612.05824].

[262] R. Acciarri *et al.* (LArIAT), JINST **15**, 04, P04026 (2020), [arXiv:1911.10379].

[263] C. E. Taylor *et al.* (CAPTAIN), Nucl. Instrum. Meth. A **1001**, 165131 (2021), [arXiv:2008.11422].

[264] A. A. Abud *et al.* (DUNE (protoDUNE-SP)) (2021), [arXiv:2108.01902].

[265] P. Abratenko *et al.* (MicroBooNE), JINST **16**, 06, P06043 (2021), [arXiv:2011.01375].

[266] M. Wang *et al.* (2020), [arXiv:2009.04509].

[267] B. Abi *et al.* (DUNE), Phys. Rev. D **102**, 9, 092003 (2020), [arXiv:2006.15052].

[268] G. Carugno *et al.* (ICARUS), Nucl. Instrum. Meth. A **292**, 580 (1990).

[269] M. Adamowski *et al.*, JINST **9**, P07005 (2014), [arXiv:1403.7236].

[270] C. Adams *et al.* (MicroBooNE), JINST **15**, 07, P07010 (2020), [arXiv:1910.01430].

[271] G. Bakale, U. Sowada and W. F. Schmidt, The Journal of Physical Chemistry **80**, 23, 2556 (1976).

[272] A. Bettini *et al.* (ICARUS), Nucl. Instrum. Meth. A **305**, 177 (1991).

[273] W. Jaskierny *et al.* (Fermilab-TM-2384-E), Technical report (2006), URL https://lss.fnal.gov/archive/test-tm/2000/fermilab-tm-2384-e.pdf.

[274] Sigma-Aldrich 4A, BASF Copper Getter CU-0226S.

[275] P. Cennini *et al.*, Nucl. Instrum. Meth. A **333**, 567 (1993).

[276] R. Acciarri *et al.* (WArP), JINST **5**, P06003 (2010), [arXiv:0804.1217].

[277] B. J. P. Jones *et al.*, JINST **8**, P07011 (2013), [Erratum: JINST 8, E09001 (2013)], [arXiv:1306.4605].

[278] M. Miyajima *et al.*, Phys. Rev. A **9**, 1438 (1974).

[279] R. T. Scalettar *et al.*, Phys. Rev. A **25**, 2419 (1982).

[280] E. Aprile *et al.*, Nucl. Instrum. Meth. A **261**, 519 (1987).

[281] P. Cennini *et al.* (ICARUS), Nucl. Instrum. Meth. A **345**, 230 (1994).

[282] S. Amoruso *et al.* (ICARUS), Nucl. Instrum. Meth. A **523**, 275 (2004).

[283] R. Acciarri *et al.* (ArgoNeuT), JINST **8**, P08005 (2013), [arXiv:1306.1712].

[284] G. Jaffe, Annalen der Physik **42**, 12, 303 (1913).

[285] L. Onsager, Phys. Rev. **54**, 554 (1938).

[286] J. Thomas and D. A. Imel, Phys. Rev. A **36**, 614 (1987).

[287] C. Adams *et al.* (MicroBooNE), JINST **15**, 03, P03022 (2020), [arXiv:1907.11736].

[288] T. Yang, Instruments **5**, 1, 2 (2020), [arXiv:2012.01319].

[289] S. Amoruso *et al.* (ICARUS), Nucl. Instrum. Meth. A **516**, 68 (2004).

[290] W. Walkowiak, Nucl. Instrum. Meth. A **449**, 288 (2000).

[291] M. Antonello *et al.* (ICARUS), JINST **9**, 12, P12006 (2014), [arXiv:1409.5592].

[292] V. Meddage (MicroBooNE), in "Meeting of the APS Division of Particles and Fields," (2017), [arXiv:1710.00396].

[293] B. Abi *et al.* (DUNE), JINST **15**, 12, P12004 (2020), [arXiv:2007.06722].

[294] Y. Li *et al.*, Nucl. Instrum. Meth. A **816**, 160 (2016), [arXiv:1508.07059].

[295] P. Agnes *et al.* (DarkSide), Nucl. Instrum. Meth. A **904**, 23 (2018), [arXiv:1802.01427].

[296] P. Abratenko *et al.* (MicroBooNE), JINST **16**, 09, P09025 (2021), [arXiv:2104.06551].

[297] M. Miyajima *et al.*, Phys. Rev. A **10**, 1452 (1974).

[298] N. Gee *et al.*, Journal of Applied Physics **57**, 4, 1097 (1985).

[299] T. Doke *et al.*, Nucl. Instrum. Meth. A **269**, 291 (1988).

[300] T. Doke, K. Masuda and E. Shibamura, Nucl. Instrum. Meth. A **291**, 617 (1990).

[301] T. Heindl *et al.*, EPL **91**, 6, 62002 (2010), [arXiv:1511.07718].

[302] M. Babicz *et al.*, JINST **15**, 09, P09009 (2020), [arXiv:2002.09346].

[303] G. M. Seidel, R. E. Lanou and W. Yao, Nucl. Instrum. Meth. A **489**, 189 (2002), [hep-ex/0111054].

[304] E. Grace and J. A. Nikkel, Nucl. Instrum. Meth. A **867**, 204 (2017), [arXiv:1502.04213].

[305] A. Hitachi *et al.*, Phys. Rev. B **27**, 5279 (1983).

[306] P. Adhikari *et al.* (DEAP), Eur. Phys. J. C **80**, 4, 303 (2020), [arXiv:2001.09855].

[307] B. Abi *et al.* (DUNE), JINST **15**, 08, T08010 (2020), [arXiv:2002.03010].

[308] M. Auger *et al.*, JINST **11**, 03, P03017 (2016), [arXiv:1512.05968].

[309] S. Kubota *et al.*, Phys. Rev. B **20**, 8, 3486 (1979).

[310] M. Kuźniak and A. M. Szelc, Instruments **5**, 1, 4 (2020), [arXiv:2012.15626].

[311] R. Acciarri *et al.* (WArP), JINST **5**, P05003 (2010), [arXiv:0804.1222].

[312] F. Spiegelmann and J.-P. Malrieu, Chemical Physics Letters **57**, 2, 214 (1978), ISSN 0009-2614.

[313] B. Jones *et al.*, JINST **8**, P12015 (2013), [arXiv:1308.3658].

[314] A. Buzulutskov, EPL **117**, 3, 39002 (2017), [arXiv:1702.03612].

[315] J. Soto-Oton (DUNE), in "International Conference on Technology and Instrumentation in Particle Physics," (2021), [arXiv:2109.05858].

[316] A. Abed Abud *et al.* (DUNE) (2021), [arXiv:2103.13910].

[317] P. Abratenko *et al.* (MicroBooNE), JINST **15**, 12, P12037 (2020), [arXiv:2008.09765].

[318] M. Antonello *et al.* (ICARUS), JINST **15**, 07, P07001 (2020), [arXiv:2001.08934].

[319] S. Palestini, Instruments **5**, 1, 9 (2021), [arXiv:2102.06082].

[320] C. Cantini *et al.*, JINST **12**, 03, P03021 (2017), [arXiv:1611.02085].

[321] J. Asaadi *et al.*, JINST **9**, P09002 (2014), [arXiv:1406.5216].

[322] O. Bunemann, T. E. Cranshaw and J. A. Harvey, Canadian Journal of Research **27a**, 5, 191 (1949).

[323] V. Radeka *et al.*, J. Phys. Conf. Ser. **308**, 012021 (2011).

[324] H. Chen *et al.*, Phys. Procedia **37**, 1287 (2012).

[325] S. Li *et al.*, IEEE Transactions on Nuclear Science **60**, 6, 4737 (2013).

[326] H. Chen *et al.*, Nucl. Instrum. Meth. A **936**, 271 (2019).

[327] R. Acciarri *et al.* (MicroBooNE), JINST **12**, 08, P08003 (2017), [arXiv:1705.07341].

[328] P. Cennini *et al.* (ICARUS), Nucl. Instrum. Meth. A **432**, 240 (1999).

[329] D. Caratelli (MicroBooNE), JINST **15**, 03, C03023 (2020).

[330] B. Ali-Mohammadzadeh *et al.* (ICARUS), JINST **15**, 10, T10007 (2020), [arXiv:2006.05261].

[331] A. Ankowski *et al.* (ICARUS), Nucl. Instrum. Meth. A **556**, 146 (2006).

[332] N. Anfimov *et al.*, JINST **15**, 07, C07022 (2020).

[333] E. Segreto *et al.*, JINST **15**, 05, C05045 (2020).

[334] M. Antonello *et al.*, JINST **9** (2014), URL https://iopscience.iop.org/article/10.1088/1748-0221/9/08/P08003/pdf.

[335] H. Chen *et al.*, 16th IEEE-NPSS Real Time Conference 159–162 (2009), URL https://ieeexplore.ieee.org/document/5322032.

[336] B. Abi *et al.* (DUNE) (2018), [arXiv:1807.10327].

[337] B. Abi *et al.* (DUNE) (2018), [arXiv:1807.10340].

[338] R. Acciarri *et al.*, JINST **12**, 08, P08003 (2017), [arXiv:1705.07341].

[339] C. Adams *et al.*, JINST **13**, 07, P07006 (2018), [arXiv:1802.08709].

[340] B. Abi *et al.*, JINST **15**, 12, P12004 (2020), [arXiv:2007.06722].

[341] R. Acciarri *et al.* (MicroBooNE), Eur. Phys. J. C **78**, 1, 82 (2018), [arXiv:1708.03135].

[342] X. Qian *et al.*, JINST **13**, 05, P05032 (2018), [arXiv:1803.04850].

[343] R. Acciarri *et al.* (MicroBooNE), JINST **12**, 03, P03011 (2017), [arXiv:1611.05531].

[344] A. Abed Abud *et al.* (DUNE), Eur. Phys. J. C **82**, 10, 903 (2022), [arXiv:2203.17053].

[345] F. Drielsma *et al.* [arXiv:2102.01033].

[346] P. Abratenko *et al.* (MicroBooNE), JHEP **2021**, 153 (2021), [arXiv:2109.02460].

[347] C. Rubbia *et al.* (ICARUS), JINST **6**, P07011 (2011), [arXiv:1106.0975].

[348] D. A. Dwyer *et al.*, JINST **13**, 10, P10007 (2018), [arXiv:1808.02969].

[349] B. Baibussinov *et al.* (ICARUS), JINST **13**, 03, T03001 (2018), [arXiv:1711.06781].

[350] A. Lowe *et al.*, Instruments **4**, 4, 35 (2020), [arXiv:2011.02292].

[351] A. Ereditato *et al.*, JINST **8**, 07, P07002 (2013), [arXiv:1304.6961].

[352] E. Segreto, Phys. Rev. D **103**, 4, 043001 (2021), [arXiv:2012.06527].

[353] "Lidine 2021," Accessed October 2021, URL https://indico.physics.ucsd.edu/event/1/book-of-abstracts.pdf.

[354] L. Bäni *et al.* (RD42), J. Phys. Conf. Ser. **2374**, 1, 012172 (2022).

[355] A. Rogalski, Adv. Opt. Photon. **11**, 2, 314 (2019).

[356] V. Saraswat, R. Jacobberger and M. Arnold, ACS Nano 15:3, 3674–3708 (2021).

[357] G. Lutz, *Semiconductor Radiation Detectors*, Springer (1999), ISBN 978-3-540-64859-8.

[358] F. Hartmann, *Evolution of Silicon Sensor Technology in Particle Physics*, volume 275 of *Springer Tracts in Modern Physics*, Springer (2017), ISBN 978-3-319-64434-9, 978-3-319-64436-3.

[359] G. Lutz and R. Klanner, *Particle Physics Reference Library (Vol. 2, Ch. 5., Solid State Detectors), Eds. Fabjan, C. W. and Schopper, H.*, Springer Nature (2020), ISBN 978-3-030-35317-9, 978-3-030-35318-6.

[360] Landolt-Börnstein, Springer (Berlin), 2002, https://doi.org/10.1007/10832182_456 and https://doi.org/10.1007/10832182_458.

[361] C. Da Via *et al.*, Nucl. Instrum. Meth. **587**, 243 (2008).

[362] C. Damerell, Nucl. Instrum. Meth. A **342**, 78 (1994).

[363] L. Rossi *et al.*, *Pixel Detectors – From Fundamentals to Applications*, Springer, Berlin (2006), ISBN 978-3-540-28332-4, 978-3-540-28333-1.

[364] M. Garcia-Sciveres and N. Wermes, Rept. Prog. Phys. **81**, 6, 066101 (2018).

[365] H.-G. Moser *et al.*, PoS **VERTEX2007**, 022 (2007).

[366] Y. Arai *et al.*, Nucl. Instrum. Meth. A **623**, 186 (2010).

[367] H. Sadrozinski, A. Seiden and N. Cartiglia, Rept. Prog. Phys. **81**, 2, 026101 (2018).

[368] M. Ferrero *et al.*, *Ultra-Fast Silicon Detectors*, CRC Press, Open Access, Creative Commons (2021), ISBN 978-1-003-13194-6.

[369] A. Lampis *et al.*, JINST **18**, 01, C01051 (2023).

[370] S. Zambito *et al.*, JINST **18**, 03, P03047 (2023).

[371] W. Riegler and G. Aglieri Rinella, JINST **12**, 11, P11017 (2017).

[372] R. Wunstorf, *Systematische Untersuchungen zur Strahlenresistenz von Silizium-Detektoren für die Verwendung in Hohenergiephysikexperimenten*, Ph.D. thesis, Universität Hamburg (1992), URL https://www-library.desy.de/preparch/desy/int_rep/fh1k-92-01.pdf.

[373] M. Moll, IEEE Trans. Nucl. Sci. **65**, 8, 1561 (2018).

[374] G. Kramberger, "Initial acceptor removal in p-type silicon," Talk at 26th CERN-RD50 Workshop, Santander (2015), https://indico.cern.ch/event/381195/contributions/905665/.

[375] G. Kramberger, *Particle Physics Reference Library (Vol. 2, Ch. 21., Solid State Detectors for High Radiation Environments), Eds. Fabjan, C. W. and Schopper, H.*, Springer Nature (2020), ISBN 978-3-030-35317-9, 978-3-030-35318-6.

[376] W. Blum, L. Rolandi and W. Riegler, *Particle detection with drift chambers*, Particle Acceleration and Detection, Springer (2008), ISBN 978-3-540-76683-4, 978-3-540-76684-1.

[377] F. S. Goulding, Nucl. Instrum. Meth. **100**, 493 (1972).

[378] V. Radeka, Ann. Rev. Nucl. Part. Sci. **38**, 217 (1988).

[379] C. Agapopoulou *et al.*, JINST **15**, 07, P07007 (2020).

[380] R. Wigmans, *Calorimetry*, International Series of Monographs on Physics, Oxford University Press (2017).

[381] S. Agostinelli *et al.* (GEANT4), Nucl. Instrum. Meth. A **506**, 250 (2003).

[382] J. Allison *et al.*, IEEE Trans. Nucl. Sci. **53**, 270 (2006).

[383] T. Gabriel and L. Charlton (1997).

[384] T. T. Böhlen *et al.*, Nucl. Data Sheets **120**, 211 (2014).

[385] A. Ferrari *et al.* (2005).

[386] J. Allison *et al.*, Nucl. Instrum. Meth. A **835**, 186 (2016).

[387] D. Buskulic *et al.* (ALEPH), Nucl. Instrum. Meth. A **360**, 481 (1995).

[388] A. M. Sirunyan *et al.* (CMS), JINST **12**, 10, P10003 (2017), [arXiv:1706.04965].

[389] M. A. Thomson, Nucl. Instrum. Meth. A **611**, 25 (2009), [arXiv:0907.3577].

[390] L. Linssen *et al.* (2012), [arXiv:1202.5940].

[391] H. L. Tran *et al.*, Eur. Phys. J. C **77**, 10, 698 (2017), [arXiv:1705.10363].

[392] M. Aleksa *et al.*, Eur. Phys. J. Plus **136**, 10, 1066 (2021), [arXiv:2109.00391].

[393] M. T. Lucchini *et al.*, JINST **15**, 11, P11005 (2020), [arXiv:2008.00338].

[394] W.R. Nelson, H. Hirayama, and D.W.O. Rogers, SLAC-265 (1985) .

[395] ATLAS Collab., CERN/LHCC 96-41 (1996).

[396] D. Hitlin *et al.*, Nucl. Instrum. Meth. **137**, 225 (1976).

[397] W. J. Willis and V. Radeka, Nucl. Instrum. Meth. **120**, 221 (1974).

[398] R. Wigmans, *Calorimetry: Energy Measurement in Particle Physics*, Inter. Series of Monographs on Phys. **107**, Second Edition, Oxford Schlarship Online (2017).

[399] R. Y. Zhu, Nucl. Instrum. Meth. **A413**, 297 (1998).

[400] R.Y. Zhu, Journal of Physics: Conference Series **587**, 012055 (2015).

[401] CMS Collab., CERN/LHCC 97-33 (1997).

[402] C. Leroy and P. Rancoita, Rept. Prog. Phys. **63**, 505 (2000).

[403] F. Sefkow and F. Simon, *Calorimeters*, in Fleck I., Titov M., Grupen C., Buvat I. (eds) Handbook of Particle Detection and Imaging, Springer (2021), ISBN 978-3-319-47999-6.

[404] C. Adloff *et al.* (CALICE), JINST **8**, 07005 (2013).
[405] T. A. Gabriel *et al.*, Nucl. Instrum. Meth. **A338**, 336 (1994).
[406] F. Ariztizabal *et al.* (RD-34), Nucl. Instrum. Meth. **A349**, 384 (1994).
[407] F. Sefkow and F. Simon (CALICE), J. Phys. Conf. Ser. **1162**, 1, 012012 (2019), [arXiv:1808.09281].
[408] (2022), [arXiv:2209.15327].
[409] CMS, CERN-LHCC-2017-023, CMS-TDR-019 (2017).
[410] N. Akchurin *et al.*, Nucl. Instrum. Meth. **A399**, 202 (1997).
[411] A. Artamonov *et al.*, JINST **3**, P02010 (2008).
[412] B. Aubert *et al.*, Nucl. Instrum. Meth. **A321**, 467 (1992).
[413] C. W. Fabjan *et al.*, Nucl. Instrum. Meth. **141**, 61 (1977).
[414] J. Brau *et al.*, Nucl. Instrum. Meth. **A238**, 489 (1985).
[415] H. Brückmann and H. Kowalski, ZEUS Int. Note 86/026 DESY, Hamburg (1986).
[416] R. Wigmans, Nucl. Instrum. Meth. **A259**, 389 (1987).
[417] R. Wigmans, Nucl. Instrum. Meth. **A265**, 273 (1988).
[418] J. E. Brau and T. A. Gabriel, Nucl. Instrum. Meth. A **275**, 190 (1989).
[419] J. C. Brient, R. Rusack and F. Sefkow, Ann. Rev. Nucl. Part. Sci. **68**, 271 (2018).
[420] E. Fretwurst *et al.* (1989), URL http://cds.cern.ch/record/368113.
[421] E. Borchi *et al.* (SICAPO), Nucl. Instrum. Meth. **A279**, 57 (1989).
[422] H. Abramowicz *et al.* (2013), [arXiv:1306.6329].
[423] N. Alipour Tehrani *et al.* (CLICdp) (2017), CLICdp-Note-2017-001.
[424] N. Bacchetta *et al.* (2019), [arXiv:1911.12230].
[425] https://twiki.cern.ch/twiki/bin/view/CALICE/CaliceDetectors.
[426] C. Adloff *et al.* (CALICE), JINST **5**, P05004 (2010), [arXiv:1003.2662].
[427] M. Chefdeville *et al.* (CALICE), Nucl. Instrum. Meth. A **939**, 89 (2019), [arXiv:1901.08818].
[428] G. Baulieu *et al.*, JINST **10**, 10, P10039 (2015), [arXiv:1506.05316].
[429] B. Acar *et al.* (CMS, CALICE), JINST **18**, 08, P08014 (2023), [arXiv:2211.04740].
[430] C. Adloff *et al.* (CALICE), JINST **8**, P09001 (2013), [arXiv:1305.7027].
[431] H. Abramowicz *et al.*, Nucl. Instrum. Meth. **180**, 429 (1981).
[432] B. Andrieu *et al.* (H1 Calorimeter Group), Nucl. Instrum. Meth. A **336**, 499 (1993).
[433] C. Cojocaru *et al.* (ATLAS Liquid Argon EMEC/HEC), Nucl. Instrum. Meth. A **531**, 481 (2004), [arXiv:physics/0407009].
[434] C. Adloff *et al.* (CALICE), J. Instr. **7**, 09, P09017 (2012).
[435] H. L. Tran *et al.*, The European Physical Journal C **77**, 10, 698 (2017).
[436] P. Mockett, SLAC-267, 335 (1983).
[437] D. E. Groom, Nucl. Instrum. Meth. **A572**, 633 (2007), erratum: Nucl. Instrum. Meth. **A593**, 628 (2008).
[438] R. Wigmans, *Proc. 7th Inter. Conf. on Calorimetry in High Energy Physics*, 182 World Scientific, River Edge, NJ, (1998);.
[439] S. Lee, M. Livan and R. Wigmans, Rev. Mod. Phys. **90**, 2, 025002 (2018).

[440] S. Lee *et al.*, Nucl. Instrum. Meth. A **866**, 76 (2017), [arXiv:1703.09120].
[441] M. Antonello *et al.*, JINST **15**, 06, C06015 (2020).
[442] E. Bernardi *et al.*, Nucl. Instrum. Meth. **A262**, 229 (1987).
[443] M. Chefdeville *et al.* (CALICE), JINST **10**, 12, P12006 (2015), [arXiv:1509.00617].
[444] T. Akesson *et al.*, Nucl. Instrum. Meth. **A262**, 243 (1987).
[445] D. Acosta *et al.*, Nucl. Instrum. Meth. **A308**, 481 (1991).
[446] R. Dubois *et al.*, IEEE Trans. Nucl. Sci. **33**, 194 (1986).
[447] B. Andrieu *et al.* (H1 Calorimeter Group), Nucl. Instrum. Meth. A **336**, 460 (1993).
[448] A. Bernstein *et al.* (ZEUS Barrel Calorimeter Group), Nucl. Instrum. Meth. A **336**, 23 (1993).
[449] J.-b. Liu (CDF), in "7th International Conference on Calorimetry in High-Energy Physics (ICCHEP 97)," 237–240 (1997).
[450] S. Abachi *et al.* (D0), Nucl. Instrum. Meth. A **324**, 53 (1993).
[451] G. Aad *et al.* (ATLAS), JINST **3**, S08003 (2008).
[452] S. Abdullin *et al.* (USCMS, ECAL/HCAL), Eur. Phys. J. C **60**, 359 (2009), [Erratum: Eur.Phys.J.C 61, 353–356 (2009)].
[453] H. Abramowicz *et al.* (ZEUS), Phys. Lett. B **718**, 915 (2013), [arXiv:1210.5511].
[454] E. Shibamura *et al.*, Nucl. Instrum. Methods **A316**, 184 (1975).
[455] L. S. Miller, S. Howe and W. E. Spear, Phys. Rev. **166**, 871 (1968).
[456] A.M. Kalinin *et al.*, ATLAS-LARG-NO-058 (1996).
[457] K. Yoshino, U. Sowada and W. F. Schmidt, Phys. Rev. **A14**, 438 (1976).
[458] A.O. Allen *et al.*, NSRDS-NBS-58 (1976).
[459] P. Benetti *et al.*, Nucl. Instrum. Methods **A32**, 361 (1993).
[460] G. Danby *et al.*, Phys. Rev. Lett. **9**, 36 (1962).
[461] S. van der Meer (1961).
[462] J. A. Formaggio and G. P. Zeller, Rev. Mod. Phys. **84**, 1307 (2012), [arXiv:1305.7513].
[463] H. Faissner, "CERN Spark Chamber Neutrino Experiment", INSPIRE-1377455.
[464] H. Faissner *et al.*, Phys. Lett. **68B**, 377 (1977).
[465] F. J. Hasert *et al.* (Gargamelle Neutrino), Nucl. Phys. **B73**, 1 (1974).
[466] N. Armenise *et al.* (BEBC TST Neutrino), Phys. Lett. **81B**, 385 (1979).
[467] A.E. Asratien *et al.*, Phys. Lett. **79**, 497 (1978).
[468] S. J. Barish *et al.*, Phys. Rev. **D16**, 3103 (1977).
[469] N. J. Baker *et al.*, Phys. Rev. **D23**, 2499 (1981).
[470] J. W. Chapman *et al.*, Phys. Rev. **D14**, 5 (1976).
[471] M. Holder *et al.*, Nucl. Instrum. Meth. **148**, 235 (1978).
[472] I. Ambats *et al.* (MINOS) (1998).
[473] K. Abe *et al.* (T2K), Nucl. Instrum. Meth. **A659**, 106 (2011), [arXiv:1106.1238].
[474] M. H. Ahn *et al.* (K2K), Phys. Rev. **D74**, 072003 (2006), [hep-ex/0606032].
[475] A. A. Aguilar-Arevalo *et al.* (MiniBooNE), Nucl. Instrum. Meth. **A599**, 28 (2009), [arXiv:0806.4201].
[476] A. C. Benvenuti *et al.*, Nucl. Instrum. Meth. **125**, 447 (1975).

[477] C. Athanassopoulos *et al.* (LSND), Nucl. Instrum. Meth. **A388**, 149 (1997), [arXiv:nucl-ex/9605002].

[478] D. S. Ayres *et al.* (NOvA) (2007).

[479] K. Hiraide *et al.* (SciBooNE), Phys. Rev. **D78**, 112004 (2008), [arXiv:0811.0369].

[480] C. Rubbia, CERN-EP-INT-77-08 (1977).

[481] S. Amerio *et al.* (ICARUS), Nucl. Instrum. Meth. **A527**, 329 (2004).

[482] C. Anderson *et al.*, JINST **7**, 10020 (2012).

[483] H. Chen *et al.*, FERMILAB-PROPOSAL-0974 (2007).

[484] B. Abi *et al.*, "Deep underground neutrino experiment (dune), far detector technical design report, volume i: Introduction to dune," (2020), [arXiv:2002.02967].

[485] T. D. Collaboration, A. A. Abud *et al.*, Journal of Instrumentation **17**, 01, P01005 (2022), URL https://dx.doi.org/10.1088/1748-0221/17/01/P01005.

[486] B. Abi *et al.*, Journal of Instrumentation **15**, 12, P12004 (2020), URL https://dx.doi.org/10.1088/1748-0221/15/12/P12004.

[487] D. H. Perkins, Nature **159**, 126 (1947).

[488] S. Aoki *et al.*, Nucl. Instrum. Meth. **A447**, 361 (2000).

[489] N. Uhida *et al.*, Nucl. Instrum. Methods **224**, 50 (1984).

[490] K. Kodama *et al.*, Nucl. Instrum. Meth. **B93**, 340 (1994).

[491] T. Adam *et al.*, Nucl. Instrum. Meth. **A577**, 523 (2007), [arXiv:physics/0701153].

[492] D. Di Ferdinando (OPERA), Radiat. Meas. **44**, 840 (2009), [arXiv:0812.0451].

[493] R. Acquafredda *et al.* (OPERA), New J. Phys. **8**, 303 (2006), [hep-ex/0611023].

[494] T. Fukuda *et al.*, PTEP **2017**, no. 6, 063C02 (2017).

[495] H. Abreu *et al.*, The European Physical Journal C **80**, 1 (2020), URL https://doi.org/10.1140%2Fepjc%2Fs10052-020-7631-5.

[496] F. Collaboration, H. Abreu *et al.*, "The faser detector," (2022), [arXiv:2207.11427].

[497] A. N. Diddens *et al.* (CERN-Hamburg-Amsterdam-Rome-Moscow), Nucl. Instrum. Meth. **178**, 27 (1980).

[498] D. Geiregat *et al.* (CHARM-II), Nucl. Instrum. Meth. **A325**, 92 (1993).

[499] L. A. Ahrens *et al.*, Nucl. Instrum. Meth. **A254**, 515 (1987).

[500] G. Gidal, LBL-91 Suppl., Rev. (1985).

[501] W. K. Sakumoto *et al.*, Nucl. Instrum. Meth. **A294**, 179 (1990).

[502] D. A. Harris *et al.* (NuTeV), Nucl. Instrum. Meth. **A447**, 377 (2000), [hep-ex/9908056].

[503] J. Altegoer *et al.* (NOMAD), Nucl. Instrum. Meth. **A404**, 96 (1998).

[504] L. Aliaga *et al.* (MINERvA), Nucl. Instrum. Meth. **A743**, 130 (2014), [arXiv:1305.5199].

[505] R. Albanese *et al.* (SND@LHC Collaboration), Phys. Rev. Lett. **131**, 031802 (2023), URL https://link.aps.org/doi/10.1103/PhysRevLett.131.031802.

[506] A. Yamamoto, Nucl. Instrum. Meth. **A453**, 445 (2000).

[507] A. Yamamoto and Y. Makida, Nucl. Instrum. Meth. **A494**, 255 (2002).

[508] T. M. Taylor, Phys. Scripta **23**, 459 (1981).

[509] R. L. Gluckstern, Nucl. Instrum. Meth. **24**, 381 (1963).

[510] V. Karimaki, Nucl. Instrum. Meth. **A410**, 284 (1998).